

Study of charged pion, kaon, and (anti)proton
production at high transverse momenta in pp
and p–Pb collisions with the ALICE experiment
at the CERN LHC

Ph.D. Thesis

Gyula Bencédi

Supervisors:

Dr. Péter Lévai (Wigner RCP, Budapest)

Dr. Gergely Gábor Barnaföldi (Wigner RCP, Budapest)

Advisor:

Dr. Antonio Ortiz Velasquez (ICN/UNAM, Mexico City)

Eötvös Loránd University

Doctoral School of Physics

Head: Dr. Jenő Gubicza

Particle Physics and Astronomy Program

Head: Dr. Sándor Katz

Wigner Research Centre for Physics of the HAS

Institute for Particle and Nuclear Physics

Budapest, 2019

Contents

1	Introduction	1
1.1	Objectives of the thesis	4
2	Physics of relativistic heavy-ion collisions in a nutshell	7
2.1	Geometry and evolution of a heavy-ion collision	7
2.2	Collective phenomena in small collision systems	12
2.3	Hadronic interactions in high-energy collisions	14
3	Probing the quark-gluon plasma with high-p_T particles	17
3.1	Particle production in proton-proton and heavy-ion collisions at high p_T . . .	17
3.2	Cold nuclear matter effects in p-A collisions	23
3.3	The role of proton-proton collisions	28
4	Revealing the source of the radial flow patterns in pp collisions	33
4.1	Motivation	33
4.2	Proposed observables for revealing the origin of flow-like effects	34
4.3	Results and discussion	34
4.4	Summary and conclusions	41
5	A Large Ion Collider Experiment at the LHC	43
5.1	Charged particle tracking	45
5.2	Track reconstruction in the central barrel	46
5.3	Primary and secondary vertex reconstruction	48
5.4	Triggering and characterization of events	49
5.5	Centrality determination in p-Pb collisions	49
5.6	Upgrade of ALICE during Long Shutdown 1 and 2	51
6	Particle identification with the ALICE TPC at high p_T	55
6.1	Introduction	55
6.2	Particle identification at the relativistic rise	56
6.3	Determination of the dE/dx signal	57
6.4	Relative resolution and separation power	59
6.5	Calibration of the dE/dx signal	60
6.6	Division into homogeneous samples	63
6.7	Parametrization of the Bethe-Bloch and the dE/dx resolution curves	65
6.8	Fit method: extraction of raw particle yields	72

7	Measurement of identified charged hadron spectra at high p_T	75
7.1	The analysis strategy	75
7.2	Kinematic range	76
7.3	Data and Monte Carlo samples	78
7.4	Event selection	80
7.5	Track selection	83
7.6	Corrections	85
7.7	Yield extraction at high p_T	95
7.8	Estimation of systematic uncertainties	96
7.9	Combination of p_T -spectra from different analyses	107
8	Energy dependence of π^\pm, K^\pm, and $p(\bar{p})$ production in pp collisions	111
8.1	Transverse momentum spectra at $\sqrt{s} = 7$ and 13 TeV	111
8.2	Construction of pp reference at $\sqrt{s} = 5.02$ TeV	117
8.3	Particle production as a function of collision energy	120
8.4	Comparisons to theoretical models	122
9	Multiplicity dependence of π^\pm, K^\pm, and $p(\bar{p})$ production in pPb collisions	129
9.1	Transverse momentum spectra as a function of charged-particle multiplicity	129
9.2	Nuclear modification factor for π^\pm , K^\pm , and $p(\bar{p})$	131
9.3	Transverse momentum and multiplicity dependence of particle ratios	135
9.4	Comparison to theoretical calculation	137
10	Summary	139
	Appendix A Kinematic variables	143
	Appendix B Aspects of improved position resolution of a novel MWPC	145
	B.1 Test beam setup	145
	B.2 Data analysis	147
	B.3 Measurement results on position resolution	149
	Acronyms	153
	Bibliography	155
	Acknowledgments	176

CHAPTER 1

Introduction

Several decades of intensive research, including the discovery of the fundamental constituents of matter and their interactions between each other, resulted in the formulation of the Standard Model (SM) of particle physics. The Standard Model of elementary particles consists of matter made of a set of fundamental spin-1/2 particles, the fermions being leptons and quarks, which are arranged further by their mass into three generations. Leptons include the electrically charged electrons (e), muons (μ), and taus (τ), with their corresponding electrically neutral partners, the neutrinos ν_e , ν_μ , and ν_τ , respectively. The ordinary matter is composed of up (u) and down (d) quarks from the first generation, which form protons and neutrons inside the nucleus of the atoms surrounded by electrons. The u and d quarks together with the strange (s) quark from the second generation are labeled as light quarks. The charm (c) quark (from the second generation), and the beauty (b), and top (t) quarks from the third generation are commonly called heavy quarks. For each of these particles, there exists an antiparticle, which carries opposite quantum numbers. The four fundamental forces that govern the interactions between particles are the electromagnetic, weak, strong, and gravitational. The SM describes the first three of these interactions and is a great triumph of particle physics because it provides good description for various experimental observations.

The underlying theoretical framework of the SM is a (gauge) quantum field theory, obeying the internal symmetries of the unitary group $SU(3)_C \times SU(2)_L \times U(1)_Y$. Here, C, L, and Y stand respectively for color, left-handedness, and the weak hypercharge which characterize the coupling of the mediating spin-1 bosons. The interactions between elements of the $SU(2)_L \times U(1)_Y$ group correspond to the massive (W^\pm and Z^0) bosons, and the photon. The massive bosons mediate the charged and neutral current of the weak interactions. The mass of the bosons is a consequence of the spontaneous electroweak symmetry breaking. Their coupling to the scalar Higgs field generates the masses of the three massive electroweak gauge bosons; the corresponding boson was discovered in 2012.

The interactions between the ground states of the $SU(3)_C$ group correspond to the strong interaction characterized by Quantum Chromodynamics (QCD), which is formulated in terms of quarks and gluons being, to our present knowledge, the basic degrees of freedom that compose hadronic matter. Quarks carry color and electric charges. There are three color charge states which are complemented by the analogous anticolors. The color is exchanged by eight colored gluons. The strength of the interaction is given by the strong coupling α_S . QCD succeeds in providing a qualitative (and quantitative) description of a wide range of observations in hadronic collisions. One of the most important properties of

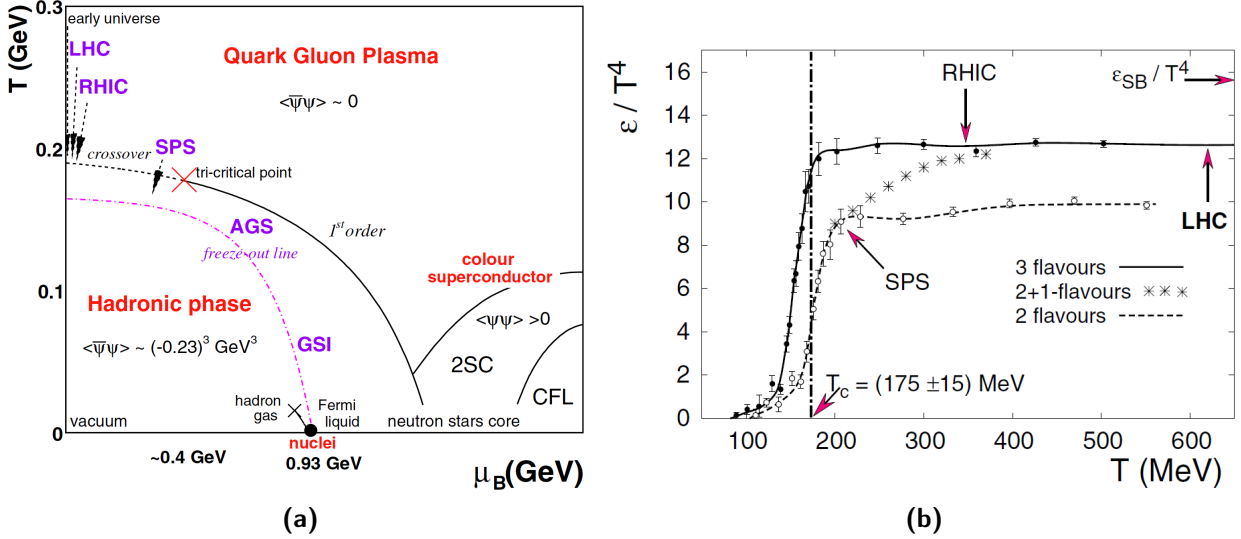


Figure 1.1: (a) QCD phase diagram in the temperature–baryochemical potential (T, μ_B) plane. (b) Energy density ϵ/T^4 as a function of temperature T for QCD with two and three degenerate quark flavors, and two light and one heavier (strange) quarks. Figures are taken from Ref. [4].

QCD is color confinement, an experimentally well-established phenomenon, although there is no analytic proof of the concept. It states that no single free quarks, carrying fractional charge, can be observed in nature, as they are bound into color singlet states with zero net-color charge, called hadrons. Conceptually, this limits the type of possible bound hadronic states to quark-antiquark ($q\bar{q}$) pairs named mesons, three quark states (qqq) named baryons and combination of these, e.g. pentaquarks ($qqqq\bar{q}$). Further property of QCD is asymptotic freedom which is a consequence of the decrease of the QCD running coupling $\alpha_S(Q^2)$ with increasing momentum transfer Q^2 .

The state of QCD matter can be visualized in a phase diagram shown schematically in Fig. 1.1a. The figure describes the behavior for changes of the thermodynamic parameters, the temperature T and the baryochemical potential μ_B which is related to the net baryon density. Ordinary nuclear matter is located at $T = 0$ MeV and $\mu_B = 0.93$ GeV/ c^2 [1], while μ_B is zero in the vacuum. At low temperature and low momentum transfer, the chiral symmetry is spontaneously broken in its ground state. In this regime, the nuclear matter behaves as a hadron gas, where the so-called chiral quark condensate $\langle \bar{\Psi}\Psi \rangle$, playing a role of an order parameter, takes a finite value [2]. Experimental access to the QCD phase diagram is rather limited. At typical hadron collider energies, i.e. at large Q^2 , the perturbative expansion of the QCD permits a detailed quantitative comparison with experimental data. It is worth noting, that the average momentum transfer in high energy collisions is still rather small. For temperatures $T \gg \Lambda_{\text{QCD}}$, where the QCD coupling becomes weak, partons, i.e. quarks and gluons, can be considered as quasi-free leading to chiral-symmetry restoration. In the non-perturbative regime of QCD (below the critical temperature T_c) only phenomenological models can be applied. In this domain, numerical methods of QCD on lattice were developed.

Lattice QCD (LQCD) calculations [3] of the QCD phase transition predict a new state of matter, a deconfined state of quarks and gluons, at energy densities (well) above a critical value $\epsilon_c \sim 1 \text{ GeV}/\text{fm}^3$ with a critical temperature $T_c \sim 150 - 190 \text{ MeV}$ [5, 6], where the chiral condensate disappears. Such a state is called the Quark-Gluon Plasma (QGP), which is believed to have existed in the early Universe, a few microseconds after the Big Bang.

The transition from hadronic phase to the QGP phase is shown in Fig. 1.1b, where the normalized energy density ϵ/T^4 is proportional to the number of degrees of freedom and T_c depends on the number of flavors and the mass of the quarks. In the thermal equilibrium of massless non-interacting particles, the bosonic and fermionic contributions to the energy density are respectively $\pi^2 T^4/30$ and $7/8 \times (\pi^2 T^4/30)$. In the QGP phase, the number of quark and gluon degrees of freedom is larger than those in the hadron gas phase. The limit where the deconfined quarks and gluons are non-interacting is called the Stefan–Boltzmann (SB) limit of this partonic state. The SB limit as a function of temperature T at zero chemical potential is determined by the corresponding number of degrees of freedom of quarks and gluons. The energy density ϵ/T^4 , obtained from LQCD calculations, is shown in Fig. 1.1b for two and three degenerate quark flavors, and for $2 + 1$ quark flavors (up, down, and strange), which was obtained from a more realistic calculation. The curves at T_c experience a rapid rise due to the sudden liberation of quarks and gluons from hadrons and approach the Stefan–Boltzmann limit ϵ_{SB}/T^4 for an ideal quark-gluon gas at high temperature, indicated by the arrow in the figure. The curve with $2 + 1$ quark flavors, representing the case at the Super Proton Synchrotron (SPS) at the European Organization for Nuclear Research (CERN) or at the Relativistic Heavy-Ion Collider (RHIC) at Brookhaven National Laboratory (BNL), flattens out above the transition region. In a pure gauge theory, the transition appears to be first-order [7]. However, the inclusion of $2 + 1$ quark flavors and their masses can change the transition from first-order to second-order to a smooth crossover, indicated by the dashed line in Fig. 1.1a.

A number of previous and current experiments try to map the phase boundary between the hadron gas phase and the QGP phase and to locate the critical end point (named as tri-critical point in Fig. 1.1a), at which the first-order phase transition changes to a smooth crossover. Ultra-relativistic heavy-ion collisions, performed at large particle accelerators like at BNL RHIC and at the CERN Large Hadron Collider (LHC), are well suited to reproduce and to study these phase transitions and the generated QGP phase in a controlled laboratory environment. The investigation of the QGP and its transition to normal hadronic matter is of crucial importance. It helps us better understand the strong interaction and allows to verify Standard Model predictions. On the other hand, it addresses cosmological questions which, in turn, could extend our knowledge about the evolution of the early Universe.

The CERN LHC provides the highest collision energies achieved so far in particle accelerators. Given the high energy and consequently high temperature, the baryochemical

potential is close to zero in the collisions. In fact, the maximum temperature achieved in heavy-ion collisions exceeds the critical temperature several times, and it is possible to reach a point above the crossover region indicated in Fig. 1.1a, where a complete transition to the QGP can take place. Studying high-energy collisions of heavy ions allows us to trace back the evolution of our Universe when it cooled down to the QGP state about $1\text{ ps} - 1\mu\text{s}$ [8] after the Big Bang and eventually into bound hadronic state as it is observed today.

1.1 Objectives of the thesis

The main characteristic features of the QGP are the bulk collectivity and opacity to jets. The collective behavior is observed for example as a mass-dependent hardening of the transverse momentum (p_T) spectra by the radial flow which is more pronounced for heavier hadrons. Hard and strongly interacting partons, forming a collimated spray of particles referred to as a jet, produced at the early stage of heavy-ion collision traverse the plasma and lose their energy. This partonic energy loss is observed as a reduction of the amount of produced high- p_T particles and fully reconstructed jets.

A Large Ion Collider Experiment (ALICE) is a dedicated heavy-ion experiment at the CERN LHC which is optimized to study the properties of the strongly interacting QGP created in ultra-relativistic heavy-ion collisions. The ALICE detector has a unique capability among the other LHC experiments to identify a large variety of particles using different particle identification (PID) techniques and to reconstruct tracks in a wide p_T range. The PID is necessary as the amount of suppression of high- p_T particles was found to depend strongly on the hadrochemical composition of the produced particles.

Measurements of inclusive hadron production at mid-rapidity at the LHC probe longitudinal parton momentum fraction, Bjorken x , in the range $10^{-4} < x < 10^{-2}$. This range extends the measurements to lower x values by an order of magnitude with respect to that reached by other colliders at lower center-of-mass energy (\sqrt{s}).

With the increase of \sqrt{s} reached at the LHC opens up domains in x , where the contribution of gluons to inclusive hadron production becomes dominant. Therefore, the spectra of identified particles at the top LHC energy in proton-proton (pp) collisions provide new constraints on the gluon fragmentation. More precisely, they effect the gluon-to-pion and gluon-to-kaon fragmentation functions which are poorly constrained and have considerable uncertainties in theoretical calculations due to limited amount of data at LHC energies.

Also, in this kinematic regime the nuclear modification to hadronic structure is expected to be sizable. By using a proton instead of a heavy nucleus as one of the projectiles, measurements of proton-lead (p-Pb) collisions have unique sensitivity to the initial state nuclear wave function. High- p_T identified particle spectra measured in p-Pb collisions provide new constraints on the nuclear-modified parton distribution functions (nPDFs) and the flavor dependence of sea-quark nPDFs, which are key inputs in interpreting a large amount of

experimental data like deuterium-gold (d–Au) and deep inelastic scattering.

In this thesis, I present measurements in collisions of protons, and of protons and lead nuclei recorded by ALICE at the CERN LHC. The interpretation of the QGP properties requires comparisons with control (or reference) measurements carried out in pp and p–Pb collisions. However, recent results on particle production at the LHC obtained in high-multiplicity pp and p–Pb collisions revealed phenomena which are similar to those seen in lead-lead (Pb–Pb) collisions—where they are attributed to bulk collective effects of the QGP formation. The origin of these phenomena is investigated, and the analysis of pp and p–Pb collision data provides further inputs to this discussion.

The prime objective of this thesis is to provide precise measurements of identified hadron spectra over wide transverse momentum ranges at different LHC energies. In order to achieve these goals, it is essential to study the production of charged pions, kaons, and (anti)protons in pp and p–Pb collisions with the best possible accuracy at high p_T (up to 20 GeV/ c). Such studies extend the existing measurements over new, yet unmeasured kinematic regimes at the LHC which are of particular importance for the quantitative description of particle production at the LHC. Furthermore, the high-precision measurements achieved in the intermediate- p_T region (2 – 10 GeV/ c) are also important, because this is the region, where initial state (cold) nuclear matter effects, such as shadowing and Cronin enhancement, have been reported by previous experiments, and where particle ratios (K/π and p/π) are affected by large final state effects in central Pb–Pb collisions. The particle species dependency of the nuclear modification factor in p–Pb collisions is important for better understanding parton energy loss mechanisms in heavy-ion collisions. On the other hand, the measurements of charged pions, kaons and (anti)protons in minimum bias pp collisions also serve as reference data to study nuclear effects in p–Pb and Pb–Pb collisions and provide input to tune the modeling of several observables in Monte Carlo event generators.

This Ph.D. thesis mainly focuses on studying particle production around mid-rapidities ($|y| < 0.5$) in minimum bias inelastic (INEL) pp collisions as a function of \sqrt{s} and in non-single diffractive (NSD) p–Pb collisions as a function of event charged-particle multiplicity measured at forward rapidities. I performed the following measurements:

- Single-inclusive identified charged particle p_T spectra have been measured in minimum bias INEL pp collisions in the mid-rapidity region at $\sqrt{s} = 7$ and $\sqrt{s} = 13$ TeV during Run 1 (2009–2013) and Run 2 (2015–2018) data taking periods of the LHC, respectively. These are important results in order to determine the collision energy dependence of various measured observables, such as p_T -differential as well as p_T -integrated particle yields, yield ratios, and average transverse momenta.
- Single-inclusive identified charged particle p_T spectra have been measured in NSD p–Pb collisions at $\sqrt{s_{NN}} = 5.02$ TeV near mid-rapidity in intervals of charged-particle multiplicity, generally called as “event activity” classes, determined in the forward

rapidity region (Pb-going side). Basic observables, such as p_T -differential as well as p_T -integrated particle yields and yield ratios, were determined based on selections made in event activity classes.

- Nuclear modification factors (R_{pPb}) have been determined in NSD p–Pb collisions at high p_T (up to 20 GeV/ c). Their dependence on particle species is investigated. Due to lack of measurements in pp collisions at $\sqrt{s} = 5.02$ TeV during LHC Run 1, the R_{pPb} for all considered particle species was constructed using data-based pp reference spectra obtained by interpolation of existing data at different collision energies.

The thesis is organized as follows. In Chapter 2, I present a theoretical introduction to heavy-ion collisions, discussing only those parts which are relevant for the physics covered by this thesis. In Chapter 3, the hard probes of the hot and dense QCD matter are discussed, in particular, the production of high- p_T particles, which is the main subject of this thesis. In Chapter 4, I discuss collective phenomena in small collision systems, and present a recently developed tool which helps to better understand the intriguing phenomena observed by several LHC experiments in high-multiplicity pp and p–Pb collisions. Chapter 5 provides a brief description of the ALICE experiment. The experimental setup is shown and the subdetectors relevant to the presented measurements are discussed. The main components of the track and vertex reconstruction as well as the concept for the triggering and characterization of events are reviewed. I shortly mention the upgrade of ALICE during Long Shutdown 1 and 2; in connection to the upgrades I introduce my contribution to the ALICE Very High Momentum Particle Identification Detector (VHMPID) upgrade project. In Chapter 6, I give a detailed description of the analysis method to identify charged hadrons at high transverse momentum by measuring the specific energy loss dE/dx in the fill gas of the ALICE Time Projection Chamber. Chapter 7 provides the technical details that are essential for my data analysis: the used data sets, and event and track selection criteria, the applied correction methods as well as the evaluation of the systematic uncertainties. Chapters 8 and 9 summarize my analysis results including their discussion. Finally, a summary is given in Chapter 10.

For clarity, a summary of the basic kinematic variables and conventions is given in Appendix A. Appendix B discusses the measurement and data analysis details for the determination of the position resolution of a novel prototype multi-wire proportional chamber with small size, which I built and tested for the ALICE VHMPID.

Figures that are labeled as “– This thesis –” contain results, which have been prepared especially for this thesis and, therefore, they are neither documented nor published elsewhere. Some of these figures which present preliminary results from the ALICE collaboration, but not labeled as “Preliminary”, are not approved by the collaboration.

CHAPTER 2

Physics of relativistic heavy-ion collisions in a nutshell

This chapter is meant to give a brief introduction to the physics background of relativistic heavy-ion collisions in which the work of this thesis partially takes place. A geometrical description of a relativistic heavy-ion collision and its space-time evolution is discussed. Fundamental properties of the Quark-Gluon Plasma (QGP) are highlighted in direct connection to the scope of the thesis. Some key experimental probes of the QGP are mentioned, and a brief review of the intriguing results regarding small collision systems is also given. Finally, I close the chapter with a short review on hadronic interactions in high-energy collisions.

2.1 Geometry and evolution of a heavy-ion collision

As mentioned in the previous chapter, the collisions of heavy ions are used at ultra-relativistic energies to study the strongly interacting QCD matter in the laboratory. Specifically, Pb–Pb collisions at the CERN LHC are a prominent tool to study the phase diagram of QCD, and the formation of the QCD matter at low baryo-chemical potential and high temperatures.

When two Pb nuclei collide, multiple interactions among the participating nucleons create an out-of-equilibrium system of partons. For this to happen, the crossing time of nuclei has to be much smaller than the characteristic time of the strong interaction $\tau_{\text{cross}} \ll \tau_{\text{strong}} \approx 1/\Lambda_{\text{QCD}} \sim 1 \text{ fm}/c$. If the energy density reached by the system is higher than the critical energy density ($\gtrsim 1 \text{ GeV}/\text{fm}^3$), a droplet of QGP is expected to be formed. The dynamical evolution of such a system is very complicated. The full description of the heavy-ion collision data crucially depends on the dynamics taking place before (local) thermalization that has significant uncertainties in predicting the final state observables. In fact, it is still an open question whether the thermalization of the deconfined matter can take place [9, 10]. Initial state even-by-event fluctuations have vital importance on the (anisotropic) collective flow effects and on other final state observables, see e.g. Refs. [11–13].

The initial state geometry and the evolution of the system formed in heavy-ion collisions can be theoretically modeled. In the following sections, I give a brief review on these subjects.

2.1.1 Glauber modeling in high-energy nuclear collisions

In a collision between heavy nuclei, the initial geometry plays an important role in describing the nature of the collision. Being related to the geometry of the collision, the concept of centrality is introduced for this purpose. Centrality is of great interest in heavy-ion collisions

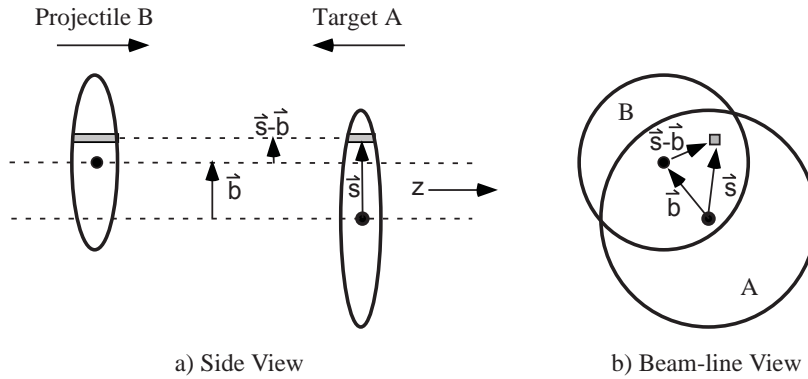


Figure 2.1: Schematic representation of the optical Glauber model geometry in the (a) transverse and (b) longitudinal views. Figure is taken from Ref. [14].

because, for instance, hard probes such as the nuclear modification factor (described in Section 3.1.1) shows strong variation with this quantity. The centrality, experimentally expressed in percentiles, depends (for spherical nuclei) on the impact parameter b which is the distance between the centers of the two colliding nuclei in the plane transverse to the beam direction, as indicated in Fig. 2.1. Collisions with small b or large overlap area between the nuclei are called central events, whereas those with larger b are called peripheral events.

Typical quantities to describe the centrality of an event are the number of participating nucleons N_{part} that undergo at least one inelastic nucleon-nucleon collision and the number of binary nucleon-nucleon collisions N_{coll} . These numbers are strongly correlated with the size of the overlap region. The more central the event is, the larger the overlap region becomes and so does the number of interacting nucleons. With the help of the Glauber model [14, 15] the geometrical quantities (N_{part} and N_{coll}) can be derived from the impact parameter b .

Since, N_{part} and N_{coll} are not directly measurable quantities, they have to be related to a measurable observable \mathcal{M} via some model. The model essentially allows one to calculate the conditional probability $\mathcal{P}(\mathcal{M} | \mathcal{G})$ to observe \mathcal{M} for a certain value of $\mathcal{G} \in \{N_{\text{part}}, N_{\text{coll}}\}$. Hence, for a given \mathcal{M} value, more precisely a given interval of \mathcal{M} often referred to as event class, an average \mathcal{G} is extracted; for details see e.g. Ref.[16]. In this (semi-classical) model, a heavy-ion collision is considered to be a superposition of multiple nucleon-nucleon collisions. Per event, the nucleons are distributed according to the Woods–Saxon potential $\rho(\vec{r}) = \frac{\rho_0}{1 + \exp(\frac{|\vec{r}| - R}{a})}$, where R is the radius of the nucleus, a is the skin depth, and ρ_0 is the nucleon density and acts as a normalization parameter, satisfying $\int d^3r \rho(\vec{r}) = A$ with A being the number of nucleons in the nucleus A. These parameters (for the different nuclei) are obtained by fits to low-energy electron scattering data [17]. The quantity $\rho(\vec{r})$ can be interpreted as the probability per unit volume to find a specific nucleon in the nucleus at the position \vec{r} . The probability per unit transverse area of a given nucleus A to be located in the considered area is $T_A(\vec{s}) = \int \rho(\vec{s}, z_A) dz_A$. Defining T_B in a similar way for a nucleon in nucleus B, one can define the nuclear overlap function over the whole overlapping

region for a given impact parameter b in an A-B collision shown schematically in Fig. 2.1: $T_{AB}(\vec{b}) = \int T_A(\vec{s}) T_B(\vec{s}-\vec{b}) d^2s$, which has the units of an inverse area. The probability of the inelastic interaction to happen between nuclei A and B is $\sigma_{\text{INEL}}^{\text{NN}} T_{AB}(\vec{b})$, where $\sigma_{\text{INEL}}^{\text{NN}}$ is the inelastic nucleon-nucleon cross section. Using that the probability of having a certain amount of such interactions is given by the binomial distribution, the total interaction probability for a given \vec{b} is

$$\frac{d^2\sigma_{\text{INEL}}^{\text{AB}}}{db^2} = 1 - \left[1 - \sigma_{\text{INEL}}^{\text{NN}} T_{AB}(\vec{b})\right]^{\text{AB}}. \quad (2.1)$$

The total number of binary nucleon-nucleon collisions follows by taking the mean value of the binomial distribution with A and B being the number of nucleons in nuclei A and B, respectively:

$$N_{\text{coll}}(b) = AB \sigma_{\text{INEL}}^{\text{NN}} T_{AB}(b). \quad (2.2)$$

The number of participating nucleons can be calculated in the current combinatoric approach as follows:

$$N_{\text{part}}(b) = A \int T_A(s) \left(1 - [1 - \sigma_{\text{INEL}}^{\text{NN}} T_B(b-s)]^B\right) d^2s \\ + B \int T_B(s) \left(1 - [1 - \sigma_{\text{INEL}}^{\text{NN}} T_A(s)]^A\right) d^2s. \quad (2.3)$$

Experimentally, Glauber Monte Carlo simulation is used for the estimation of $N_{\text{part}}(b)$ and $N_{\text{coll}}(b)$; the procedure, for the case of p-Pb collisions, is discussed later in Section 5.5.

2.1.2 Space-time evolution of heavy-ion collisions

The space-time evolution of a heavy-ion collision is summarized schematically in Fig. 2.2. Without the presence of the QGP phase (shown in the left side of the figure), it is usually discussed within the Landau hydrodynamical model [18] in which an interacting hadron matter forms after the de-excitation of the initial phase, which freezes out into single hadrons at a later stage. If a QGP phase exists, the evolution can be treated by the Björken scenario [19] which was developed for increased incident energies that resulted in high energy density matter with low net baryon content [20, 21]. In Pb-Pb collisions at the CERN LHC, the initial energy density is approximately three times higher than in Au-Au collisions at $\sqrt{s_{\text{NN}}} = 200$ GeV at BNL RHIC [22]. In the Björken picture, the two incoming highly Lorentz contracted nuclei (propagating near the light cone) approach each other at the collision time $t = 0$ and interaction point $z = 0$. The matter evolves according to the following stages:

- (1) In the initial, pre-equilibrium phase ($\tau < \tau_0$), the parton constituents scatter until they reach a local thermal equilibrium at τ_0 . The duration of this process is estimated to be around 1 fm/c [19]. The production mechanism of the initial parton-parton scattering is not well understood. For its dynamical description several models are proposed, for example, the color glass condensate which is capable of describing the properties of the

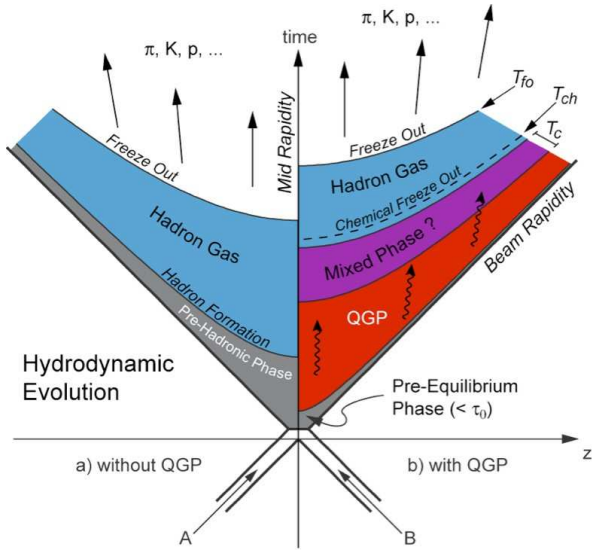


Figure 2.2: Schematic representation of the hydrodynamic evolution of a heavy-ion collision without (left side) and with (right side) the QGP phase in time t and longitudinal z Minkowski coordinates. Both situations are displayed within the physical light cone, where different stages are separated by hyperbolic curves corresponding to the proper time $\tau = \sqrt{t^2 - z^2}$. Figure is taken from Ref. [24].

high-density gluon fields within heavy ions, see Ref. [23] for a review.

- (2) The temperature from the initial state is increasing and if the energy density ϵ of the thermalized medium exceeds that of the phase transition, i.e. $\epsilon > 1 \text{ GeV}/\text{fm}^3$, the QGP is formed. Due to the pressure gradient between the high-density medium and the surrounding vacuum, the system expands rapidly according to ideal (reversible) relativistic hydrodynamics—assuming an (almost) perfect liquid without or with low viscosity [25]. During the expansion the QGP cools down to the point of a phase transition from deconfined to confined matter.
- (3) After the phase transition which happens at the critical temperature T_c , hadronization of quarks and gluons starts. This stage includes two subsequent stages. In one of the stages, the fragmentation which involves parton-shower and recombination (or coalescence) where thermal or shower partons which are close in phase space recombine to form hadrons; microscopic kinetic models successfully describe this stage [26]. In another intermediate state called mixed phase, both QGP and hadron gas are present.
- (4) As the temperature drops, the QGP phase is no longer sustainable and the system freezes out. The chemical freeze-out occurs at the temperature T_{ch} . The relative abundances of hadrons, i.e. the hadrochemical composition of particles (except for decays and resonances) is fixed when the inelastic collisions between hadrons cease. The generated hadrons may still interact and can be described by a thermal statistical model for a hadron gas [27].
- (5) The elastic scatterings keep continuing beyond chemical freeze-out, and change the momenta of the particles. It happens until the hadron gas becomes so dilute that the mean free path of the particles is comparable to size of the system itself, and the time scale of the collisions becomes larger than the time scale of the expansion, making rescattering negligible [28]. This stage is called the kinetic freeze-out which transforms the strongly coupled system to a weakly coupled one. After this stage, in the final state, the mo-

momentum distributions are fixed, and the particles stream freely to the detectors without further interactions.

The kinetic freeze-out stage is reached in the order of 10 fm/c after the collision which was measured by the ALICE collaboration at the LHC in two-pion Bose–Einstein correlations in central Pb–Pb collisions at $\sqrt{s_{\text{NN}}} = 2.76$ TeV [29]. The obtained values (which are larger by 40% than that at RHIC) showed that the decoupling time at mid-rapidity is so short that it makes the direct observation of the QGP impossible. However, final state hadrons encode information on the whole evolution of the system and are well-accessible to the experiments. As the QGP is composed of low- and high-momentum partons, commonly called as “soft” and “hard”, after hadronization the respective soft and hard particles are used as probes to measure the properties of the deconfined matter. Soft particles are the dominant contribution and behave as a relativistic fluid, while hard partons are produced at the very early stage of the collision; they traverse the QCD matter and lose energy [30]. I will discuss hard probe observables in Chapter 3, paying particular attention to those which are related to my work.

Global event properties describe the state and the dynamical evolution of bulk matter created in heavy-ion collisions. They serve as a measure for the characteristics of substantially all the particles which have momenta below a few GeV/c. Most of these bulk observables have the property that they are related to soft processes which have small momentum transfer, i.e. $Q \lesssim \Lambda_{\text{QCD}}$. Hence, these are typically determined using non-perturbative (lattice) QCD calculations and phenomenological as well as statistical thermodynamical models. Assuming that the created medium is in local thermal equilibrium allows one to describe the main features of bulk particle production with two basic concepts. Related to chemical equilibrium, the p_{T} -integrated particle yields or abundances follow the expectations from thermal-statistical models [31]. In the view of kinetic equilibrium, the spectral shapes and azimuthal anisotropies [32] can be explained by a common hydrodynamic expansion of the studied system [33].

The azimuthal anisotropy of the particle yield is the clearest signature of collective flow in heavy-ion collisions, which is sensitive to early-evolution effects (such as rescattering) and carries information from the partonic and hadronic stage of the collision. In non-central heavy-ion collisions, there is an initial spatial anisotropy in the collision zone. The almond-shaped interaction volume between colliding nuclei can be approximated with an ellipsoid. The overlap causes local pressure gradients that are largest in the direction of the reaction plane¹ Ψ_{RP} , and more moderate in directions orthogonal to it [34, 35]. The spatial anisotropy with respect to the reaction plane translates into a momentum anisotropy of the produced particles (anisotropic flow) [36] which can be observed in the azimuthal distribution of hadrons. The final state invariant cross section can be written by a Fourier

¹The reaction plane is spanned by the direction of the impact parameter and the beam direction.

series, to show the azimuthal dependence:

$$E \frac{d^3N}{dp^3} = \frac{d^2N}{2\pi p_T dp_T dy} \left[1 + 2 \sum_{n=1}^{\infty} v_n \cos \left(n(\phi - \Psi_{RP}) \right) \right]. \quad (2.4)$$

The strength of the asymmetry is characterized by the Fourier coefficients v_n . The isotropic (or azimuthal angle-averaged) component is called directed flow, whereas the second-order coefficient v_2 is called the elliptic flow. The p_T -differential v_2 for $p_T < 2 \text{ GeV}/c$ reveals a smaller value for heavier particles. This mass ordering is a combined effect of elliptic flow and radial flow. The latter component aims to equalize the velocities of particles and, in turn, shifts heavier particles to higher p_T than the light ones. The effect of a given azimuthal flow asymmetry thus manifests itself at higher momenta for particles with a larger mass. Measurements on the elliptic flow of identified hadrons in Pb–Pb collisions by the ALICE collaboration indicate that the created, strongly interacting medium behaves like a nearly perfect liquid with small value of shear² viscosity, i.e. the viscosity to entropy density ratio η/s is about $1/4\pi$, see Ref. [37] for more details.

2.2 Collective phenomena in small collision systems

Two key evidences for the formation of strongly interacting, hot and dense Quark-Gluon Plasma (sQGP) in relativistic heavy-ion collisions are the bulk collectivity [38] and the presence of jet quenching [39]. These effects are absent in control measurements performed in proton–proton (pp) and proton-nucleus (p–A) collisions [40]. Note that control measurements are vital to characterize to which extent the initial state effects can be differentiated from the final state ones related to interactions in the QGP [41].

In 2010, soon after the start of the LHC physics program, the measurement of two-dimensional angular correlation function in high-multiplicity pp collisions at $\sqrt{s} = 7 \text{ TeV}$ [42] revealed a pronounced longitudinal structure (ridge). The measurements of multi-particle correlations over large η range in high-multiplicity p–Pb collisions [43–47] exhibited remarkable similarities with results related to collective effects seen in Pb–Pb collisions at $\sqrt{s_{NN}} = 2.76 \text{ TeV}$ [48].

Further measurements studying particle production in high-multiplicity pp and p–Pb events resemble some characteristic features seen in Pb–Pb. Hydrodynamic models, assuming strong collectivity, quantitatively describe most observables of the small-system data [49]: the radial flow [50–53] and the transverse momentum (p_T) and pseudorapidity (η) dependence of azimuthal anisotropies v_n [44, 54–58] as well as their characteristic particle mass dependence [37, 59–62]; and also the strangeness enhancement [63–65].

In p–Pb, and even more in pp, collisions the p_T spectra of identified particles at low p_T

²Besides bulk viscosity, shear viscosity is particularly important because it reduces the medium’s ability to convert initial transverse pressure anisotropies into final transverse momentum anisotropies.

harden with increasing multiplicity [52, 53, 66] and, if interpreted in the same way as in Pb–Pb collisions, reveal even stronger radial flow at similar multiplicities — accounting for the longer cooling and expansion of the system [67, 68].

At intermediate p_T , in particular for $2 \lesssim p_T \lesssim 5 \text{ GeV}/c$, the yield of heavier particles is enhanced compared to that of lighter particles [52, 65, 69–71] which effect is typically described by employing a combination of hydrodynamical calculations and models which include the effect of recombination [72] or quark coalescence [73]. In the same p_T region, particle ratios, for example the proton-to-pion, also show an enhancement, whose magnitudes increase and their maxima shift to higher p_T with increasing multiplicity, depicting a similar p_T dependence to Pb–Pb collisions [53]. While no evidence for direct jet quenching has been observed yet in p–Pb collisions [74, 75], a possible non-zero v_2 value of about 5% at p_T up to $10 \text{ GeV}/c$ (albeit with rather large uncertainty) have been reported [76]. In analogy to Pb–Pb, this observation may be a hint of parton energy loss. Besides, energy loss effects in cold nuclear matter might have chance to be considered in small systems too [77–79].

Apart from assuming that the underlying physics is the same for the observed phenomena, there are other possibilities for their explanations. Alternatively, microscopic effects such as Multiple Parton Interaction (MPI) [80] and the Color Reconnection (CR) mechanism of strings implemented in the PYTHIA model [81] can also qualitatively explain the data [82]. PYTHIA with CR produces radial flow patterns via boosted color strings and describes the increase of the average p_T with multiplicity [83]. The same observables have been studied with parton transport models, such as the A Multi-Phase Transport model [84], which employ non-equilibrium parton dynamics. These calculations attempt to microscopically describe the underlying physics, leading from weak to strong collectivity depending on the parton density and interaction cross sections. The ridge structure in two-particle correlations can be generated assuming incoherent elastic scatterings of partons and the string melting mechanism — which concept, however, is not yet fully understood. Other mechanisms like “color ropes”, which are formed by the fusion of color strings close in space, are also successfully applied, leading to the increase of both strangeness production and radial flow-like effects [85, 86]. Another possibility is the glasma graph framework (IP-Glasma) derived in the context of the color glass condensate effective theory of QCD [87]. Recent calculations combining the initial state gluon momentum anisotropy from the IP-Glasma with a Lund string fragmentation (implemented in PYTHIA) are able to describe many features of two-particle correlations [88–90], including the long range nature, the double-ridge structure, the strength and shape, the non-trivial multiplicity dependence, as well as mass ordering of average p_T and v_2 both in pp and p–Pb collisions.

These results suggest that, in general, there is no single framework on the market yet that can quantitatively describe all data on equal footing; for a recent review see e.g. Ref. [91].

2.3 Hadronic interactions in high-energy collisions

In a high-energy hadron-hadron collision, e.g. in a pp collision, where the colliding nucleons have much larger energy than their rest masses, the transferred momentum between them can be so large that the collision actually takes place among constituent partons, referred to as (hard) parton scattering. This hard interaction is governed mainly by the differential cross section for $2 \rightarrow 2$ parton scattering processes. Simultaneously to the hard process, other semi-hard processes can occur between the other partons; this process is likely to occur more than once, referred to as multiple-parton interaction.

Apart from (semi-)hard parton scatterings, several other processes take place during the collision. The attained high energy allows the formation of new partons between scattered partons in a way that one parton may branch into many partons (e.g. $q \rightarrow qg$) which is dominated by perturbative splitting described by the Dokshitzer–Gribov–Lipatov–Altarelli–Parisi (DGLAP) equations [92–95]. Depending on which state of the interaction it happens the process is called initial- or final state parton shower. Final-state shower becomes more relevant with larger collision energies influencing the structure of jets. Partons which do not take part in the hard scattering are considered as remnants of the incoming protons. Since QCD confinement forbids free color charges, the separated partons have to fragment into color-neutral hadrons. This hadronization process happens when a parton’s virtuality scale Q^2 is below $\mathcal{O}(1 \text{ GeV})$ and is described by phenomenological models. Hadrons which are unstable may decay further.

In hadron-hadron scatterings, interactions are classified by the characteristics of the final states. Interactions can be either elastic or inelastic (INEL). If the scattering is elastic, both protons remain intact and no other particles are produced. The scattered protons change direction but still appear in the forward scattering region. Typical detectors at hadron colliders cover only a limited range around mid-pseudorapidity ($\eta \sim 0$); thus elastic events are usually invisible to the detectors. A common classification of INEL pp collisions is into diffractive and non-diffractive (ND). In diffractive reactions, no internal quantum numbers (e.g. color or charge) are exchanged between the colliding particles. In a diffractive scattering, the energy transfer between the two interacting protons is still small (soft collision), but one or both protons dissociate into multi-particle final states with the same internal quantum numbers as the colliding protons. If only one of the protons dissociates then the interaction is single-diffractive (SD); double-diffractive (DD) events are those in which both protons dissociate. Central diffractive collisions leave both protons intact, but particles around mid-rapidity are additionally produced. The transverse momenta of particles generated in diffractive collisions are much smaller compared to ND processes. Nevertheless, diffractive processes account for a large fraction of the total cross section [96, 97] and need to be taken into account when calculating the inelastic cross sections. In non-diffractive interactions, there is an

exchange of color charge, and subsequently, more hadrons are produced in the mid-rapidity region; their yield is steeply falling towards higher rapidities. Non-diffractive interaction is the dominant process in pp interactions. At LHC energies, the ND cross section dominates. According to measurements by the ALICE collaboration, about 68% of inelastic collisions are ND-type [98].

Inclusive particle production in high-energy hadronic collisions has contributions from both “soft” and “hard” interactions. Semi-hard (and hard) parton-parton scatterings contribute dominantly to the inelastic hadron production cross sections at LHC energies. Besides, soft scatterings have a non-negligible importance which dominantly includes multi-gluon exchanges (identified as pomerons) and accounts for about a fourth of the total inelastic cross section at high energies [96, 97]. Soft processes have momentum exchanges at the order of Λ_{QCD} ($\sim 0.2 \text{ GeV}$), and they cannot be treated within perturbative QCD (pQCD). However, their cross sections regarding the exchange of virtual quasi-particle states, pomerons and reggeons, can be calculated using basic quantum field-theory principles as implemented in Gribov’s Reggeon Field Theory [99, 101].

Since hard processes, involving partons with momentum transfer scale typically above $\sim 1-2 \text{ GeV}$, are important ingredients of high- p_{T} physics phenomena, I leave their discussion in terms of experimental probes of the QGP to the next chapter.

CHAPTER 3

Probing the quark-gluon plasma with high- p_T particles

In this chapter, a special focus is given on the so-called “hard probes” of heavy-ion collisions, discussing the production of high- p_T particles, which is the main interest of this work. Moreover, in the context of p–Pb collisions, nuclear matter effects are discussed briefly. Among these, the so-called cold nuclear matter (CNM) effects have particular importance. The CNM effects need to be kept under good control, allowing the correct interpretation of the nucleus-nucleus (Pb–Pb) data. Cold nuclear matter, entering into a modification of the nuclear PDFs with respect to the proton PDFs or into a modification of the hadronization, is constrained by p–Pb collisions at the LHC.

The role of minimum-bias pp collisions is also discussed. Proton-proton collision data contribute as a reference to study nuclear effects in p–Pb and Pb–Pb collisions, and they also provide necessary input to tune the modeling of several observables in Monte Carlo (MC) event generators.

3.1 Particle production in proton-proton and heavy-ion collisions at high p_T

The QGP can be “tomographically” studied by hard probes through hard processes characterized by large momentum transfers, $Q \gg \Lambda_{\text{QCD}}$, which is well described by pQCD calculations based on the factorization theorem. In minimum bias Pb–Pb collisions at the LHC about 98% of the initial partons are exclusively generated in hard scattering processes [102], meaning that they are either produced with large momentum or mass. Hard partons being produced in the initial hard scattering have short production timescale of the order of $\sim 1/Q$. As a consequence, hard partons carry information about the entire evolution of the system, from the pre-equilibrium phase until the hadronization and freeze-out. Their production can be affected in the initial state by cold nuclear matter (CNM) effects. Afterwards, their kinematics can be modified due to elastic or inelastic collisions with partonic constituents of the medium. Due to re-scatterings, they can participate in the collective expansion, resulting in positive v_2 for the particles under study. In fact, any change in a hard probe-related observable is either a CNM effect or due to interaction with the medium in the final state.

Hadron production of particles with high transverse momentum ($p_T \gg 2 \text{ GeV}/c$), which originates from the fragmentation of hard-scattered partons, is theoretically well understood and experimentally well verified. The fragmentation of hard-scattered partons into hadrons

is described by the probability of finding a hadron carrying a specific fraction of the final state parton momentum z known as the fragmentation function (FF). In hadronic collisions, a full description also requires knowledge of the distribution of the initial partons within the colliding hadrons, known as the parton distribution function (PDF), which depends on the fraction of the proton's longitudinal momentum x carried by a scattered parton. The measurement of the inclusive charged particle p_T spectrum at large transverse momentum, therefore, measures in essence the convolution of three pieces: the hard-parton scattering cross section, the PDF, and the FF.

The QCD factorization theorem [103] provides a prescription for separating long-distance and short-distance effects in hadronic cross sections. The leading power contribution to a general hadronic cross section involves only one hard collision between two partons from the incoming hadrons A and B , with momenta p_A and p_B . The invariant cross section for inclusive high p_T hadron production is given by:

$$E_h \frac{d^3\sigma_{AB \rightarrow h(p)}}{dp^3} = \sum_{ijk} \int dx f_{i/A}(x) \int dx f_{j/B}(x) \int dz D_{h/k}(z) E_h \frac{d^3\hat{\sigma}_{ij \rightarrow k}}{dp^3}(xp_A, xp_B, \frac{p}{z}), \quad (3.1)$$

where i , j , and k run over all parton species and all scale dependence is implicit, hence not shown. The quantity z is the momentum fraction of the parton momentum. The last term, $\hat{\sigma}_{ij \rightarrow k}(xp_A, xp_B, \frac{p}{z})$ is the short-distance parton-parton scattering cross section, whereas the long-distance terms are the $f_{i/A}(x)$ PDFs of parton type i in hadron A , and the $D_{h/k}(z)$ FFs for a parton of type k to produce a hadron h . The latter two types of long-distance terms, which contain the non-perturbative contributions from the large (QCD) scales of both the colliding and the produced hadrons, provide the necessary tools to study the QCD matter with hard processes. The energy scale dependence of both the FFs and PDFs can be described by the DGLAP equations.

The fragmentation functions $D_{h/k}(z)$ can be precisely determined in a clean environment, i.e. in vacuum, provided by measurements of e^+e^- annihilations where no initial state hadron remnants are present and, at leading order, only quarks are produced. In hadron-hadron collisions, additionally, there are gluon FF present. Due to the universality of FFs, measurements in different collision systems can be combined and, in turn, can help in reducing theoretical model uncertainties.

Due to the presence of the medium, the FFs will be modified which might differ significantly from the vacuum FFs due to medium-induced final state soft gluon exchanges taking place after the hard scattering process. By studying this modification leads to a better knowledge of the properties of the medium. This implies, however, that the other type of long-distance term, the PDFs is well under control—provided that the factorization formula given in Eq. (3.1) still applies; this requirement needs to be tested.

Cold nuclear matter effects (see later in Section 3.2) modify the nuclear PDFs (nPDFs)

with respect to the free proton PDFs and the hadronization. In order to constrain these effects, control p–Pb measurements are performed as benchmarks on top of which hot QCD matter effects are identified. In the nuclear case, the incoherence of the hard collisions implies that the nPDFs contain a geometric factor so that the hard cross sections are proportional to the overlap between the two nuclei. The degree of overlap can be estimated experimentally in a probabilistic approach within the Glauber model. This determines the equivalent number of pp collisions N_{coll} as a baseline, to which the central Pb–Pb cross section measurements are compared. Note, however, that the Glauber model is not a first-principles calculation therefore experimental checks are crucial for the proper interpretation of the measurements done in Pb–Pb collisions.

3.1.1 Jet quenching with single-inclusive particles and the nuclear modification factor

In a collision of two nuclei, a jet originates from hard-scattered partons, which produces a collimated parton shower via the fragmentation process. This yields to the creation of color neutral particles with subsequently lower momenta than that of the original parton. The collimation into a certain angular region (i.e. into a cone, also termed as a jet cone) is caused by the scale dependence of the strong coupling, which leads to a suppression of large-angle radiation. Energetic partons forming a jet traverse the medium and lose their energy mainly by medium-induced gluon radiation and partially by collisional energy loss. This process of partonic energy loss is referred to as jet quenching [104, 105].

The simplest observable of jets in nuclear collisions is the measurement of the production yields of single-inclusive hadrons at high p_T . The medium-modified fragmentation of partons results in the modification of parton showers which, in turn, causes the suppression of hadron spectra at high p_T . A quantitative way to study the medium modification is to form a ratio of p_T spectra which is called the nuclear modification factor. Due to the low-probability nature of hard scattering processes (with respect to soft processes), a given nucleon is expected to suffer one hard collision in a nuclear collision at most. Hence, hard scattering processes at the nucleon-nucleon level, in general, are expected to scale with the number of binary nucleon-nucleon collisions N_{coll} . Note that N_{coll} is obtained from Glauber MC simulations.

The nuclear modification factor is defined as the ratio of the particle yield in nucleus-nucleus (A–A) collisions and the expectation from N_{coll} -scaled superposition of nucleon-nucleon collisions at equivalent collision energy \sqrt{s} :

$$R_{AA}(p_T, y) = \frac{d^2 N_{AA}/dydp_T}{\langle T_{AA} \rangle d^2 \sigma_{pp}^{\text{INEL}}/dydp_T} = \frac{1}{\langle N_{\text{coll}} \rangle} \frac{dN_{AA}(p_T, y)}{dN_{pp}(p_T, y)}, \quad (3.2)$$

where N_{AA} and $\sigma_{pp}^{\text{INEL}}$ represent the particle yield and the inelastic (INEL) cross section in A–A and pp collisions, respectively. The nuclear overlap function $\langle T_{AA} \rangle$ is determined from

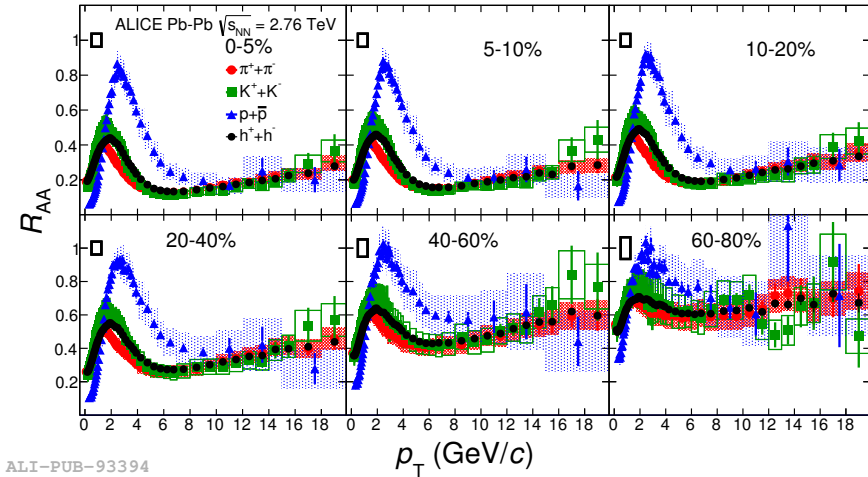


Figure 3.1: The nuclear modification factor R_{AA} as a function of transverse momentum for different particle species and collision centralities in Pb–Pb collisions at $\sqrt{s_{NN}} = 2.76$ TeV measured by the ALICE collaboration. Figure is taken from Ref. [111].

the Glauber model as described in Section 2.1.1 and it is related to the average number of binary nucleon-nucleon collisions and the inelastic nucleon-nucleon cross section in the following way: $\langle T_{AA} \rangle = \langle N_{\text{coll}} \rangle / \sigma_{\text{INEL}}^{\text{NN}}$ [106].

In the absence of nuclear effects, the R_{AA} is, by definition, expected to be equal to unity for hard processes which exhibit binary collision scaling. Binary scaling can be broken because of initial state effects in nuclei or final state effects present in A–A collisions. The former might occur through cold nuclear matter effects whereas the latter can be related to jet quenching. Any deviation from unity in the R_{AA} implies that hadron production in A–A is suppressed or enhanced. Note that, in this regard, the relevant part of the R_{AA} is the intermediate-to-high p_T region, since the bulk particle production from soft processes should rather scale with the number of participants.

At the LHC, jet quenching was experimentally observed in Pb–Pb collisions first by the ATLAS experiment [107], followed by the experiments ALICE [108] and CMS [109]. In Fig. 3.1 the R_{AA} is shown for different collision centralities in Pb–Pb collisions at $\sqrt{s_{NN}} = 2.76$ TeV measured by the ALICE collaboration [110, 111]. For unidentified charged particles [110], shown with black markers, in peripheral (60 – 80% centrality) collisions the shape of the invariant yield is similar to that observed in pp collisions; the amount of suppression and its p_T dependence becomes weaker, which is observed as a flattening behavior of the R_{AA} approaching unity. In contrast, for most central (0 – 5%) collisions, a strong suppression ($R_{AA} \ll 1$) is observed, which is the sign of the jet quenching. It is worth noting that the measured suppression is larger — by about 40% at $p_T = 10$ GeV/ c [112] — than that observed at RHIC [113] due to the higher energy density reached at the LHC.

Also shown is the measurement for identified light flavor charged hadrons. The R_{AA} for identified particles gives more details about the in-medium interactions of partons fragment-

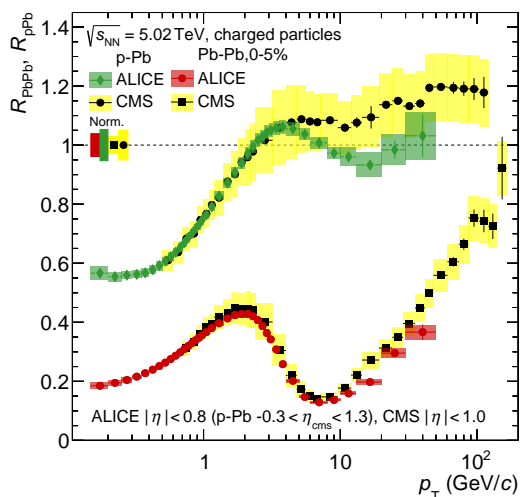


Figure 3.2: A comparison of the nuclear modification factors for central (0 – 5%) Pb–Pb and p–Pb collisions measured by the ALICE and the CMS collaborations. The p_T -dependent systematic (normalization) uncertainties are shown as boxes around data points (around unity). Figure is taken from Ref. [118].

ing into hadrons due to the different color Casimir factors of quarks and gluons. At high p_T ($> 10 \text{ GeV}/c$), results show that the R_{AA} for all particle species is equally suppressed. This points out the fact that particle ratios are similar to those of jets in the vacuum, and the medium does not modify the hadrochemistry of the leading particle, i.e. the one with largest momentum, of the quenched jet, all fragments lose energy coherently. For $p_T < 10 \text{ GeV}/c$ and for all centralities, protons are less suppressed as compared to pions and kaons in the low-to-intermediate p_T range. This mass dependence is related to effects arising from collective (radial) flow—which is well described by hydrodynamics in the soft regime. When approaching the intermediate p_T range, the mass ordering seen in v_2 starts to be broken and it is attributed more to the baryon-to-meson anomaly, i.e. to an excess of the yield of baryons with respect to that of mesons. While the medium is opaque for high- p_T colored probes, on the other hand it is transparent for particles that do not interact strongly (like photons) and other colorless probes which roughly scale with N_{coll} , i.e. have $R_{AA} = 1$ [114–116]. It is important to note that R_{AA} is successfully used in the determination of the medium properties for the jet transport coefficient (\hat{q}) which was calculated by the Jet collaboration [117].

These measurements alone, however, do not allow to judge whether the observed energy loss is an initial state or final state effect. To disentangle these two, the nuclear modification factors have to be measured in (control) p–Pb collisions as well. The corresponding modification factor for inclusive charged particle is measured in non-single diffractive p–Pb collisions at $\sqrt{s_{NN}} = 5.02 \text{ TeV}$ by ALICE [118, 119] and is shown in Fig. 3.2. While initial state effects are important at low and intermediate p_T , at high p_T , it is established that for $p_T \gtrsim 10 \text{ GeV}/c$ the R_{pPb} is consistent with unity. Therefore, the observed suppression seen in Pb–Pb collisions is due to a final state effect such as jet quenching. Whether this is the case for identified particles, it is investigated in this work and the results will be discussed later in Chapter 9.

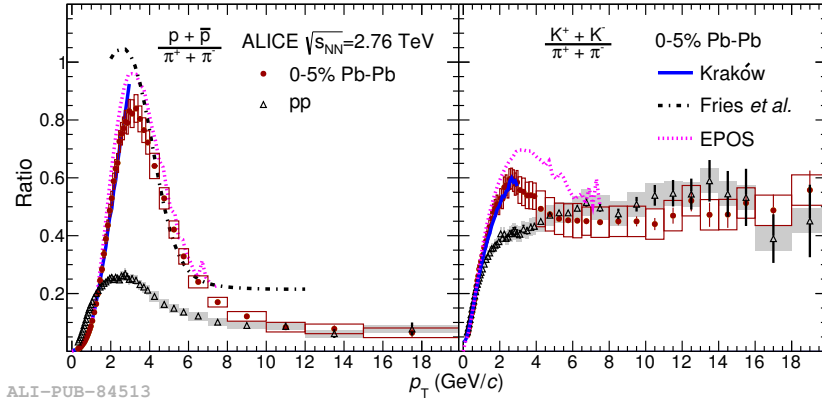


Figure 3.3: Proton-to-pion $(p + \bar{p})/(\pi^+ + \pi^-)$ and kaon-to-pion $(K^+ + K^-)/(\pi^+ + \pi^-)$ particle ratios as a function of transverse momentum measured in pp and the most central (0 – 5%) Pb–Pb collisions at $\sqrt{s_{NN}} = 2.76$ TeV by the ALICE collaboration. Data are compared to theoretical predictions, see the text for details. Figure is taken from Ref. [125].

3.1.2 Parton recombination and coalescence

Another mechanism beside parton fragmentation which might be relevant in the production of hadrons is parton recombination or coalescence [72]. In contrast to parton fragmentation, which splits the momentum of the parent parton into smaller momenta of the produced hadrons, recombination leads to the production of hadrons with momenta larger than that of their parent partons. Given the exponentially falling thermal (low- p_T) region of the parton spectrum in heavy-ion collisions, the probability to create high- p_T partons is low. Due to the large number of soft partons in the intermediate p_T region, the recombination process might be the dominant hadronization mechanism over fragmentation [120, 121]. In that p_T regime, the production of baryons from recombination of three soft quarks would be more probable than production of mesons from a pair of less soft $q\bar{q}$ pairs. In the high- p_T region where the parton density gets lower and the shape of the spectrum turns into power-law fragmentation takes over the hadron production.

The baryon-to-meson ratio for inclusive light flavor hadron production measured in heavy-ion collisions is enhanced with respect to the ratio measured in pp collisions. This effect was first observed for p/π and Λ/K_S^0 at RHIC [122–124] and was measured later at the LHC by the ALICE collaboration [69]. Figure 3.3 shows the p_T -dependent $(p + \bar{p})/(\pi^+ + \pi^-)$ ($\equiv p/\pi$) and $(K^+ + K^-)/(\pi^+ + \pi^-)$ ($\equiv K/\pi$) particle ratios measured in pp and the most central (0 – 5%) Pb–Pb collisions at $\sqrt{s_{NN}} = 2.76$ TeV by ALICE. Both of them indicate the clear enhancement at intermediate p_T with a distinct peak at $p_T \simeq 3$ GeV/c. No clear explanation for the observed phenomena exists, however there are different scenarios to describe the observed behavior, such as medium-modified jet fragmentation or various hadronization models based on parton recombination. In the low- p_T ($\lesssim 2$ GeV/c) region, where the dominant particle production is thermal, hydrodynamical calculations (e.g. Kraków [126, 127]) show excellent agreement with data. This indicates that the rise of the peak can be described

by the mass ordering induced by (azimuthally symmetric) radial flow — and not by the azimuthally asymmetric flow which causes the ridge structure seen in azimuthal two-particle correlations. It was also observed that the shift of the peak with centrality (not shown in the figure) is consistent with an increasing radial flow towards more central collisions. At intermediate p_T ($2 \lesssim p_T \lesssim 8 \text{ GeV}/c$) the data are qualitatively well described by recombination models. The prediction by Fries et al. [72] considering recombination of thermal quarks gives a consistent description of the data. At higher p_T , the EPOS model [128, 129] (which will be discussed in Section 3.3.1) combines hydrodynamics with the interaction between jets and the hydrodynamically expanding medium captures the shape qualitatively rather well, although the enhancement is overestimated [125]. Above $p_T \gtrsim 8 - 10 \text{ GeV}/c$, all the ratios come together indicating that the process is dominated by vacuum-like (unmodified) fragmentation. According to recent studies, the origin of the enhancement of the baryon-to-meson ratio might be better unraveled by measuring production of hadrons from individual sources, see e.g. Ref. [131]. In that work, the discrimination to disentangle contributions of processes in jet and bulk have been made. The jet contribution represents pure fragmentation while the bulk distribution resembles those seen for the inclusive case. The K/π ratio shows a bump-like structure at $p_T \sim 3 \text{ GeV}/c$ being completely absent in pp data, making it a genuine heavy-ion effect. The effect is also observed in the soft coalescence model [72]. The evolution of the magnitude of the peak with centrality is also observed which might be explained by a reduced canonical suppression of the strangeness production in larger freeze-out volumes [132], and by an enhanced strangeness production in the QGP [133].

It will be interesting to see how these particle ratios behave in p–Pb collisions as a function of charged-particle multiplicity and in pp collisions at higher collision energies. The corresponding ratios are studied in this work, and will be discussed in Chapters 8 and 9.

3.2 Cold nuclear matter effects in p–A collisions

High-energy nuclear collisions at the LHC have reached the TeV energy scale, which in turn translates into a kinematical reach at parton fractional momenta, Bjorken- x , and virtuality Q^2 that is several orders of magnitude beyond that achieved in all other previous experiments with nuclear collisions. Figure 3.4 shows the present and the expected kinematical regions measured in the $x - Q^2$ plane for different ($2 \rightarrow 2$ or $2 \rightarrow 3$) processes accessible with an integrated luminosity of 0.1 pb^{-1} in a p–Pb run at the design energy of $\sqrt{s_{\text{NN}}} = 8.8 \text{ TeV}$, predicted in Ref. [134]. Proton-nucleus collisions have long been recognized as a crucial component of the physics program with nuclear beams at high energies, in particular for their reference role to interpret and understand nucleus-nucleus collision data as well as for their ability to enlighten the partonic structure of matter at small Bjorken- x [41]. Specifically, p–Pb collisions provide an appropriate tool to study the partonic structure of cold nuclear matter, and this way they give essential information on initial state effects. To distinguish

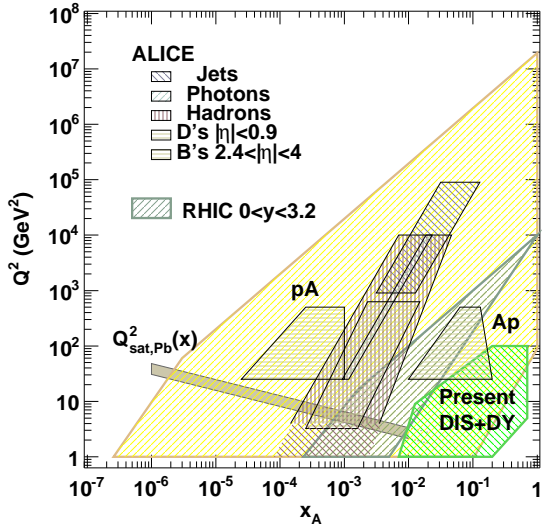


Figure 3.4: Total kinematical reach of p–Pb collisions at $\sqrt{s_{\text{NN}}} = 8.8$ TeV at the LHC for different rapidities in the laboratory frame. The figure shows the region of phase space studied by experiments of DIS with nuclei and Drell–Yan production in p–A collision, and the total reach of RHIC for $0 < y < 3$. Figure is taken from Ref. [41].

final state effects, which are related to the QGP medium, from initial state effects caused by nucleon interactions one has to study observables produced in the cold nuclear matter through p–Pb collisions. Being different from Pb–Pb collisions, where both cold and hot nuclear matter effects are present due to the formation of a QGP and due to the presence of a nuclear environment, in p–Pb it is expected that there might be no QGP formed during the evolution of the system, and particle production is controlled by the cold medium. It is assumed that physical processes in the initial state can be well isolated since the effect of the QGP medium, even if it is produced in the light–heavy ion reactions, is expected to be weak. In fact, cold nuclear matter effects are predicted to be small compared to the hot nuclear matter effects due to the QGP formation in Pb–Pb collisions [135]. Nevertheless, detailed knowledge of CNM effects is required in order to interpret the measurements in p–Pb collisions accurately.

3.2.1 Nuclear parton distribution functions

It is known experimentally that in p–A collisions the parton distribution functions are modified within the nucleus compared to a free nucleon, for example the proton. Nuclear parton distribution functions, $f_i^A(x, Q^2)$, are defined for each parton flavor i , extending this way the PDF concept to nuclei. They can be defined on the basis of PDFs, e.g. for a nucleus A :

$$f_{i/A}(x, Q^2) \equiv R_i^A(x, Q^2) \cdot f_{i/p}(x, Q^2). \quad (3.3)$$

Here, $f_{i/p}(x, Q)$ represents the free proton PDF and $R_i^A(x, Q^2)$ is the nuclear modification at a given energy scale Q^2 and longitudinal momentum fraction x of the parton in the nucleon. The Q^2 evolution of nPDFs can be determined through DGLAP evolution equations but can only be applied in perturbative calculations. Therefore, an initial scale is set, typically around $Q^2 = 1 \text{ GeV}^2/c^2$ and only data above this scale are considered.

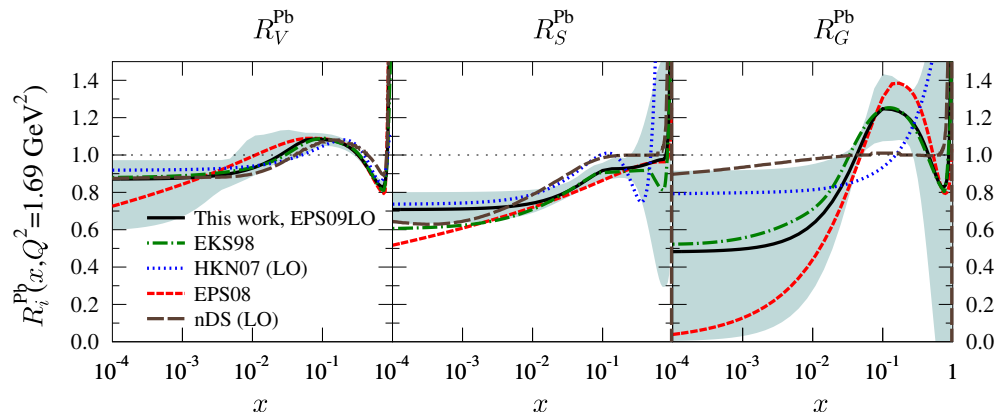


Figure 3.5: Comparison of the average valence and sea quark, and gluon modifications at $Q^2 = 1.69 \text{ GeV}^2$ for Pb nucleus from LO global DGLAP analyses EKS98 [141, 142], EKPS [143], nDS [139], HKN07 [144], and EPS09LO [137]. Figure is taken from Ref. [137].

For the proton case, the PDFs are constrained by a large number of experimental data—especially from HERA and the Tevatron—in global fits performed in Leading Order (LO), Next-to-Leading Order (NLO) or Next-to-Next-to-Leading Order (NNLO) calculations. There are various free proton PDF sets, such as e.g. the general-purpose CT14 [136]. The CT14 PDFs include data from the LHC as well as updated data from the Tevatron and from HERA experiments.

In contrast, much less comprehensive set of experimental data on nuclear PDFs are available in the perturbative regime ($Q^2 \gtrsim 1 \text{ GeV}^2/c^2$), especially for the region $x \lesssim 0.01$. Due to insufficient data constraint, as a result, there are large uncertainties in the nPDFs relevant for LHC kinematics. Some of the frequently used versions of global fits for nPDFs at NLO are the following sets: EPS09 [137], HKN07 [138], nDS [139], and DSSZ [140]. All sets of nPDFs fit data on charged leptons deep inelastic scattering (DIS) with fixed nuclear targets and Drell–Yan (DY) process in proton–nucleus collisions, and also hadronic final state results from p–A (d–A) collisions are taken into account. Nuclear PDFs are often presented by their nuclear modification $R_i^A(p_T)$ defined in Eq. (3.3) to emphasize the effect from the nuclei. For each parton flavor i , they are given by a parametrized function. Some of the parameters can be fixed while others are determined based on assumptions. QCD global analyses on experimental data allow parametrizing the nuclear PDFs as well as their dependence on Q^2 values and atomic mass number. For example, the most popular EPS09 parametrization of PDFs is extracted from an NLO pQCD analysis with three different experimental inputs: charged lepton DIS off nucleus, dilepton production in the DY process, and inclusive pion production in d–Au collisions measured at RHIC. The resulted nuclear modifications for Pb at the initial scale $Q^2 = 1.69 \text{ GeV}^2$ are shown in Fig. 3.5 together with parametrizations from other analyses, see Ref. [137] for more details. Nuclear modifications R_v , R_s , and R_g are derived for valence quarks, sea quarks and antiquarks, and gluons, respectively.

The presence of a nucleus in the initial state induces modifications in particle production

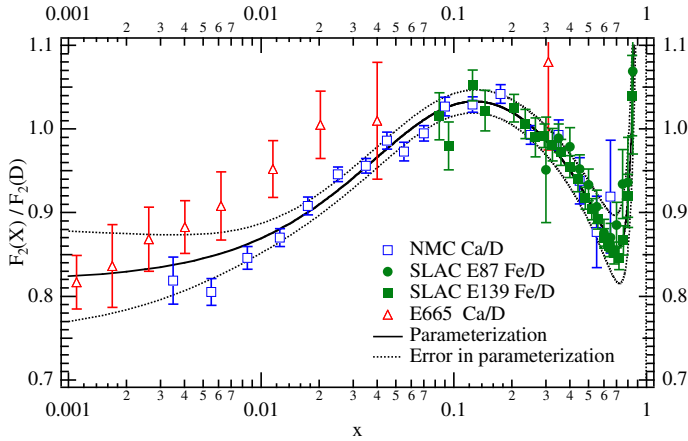


Figure 3.6: Typical nuclear effects seen in DIS measurements. Figure is taken from Ref.[148].

mechanism of the light quarks with respect to that in pp interactions, and in turn, this influences the high- p_T particle production. Understanding the structure of the initial state is interesting, because one can probe the structure of the nucleus in the unexplored QCD regime of the longitudinal parton-momentum fraction ($x < 10^{-3}$), where the extremely high gluon density is expected to saturate.

3.2.2 Multiple scattering and the Cronin enhancement

Measurement of hadron production with a wide p_T range in p-Pb (and also in Pb-Pb) collisions is essential to constrain gluon shadowing at region of small values of the longitudinal parton momentum fraction x , see e.g. Ref. [145]. Based on studies on structure functions F_2 , for example in Refs. [146, 147], four effects on the nuclear modification $R_i^A(x, Q^2)$, defined in Eq. (3.3), are typically considered. Going from low to high Bjorken- x these are the shadowing, anti-shadowing, EMC (named after the European Muon collaboration), and Fermi motion effects. Figure 3.6 shows the nuclear effects, which were seen in lepton-nucleon deep inelastic scattering, as a function of Bjorken- x . The DIS data are analyzed in the form of structure function ratios from, for example, the NMC [149] and SLAC E-139 [150] experiments. The F_2^A structure function of heavy nuclei is compared to the deuteron structure function F_2^d as a function of Bjorken- x . This ratio shows directly the different regions of the nuclear modification. These data constrain the quark distributions in the measured range $0.01 < x < 1$. Note that the given x values are approximate numbers and their values vary on the choice of different nPDFs and values of Q^2 . Cross sections are calculated in the collinear factorization formalism [151] folding the PDFs with perturbatively calculable parton level cross sections. For this particular case of DIS, it is given as $\sigma_{\text{DIS}}^{l+A \rightarrow l+X} = \sum_{i=q,\bar{q},g} f_i^A(Q^2) \otimes \hat{\sigma}_{\text{DIS}}^{l+i \rightarrow l+X}(Q^2)$. The factorization, renormalization, and fragmentation scales are chosen to be equal and are fixed to a characteristic scale in the process; which is the photon virtuality Q^2 for the case of DIS. The relevant kinematic region for the work presented in this thesis is for $x < 0.01$. In this domain, the observed depletion of low- x partons in a nucleon inside a nucleus as compared to a free nucleon is termed shadowing. To date, the effect is not fully understood, however it might be connected to (coherent) multiple

scattering of partons and saturation effects in the nucleus, see Ref. [152] for a review.

All PDFs show rising behavior at low x . In particular, the gluon distribution grows rapidly as $x \rightarrow 0$ for a given momentum transfer. Moreover, higher virtualities lead to larger gluon densities, as seen from NLO pQCD calculations on DIS data by ZEUS [153]. The increase in the gluon density for high virtualities is limited by the Froissart bound for the cross section [154]. This so-called “small- x ” problem can be resolved by the concept of gluon saturation.

For a given x , saturation happens for a given momenta below a certain critical value called the saturation scale. Since the transverse momentum of the produced particles scales with the momentum transfer of the hard scattering, saturation affects the particle production below a certain p_T value. The relevant information for a high- p_T study is then the size of this scale. In central Au–Au collisions at RHIC energies, the saturation scale is estimated to be around $1 - 2 \text{ GeV}/c$ at mid-rapidity [23], which is quite small and does not have effect in the high p_T region. It is worth noting that the idea of saturation is formulated in an effective QCD theory [23], the color glass condensate as mentioned previously. It describes the low- x partons as a coherent state of matter.

A modified production of hadrons can be observed when one compares their production yields in p–A collisions relative to those in pp collisions. It is then observed that the invariant cross section does not scale linearly with the number of target nucleons. An enhancement of hadron production has been observed by Cronin et al. [155] at intermediate p_T (around $2 - 4 \text{ GeV}/c$), whereas, at low p_T (below a few GeV/c) a suppression is seen. This observation was confirmed by several other experiments as well.

The enhancement is usually interpreted as a sign of multiple scattering of the partons in the nucleus prior to the hard scattering, for a review, see Ref. [156]. Historically, the accurate way in quantifying the Cronin enhancement is obtained with the nuclear modification factor introduced in Eq. (3.2), which can be easily defined for the case of p–A collisions. Measurements at RHIC showed that the evolution of the Cronin peak is dependent on the centrality of the collision while being weakly dependent on the collision energy going from the CERN SPS to BNL RHIC energies. Measurements of charged hadron p_T spectra at the LHC indicate a reduction of the enhancement, where only a hint of the Cronin peak can be observed [119]. Due to the explored low- x region at LHC energies, shadowing effects become more important besides the effect of multiple scattering, which in turn tend to suppress the enhancement. Furthermore, the magnitude of the effect follows a hierarchy determined by the hadron mass, showing increasing trends with larger masses of the measured particles.

I will further discuss the particle species dependent behavior of the Cronin effect in Section 9.2 for identified charged hadrons (pions, kaons, and (anti)protons) measured in non-single diffractive $\sqrt{s_{NN}} = 5.02 \text{ TeV}$ p–Pb collisions near mid-rapidity.

3.3 The role of proton–proton collisions

Proton–proton collisions are important to be studied on their own apart from their crucial importance as they provide baseline measurements to investigate nuclear effects in p–Pb and Pb–Pb collisions.

As was discussed, the parametrizations of both the PDFs and the FFs are derived from global analyses [158, 159] based on fits to the experimental data at various collision energies with next-to-leading order accuracy. These include single-inclusive hadron production in semi-inclusive electron-positron annihilation data, semi-inclusive deep-inelastic scattering, and single-inclusive identified (charged) hadron spectra at high p_T , notably including results at LHC energies. With the growth of the collision energy the lower fractional parton momenta x is probed and the contributions from hard-scattering processes increase. In this x region, high- p_T particles dominantly stem from the fragmentation of gluons [157]. The measurements of identified (charged) particle spectra in pp collisions at high p_T provide new constraints on the gluon-to-pion and, in particular, on gluon-to-kaon fragmentation functions to have their large theoretical uncertainties under better control. Results presented in this thesis can be used as further input for these studies.

Moreover, minimum-bias pp collisions provide essential input to tune the modeling of several observables in Monte Carlo (MC) event generators. Therefore, in the following, I briefly outline how the different components of physics processes, relevant to the presented studies, are implemented in MC models used in this thesis.

3.3.1 Monte Carlo modeling of pp collisions

To model hadron-hadron, particularly pp collisions, MC event generators are used which provide simulated events. Event generators combine perturbative QCD description for hard scatterings in a collision and phenomenological approaches to manage soft processes that can only be modeled. Generated events are primarily used either to have better understanding of the data or to estimate the needed corrections to be applied to retrieve the real signal from the measurement. The description of reality by the generators is limited by various input parameters which influence their prediction power.

The characterization of physics observables with the proper choice of parameters are found by the so-called “tuning”. This results in numerous tunes for a given generator depending on a certain observable a tune is expected to describe. Therefore, the existence of experimental results are of crucial importance in constraining a set of parameters. For instance, the center-of-mass energy or multiplicity dependence of a given observable, such as the average transverse momentum, modeled by the generator can be re-tuned in view of new measurements performed at unprecedented energies or multiplicities.

In this thesis, I use MC models, such as PYTHIA and EPOS. These are general-purpose

event generators meaning that they are often used and tested to describe hadron collisions at high energies. The PYTHIA model is widely applied in high-energy collider physics which is entirely based on a pQCD framework, incorporating soft diffractive scatterings. Conversely, the EPOS model is commonly used in cosmic-ray physics which is based on the Gribov’s Reggeon Field Theory [99].

PYTHIA: Lund string fragmentation and color reconnection

PYTHIA [81, 100] is a full event generator for pp collisions, which contains a rigorous treatment of hard scatterings through pQCD combining with phenomenological models for semi-hard/soft processes. The connection between the two is realized via a tunable cut-off parameter $p_{T,\min}$ which accounts for the momentum transfer in the hard interaction. For inelastic collisions, which is the main interest in this thesis, each collision is modeled via one or more parton-parton interactions. The decomposition of the inelastic cross section into diffractive and non-diffractive (ND) components is based on the Regge Field Theory [160], where the ND component dominates (see the discussion in Section 2.3). PYTHIA with versions 6 and 8 are widely used in the high energy physics (HEP) community, though the method of diffraction has improved in PYTHIA 8. The event generation in PYTHIA is optimized for leading-order (LO) pQCD $2 \rightarrow 1$ and $2 \rightarrow 2$ hard scattering processes, which by default take the initial states from the CTEQ5L [161] PDFs. The calculations of the LO matrix elements are complemented with initial- and final state parton radiation, multiparton interactions (MPI), beam remnants, final state color reconnection (CR), and hadronization. The average number of initial hard parton-parton interactions obtained as $\sigma_{\text{hard}}(p_{T,\min})/\sigma_{\text{ND}}$, where $\sigma_{\text{hard}}(p_{T,\min})$ is the hard cross section for the parton scattering calculated with a $p_{T,\min}$ cut-off in order to avoid divergences, and σ_{ND} is the non-diffractive cross section.

After hard collisions, a hadron can be emitted from the proton remnant and the rest of the remnant form the multiparton system which hadronizes using the Lund string fragmentation model [162]. A typical fragmentation process in the Lund-model contains a (color) string stretching between a quark q and an antiquark \bar{q} . If the potential energy in the string is large enough, the string breaks up producing additional $q - \bar{q}$ pairs in different vertices. A quark can join with an antiquark from the neighbouring vertex ($q' - \bar{q}$ and $q - \bar{q}'$) to form a meson. In a similar way, during string breaking a diquark-antidiquark pair may be produced in a color triplet state. This pair can connect with the neighbouring q or \bar{q} and form eventually a baryon. It is worth noting that PYTHIA 8 has an updated parameter set of Lund hadronization for light- and heavy-quarks with respect to PYTHIA 6.

Throughout this thesis two different versions of the PYTHIA event generator are used, PYTHIA 6.4 and PYTHIA 8.2, which mainly differ in their implementation language and the level of tuning to the available experimental data. One of the most commonly used tunes at LHC energies for PYTHIA 6 and PYTHIA 8 is respectively the Perugia-2011 tune [163]

and the Monash 2013 tune [164], accounting for different sets of the parameters. For both tunes, the sets of parameters have been obtained from recent (2011 and 2013) analysis of MB, underlying event, and/or Drell–Yan data in pp collisions at $\sqrt{s} = 7$ TeV; the Monash 2013 tune was optimized to describe early data collected by the LHC experiments as well as lower energy data. Moreover, both versions of the model have strong final state parton interactions implemented through different CR models [81, 165] which, as a consequence, reduces the number of final state particles. Such a model allows partons of each MPI system to form their own structure in color space and then, they are merged into the color structure of a higher p_T MPI system, with a probability \mathcal{P} given by: $\mathcal{P}(p_T) = \frac{(R \times p_{T0})^2}{(R \times p_{T0})^2 + p_T^2}$, where R is the reconnection range ($0 \leq R \leq 10$) and p_{T0} is the energy-dependent parameter used to damp the low- p_T divergence of the $2 \rightarrow 2$ QCD cross section. As a consequence of the different energy evolution of the MPI cut-off, the Monash tune has larger MPI activity at a given \sqrt{s} than the Perugia tune.

EPOS 3: core – corona separation and hydrodynamics

EPOS 3 [128–130] is a hydrodynamical approach for the generation of complete events (having soft and hard components) which contains hard scatterings and MPI. The model for multiple scatterings invokes a parton-based Gribov–Regge theory, for a detailed review see Refs. [101, 166]. Essentially, each parton scattering involves a hard scattering complemented by initial- and final state radiation, which forms a parton ladder (also called as a cut-pomeron). Each ladder has its own saturation scale which separates soft and hard processes. After multiple scattering, the final state partonic system consists of mainly longitudinal flux tubes, carrying the transverse momentum of the hard scattered partons in the transverse direction, termed as kinks. The total cross section can be expressed with pomeron and cut-pomeron exchanges. Cut-pomerons form color flux tubes between the two nuclei and they are the origin of particle production. These flux tubes will constitute both bulk matter and jets. The bulk matter is defined by the region of high energy density flux tubes; they fragment into string pieces which will later constitute particles.

For high string densities, e.g. those achieved in high-multiplicity pp collisions, the model does not allow the strings to decay independently, instead, if the energy density from string segments is high enough they fuse into the so-called “core” region [167]. The strings in the core region evolves hydrodynamically. The hydrodynamical evolution is done on an event-by-event basis and its initial conditions are given by the distribution of the cut-pomerons. After the hydrodynamical expansion, the strings finally hadronize to form the bulk part of the system.

On the other hand, in the low-density region the strings expand and eventually break via the production of $q - \bar{q}$ (or $qq - \bar{q}\bar{q}$) pairs which hadronize using the unmodified string fragmentation (Schwinger mechanism [168]) forming the “corona” region. In high-multiplicity

events, where the string density is considerably larger than that in minimum bias events, the strings cannot decay independently and they constitute both bulk matter and jets based on their energy loss.

The core region gives around 30% of the central particle production for an average pp collision at $\sqrt{s} = 7$ TeV, where the pseudorapidity density $\langle dN_{\text{ch}}/d\eta \rangle_{|\eta| < 2.4}$ of charged particles produced in the pseudorapidity region $|\eta| < 2.4$ is ~ 6.25 ; this fraction might reach around 75% for $\langle dN_{\text{ch}}/d\eta \rangle_{|\eta| < 2.4} \approx 20.8$ [169]. Concerning the hard component, the inclusive jet cross section for pp collisions at $\sqrt{s} = 200$ GeV obtained with EPOS 3 agrees within 4% and 5% with NLO pQCD calculations and the data measured by the STAR collaboration, respectively [170]. Therefore, the use of EPOS 3 for the analysis, will be presented in the next chapter as a function of event multiplicity and the p_{T} of a leading (highest transverse momentum) jet, is reasonable.

It is worth noting that EPOS 3 is able to reproduce many features of hadron production quite well. For instance, the observed baryon-to-meson enhancement in $\sqrt{s_{\text{NN}}} = 5.02$ TeV p–Pb collisions can be qualitatively described by the model [128, 171]. Moreover, in high-multiplicity events, it predicts the mass-ordering of the elliptic flow coefficient (v_2) of identified particles and the ridge-like structure of two-particle azimuthal correlations in pp [172] and p–Pb [166] collisions. Latter feature has been discussed in terms of hydrodynamical evolution of the medium. Also, in high-multiplicity events the larger fraction of particles originating from the corona are expected to be formed from the bulk (core), rather than to hadronize via Schwinger mechanism. Studies based on the relative contributions between core and corona are ongoing. For example, for a recent study on two-particle azimuthal correlations performed in p–Pb collisions, see Ref. [173].

In the next chapter, I employ both the EPOS 3 and the PYTHIA MC models, and by comparing the two in terms of the studied (radial flow) observables I pursue a study to show how the presence of jets effects the low-multiplicity particle production.

CHAPTER 4

Revealing the source of the radial flow patterns in pp collisions

In this chapter, I discuss a method in order to help to better understand the origin of the collective-like phenomena in high-multiplicity pp and p-Pb collisions observed by several experiments at the CERN LHC.

The present study focuses on the investigation of the transverse momentum (p_T) distributions of charged pions, kaons and (anti)protons in minimum bias inelastic pp collisions at $\sqrt{s} = 7$ TeV at mid-rapidity ($|y| < 1$). The physical observables were studied using general-purpose Monte Carlo event generators, PYTHIA 8 and EPOS 3, which implement different underlying modeling of hadronic interactions through the description of soft and hard components of a physics process in an event. A double-differential study has been performed including a selection on the charged-particle multiplicity and the hardness of the event, both determined at mid-pseudorapidity ($|\eta| < 1$). The results are reported as the sum of particles and antiparticles. Such an analysis provides a more powerful tool for testing the above-mentioned models than the one which considers selection of events based on multiplicity alone. The presented results were published in Ref. [174].

4.1 Motivation

The measurements of the transverse momentum spectra of identified particles as a function of charged-particle multiplicity in pp collisions from the ALICE collaboration have shown that the general-purpose Monte Carlo (MC) models fail to describe the data quantitatively [63]. Therefore, the results of those comparisons alone are not enough to give desired information about the origin of the observed effects such as radial flow-like patterns. To extract more information, I propose the implementation of a differential study based on the classification of the events according to the multiplicity and the jet content. To this end, I simulated minimum bias pp events using PYTHIA 8.212 (tune Monash 2013) and EPOS 3.117 MC event generators. The obtained samples were analyzed as a function of charged-particle multiplicity N_{ch} determined at mid-pseudorapidity ($|\eta| < 1$), and transverse momentum of the leading (highest transverse momentum) jet p_T^{jet} .

In the so-called MPI-based model of color reconnection (CR) [81], the interaction between scattered partons at soft and at hard p_T scales is imposed as follows. All gluons of low- p_T interactions can be inserted onto the color-flow dipoles of a higher- p_T one, keeping the total string length as short as possible. Since the probability of having a hard scattering increases

with the number of MPI, color reconnection can give a strong correlation between the radial flow-like patterns and the hard component of the collision in high-multiplicity events [175].

On the contrary, in the scenario where the hydrodynamical evolution of the system is the prime mechanism, jets are not expected to strongly modify the radial flow patterns. Albeit hard partons cannot thermalize, momentum loss of jets could affect the fluid dynamic evolution of the medium. However, the effect has been studied for heavy-ion collisions and it was found to give only a minor correction [176]. In the present work, I argue that by exploiting such a fundamental difference between both models, one might say whether or not the observed effects are driven by hydrodynamics.

4.2 Proposed observables for revealing the origin of flow-like effects

The present study has been investigated using pp collisions at the center-of-mass energy of $\sqrt{s} = 7$ TeV considering sets with and without the mechanism which produces radial flow patterns. The results are presented both for PYTHIA 8 and EPOS 3 MC event generators which use parton-to-hadron fragmentation approaches fitted to the experimental data—such as the Lund string [177] and area law hadronization [178] models (for details see Section 3.3.1).

The studied observables include the invariant p_T distributions of light flavor charged hadrons such as π^\pm , K^\pm , and $p(\bar{p})$ as well as the baryon-to-meson ratio p/π . For both MC samples, only primary charged particles have been considered, requiring no selection on their minimum p_T . Primary particles—following the definition applied in the ALICE experiment at the LHC—are defined as all charged particles produced in the collision including the products of strong and electromagnetic decays but excluding products of weak decays. Results were obtained from generated samples of about 100 million inelastic events, including diffractive and non-diffractive components. A non-diffractive event includes a parton-parton interaction with a large momentum transfer (more than a few GeV/ c). On the other hand, some inelastic collisions can be diffractive in which a virtual particle, the pomeron, is responsible for the interaction. This sample was subsequently split into sub-samples based on the selection of charged-particle multiplicity determined at mid-pseudorapidity and on the hardness of the event. The latter selection is done by imposing a minimum cut on the transverse momentum p_T^{jet} of the leading jet, which is found in the same acceptance.

4.3 Results and discussion

First, to illustrate how PYTHIA 8 and EPOS 3 describe the experimental data measured by the ALICE collaboration [71], Fig. 4.1 shows the proton-to-pion ratio for inclusive charged particles simulated in inelastic pp collisions at $\sqrt{s} = 7$ TeV. For the p_T region around the p/π enhancement, PYTHIA 8 (in panel (a)) shows a qualitative agreement with data but

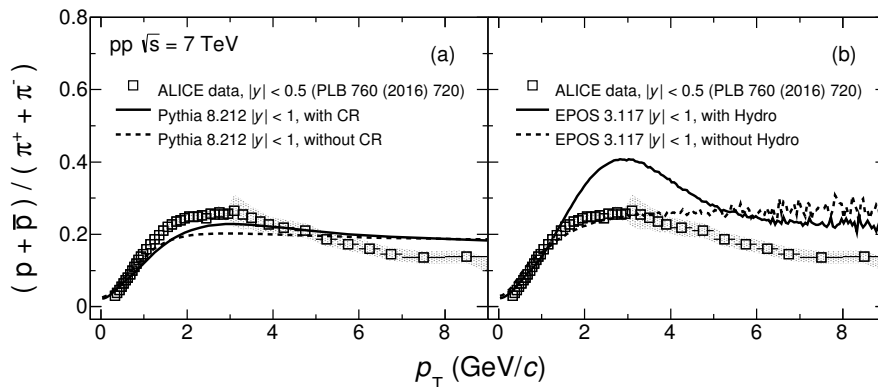


Figure 4.1: Proton-to-pion ratio as a function of transverse momentum for inelastic pp collisions at $\sqrt{s} = 7$ TeV measured by the ALICE collaboration [71]. Results are compared to (a) PYTHIA 8 and (b) EPOS 3 MC event generators. Cases with and without color reconnection (CR) and hydrodynamics (Hydro) are plotted as solid and dashed lines, respectively. Figure is taken from Ref. [174].

the size of the effect is underestimated, as also discussed in Ref. [82]. The EPOS 3 model (in panel (b)) gets the overall trend better for the full p_T range with the implementation of hydrodynamics (Hydro), though it clearly overestimates the measurement. Obviously, still, there is room for improvements in the models, which investigation is outside of the scope of the current work. Instead, a differential study is carried out to study differences attributed to the fundamental underlying physics mechanisms which produce radial flow effects.

4.3.1 Multiplicity-dependent baryon-to-meson ratios

Beyond the inclusive case, it is interesting to study the flow observable, namely the p/π ratio, as a function of charged-particle multiplicity. To this end, results are presented in intervals of z defined as $z = dN_{ch}/d\eta / \langle dN_{ch}/d\eta \rangle$, where $\langle dN_{ch}/d\eta \rangle = 5.505$ is the average charged-particle multiplicity measured at mid-pseudorapidity $|\eta| < 1$ for inelastic pp collisions at $\sqrt{s} = 7$ TeV. According to the pp results from ALICE [63], $\langle dN_{ch}/d\eta \rangle \sim 25$ would be already large enough to see new phenomena occurring in small collision systems. In this study, for the presented highest multiplicity case, even $\langle dN_{ch}/d\eta \rangle \sim 30$ is reached.

Figure 4.2 shows the multiplicity-dependent p/π ratios both for PYTHIA 8 and EPOS 3 MC models for two cases each: with and without color reconnection or hydrodynamics. The bottom panels indicate the situation in which no CR or Hydro option is set in the generators; they show no or only little dependence on z . When CR and Hydro is activated, the ratios exhibit a sudden change with p_T , that is a depletion (enhancement) for $p_T < 1$ GeV/ c ($1 < p_T < 6$ GeV/ c). This feature of the evolution is usually attributed to the phenomenon of radial flow which modifies the spectral shapes of the p_T distribution depending on the hadron mass.

In EPOS, a clear evolution with z is observed in the p/π ratios when the system is allowed to evolve hydrodynamically. In PYTHIA, a similar indication for the radial flow effect is present. Here, the radial flow-like behavior is attributed to color reconnection [82].

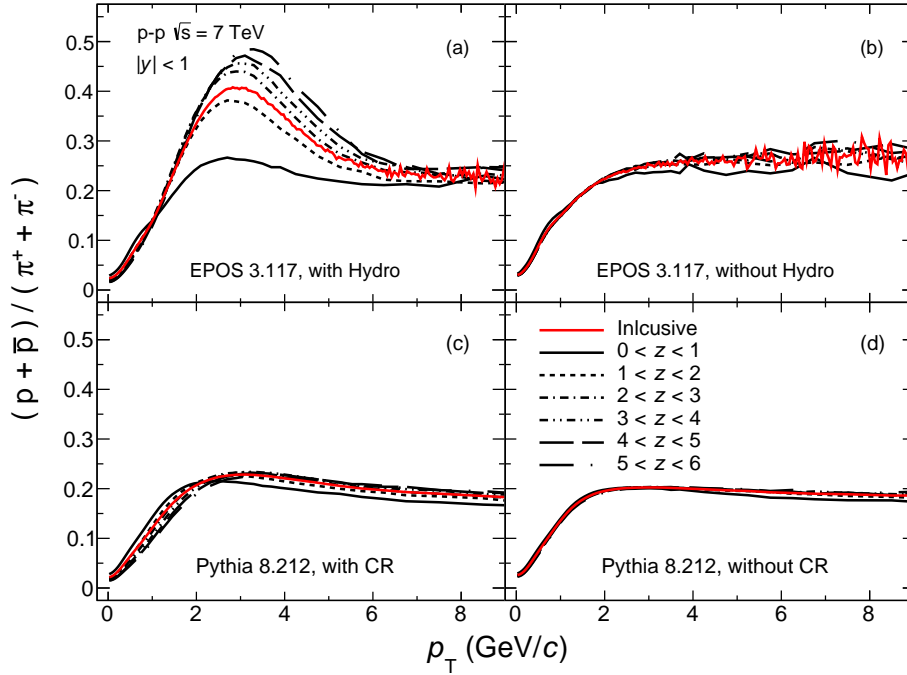


Figure 4.2: Proton-to-pion ratio as a function of transverse momentum for different z values of the average charged-particle multiplicity measured at mid-rapidity $|\eta| < 1$. Results are presented for pp collisions at $\sqrt{s} = 7$ TeV generated with EPOS 3 and PYTHIA 8. For PYTHIA 8 and EPOS 3, the ratios are displayed for simulations with, (a) and (c), and without, (b) and (d), color reconnection (CR) and hydrodynamical (Hydro) evolution of the system. Figure is taken from Ref. [174].

The magnitude of such evolution with z is not as progressive as that seen in EPOS. So far, the observations are similar to those seen by the experiments, see e.g. Ref. [179]. In the following, in a more differential study, it will be investigated in which z event class one might expect collective-like effects (if present at all) start to emerge.

4.3.2 Multiplicity dependence of the leading jet p_T^{jet}

On the top of the multiplicity selection, one can also classify events based on the transverse momentum p_T^{jet} of the produced jets. Per event, jets are reconstructed with the well-known anti- k_T algorithm implemented in FASTJET 3.1.3 [180], using charged and neutral particles, considering a cone radius of 0.4 and a minimum transverse momentum $p_{T,\text{min}}^{\text{jet}} = 5$ GeV/ c . The lower requirement on the value of p_T^{jet} acts to suppress soft interactions by ensuring that at least one semi-hard scattering is present in the acceptance. In the following, the jet searching is done within a given pseudorapidity interval, which defines the maximum pseudorapidity of the jet. It is important to highlight that FASTJET is a well-known tool for jet reconstruction in heavy-ion collisions, where it has been extensively used, even in most central Pb–Pb collisions.

In the used sample generated by PYTHIA 8, going from low- to high-multiplicities, respectively from $\langle dN_{\text{ch}}/d\eta \rangle = 2.12$ to $\langle dN_{\text{ch}}/d\eta \rangle = 29.8$, the average leading jet p_T^{jet} ranges from 7.1 GeV/ c up to 11.1 GeV/ c . Note that similar behavior was found for the leading

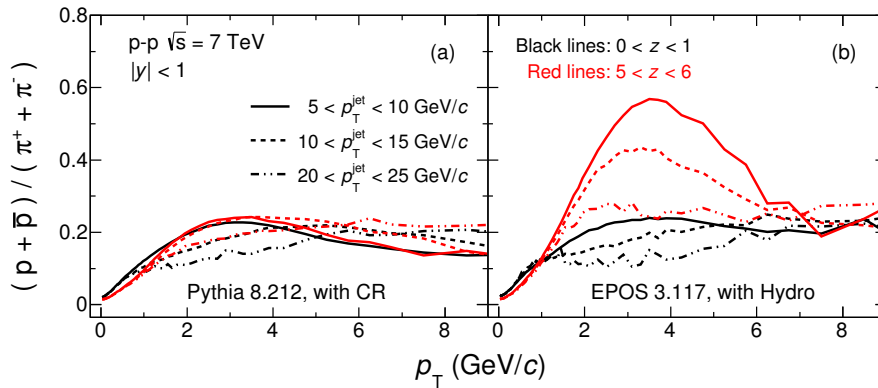


Figure 4.3: Proton-to-pion ratio as a function of transverse momentum for two multiplicity classes, $0 < z < 1$ (black lines) and $5 < z < 6$ (red lines); and for different p_T^{jet} intervals. Results are shown for both (a) PYTHIA 8 and (b) EPOS 3. Figure is taken from Ref. [174].

parton transverse momentum, obtained at mid-pseudorapidity as a function of $\langle dN_{\text{ch}}/d\eta \rangle$. In PYTHIA, this effect is explained in terms of the number of multiple-parton interactions, N_{mpi} . The probability of finding a hard parton is higher in high-multiplicity events (large average N_{mpi}) than in low-multiplicity events (small average N_{mpi}). This effect is also reflected in the behavior of the fraction of events having at least one jet with momentum above 5 GeV/c. Only around 1% of the low-multiplicity events contain jets with $p_T^{\text{jet}} > 5$ GeV/c. At the same time, at high multiplicities about 94% of the events have jets with $p_T^{\text{jet}} > 5$ GeV/c. This feature is simply the result of the jet selection bias, i.e. the higher the multiplicity at mid-pseudorapidity the higher the probability to find jets within the same η region.

4.3.3 Multiplicity-dependent p/π ratio as a function of jet p_T^{jet}

The p/π ratio is shown in Fig. 4.3 as a function of p_T for low- and high-multiplicity event classes, corresponding to $0 < z < 1$ (black lines) and $5 < z < 6$ (red lines), respectively. The low-multiplicity results indicate that already for $5 < p_T^{\text{jet}} < 10$ GeV/c the ratios exhibit an enhancement at $p_T \approx 3$ GeV/c for both PYTHIA 8 and EPOS 3. If the p_T^{jet} is increased then the region of the observed enhancement is shifted towards higher p_T . This observation suggests that the enhanced production is not an exclusive effect of radial flow (as suggested by Fig. 4.2), but also a feature of the parton fragmentation. It is worth noticing that the same effect has been observed in ALICE data, where the jet hadrochemistry has been measured in minimum bias pp collisions at $\sqrt{s} = 7$ TeV [181].

High-multiplicity results indicate that in EPOS the magnitude of the p/π ratio is remarkably increased with respect to the low-multiplicity case whereas no or only little change is seen in PYTHIA. Also, an enhanced production is seen with respect to the inclusive case reported in Fig. 4.2 without any selection on p_T^{jet} . In EPOS (Fig. 4.3, panel (b)) the p/π ratio experiences a monoton decrease with the increase of p_T^{jet} which approaches the values of low multiplicities and this way going beyond the inclusive curve. The development of such a

behavior vanishes when hydrodynamical effects are switched off—in a similar way as seen in Fig. 4.2(b). It can be related to the “core-corona” separation, where low-momentum partons are more likely forming the core region. It is worth mentioning that this difference between the two event classes could contribute to the differences observed in the hadrochemistry measured in the so-called bulk (outside the jet peak) and the jet regions in p–Pb and Pb–Pb collisions at the LHC reported in Refs. [182, 183]. Such an evolution in PYTHIA as opposed to that seen in EPOS is not that pronounced and only a modest (but still existing) change is present.

4.3.4 Double-differential blast wave analysis of p_T -spectra

The interpretation of the experimental results in terms of collective expansion of the matter [51, 184] described by hydrodynamical calculations is largely facilitated by the use of the analytical so-called blast wave parametrization [185–187]. The blast wave model describes a locally thermalized medium which experiences a collective expansion with a common velocity field and undergoing an instantaneous common freeze-out [188]. The functional form of the model is given by:

$$\frac{dN}{p_T dp_T} \propto \int_0^R r dr m_T I_0 \left(\frac{p_T \sinh \rho}{T_{\text{kin}}} \right) K_1 \left(\frac{m_T \cosh \rho}{T_{\text{kin}}} \right), \quad (4.1)$$

where m_T is the transverse mass defined in Appendix A, I_0 are the modified Bessel functions, and T_{kin} is the kinetic freeze-out temperature. The velocity profile ρ is described by $\rho = \tanh^{-1}(\beta_T)$, where β_T is the radial profile of the transverse expansion velocity. The blast wave model, although being a simplified hydrodynamic model, can be used to systematically compare the p_T -differential spectral shapes in different collision systems.

Blast wave model fits

From the simultaneous fit of the blast wave model to the π^\pm , K^\pm , and $p(\bar{p})$ p_T -spectra one can extract the two parameters of the model: T_{kin} and $\langle \beta_T \rangle$. In the current study the p_T ranges were considered to be as follows: $0.5 < p_T < 1.0 \text{ GeV}/c$, $0.3 < p_T < 1.5 \text{ GeV}/c$ and $0.8 < p_T < 2.0 \text{ GeV}/c$ to fit the model to the p_T distributions of charged pions, kaons and (anti)protons, respectively. This specific selection of the p_T ranges was successfully applied in previous studies where the parametrizations, obtained from the fits, were shown to describe the strange and multi-strange baryon p_T spectra within 10% [175].

The p_T -spectra for the particle species under study are reported in Fig. 4.4, which were obtained for both PYTHIA 8 (Fig. 4.4a) and EPOS 3 (Fig. 4.4b). Here, the more interesting low-multiplicity ($0 < z < 1$) case is examined where CR effects are known to be less important in PYTHIA, and the core region in EPOS is known to be less dominant with respect to the corona one. The average multiplicities reach only around 40% of the minimum

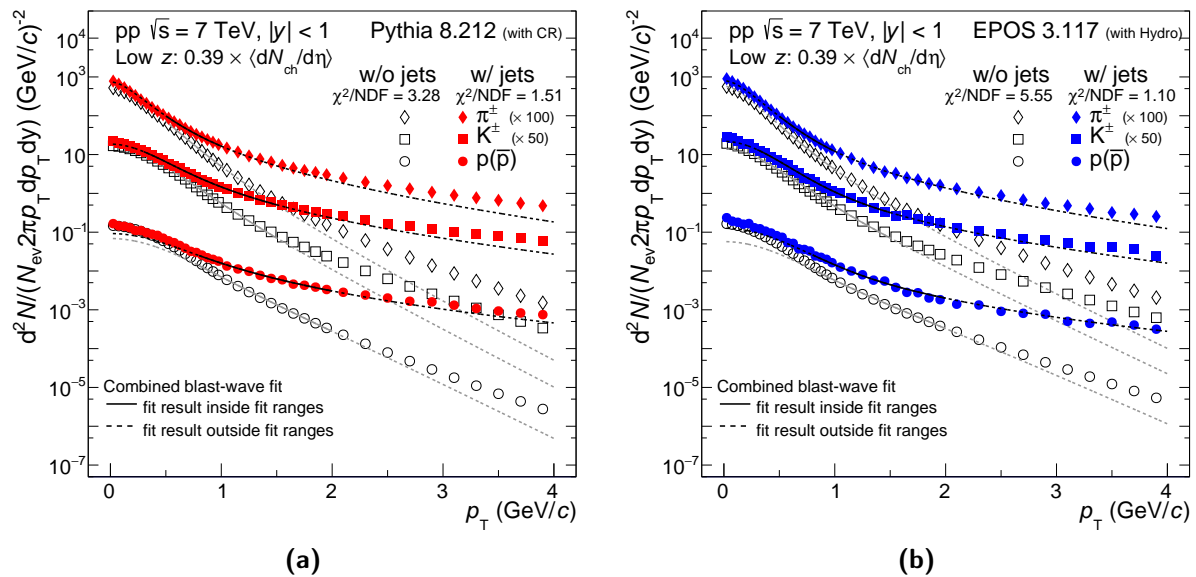


Figure 4.4: Transverse momentum distributions of charged pions, kaons and (anti)protons for low-multiplicity ($0.39 \times \langle dN_{ch}/d\eta \rangle$) pp collisions at $\sqrt{s} = 7$ TeV generated with (a) PYTHIA 8 (with CR) and with (b) EPOS 3 (with Hydro). Two cases are compared: events without a leading jet (open symbols) and with jets $20 < p_T^{jet} < 25$ GeV/c (full symbols). Figures are reproduced from Ref. [174].

bias average charged-particle multiplicity ($\langle dN_{ch}/d\eta \rangle \approx 5.5$). On the top of multiplicity selection, events were split into specific sub-classes based on the selection of the p_T^{jet} of the reconstructed jets. That is, in one case no jets were considered, whereas on the other, jets having $20 < p_T^{jet} < 25$ GeV/c were selected by the jet finder algorithm. The fit results show that the MC data is poorly described by the combined fit for events containing no jets. It is remarkable that the fit significantly improves in describing the spectral shapes when jets with high p_T^{jet} were found in the event. The observed behavior is also supported by the goodness-of-fit values χ^2 , that is, fit results give for PYTHIA 8 (EPOS 3) $\chi^2/ndf = 3.28$ ($\chi^2/ndf = 5.55$) for events without jets and $\chi^2/ndf = 1.51$ ($\chi^2/ndf = 1.10$) for events including jets with $20 < p_T^{jet} < 25$ GeV/c. It is noteworthy that in case of EPOS it is hard to make a strong conclusion for the p_T^{jet} event class due to lack of statistics. Nevertheless, the fits tend to show similar behavior then that seen for the case of PYTHIA 8. That being said, there are indications that collective-like phenomena might be also important in the presence of jets even if the event contains much less particles on average with respect to the inclusive case, i.e. when no selection is applied on event charged-particle multiplicity. It is important to emphasize that similar effects are observed for high-multiplicity events having about 5 to 6 times larger charged-particle multiplicity on average with respect to minimum bias case. Even though, the role of jets are naturally less important due to the possible autocorrelation bias introduced by the selections. The observed effects point out that in PYTHIA 8 the interaction between jets and underlying event³ is crucial for generating a collective-like behavior.

³In non-diffractive inelastic proton-proton collisions, the main momentum transfer occurs between only

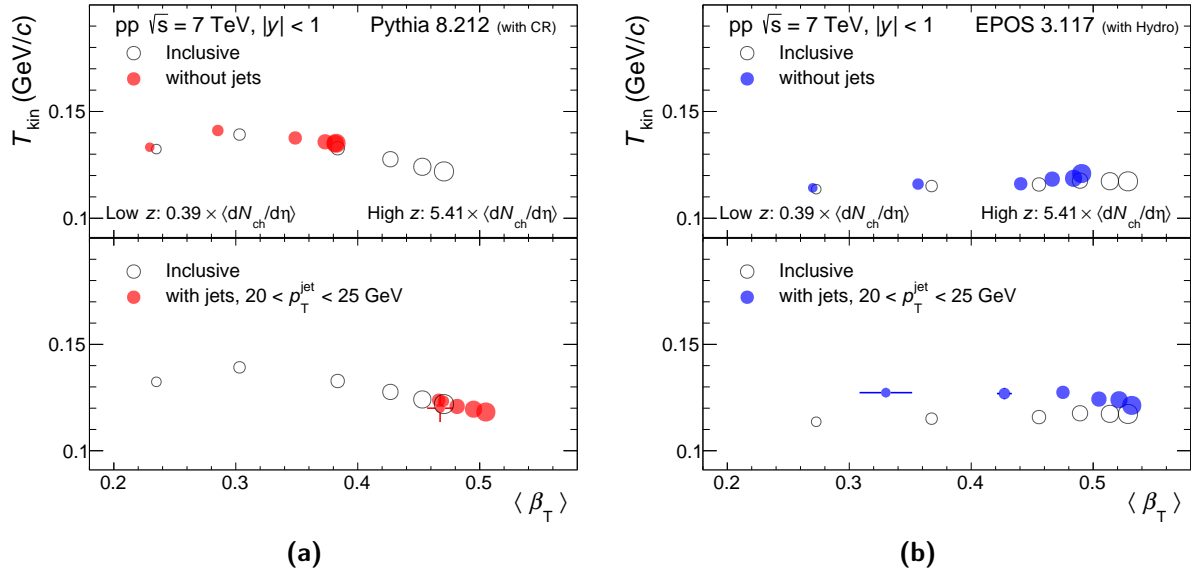


Figure 4.5: Correlation between two fit parameters obtained from the blast wave analysis, the kinetic temperature T_{kin} and the average transverse expansion velocity $\langle\beta_T\rangle$ of the system. Results are shown for $\sqrt{s} = 7$ TeV pp collisions generated with (a) PYTHIA 8 (with CR) and with (b) EPOS 3 (with Hydro). Figures are reproduced from Ref. [174].

Another essential test to quantify the importance of jets in events where flow patterns are generated with hydrodynamics or color reconnection is shown in Fig. 4.5. The figure summarizes the correlation of blast wave parameters, T_{kin} and $\langle\beta_T\rangle$, resulted from the combined fits performed in each multiplicity class. Again, cases for events based on their hardness are compared with each other. Note that along the x -axis the larger the $\langle\beta_T\rangle$ the larger the average charged-particle event multiplicity measured at mid-pseudorapidity. This change is emphasized by the increasing marker size towards larger $\langle\beta_T\rangle$.

Looking at events containing jets (lower panels of Fig. 4.5a and Fig. 4.5b) it is observed that for a given multiplicity class $\langle\beta_T\rangle$ increases with respect to the inclusive class. Along with the observation seen in Fig. 4.4 this corresponds to the fact that the selection of hard partons induce typically larger boost. For the highest z class ($5 < z < 6$, corresponding to $5.41 \times \langle dN_{\text{ch}}/d\eta \rangle$), this effect is weaker in EPOS 3 ($\sim 0.6\%$) than in PYTHIA 8 ($\sim 6.8\%$).

As it was shown previously, low- z events behave in a different way than high- z events in the absence of jets. In the former case, the blast wave model description gives worse result with respect to high-multiplicity events, and the situation improves with the selection of jets. In connection to those observations, taking low- z fit parameters in Fig. 4.5a and in Fig. 4.5b one sees a weak p_T^{jet} dependence as a function of $\langle\beta_T\rangle$ in EPOS 3. Contrary, in PYTHIA 8 for a given low- z class events with increasing p_T^{jet} experience a larger radial flow velocity $\langle\beta_T\rangle$.

two partons, which are complemented with initial and final state radiation, and multiple-parton interaction. The additional activity in the collision, which cannot be uniquely separated from initial and final state radiation, is referred to as the underlying event.

For PYTHIA 8, the larger the $\langle\beta_T\rangle$ the smaller the T_{kin} , and $\langle\beta_T\rangle$ reaches slightly smaller values for the highest z class compared to that in EPOS 3, where the T_{kin} shows no significant dependence on $\langle\beta_T\rangle$.

4.4 Summary and conclusions

To summarize, I performed a double-differential analysis to study the p_T spectra for identified charged hadrons using the EPOS 3 and PYTHIA 8 Monte Carlo event generators. Apart from the multiplicity selection, a more differential classification was done by using the leading jet transverse momentum. With the help of these studies I explored an observable which is aimed at ruling out or validating the underlying physics mechanism (hydrodynamics or color reconnection) generating radial flow patterns in pp collisions.

I found that in extremely-low multiplicity events containing jets, it is possible to find an event class where radial flow patterns arise, regardless of the weakness of collective flow effects caused by either hydrodynamics or color reconnection mechanism.

The observation of the collective-like effects was first based on studying the evolution of the p/π particle ratio as a function of p_T and p_T^{jet} . The evolution of this ratio is better seen in EPOS 3 where there is no strong correlation between soft and hard components of the collision; instead the interplay of core and corona determines particle production for the two components. The depletion at low p_T and an enhancement towards mid- p_T (ending up in a peak structure) is witnessed, which is also present between the low- and high-multiplicity events for a given jet p_T . The relative contribution of core and corona changes with multiplicity and results in similar effects in the hadrochemistry of the jet and bulk regions, as seen in experimental data.

Furthermore, from the blast wave model studies it turns out that the agreement between the model and the $\pi^\pm/K^\pm/p(\bar{p})$ p_T spectra in events classified using multiplicity and p_T^{jet} significantly improves with the increase of the leading jet p_T^{jet} . Remarkably, this agreement was found to be the best in low-multiplicity events having jets, which suggests that jets have crucial role in generating the observed collective-like behavior. This is also concluded from the evolution of the blast wave parameters, T_{kin} and $\langle\beta_T\rangle$. The trend seen in PYTHIA is qualitatively similar to those reported by ALICE in Ref. [53] in a multiplicity-dependent analysis of p–Pb data but without the explicit selection on jets. In that work, the corresponding parameters show a similar trend as the ones obtained in Pb–Pb collisions, which is argued to be consistent (within the limitation of the blast wave model) with the presence of radial flow in p–Pb collisions.

CHAPTER 5

A Large Ion Collider Experiment at the LHC

The main physics goal of ALICE [189] at the CERN LHC [190, 191] is to identify and study the hot and dense strongly interacting QCD matter, the sQGP, and its phase transition from the deconfined to the confined hadronic state created in high-energy relativistic heavy-ion collisions [192, 193]. The design of ALICE was driven by the experimental conditions expected in Pb–Pb collisions at the center-of-mass energies up to 5.5 TeV per nucleon pair. It has to be able to endure with the large multiplicities associated with these collision systems and at the same time has to comprise as many QGP-related observables as possible. Besides the heavy-ion physics program, ALICE also has a rich pp physics program; and those are complemented by measurements of p–Pb collisions.

The detector capabilities were designed for excellent tracking and particle identification (PID) in a high-particle density environment of up to 8000 charged particles per unit of pseudorapidity. Having a good tracking performance in such a high-multiplicity environment requires the use of high granularity detectors which can only operate at a reduced luminosity in pp collisions. The detector’s unique feature, besides the great tracking, is the PID over a broad range of momenta, from hundreds of MeV/ c up to about 100 GeV/ c , therefore including physics topics from soft to jet physics as well as high- p_T particle production. The low-momentum regime, which is the bulk part of particle production in pp and heavy-ion collisions, is achieved by a moderate magnetic field and a low amount of material to suppress energy loss and multiple scattering of low-momentum particles.

Figure 5.1 presents the schematic view of the ALICE apparatus during the LHC Run 1 data taking period (2009–2013). The ALICE’s central barrel consists of detectors which are capable of measuring hadrons, electrons, and photons, and a forward spectrometer for identification of muons; as well as additional forward and trigger detectors. The central barrel detectors are contained inside a large solenoid magnet of magnetic field strength $B = 0.5$ T and measure particles around mid-rapidity ($|\eta| < 0.8$). The main components of the ALICE’s central barrel going from the interaction point (IP) in outward direction, are the Inner Tracking System (ITS), the Time Projection Chamber (TPC), the Time of Flight (TOF) detector, and the High-Momentum Particle Identification Detector (HMPID). The ITS and the TPC are the major tracking detectors, which cover the full azimuth and also have particle identification capabilities. The TOF and HMPID detectors are dedicated to particle identification at different kinematic ranges. Furthermore, some other subsystems

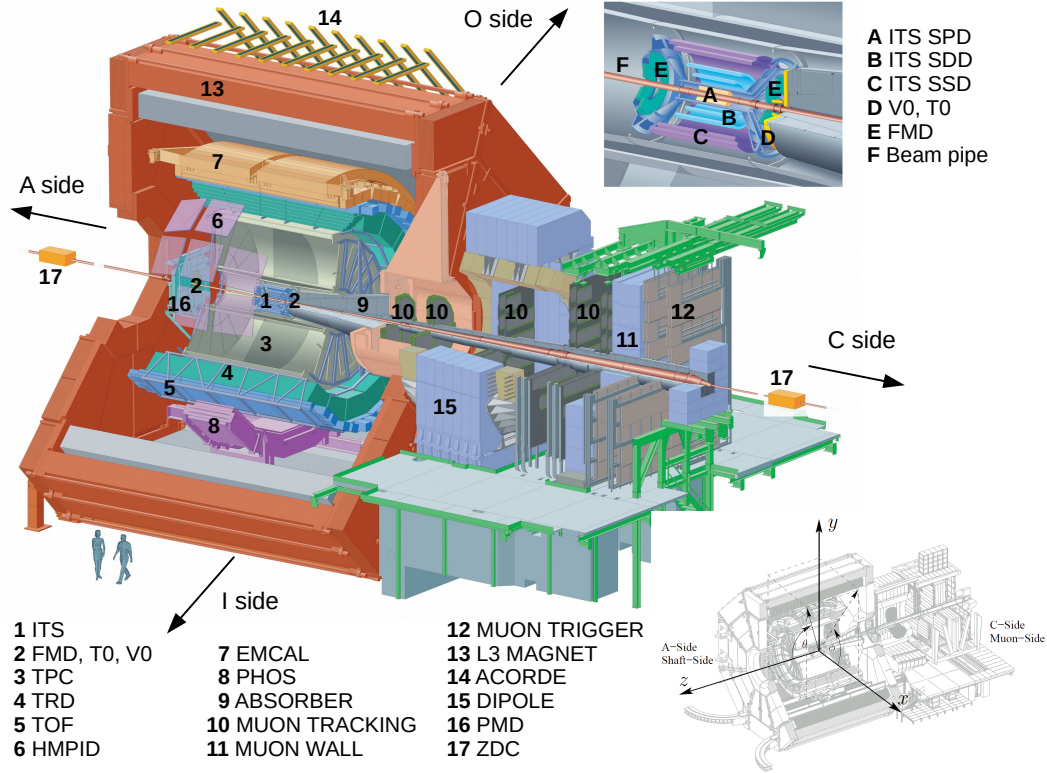


Figure 5.1: Schematic view of the ALICE apparatus during the LHC Run 1 [193]. The central barrel (embedded in the L3 solenoid magnet) and the muon arm in the forward direction are shown together with the inset of the ITS. The definition of the ALICE’s global coordinate system is depicted in the bottom right corner of this figure. Figure is edited from Refs. [193, 194].

are installed for event characterization and triggering purposes: The V0 detectors, and the Zero Degree Calorimeter (ZDC) outside of the central barrel, located on both sides of the IP. A detailed description of the ALICE detector and its performance during LHC Run 1 can be found in Refs. [189, 193]. In the following subsections, I describe those subsystems, which are relevant to the analyses presented in this thesis.

The ALICE’s global coordinate system [194], shown by the inset at the bottom right of Fig. 5.1, is a right-handed orthogonal Cartesian system which has its origin at the nominal interaction point. The z -axis is parallel to the LHC beam axis and is pointing towards the access shaft to the ALICE cavern called A-side, away from the muon arm. The opposite side (negative z values) is called C-Side. The horizontal x -axis points towards the center of the LHC ring. The side with positive x values is also called I-Side (inner), the opposite side correspondingly O-Side (outer). The y -axis is chosen to define a right-handed system, thus pointing upwards. The azimuthal angle ϕ is increasing counterclockwise, starting from the x -axis ($\phi = 0$) and looking from the A-Side towards the C-Side. The polar angle θ is increasing from the z -axis towards the xy -plane.

5.1 Charged particle tracking

Tracking devices are among the most important components of the detector setup since they are able to provide tracking information through the measurement of the primary interaction vertex and secondary vertices from decay particles, and the momentum of the particles by the track curvature in a magnetic field. Track finding in heavy-ion collisions at the LHC is challenging because of the extremely high track density. The tracking is performed mainly using information from the ITS and the TPC. Additionally, information from the TRD can be used to improve the p_T resolution of the tracks at high p_T .

5.1.1 The Inner Tracking System

The ITS [195, 196] is a silicon tracking detector made up of six concentric cylindrically-shaped layers, measuring high-resolution space points near the collision vertex. The two innermost layers consist of two arrays of Silicon Pixel Detector (SPD) located at average radial distance of $r = 5$ cm and $r = 7.6$ cm from the beam axis and cover $|\eta| < 2$ and $|\eta| < 1.4$, respectively. The SPD is used to reconstruct the primary vertex (PV) of the collision and short track segments with a hit in each of the SPD layers pointing to the PV, termed as tracklets. The resolution of reconstructed PV both for the longitudinal and transverse directions scales with the square root of the number of contributing tracks. The four outer layers are equipped with silicon drift (SDD) and strips (SSD) detectors, with the outermost layer being at $r = 43$ cm, covering $|\eta| < 1$. They are also capable of measuring the specific energy loss dE/dx with a relative resolution of about 10%. The ITS is also used as a stand-alone tracker to reconstruct charged particles with momenta below 200 MeV/ c that are deflected or decay before reaching the active volume of the TPC, and to recover tracks crossing dead regions of the TPC. The ITS takes part in the triggering as well.

5.1.2 The Time Projection Chamber

The TPC [197] is the main tracking detector of ALICE. It is a large volume cylindrical drift detector filled with a gas mixture of Ne–CO₂–N₂ (85.7% – 9.5% – 4.8%) which has a radial and longitudinal size of about 85 cm $< r < 250$ cm and -250 cm $< z < 250$ cm, respectively. It covers a pseudorapidity range of $|\eta| < 0.9$ for full radial length⁴ in full azimuth — except for small dead zones (2°) between the 18 TPC sectors amounts to 10%, where very straight tracks of high-momentum particles can be lost. The end-caps of the TPC are equipped with multi-wire proportional chambers (MWPCs) segmented radially into pad rows. Together with the measurement of the drift time, the TPC provides three-dimensional space point information up to 159 samples per track. Charged tracks originating from the PV can be reconstructed

⁴A track without full radial length traverses the TPC in a way that it leaves the TPC before reaching the outer radius; therefore it produces less tracking information than a track with full radial length; with 1/3 of radial track length the acceptance increases to $|\eta| < 1.5$.

down to ~ 100 MeV/ c and charged secondary particles down to ~ 50 MeV/ c [193]. The ITS and the TPC were aligned with respect to each other to a precision better than $100\ \mu\text{m}$ using tracks from cosmic rays and proton-proton collisions [196]. The combined information of the ITS and TPC allows one to determine the momenta of charged particles in the range of $50\ \text{MeV}/c < p < 100\ \text{GeV}/c$ with a resolution of $1 - 10\%$, depending on p . For tracks at small rapidities, the overall low material budget of the TPC is around 3.5% of radiation length⁵ x/X_0 . The TPC provides charged-hadron identification via the measurement of dE/dx in the fill gas, with a resolution of $\sim 5\%$ [197]. Further details on PID, focusing primarily on the relativistic rise regime of the Bethe–Bloch curve, will be discussed in Chapter 6.

5.2 Track reconstruction in the central barrel

The tracks of the charged particles in the presented analyses are measured by the two major tracking detectors of the ALICE central barrel, the ITS and the TPC. Each of them is capable of measuring tracks on their own. The ITS is able to construct tracklets from two hits in the SPD layers, as well as ITS-standalone (ITS-sa) tracks from all six layers including the SPD. The optimal tracking efficiency comes from combining both the ITS and the TPC detector information. This can be done by tracking a given particle either through both detectors or with a given detector that detects particles the other does not, called standalone. Tracks that are reconstructed only with the TPC have larger efficiencies compared to the ITS-TPC combined tracks, but at the same time have worse p_T resolution and higher contamination from secondaries. A better p_T resolution, which is crucial at high p_T , can be achieved using ITS-TPC combined tracks which will be referred to as global tracks in the following. Besides the global tracks, particles not detected by the TPC but by the ITS are reconstructed as so-called ITS-complementary tracks.

The global track reconstruction is based on the Kalman filter approach [199], and the different steps are schematically reported in Fig. 5.2. As indicated in the figure, in this procedure an inward-outward-inward (1st, 2nd, and 3rd paths) scheme is followed. The procedure starts with the clusterization in which the raw data of individual detectors are converted into clusters. After a preliminary vertex position has been determined using clusters from the SPD, the TPC track finding is performed. In the first iteration, tracking is performed from the TPC to the ITS and the information is used to update the position of the preliminary primary vertex. Afterwards, the first track seeds are built based on the information of two TPC clusters reconstructed at the outer radius and the vertex. These seeds are further propagated inwards along the nearest clusters, which satisfy a proximity criterion.

Out of the 159 possible clusters per track in the TPC, it is required that the seed contains at least 20 TPC clusters, indicating that the particle passed through at least about one

⁵The radiation length X_0 is characterizing the energy loss of high-energy photons (7/9 of the mean free path for pair production) and electrons (distance in which the energy drops to $1/e$ by radiation) [198].

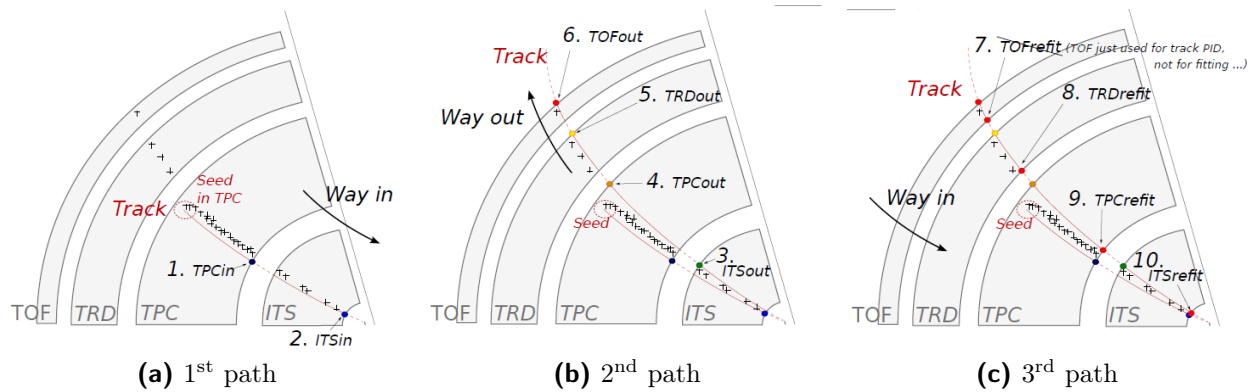


Figure 5.2: Principle of track reconstruction in an ALICE event. Figure is edited from Ref. [200].

third of the total length of the inner readout chamber. The track candidates are propagated towards the inner TPC radius, and based on the specific energy loss dE/dx in the TPC, the mass of the most probable particle identity is assigned. Propagating towards the outermost layer of the ITS, the TPC tracks serve as seeds for the ITS track finding. The seeds are then propagated inwards within the ITS, layer-by-layer, using clusters within a proximity cut in the sensitive areas. The information on the track position and the corresponding uncertainty are updated and saved as a new seed after each of these steps. After the reconstruction is completed in the ITS, all tracks are propagated outward along the previously determined clusters. Reaching the outer radius of the TPC the propagated tracks are attempted to be paired to TRD tracklets in each of the six TRD layers, and afterwards they are matched to the clusters of the TOF detector. The integrated track length and time-of-flight are computed step-by-step for different particle species hypotheses (e , μ , π , K , p) during particle identification. The tracks are further matched with the signals of other detectors in central barrel, e.g. EMCal, PHOS, and HMPID. In the very last stage, the tracks are refitted inwards with the Kalman filter algorithm. The fit is performed beginning at the outer TPC radius and using clusters determined previously, and the track parameters (position, direction, and inverse curvature) and the corresponding covariance matrix are determined. Based on these informations the final primary vertex is evaluated and further algorithms, e.g. the secondary vertex reconstruction, are initiated.

As already anticipated, it is crucial to have a good transverse momentum resolution $\sigma(p_T)$ for the measurement of p_T distributions up to very large momenta. The reconstruction procedure yields to track parameters and error estimates for those parameters. The inverse of the transverse momentum $1/p_T$ is one of these parameters and is directly related to the track curvature: $\sigma(p_T)/p_T \approx p_T \cdot \sigma(1/p_T)$. For small transverse momenta ($p_T < 1 \text{ GeV}/c$), the resolution is dominated by multiple scattering. In this p_T regime, the resolution improves with increasing p_T to an optimum of $\sigma(p_T)/p_T \approx 1\%$ around $p_T = 1 \text{ GeV}/c$. Towards larger p_T , the resolution degrades and becomes limited by the spatial resolution of the measured

track points. The performance in central Pb–Pb collisions is worse for high momentum than in pp or p–Pb collisions, due to an increased fraction of cluster overlaps, fake clusters, and clusters within ion tails.

For tracks at high p_T , the resolution improves by up to a factor of six for ITS-TPC tracks compared to the standalone TPC case. With the use of additional vertex constraint in the reconstruction, the performance of TPC standalone tracking is similar to the ITS-TPC combined tracking. A subsequent improvement is observed when the full ITS information is used since beside spatial coordinates the direction of the propagation is also used. For p–Pb collisions at high multiplicities, the performance worsens by up to 15%. The relative resolution $\sigma(p_T)/p_T$ at $p_T = 50 \text{ GeV}/c$ is around 10% in pp data of 2010 and around 4% in p–Pb data of 2013.

5.3 Primary and secondary vertex reconstruction

As discussed above, in the first step of the track reconstruction stage an estimate of the primary interaction vertex is determined [193]. Various informations are used to find the primary vertex position of the interaction: clusters from the SPD, tracks in the TPC, and global tracks from both the ITS and the TPC. As was mentioned in Section 5.1, one of the main purpose of the ITS is the localization of the primary vertex of the collision — with a resolution of better than $100 \mu\text{m}$ — and to reconstruct the secondary vertices of particle decays. The reconstruction of the primary vertex is performed using hit points and tracklets reconstructed in the two layers of the SPD. The reconstructed points in the two layers that are close in azimuth and z directions are paired together, and they are used separately to estimate the position of the primary vertex along the beam axis and in the transverse plane. The estimated vertex position along the beam axis is corrected using the result obtained for the transverse plane, and this position is used as a constraint in the first pass of the track reconstruction. Tracks reconstructed in the TPC and the ITS are then used for recalculating the position of the primary vertex which improves the precision of the measurement. The resolution of the vertex position depends on multiplicity and is normally better than $10 \mu\text{m}$ ($110 \mu\text{m}$) in z and about $35 \mu\text{m}$ ($70 \mu\text{m}$) in the transverse plane for 0 – 5% central heavy-ion (minimum bias pp) collisions.

Particles with short lifetimes ($c\tau$) cannot be directly reconstructed by the procedure described above since they decay before they could reach any active detector volume; hence, these particles must be reconstructed from the secondary vertices at which they decay. The reconstruction of secondary vertices from such decays can be illustrated via neutral strange particles in the material with the decay channels $K_S^0 \rightarrow \pi^+ + \pi^-$, and $\Xi^- \rightarrow \Lambda^0 \rightarrow p + \pi^- + \pi^-$. The two primary particles decay at some point between the first and second layers of the ITS, without any hit in the SPD since they are neutral. Their decay daughters can be reconstructed in the outer layers. Tracks that are reconstructed from Kalman filter approach

described above and lie outside a maximal requirement of the DCA with respect to the primary vertex are matched in pairs of opposite charges, known as neutral vertex candidates or V^0 candidates [193]. If their Distance of Closest Approach (DCA)⁶ lies closer to the primary vertex than the innermost measured point of any track, the pair is stored as a V^0 particle candidate. In order to accept candidates with momenta pointing from the primary vertex, a selection criterion is applied on the cosine of the pointing angle between the V^0 's momentum and the line connecting the V^0 vertex and the primary vertex, for more details see Refs. [189, 193, 199].

5.4 Triggering and characterization of events

The V0 detector [201] system contains two detectors, V0A and V0C, which are situated on both sides of the IP. The V0 is a small angle detector consisting of two arrays of plastic scintillator counters segmented into four rings in radial direction and eight sectors in azimuth. Its 32 scintillator tiles cover the full azimuth within $2.8 < \eta < 5.1$ (V0A) and $-3.7 < \eta < -1.7$ (V0C). Due to the asymmetrically positioned detectors with respect to the IP, timing measurements can be applied with time resolution of 1 ns allowing beam-gas events to be identified that occurred outside of the nominal interaction region to perform background suppression. The detector provides a minimum-bias trigger for the central barrel detectors using all scintillator signals above a certain threshold.

The V0 detector is used to measure global event properties in pp and p–Pb collisions such as the charged-particle multiplicity of the event⁷. In case of Pb–Pb collisions, the V0 detector system also allows estimating the centrality of a collision — with a resolution of around 0.5% centrality bin width in the most central collisions and better than 2% for more peripheral collisions. For p–Pb collisions which are analyzed in this work, only the V0A (on the Pb fragmentation side, Pb-going side) is used for this purpose; the method to determine the centrality of the collision is discussed in the next section. It is worth noting that the V0 also participates in the measurement of luminosity in pp collisions with moderately good precision of about 10%.

5.5 Centrality determination in p–Pb collisions

In the Glauber Monte Carlo simulation, the nucleons are randomly generated event-by-event according to their nuclear density distributions. When a single nucleon-nucleon collision takes place, a nucleon is considered a participant if its distance to another nucleon is below a certain threshold in the modeled collision. This range depends on the (inelastic) nucleon-nucleon cross section of the collision system.

⁶The distance of closest approach (DCA or alternatively impact parameter) of a track to the collision vertex is the minimal distance between the track's trajectory and the vertex position.

⁷The amplitude of the signal measured by the V0 corresponds to the charged-particle multiplicity produced in the collision.

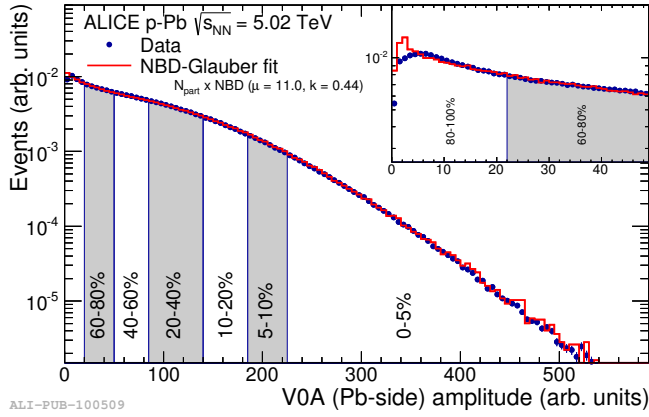


Figure 5.3: Distribution of the sum of V0A (Pb-going side) amplitudes measured in p–Pb collisions at $\sqrt{s_{NN}} = 5.02$ TeV. Multiplicity event classes are indicated by regions under the distribution separated by vertical lines. The inset shows a zoom-in on the most peripheral events. Red curve shows the result of the NBD–Glauber fit to the measured data points. Figure is taken from Ref. [16].

Geometrical quantities that are not accessible experimentally can be correlated to measurable signals in the detector, such as the charged-particle multiplicity. This is based on the reasonable assumption that the measured multiplicity is proportional to the number of nucleons which participated in the collisions, and it increases monotonically at mid-rapidity. In order to extract the dependence on geometry, the events are classified in intervals of multiplicity. These intervals are expressed as percentages of the total inelastic hadronic cross section and called centrality percentiles. The categorization is conducted by fitting the measured multiplicity distribution to a generated distribution produced by the Glauber model. The multiplicity per nucleon-nucleon collision in an event can be parametrized by the negative binomial distribution (NBD) [202] combined with the Glauber MC model. Applying the model for any collision with given N_{part} and N_{coll} values one has to introduce the concept of the wounded nucleon model [203]. It essentially states that nucleus-nucleus collisions can be decomposed into soft and hard interactions, where the soft interactions produce particles with an average multiplicity proportional to N_{part} , and the probability for hard interactions to occur is proportional to N_{coll} .

The estimation of multiplicity is based on the measurement of charged particle multiplicity via the total charge deposited in the V0A scintillator hodoscopes located on the Pb-going side. The distribution of the sum of amplitudes in the V0A hodoscopes is fitted with a parametrization based on the Glauber MC model and the NBD distribution (henceforth NBD–Glauber), and it is shown in Fig. 5.3 together with the extracted parameters. The event sample was divided into seven multiplicity classes, which are indicated by shaded areas corresponding to the different centrality classes of hadronic collisions.

One has to take into account that fluctuations of N_{part} arise caused by the NBD, and they are significantly larger than in the standard Glauber MC. Moreover, they are relatively stronger in p–Pb compared to Pb–Pb. The other approach which considers these fluctuations is the Glauber–Gribov model. It is worth noting that the standard NBD–Glauber fit together with a Glauber–Gribov fit show an equally good description of the measured V0A distribution. As discussed in Ref. [16], due to the presence of multiplicity fluctuations in the p–Pb sample where the entire multiplicity reach is comparable to the magnitude of the fluctuations

Event class	0 – 5%	5 – 10%	10 – 20%	20 – 40%	40 – 60%	60 – 80%	80 – 100%
V0A range (arb. unit)	> 227	187 – 227	142 – 187	89 – 142	52 – 89	22 – 52	< 22
$\langle dN_{\text{ch}}/d\eta \rangle_{ \eta <0.5}$	45 ± 1	36.2 ± 0.8	30.5 ± 0.7	23.2 ± 0.5	16.1 ± 0.4	9.8 ± 0.2	4.4 ± 0.1

Table 5.1: Definition of the event classes in the multiplicity-dependent p–Pb analysis at $\sqrt{s_{\text{NN}}} = 5.02$ TeV as fractions of the analyzed event sample and their corresponding average pseudorapidity density of charged particles $\langle dN_{\text{ch}}/d\eta \rangle_{|\eta|<0.5}$ measured at mid-pseudorapidity, $|\eta| < 0.5$. Reported uncertainties are the dominant systematic ones. Table is reproduced from Ref. [53].

introduce a dynamical bias in the definition of centrality classes based on charged-particle multiplicity. The selection of high multiplicity implies large average $\langle N_{\text{part}} \rangle$ together with fluctuations leading to deviations from the binary scaling of hard processes. The ALICE collaboration developed the so-called “hybrid method” to eliminate the above-mentioned bias. In this method, p–Pb events are categorized by their energy signature measured by the Zero Degree Calorimeter (ZDC) which has large η -separation from the mid-rapidity region. Applying this method, ALICE has presented several new measurements which demonstrate binary-collision scaling, see e.g. Refs. [204, 205].

The V0A event multiplicity classes as fractions of the analyzed event sample are summarized in Tab. 5.1. The corresponding average pseudorapidity density of charged particles $\langle dN_{\text{ch}}/d\eta \rangle_{|\eta|<0.5}$ measured at mid-pseudorapidity ($|\eta| < 0.5$) for a given V0A class is also reported. It is worth noticing that the average multiplicity in the 80 – 100% V0A class is considerably lower than that in MB pp collisions at $\sqrt{s} = 7$ TeV, $\langle dN_{\text{ch}}/d\eta \rangle_{|\eta|<0.5} = 6.01 \pm 0.01$ (stat.) $^{+0.20}_{-0.12}$ (syst.) [206], which indicates a strong selection bias. These quantities are corrected for acceptance and tracking efficiency as well as contamination of secondary particles. Unlike in Ref. [53], in this work, they are also corrected for trigger and vertex-reconstruction inefficiencies (for details see Section 7.6.3).

5.6 Upgrade of ALICE during Long Shutdown 1 and 2

During the first Long Shutdown (LS 1, 2013 Feb–2015 March) of the LHC, the ALICE detector was upgraded; it was completed and extended with new detector elements. Relevant to this thesis to be mentioned is that the TPC was filled with a new gas mixture Ar–CO₂ which has a larger primary ionization and thus an improved momentum resolution despite the increased diffusion and high particle fluxes generated during proton-lead and lead-lead modes. Also, the LHC itself was prepared for the final design energy of up to 14 TeV, with a planned instantaneous (design) luminosity of $10^{34} \text{ cm}^{-2} \text{ s}^{-1}$ and an expected bunch spacing time of 25 ns (for more details see Ref. [207]).

The upgrade of the CERN LHC during Long Shutdown 2 (LS 2, 2018–2020) will provide higher luminosity in Pb–Pb collisions, which is of special interest for ALICE. The currently approved running scenario is valid for data set of an integrated luminosity of

$\mathcal{L}_{\text{int}} = 1 \text{ nb}^{-1}$. However, in a more optimistic scenario—under the assumption of stable LHC beam conditions with Pb–Pb beams of one month per year—an integrated luminosity of $\mathcal{L}_{\text{int}} = 2.85 \text{ nb}^{-1}$ per year can be recorded. Till the end of LS 3 ALICE expects a peak luminosity of $6 \times 10^{27} \text{ cm}^{-2} \text{ s}^{-1}$ and an average luminosity of $2.4 \times 10^{27} \text{ cm}^{-2} \text{ s}^{-1}$, allowing to record $\mathcal{L}_{\text{int}} = 10 \text{ nb}^{-1}$ of Pb–Pb collisions between 2020 and 2026. Furthermore, besides Pb–Pb collisions, it is also planned to record $\mathcal{L}_{\text{int}} = 6 \text{ pb}^{-1}$ of pp and $\mathcal{L}_{\text{int}} = 50 \text{ nb}^{-1}$ of p–Pb collisions at equivalent center-of-mass energies until the end of 2029. These luminosity values will result in about a factor of 100 more data than is currently available (till the end of LHC Run 2, 2018).

In order to reach these goals, both the data-taking rate and the tracking performance have to be improved. These involve, for example, the upgrade of the trigger system, the readout electronics of several detectors (e.g. TPC, TRD, and TOF) to deal with the increased data-taking rates, and the data acquisition system to handle the large amount of data. The multi-wire chambers of the TPC will also be replaced by Gas Electron Multiplier (GEM) detectors, which will allow faster data taking.

Some of the main physics goals of ALICE after LS 2 include the studies of the thermalization of partons in the QGP (in particular heavy-flavor quarks), further investigation of jet-quenching mechanisms, the initial temperature and the equation of state of the QCD medium using low-mass dileptons, and the search for the existence of heavier nuclear states [207].

5.6.1 The concept of a Very High Momentum Particle Identification Detector

Among many other interesting physics topics which are in the scope of the upgrade program of ALICE, one important example would be the measurement of the identified jet fragmentation functions and their in-medium modification over a wide p_T range. The measurement of the high-momentum hadrochemistry in jets might enable us to gain a better understanding of the baryon-meson formation and flavor specific effects of fragmentation of hadrons in jets. To measure hadron formation in jets, a detector is needed which can identify hadrons on a track-by-track basis at high p_T (up to $25 \text{ GeV}/c$). A suitable choice being capable of performing such a measurement is the one based on the Ring Imaging Cherenkov (RICH) technique. Such a RICH detector consists of a gas radiator vessel, a photon detector, and a MIP detector. In the new concept, the radiator volume is pressurized (at $\sim 3.5 \text{ bar}$) and contains octafluorotetrahydrofuran ($\text{C}_4\text{F}_8\text{O}$) as fill gas. Moreover, in order to avoid condensation, it is heated. The photon detector is an MWPC—alternatively based on Thick-GEMs [208]—with CsI-coated photocathode, sensitive in the vacuum ultraviolet spectral range ($< 200 \text{ nm}$) and operated in methane (CH_4). It has a similar structure as that of the HMPID’s version. A sapphire window provides an interface between the pressurized and heated radiator gas volume and the photon detector part being at atmospheric pressure. These components are

bracketed by MIP detectors which serve as triggering as well as tracking devices positioned in front and behind of the presented layout.

An extension of the currently operating HMPID detector would be a novel RICH detector called the Very High Momentum Particle Identification Detector (VHMPID) [209, 210]. For this detector concept, a High Momentum Trigger Detector was developed by the MTA Lendület Innovative Detector Development Research (REGARD) group at the Wigner RCP in Budapest. Later on, these trigger detectors were realized as novel MWPC detectors specialized for tracking which are called as Close Cathode Chamber (CCC) [208, 211–213]. The CCC comes with two essential benefits relevant for the applications. One is that the tolerance to cathode-anode gap variations makes it unnecessary to build robust frames for the chamber thus minimizing the material budget. The other being that having narrow pad response function the chamber can be read out digitally while keeping the required spatial resolution at reasonable level.

Based on the already developed CCC layout, I designed and built several prototype CCC detectors with a small size. To evaluate their excellent position resolution—obtained via analog readout—and their applicability in the VHMPID layout, I successfully tested them during beam test measurements at the T10 beamline located in the East Hall experimental area of the CERN Proton Synchrotron accelerator. With analog readout, a significant (factor of 6) improvement in position resolution of $90\ \mu\text{m}$ with a relative error of $\pm 4\%$ could be achieved on pads with 2-mm-wide segmentation. In case of field wires with a wire pitch of 4 mm a resolution of $0.41\ \text{mm} \pm 1\%$ could be obtained which is only slightly below the ideally achievable performance value. Overall, the obtained results are already proven to be useful thanks to the two-dimensional projective geometry of the constructed system. My results were published in Ref. [212]. For details on the analysis procedure as well as on the applied method for the extraction of high-quality position information, see Appendix B. For further studies, this layout can provide precise position information for tracks passing through the photon detector in the VHMPID. This information gives useful input for the matching with global tracks reconstructed in the central barrel of ALICE. For this reason, it contributes to the improvement of the Cherenkov-ring finding algorithm and the resolution of the PID.

Apart from hardware developments, I contributed with a physics performance study to the Letter of Intent (LoI) document of the ALICE VHMPID upgrade project; where the results obtained from the detector and physics performance studies are summarized. I wrote a dedicated section (Sec.4.4.2) in the LoI document, summarizing my Monte Carlo simulation studies performed using identified two-particle angular correlations. My results help to verify the applicability of the ALICE VMHPID for physical analysis [209, 214].

CHAPTER 6

Particle identification with the ALICE TPC at high p_T

This chapter summarizes the main technical aspects of the method used for particle identification with the ALICE TPC at the relativistic rise regime of the Bethe–Bloch curve. The minimum-bias $\sqrt{s} = 7$ TeV pp data will be taken as an example to show how each step of the procedure is carried out. However, without loss of generality, the presented concepts are also valid for both $\sqrt{s} = 13$ TeV pp and $\sqrt{s_{NN}} = 5.02$ TeV p–Pb data, which were analyzed using the same technique — with the latter being performed as a function of charged-particle multiplicity determined in the forward rapidity region (Pb-going side).

For the presented light flavor hadron species, the extracted quantities for separate charges (i.e. positively and negatively charged particles) are found to be compatible within statistical errors, as expected at these collision energies at mid-rapidity. Therefore, all the results shown here and in the following chapters are presented for summed charges. I refer to the sum of particles and antiparticles, $\pi^+ + \pi^-$, $K^+ + K^-$, $p + \bar{p}$ as π^\pm , K^\pm , $p(\bar{p})$, or simply as π , K , p , respectively, unless explicitly written.

6.1 Introduction

Charged particles traversing the gaseous medium can be detected via the measurement of their energy deposition per unit path length dE/dx in the gas which is described by the Bethe–Bloch function [215]. The ALICE TPC besides track reconstruction measures this energy deposition providing charged-particle identification. The resolution of the dE/dx is about 5% (for pp collisions) which allows to discriminate between different particle species from a p_T of a few hundred MeV/ c up to $p_T = 20$ GeV/ c .

In Fig. 6.1 the specific energy loss dE/dx of the charged tracks is plotted as a function of the track momentum p measured in minimum bias pp collisions at $\sqrt{s} = 13$ TeV. The solid colored lines are parametrisations of the Bethe–Bloch curves for the individual species which are under study in this thesis. At low momenta ($p \lesssim 0.5$ GeV/ c), the dE/dx for the different hadron species are well separated, hence a track-by-track particle identification is feasible; it can be done by comparing the measured PID signal with the expected values for different mass hypotheses. For each particle hypotheses, the distance between the measured and the expected value is calculated in multiple times the standard deviation σ of the measured energy loss distribution. An identity is assigned to a track if the measured signal differs from the expected value by less than typically several times its resolution σ . Other methods

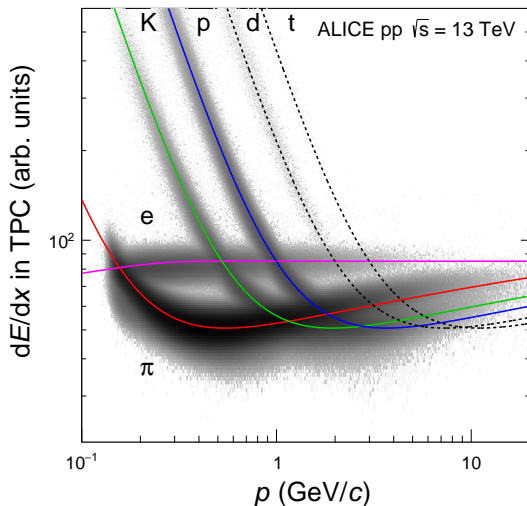


Figure 6.1: Specific energy loss dE/dx as a function of momentum p of charged particles measured in the ALICE Time Projection Chamber in minimum bias pp collisions at $\sqrt{s} = 13$ TeV. Solid and dashed lines indicate the parametrizations of the expected mean energy loss. Figure is reproduced from Ref. [216].

based on PID probabilities for a given particle to be a certain kind can be also assigned on a track-by-track basis using the Bayesian approach [217]. At higher momenta (especially for $p \gtrsim 2$ GeV/ c), the particle separation becomes small and approximately constant as a function of p . In the so-called relativistic rise region ($p \gtrsim 5$ GeV/ c), the dE/dx of the different particle species overlap, hence the track-by-track identification is not viable. Still, the PID is possible by exploiting a statistical unfolding technique. In this method, the Bethe–Bloch parametrization of the specific energy loss — characteristic to each particle trajectory — is performed as a function of the track momentum.

6.2 Particle identification at the relativistic rise

Since the specific energy loss dE/dx depends (theoretically) only on the particle’s velocity, and on the square of its charge, the dE/dx information can be used directly for mass measurement, together with the momentum information supplied by the track reconstruction.

By specific energy loss measurement we mean an indirect estimate of the mean energy loss of a charged particle as it passes through a gas-filled volume. The energy loss of a charged particle rises with $\beta\gamma = p/mc$, and the measurement of it may be used to estimate the velocity. The physics of the energy loss is well understood for many years, and the applied techniques to measure it have been extensively used in high-energy physics in the past couple of decades, see e.g. Ref. [218]. For a given incident particle with electric charge z and relativistic velocity β (relative to the speed of light in the rest frame of the traversed medium), the mean energy loss is given by the Bethe–Bloch formula [219]:

$$-\langle dE/dx \rangle = K z^2 \frac{Z}{A} \frac{1}{\beta^2} \left[\frac{1}{2} \ln \left(\frac{2m_e c^2 \beta^2 \gamma^2 E_{\max}}{I^2} \right) - \beta^2 - \frac{\delta(\beta\gamma)}{2} \right], \quad (6.1)$$

where $K = 4\pi N_A r_e^2 m_e c^2$, r_e and m_e are, respectively, the classical radius and mass of the

electron, N_A Avogadro's number, Z and A the atomic number and mass number of the material, $\gamma = (1 - \beta^2)^{-1/2}$ is the Lorentz factor, I is the average ionization energy of the material, and $E_{\max} = \frac{2m_e c^2 \beta^2 \gamma^2}{1 + 2\gamma m_e/M + (m_e/M)^2}$ is the maximum energy transfer in the ionization process for an incident particle of mass m . In the so-called low-energy approximation, i.e. if $2\gamma m_e/m \ll 1$, the maximal energy transfer $E_{\max} \approx 2m_e c^2 \beta^2 \gamma^2$ is independent of m and thus only depends on the velocity β . It is worth noting that in case of a particle with momentum p , $\beta = p/(mc) \times \sqrt{1 + (p/(mc))^2}$. Consequently, $\beta\gamma$ and the $\langle -dE/dx \rangle$, in turn, depends only on p/mc . Equation (6.1) is valid for $0.1 \lesssim \beta\gamma \lesssim 1000$ since at the lower limit the velocity of the incident particle becomes comparable with the atomic electron velocity and at the upper limit radiative losses start to be important [218].

One distinguishes mainly four regions in the Bethe–Bloch curve. At low velocities, $\langle dE/dx \rangle$ is dominated by the overall $1/\beta^2$ factor and is steeply decreasing with increasing velocity until it reaches the minimum ionizing particle (MIP) region, which is typically at $\beta\gamma \approx 3.6$. As the momentum increases beyond this point, the term $1/\beta^2$ is almost constant and dE/dx grows as $\ln(\beta\gamma)$ for particles with velocity $\beta \sim 1$. This effect is due to the fact that the E_{\max} increases as $\beta^2 \gamma^2$ causing higher mean energy loss and that the Lorentz contraction increases the electromagnetic field in the transverse direction leading to a higher cross section for excitation and ionization. This region is known as the relativistic rise. At very high velocities, the Bethe–Bloch curve shows a saturation, the so-called Fermi plateau. It is worth noting that the separation between the Fermi plateau and the minimum ionizing region strongly depends on the used detector material. In gaseous detectors, the separation is usually sufficient to distinguish between particles in these regions. In fact, only relative values of the ionization need to be known to distinguish between different particle types. The logarithmic rise of the mean energy loss at high $\beta\gamma$ is tamed by the polarization of the medium traversed by the charged particle. This phenomenon, also called density effect, is encoded in the $\delta(\beta\gamma)$ -term of the equation and normally it is a linear function of $\ln \gamma$ [219].

The dE/dx in thin material, as given by Eq. (6.1), is governed by large fluctuations due to the limited number of ionizations, excitations, and large energy transfer events. Even with hundreds of dE/dx samples measured from a track a proper value for the mean energy loss cannot be determined. These fluctuations are not Gaussian but are asymmetric with a high energy loss tail due to the large single-collision energy transfers discussed above, giving rise to a Landau-distribution [220]. Different methods have been investigated to deal with this difficulty, and the best (and easiest) way is to calculate the most probable energy loss—usually its value is below the mean value given by the Bethe–Bloch equation.

6.3 Determination of the dE/dx signal

Experimentally, the dE/dx information for a given track in a drift chamber is reconstructed from a set of ionization clusters which are assigned to the track. In the ALICE TPC, there

are up to 159 such clusters corresponding to the number of pad rows in the readout plane. In contrast to the tracking, the PID signal also considers single-pad clusters associated to the corresponding track. However, since the amplification at the chamber borders is not perfectly calibrated due to non-linearities in the response—since the average size of the Krypton ($^{86}_{36}\text{Kr}$) clusters (see Section 6.5) is larger than the pad size—, the clusters in the vicinity of the edges of the wire chambers are not used for PID information. Therefore the number of clusters N_{cl} , used for the calculation of the dE/dx PID signal, can be different from the one used for tracking purposes. Since the position information is significantly less affected, the rejected clusters can still be used for tracking.

In each pad row, the charges deposited by the track via ionization are detected, from which the corresponding energy can be calculated. This energy fluctuates from pad row to pad row and its probability follows a Landau distribution. Since the underlying ionization distribution has neither a finite mean nor a finite variance [221], a reasonable estimation of the PID signal of the TPC associated to a track is retrieved from a truncated mean of the distribution of the maximal or the total charge associated to the clusters of a given track. In pp collisions, the total (or integrated) charge of each cluster is used as it is found to provide the best separation power. The integrated charge is corrected for the tails of the charge distribution that are below the readout threshold. At the same time, in p–Pb collisions, the maximum charge in the cluster is used to calculate the dE/dx due to its less sensitivity of cluster overlaps⁸

The truncated dE/dx is characterized by a parameter $t \in]0, 1]$ and defined as the average of the (tn) lowest values among the n values of $(\Delta E/\Delta x)_i$:

$$-\langle dE/dx \rangle_{\text{truncated}}^t = \frac{1}{l} \sum_{i=1}^l (\Delta E/\Delta x)_i, \quad (6.2)$$

where l is an integer closest to tn and $(\Delta E/\Delta x)_i \leq (\Delta E/\Delta x)_{i+1}$ for all $i \in [1, n-1]$. The value of t is chosen to remove the tail of the Landau-like cluster charge distribution and, at the same time, to maximize the separation power⁹, which yields $t = 0.6$ [222]. For the analyzed data in this thesis, it was verified that the dE/dx distribution in a given momentum bin, determined with the truncated mean method with such a value for t , i.e. considering only the 60% lowest cluster charge values, exhibits a Gaussian shape to a good approximation. Due to these beneficial properties, the truncated mean $-\langle dE/dx \rangle_{\text{truncated}}^t$ is used as the mean of TPC dE/dx signal. Hereafter, the dE/dx always refers to this truncated mean definition.

⁸The maximum charge is the largest charge in a cluster cell (both in pad and time bin). The measured maximum charge is largest if the center of the cluster coincides with the center of the pad, and smallest if it is between two pads.

⁹In this case, the separation power is defined as the dE/dx distance between the minimum ionizing and the plateau regions divided by the average dE/dx resolution in these two regions.

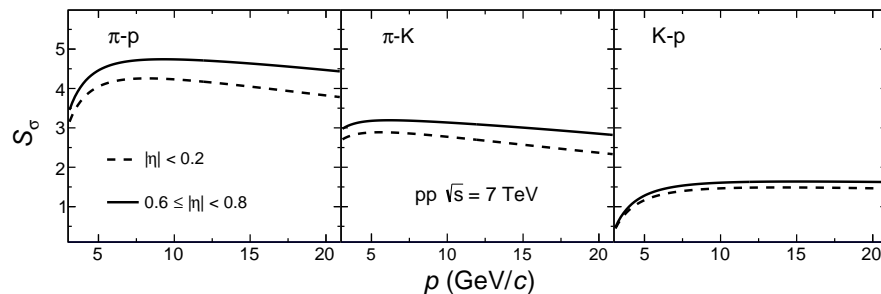


Figure 6.2: Separation in number of standard deviations between: pions and protons (left panel), pions and kaons (middle panel), and kaons and protons (right panel). Results obtained for minimum bias pp collisions at $\sqrt{s} = 7$ TeV are shown for two specific pseudorapidity intervals as indicated in the legends. Figure is reproduced from Ref. [223].

6.4 Relative resolution and separation power

The $\sigma_{dE/dx}$ resolution is given by the variance of the Gaussian distribution of the dE/dx defined in Eq. (6.2). The decisive quantity for particle identification is the separation power mentioned earlier. It quantifies the performance of a PID technique by expressing the absolute $\langle dE/dx \rangle$ difference between two particle species normalized to the arithmetic mean of the resolutions. The separation power for two particle species, e.g. for pions and kaons can be calculated as

$$S_\sigma = \frac{\langle dE/dx \rangle_\pi - \langle dE/dx \rangle_K}{0.5 \times (\sigma_{dE/dx,\pi} + \sigma_{dE/dx,K})}, \quad (6.3)$$

where, for example, $\langle dE/dx \rangle_\pi$ represents the dE/dx signal for pions at a given momentum. The separation power between particle species is shown in Fig. 6.2 for $\sqrt{s} = 7$ TeV pp collisions in case of short- and long tracks, determined via a cut imposed on their pseudorapidity values, resulting in $|\eta| < 0.2$ and $0.6 \leq |\eta| < 0.8$, respectively. The separation power S_σ is the largest (smallest) between pions and protons (kaons and protons) and it is nearly constant towards larger momenta. At high p_T , when all particles are on the relativistic rise then $dE/dx \propto \ln(\beta\gamma) \propto \ln(p/m)$. From which it follows that $\langle dE/dx \rangle_\pi - \langle dE/dx \rangle_K \propto \ln(p/m_\pi) - \ln(p/m_K) \propto \ln(m_K/m_\pi)$, i.e. S_σ is independent of rapidity, $p = p(\eta)$.

One can see that the typical value of S_σ is only a few standard deviations—between pions and kaons (pions and protons) is around 3.2σ (4.7σ) at momentum $p \approx 6$ (9) GeV/c for $0.6 \leq |\eta| < 0.8$ where the separation is the largest—making the PID quite challenging. Since the best particle identification performance is required on the relativistic rise, a natural choice for a quantitative estimate of the achieved performance is given by the separation power between minimum ionizing particles and particles on the Fermi plateau. Optimizations of the performance can be either achieved by increasing the distance between minimum ionizing particles and the Fermi plateau or by minimizing the resolution. It is worth noting that the dE/dx resolution $\sigma_{dE/dx}$ has a dominating dependence on the number of PID

clusters N_{cl} , which is used in the calculation of the dE/dx signal. Moreover, it exhibits further dependencies on several other variables, such as the primary ionization. This results in a dependence which is inversely proportional to the dE/dx signal: $\sigma_{dE/dx}/\langle dE/dx \rangle \sim \langle dE/dx \rangle^{-t}$. The quantity $\sigma_{dE/dx}/\langle dE/dx \rangle$ will be called subsequently relative resolution.

Particle identification in the relativistic rise region will require the precise knowledge of the dE/dx response and the resolution $\sigma_{dE/dx}$ (or $\sigma_{dE/dx}/\langle dE/dx \rangle$) by the optimization of the signal itself. This will be accomplished with the use of external PID constraints to calibrate the response.

6.5 Calibration of the dE/dx signal

The particle identification performance critically depends on the quality of the calibration [193]. Prior to particle identification, the precise calibration of the cluster charges and the TPC dE/dx signal is required. There are several levels of calibration phases which have to be carried out in the TPC. The focus of the following subsections is laid on the brief description of some basic so-called built-in calibration techniques applied during the official reconstruction. Afterwards, I discuss the main analysis-level calibration, which I applied to achieve the best experimentally possible dE/dx performance.

6.5.1 Built-in calibration techniques

After careful construction and installation, the TPC was subject to its final calibration which is used to improve the overall physics performance of the detector. The static and dynamic imperfections of the detector influence the track and space point resolution.

The Lorentz force causes the migration of the cluster position by driving the charge in opposite directions depending on the polarity of the magnetic field of the experiment. This is called the $\mathbf{E} \times \mathbf{B}$ effect. Due to the $\mathbf{E} \times \mathbf{B}$ effect, non-linear space point distortions occur within the drift volume which can be corrected by the measurements of the magnetic field B and calculations of the electric field imperfections. Besides, electric field inhomogeneities due to mechanical and structural imperfections influence the electron drift direction and so the space point resolution in x , y , and z directions. In order to resolve space point calibration issues, the built-in laser calibration system can be available.

Regarding signal variations such as timing, signal shaping and gas gain fluctuations, the built-in pulser as well as the Krypton calibration¹⁰ techniques can be used. By using the stable isotope of $^{86}_{36}\text{Kr}$ the energy deposit within the drift gas can be calibrated, resulting in an improvement of the dE/dx resolution of the detector. More details can be found in Refs. [224–226].

In the ALICE TPC, essentially four different input sources are used for the calibration to obtain the relevant calibration parameters. These are cosmic-, laser-, Krypton-, and beam

¹⁰This calibration technique was successfully used in the CERN NA49 and in the RHIC STAR experiments.

events. Krypton events are used for the extraction of the gain map; laser events are taken at the beginning and frequently during the runs for online calibration of the drift velocity and alignment purposes; cosmic ray events — when beam events are not yet available — are essential for the initial calibration of the dE/dx and they are also to be used to measure the p_T resolution at high transverse momenta [222].

6.5.2 Analysis-level calibration

While the Bethe–Bloch specific energy loss depends only on $\beta\gamma = p/m$, the one obtained from the measurement after the truncated mean procedure also depends on other parameters such as the cluster sample length, i.e. the pad length and track inclination over the pad. The relationship between the two types of specific energy losses can be described by a transfer function which is the one indeed to be optimized during the dE/dx calibration; and the one to be used as an input for the analysis strategy discussed later in Chapter 7.

As discussed above, each of the up to 159 clusters used to reconstruct a track contains information on the ionization energy loss in the TPC. To equalize the gain, each readout channel has been calibrated using ionization clusters produced by $^{86}_{36}\text{Kr}$, released into the TPC gas [197]. Clusters with a low charge might have a signal only on one pad and the signal on the neighboring pads is below the readout threshold. These clusters are not used for track fitting, but still contain valid information and can be used for the dE/dx calculation. In order to improve the performance and stability of the dE/dx transfer function in terms of gain variations, a virtual charge is added to the cluster based on the known pad response function. The virtual cluster is then included in the calculation of the truncated mean. This procedure is similar to that used by ALEPH at LEP, but without changing the truncation range [227]. From the studies of the transfer function, it turns out that one expects a significant track-length dependence. Particles traversing the TPC at some polar angle θ with respect to the beam axis change the induced charge on the single readout pads, which in turn has an impact on the dE/dx resolution and the mean dE/dx . The closer the angle of incidence of the track on the pad plane is to 90 degrees, the larger is the fraction of path length projected onto a single pad row. This, in turn, makes the deposited charge per pad row larger for tracks in the forward direction than for those at mid-rapidity. This causes dE/dx to depend on the pseudorapidity through the tangent of the polar angle, $\tan(\theta)$, whereas dE/dx resolution scales roughly as the inverse of the track-length in $\eta(1/\sqrt{1 + \cos^2 \theta})$. The pseudorapidity dependence of the dE/dx is sensitive to corrections for the track-length and the diffusion. For inclined tracks, the track-length sampled per pad row is larger — which is also true for tracks having larger η — and they are less affected by diffusion. At the same time, considering tracks at $\eta \approx 0$ the ionization electrons drift the full length of the TPC resulting the signal to spread due to diffusion, which makes threshold effects more prominent than for tracks with $\eta \approx \pm 0.8$.

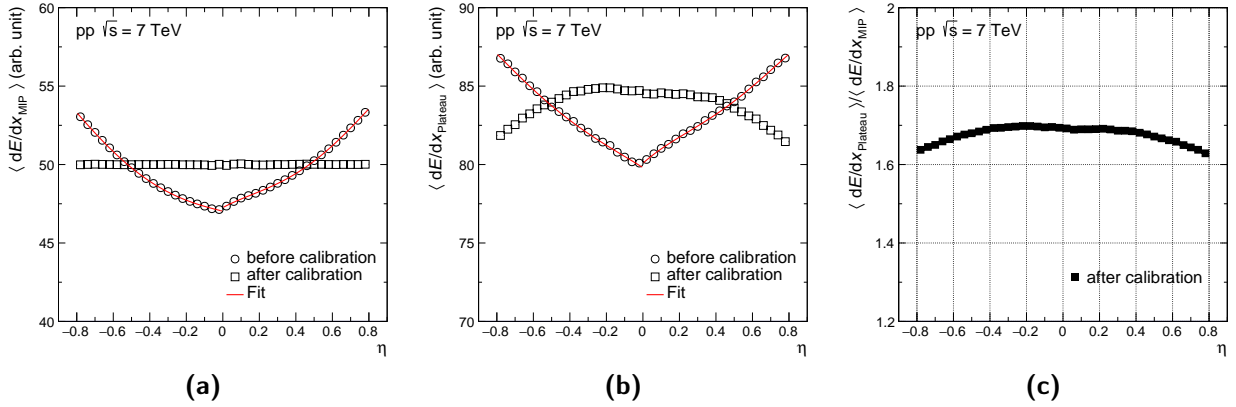


Figure 6.3: The dE/dx as a function of pseudorapidity (η) for (a) MIP pions and (b) electrons on the Fermi plateau measured in pp collisions at $\sqrt{s} = 7$ TeV. Panel (c) shows the ratio of dE/dx for the electrons at the Fermi plateau to MIP pions; the selection criteria are described in the text. Solid red lines over the data points represent fitted curves; see the text for more details. The statistical error is smaller than the marker sizes. Figures are reproduced from Ref. [223].

In the relativistic rise analysis, I performed the dE/dx calibration, which was validated using charged pions around the MIP region and electrons in the Fermi plateau region. A clean sample of MIP pions is selected using tracks with momentum range $0.4 < p < 0.6$ GeV/ c and typically in the range $40 < dE/dx < 60$ (or $0.8 \lesssim dE/dx / \langle dE/dx \rangle_{\text{MIP}} \lesssim 1.2$ in units of $\langle dE/dx \rangle$ for MIP pions). To understand the calibration performance for tracks with larger dE/dx (and therefore for more clusters above threshold), the method is tested by using clean electron sample having $dE/dx > 65$ (arbitrary unit) in the same momentum range — which also has a constant dE/dx , as they are on the relativistic plateau. Charged kaons are rejected with the requirement $|\beta_{\text{TOF}} - 1| < 0.1$, where β_{TOF} is the velocity of the particle determined by the TOF detector.

High- p_T tracks, used in the relativistic rise analysis, are barely bent in the moderate ($B = 0.5$ T) magnetic field of ALICE and their track-length in the transverse bending plane is rather similar. A significant η dependence can be observed in Fig. 6.3 where two extreme cases for samples of MIP pions (Fig. 6.3a for low dE/dx) and electrons at the Fermi plateau (Fig. 6.3b for high dE/dx) are shown. Note that it is enough to examine these two extremes for correction purposes, since the dE/dx for all particle species with high momentum lie between these two extreme regions. Plotted in Figs. 6.3a and 6.3b are the uncalibrated dE/dx signals (open circles) together with a 4th-order polynomial fits (solid red lines) used to eliminate (or at least reduce) the observed η dependence. Open square markers show the η -corrected signals, whereas Fig. 6.3c indicates the ratio between high and low dE/dx tracks. The calibration is applied as a scale factor so that the effect is numerically larger for larger values of dE/dx , i.e. larger for electrons than for MIP pions. The remaining η dependence seen in Fig. 6.3c of the signal towards higher $|\eta|$ after calibration is at the level of 1%. As a consequence, to analyze homogeneous samples, this motivates performing the analysis in

narrow, equidistant $|\eta|$ intervals: $|\eta| < 0.2$, $0.2 \leq |\eta| < 0.4$, $0.4 \leq |\eta| < 0.6$, and $0.6 \leq |\eta| < 0.8$. Note that the binning in η is chosen to set a compromise between the available statistics and the adequate accuracy of the calibration method. This choice turns out to be sufficient at the present calibration stage.

As was mentioned above, one cannot expect the dE/dx to depend significantly on the azimuthal track angle for the straight high- p_T tracks, but in general, one has to be certain that there are no residual dependencies left after the calibration. Therefore, I also determined the $\langle dE/dx \rangle$ as a function of azimuthal track angle (φ) for both long and short tracks in case of MIP pions and electrons at the Fermi plateau. Since I found no significant φ dependence neither for short nor for long tracks, no further calibration applied in terms of azimuthal track angle.

6.6 Division into homogeneous samples

Besides calibration, the dE/dx performance must be improved further by rejecting tracks which cause the degradation of the dE/dx signal. This can be done by simply applying a geometrical cut apart from specific track selection criteria described in the next chapter.

6.6.1 Geometrical cut

In the previous section I concluded that the sample of tracks has to be divided into subsamples of narrow $|\eta|$ intervals. Furthermore, tracks close to or crossing the TPC sector boundaries have significantly fewer clusters assigned. Since the considered high- p_T tracks are straight, those which are close to the sector boundaries can be easily rejected using a purely geometrical cut (in the following referred to as geo. cut) in the azimuthal track angle φ . Tracks that are close to the TPC edges will in general have a worse performance than those being far from the edges, because of cluster losses, and also because clusters which are close to the edge are not included in the dE/dx calculation there — as the gain calibration is worse for these pads (see Section 6.5.1).

To get a reliable dE/dx from the truncated mean, the number of PID clusters N_{cl} should be at least 70. This requirement is taken into account for track selection (see later in Ch. 7) as well as for the geo. cut. The geo. cut is applied for high- p_T tracks, i.e. for those having $p_T \geq 2 \text{ GeV}/c$, and considers situations with different magnetic polarities, and positive and negative charge settings by setting $\varphi \rightarrow 2\pi - \varphi$ if the charge $q < 0$ and/or the magnetic field $B < 0$. Figure 6.4 shows how the geo. cut is applied and the effect of it by studying φ modulo $\pi/9$, which is equivalent to a TPC sector with an azimuthal angle of 30° . In addition, a $\varphi \rightarrow \varphi + \pi/18$ shift is applied to align the sector gap at the center of the figure. Figures 6.4a–6.4f show the azimuthal angle φ of the tracks as a function of p_T for different sets of N_{cl} each, without (Figs. 6.4a, 6.4c, and 6.4e) and with (Figs. 6.4b, 6.4d, 6.4f) the applied geo. cut.

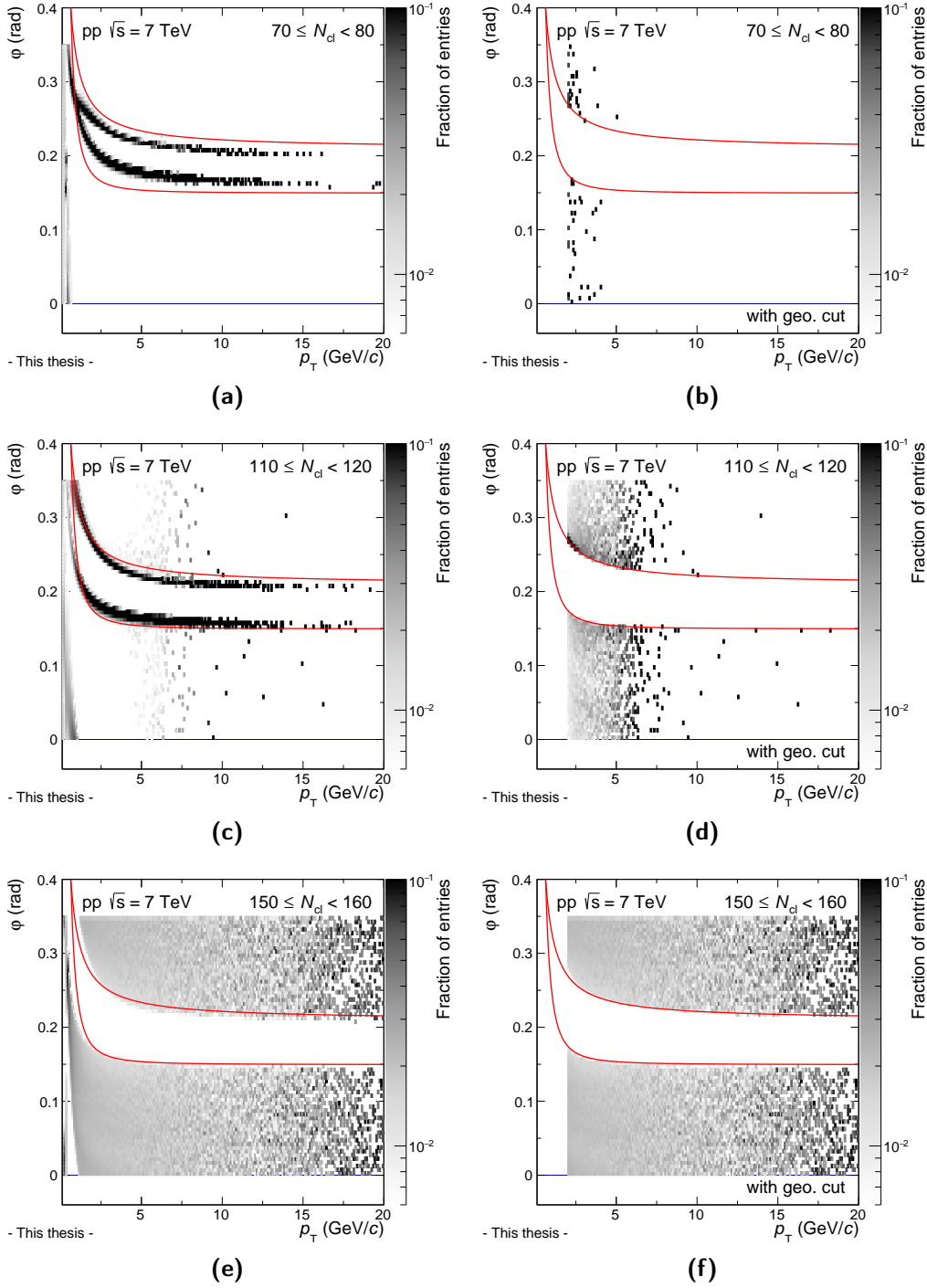


Figure 6.4: The azimuthal angle φ of tracks (in units of radian) as a function of transverse momentum with different number of PID clusters N_{cl} , before (panels (a), (c), and (e)) and after (panels (b), (d), and (f)) applying the geometrical (geo.) cut indicated by solid (red) lines.

It is remarkable that the geo. cut significantly improves the dE/dx performance by rejecting tracks with less information (fewer clusters) in regions where the calibration is more sensitive to complex edge behaviors that can have larger effects on straight tracks. The cut removes tracks with worse resolution, mainly resulting from the lower number of PID clusters. As a result, this ensures selecting tracks with optimal tracking (p_T resolution) and dE/dx conditions ($\sigma_{dE/dx}$ resolution).

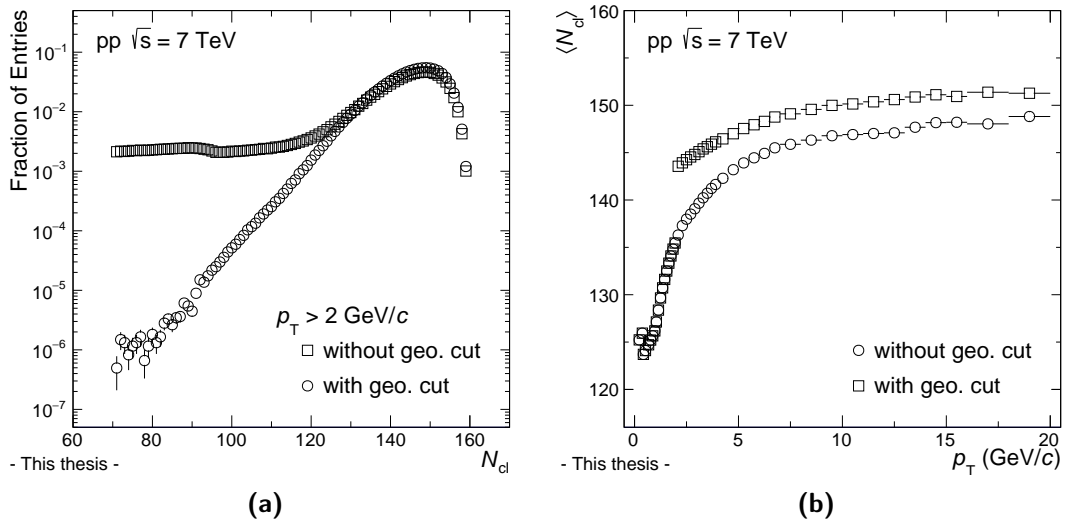


Figure 6.5: (a) Number of PID clusters N_{cl} used in the dE/dx calculation for tracks having $p_T \geq 2 \text{ GeV}/c$ without (open squares) and with (full circles) the geometrical cut. (b) Average number of clusters $\langle N_{cl} \rangle$ as a function of transverse momentum without (open squares) and with (full circles) the geometrical cut. The minimum number of clusters on a track is required to be 70.

Figure 6.5a shows the effect of the φ geo. cut on the distribution of the number of clusters per track N_{cl} , where the cases before and after applying the cut are indicated. Here, again, one can see that the cut removes tracks with fewer clusters improving the dE/dx performance this way. An important observation from Fig. 6.5b is that, for $p_T \gtrsim 4 - 5 \text{ GeV}/c$, the N_{cl} is much larger than at lower p_T , in particular after the applied geo. cut, and that the $N_{cl}(p_T)$ is nearly independent of p_T towards higher p_T values — as one can see, the efficiency of the cut in this case is about 98%. Therefore, it is a good approximation ignoring any dependence of $\sigma_{dE/dx}$ on N_{cl} , which, in turn, also simplifies the analysis considering a single resolution parameter to describe individual particles species for a given momentum bin in each η interval. With the applied settings, the track survival rate at $p_T = 2 \text{ GeV}/c$ is reduced considerably by about 20% for the geo. cut compared to the default cut, which requires at least 70 PID clusters, whereas the reduction is only $\sim 10\%$ for $p_T \gtrsim 6 \text{ GeV}/c$.

6.7 Parametrization of the Bethe–Bloch and the dE/dx resolution curves

The mean TPC dE/dx as a function of $\beta\gamma$ can be described by a proper parametrization of the Bethe–Bloch function defined in Eq. (6.1). In this work, a model based on the ALEPH parametrization [221] and developed further in Lund [228] with parameters a_0, \dots, a_5 is used:

$$\langle dE/dx \rangle = a_0 \left(\frac{1 + (\beta\gamma)^2}{(\beta\gamma)^2} \right)^{a_4} + \frac{a_1}{a_2} \ln \left(\frac{(1 + \beta\gamma)^{a_2}}{1 + a_5(1 + \beta\gamma)^{a_2}} \right), \quad (6.4)$$

$$a_5(a_0, a_1, a_2, a_4) = \exp \left(\frac{a_2(a_0 - a_3)}{a_1} \right),$$

where a_0, a_1, a_2, a_3, a_4 are free parameters and a_3 is the $\langle dE/dx \rangle$ in the Fermi plateau region ($\beta\gamma \gtrsim 1000$). Moreover, β can be expressed using $\gamma = (1 - \beta^2)^{-1/2}$ as $\beta = \beta\gamma \left[1 + (\beta\gamma)^2 \right]^{-1/2}$. Using $(1 + \beta\gamma)$ in Eq. (6.4) ensures that the logarithmic term is always positive. For $a_5 \ll 1$, as is the case in this work, the parametrization has a simple behavior in different regions of $\beta\gamma$. For $\beta\gamma \ll 3 - 4$, i.e. well below the minimum ionizing region $\langle dE/dx \rangle \approx a_0 / (\beta\gamma)^{2a_4}$, whereas on the logarithmic rise $\langle dE/dx \rangle \approx a_0 + a_1 \ln(1 + \beta\gamma)$.

To extract the parameters of $\langle dE/dx \rangle$ in Eq. (6.4), data points over a broad $\beta\gamma$ range are required. Since the recorded data statistics decreases exponentially with rising momentum, it is necessary to select different particle species in certain momentum ranges where these species can be clearly identified. For the determination of the parameters a_0, a_1, a_3 , and a_4 so-called external PID information is used based on clean identified particle samples.

Secondary pion (proton) tracks are identified via the reconstruction of weak decay topology of K_S^0 (Λ): π^\pm and $p(\bar{p})$ daughters coming from decay channels $K_S^0 \rightarrow \pi^+ + \pi^-$ (with decay length $c\tau = 2.68$ cm) and $\Lambda(\bar{\Lambda}) \rightarrow p(\bar{p}) + \pi^-(\pi^+)$ (with decay length $c\tau = 7.89$ cm), respectively. Clean data samples of primary pions provided by TOF with the selection criterion $\beta_{\text{TOF}} > 1$ is also used. The selection of V^0 candidates used in this work is similar to that used in the dedicated analysis [53, 229]. It is worth noting that kaons are not used at all since there are no V^0 for kaons and the purity after TOF selection is rather limited.

Having these clean samples, the Bethe–Bloch function is constrained in the $\beta\gamma$ interval of 2–80. For this, secondary pions and protons are used to constrain the regions $30 < \beta\gamma < 50$ and $2 < \beta\gamma < 7$, respectively. A similar algorithm to the V^0 decay is used to reconstruct a γ conversion and identify electrons from the low invariant mass, to fix the dE/dx Fermi plateau for $\beta\gamma \gtrsim 1000$. Additionally, the relative pion sample can be enhanced and complemented by tracks which can still be purely identified by the TOF for the range $16 < \beta\gamma < 80$. The relative resolution $\sigma/\langle dE/dx \rangle$ as a function of $\langle dE/dx \rangle$ decreases towards higher $\langle dE/dx \rangle$, which behavior can best approximated by a polynomial function. For $\sigma/\langle dE/dx \rangle$, the same external PID informations are used to measure its dependence on $\langle dE/dx \rangle$.

Before showing the obtained results for the parametrizations, it is important to discuss how the clean samples are extracted and how they compare to the primary selection made from the TPC. Nevertheless, it is rather important to verify the purity of the V^0 sample.

6.7.1 Inclusion of pure particle samples

The V^0 candidates K_S^0 and Λ ($\bar{\Lambda}$) are selected via selection criteria imposed on the invariant mass distributions of their weakly decaying daughter tracks (π^\pm and $p(\bar{p})$) as shown in Fig. 6.6. The selection made on the mass difference is defined, for example, for the decay process $\Lambda \rightarrow p\pi^-$ as follows

$$\Delta m_\Lambda = |V^0 \text{ mass assuming proton and negative pion} - m_\Lambda|, \quad (6.5)$$

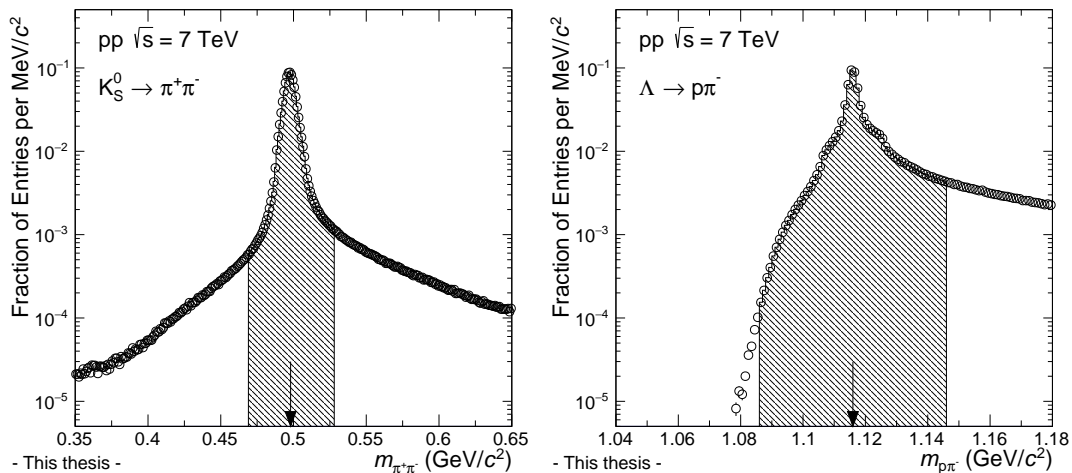


Figure 6.6: Invariant mass distributions of V^0 mothers of particles used to extract the TPC-PID response for $\sqrt{s} = 7$ TeV pp data. The shaded areas applied around the peak region (symmetrically to both sides) represent the selection criteria used in order to obtain clean samples. Vertical arrow indicates the mass value taken from the Particle Data Group [218]. See the text for more details.

where m_Λ is the mass value of the Λ candidate taken from the Particle Data Group [218]. For each V^0 then one has the following variables: Δm_Λ , $\Delta m_{\bar{\Lambda}}$, $\Delta m_{K_S^0}$, and Δm_γ . Only electrons are assumed for Δm_γ . To reject conversions, in all cases it is required to make $\Delta m_\gamma > 100$ MeV/ c^2 ; without this cut there are a few electrons observed. For $\Lambda(\bar{\Lambda})$ it is required to have $\Delta m_\Lambda(\Delta m_{\bar{\Lambda}}) < 10$ MeV/ c^2 and $\Delta m_{K_S^0} > 10$ MeV/ c^2 , whereas for the case of K_S^0 the requirement is set to $\Delta m_{K_S^0} < 10$ MeV/ c^2 and that both Λ and $\bar{\Lambda}$ should be more than 10 MeV/ c^2 away. The applied cuts have been chosen in order to maximize statistics and purity, in turn, to reach high signal-to-background ratio.

Figure 6.7 presents the dE/dx distributions as a function of momentum p for the V^0 secondary daughter tracks and primary tracks identified by the TOF detector. The distributions are obtained for the case of long tracks having $0.6 \leq |\eta| < 0.8$, however similar observations can be made for other pseudorapidity intervals as well; therefore the same conclusions can be drawn for any η interval.

The V^0 electrons (Fig. 6.7a) have negligible contamination from kaons and protons. The pion contamination is well visible as the separated, lower dE/dx branch, but the peak height of this branch significantly lower than that of the electrons. For the V^0 pions (Fig. 6.7b), there is no contamination from electrons and there is negligible contamination for the other species in the considered momentum range ($p > 3.5$ GeV/ c). In particular, the proton and kaon distributions for $p > 3.5$ GeV/ c have contamination of less than 0.5%. Regarding the V^0 proton sample (Fig. 6.7c), apart from a negligible contamination of electrons at low p , the main contribution to the impurities of the sample stems from pions at higher p values. Finally, in case of primary pions identified by TOF (Fig. 6.7d) one can see a small amount of electrons at low p , whereas towards higher p values the contamination from other species arises. As a matter of fact, for clean samples (with clean separation), comparing the integrals

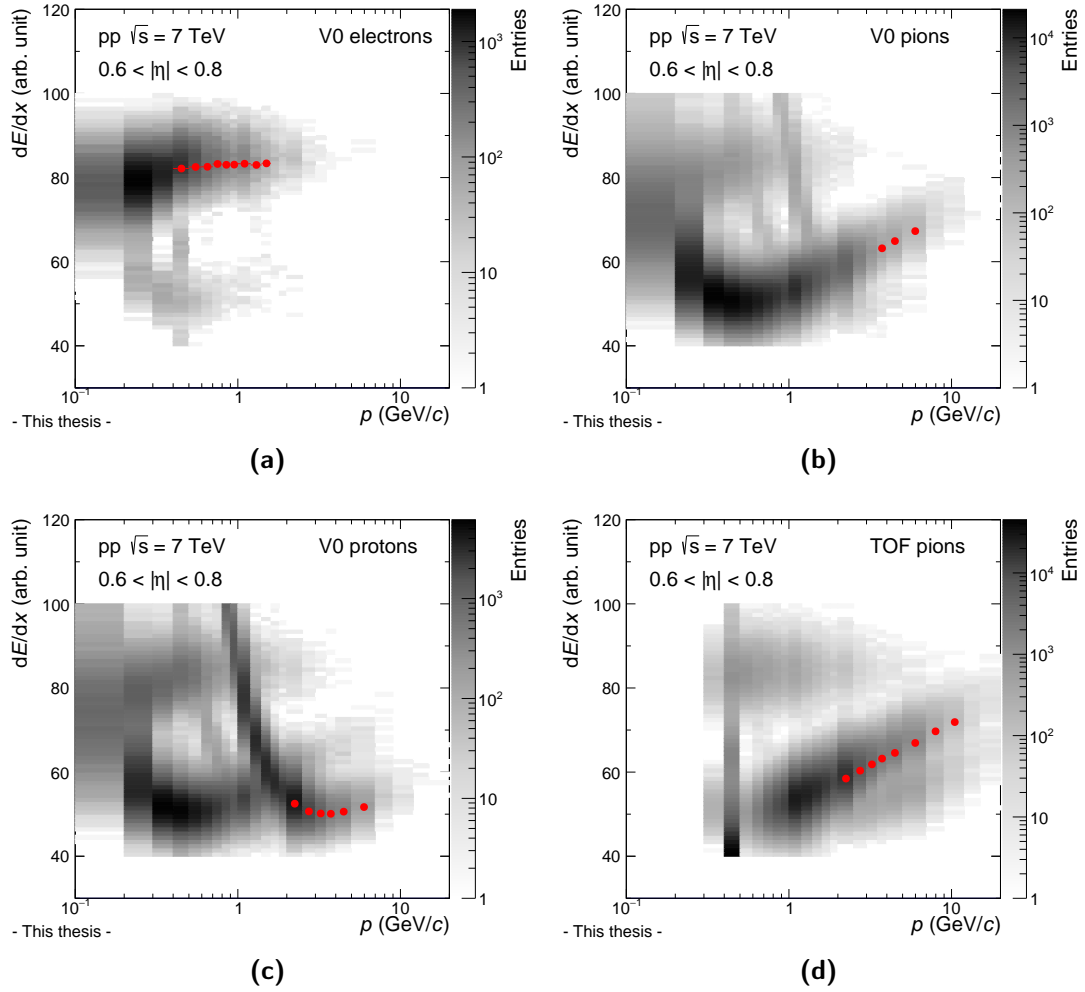


Figure 6.7: The dE/dx distributions of the V^0 daughter tracks (panels (a), (b), and (c)) and primary pions identified by the TOF detector (panel (d)) as a function of momentum. The red full circles indicate the mean of Gaussian fits applied to the dE/dx distributions in bins of momentum.

in momentum bins, the contamination is mostly around a few per mille. These data samples will be referred to as shortly external PID data in the following.

Figure 6.8a shows examples of the dE/dx spectra for secondary pions and protons for a given momentum bin $3.5 < p < 4.0 \text{ GeV}/c$. To verify that the dE/dx response is Gaussian, the secondary pion and proton peaks are fitted with single Gaussians. Note that a $10 \text{ MeV}/c^2$ wide invariant-mass cut is already applied to the pp data sample in order to obtain such a sample where the V^0 reconstruction is the cleanest. The results are shown in Fig. 6.8a where the χ^2/ndf value of a single Gaussian fit is reported and it shows the expected value for a valid fit model. It is worth noticing that the proton sample from the Λ decay is not quite clean, it has some contamination from pions since the invariant mass peak region still contains considerable combinatorial background. This contamination is seen in the asymmetry towards the higher values of dE/dx in the proton sample. Regarding the pion sample from the K_S^0 decay, proton contamination creates the asymmetry towards lower values of dE/dx in the distributions. It is noteworthy that the asymmetric tail of the distributions

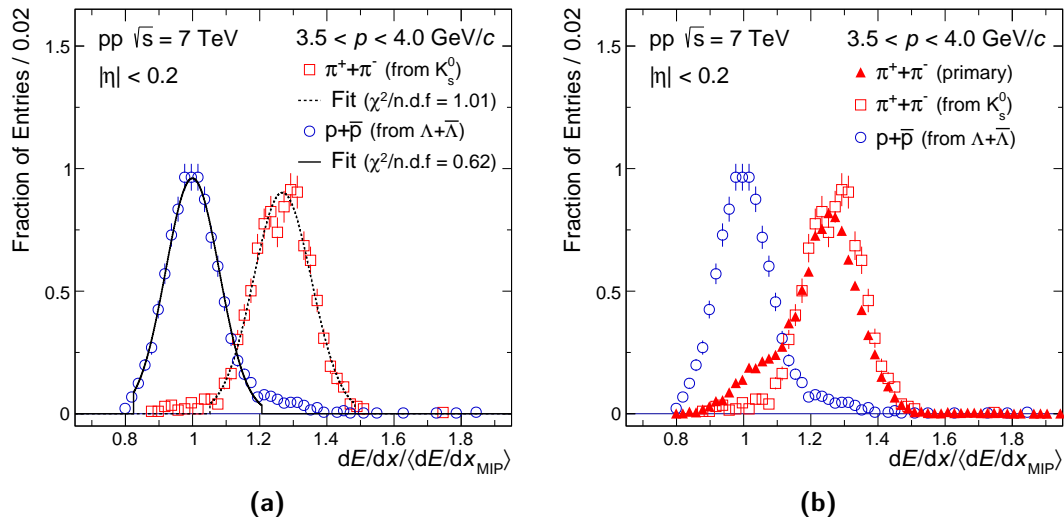


Figure 6.8: The dE/dx spectra for secondary pions (open squares) and protons (open circles) identified via the reconstruction of the weak decay topology of K_S^0 and Λ , respectively, and primary pions (full triangles) identified by the TOF detector. The tracks were chosen in the momentum interval $3.5 < p < 4$ GeV/c having pseudorapidity $|\eta| < 0.2$. Note that the V^0 pion and proton signal also contains a well-understood background. Figures are reproduced from Ref. [223].

was found to have negligible effect in the calculation of the dE/dx for these samples.

Since all the corrections that are applied during the reconstruction are optimized for primary tracks, the dE/dx is only reliable if the topology is not too different from that of the primaries. It has been checked that for both V^0 pions and protons the mean dE/dx is in the acceptable range with that of primaries. Primary pions, selected by TOF, are also depicted in Fig. 6.8b which shows that the agreement between the two samples is $\mathcal{O}(1\%)$.

6.7.2 Extraction of $\langle dE/dx \rangle$ and $\sigma_{dE/dx}$ for final parametrization

In the following, the procedure for the extraction of the mean dE/dx and the associated resolution $\sigma_{dE/dx}$ will be discussed relying on the clean samples from the V^0 and TOF selections. For the determination of these quantities, the dE/dx distributions for external PID data presented in Fig. 6.7 are fitted in momentum bins using Gaussian functions. The performed fits are plotted in Fig. 6.9, where a given row corresponds to a certain particle species, whereas a column refers to a given momentum bin, which does not necessarily identical for every species. Note that for samples of primary pions and V^0 protons which contain a larger fraction of impurities from other species, the fit range (considered in the determination of the dE/dx) was chosen in a way to avoid a possible bias caused by contamination. Since the external PID data can be extracted in a restricted momentum range with required high enough purity, only a subset of the extracted fit results was taken into account. This observation is also supported by the degradation of the quality (χ^2/ndf) of the fit results when additional momentum bins are considered—where the fraction of contamination from other species increases.

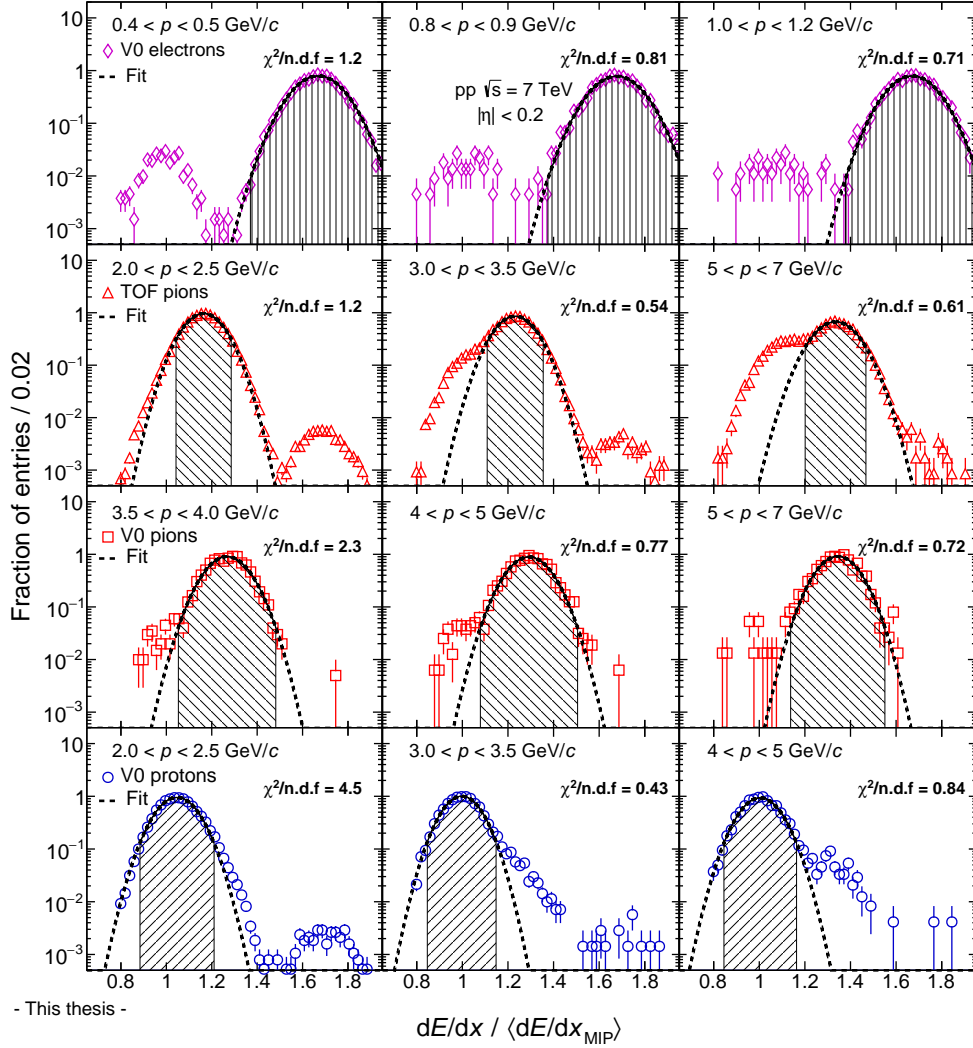


Figure 6.9: Gaussian fits to the dE/dx distributions of the external PID data samples (V^0 's and TOF primary pions). The obtained $\langle dE/dx \rangle$ and $\sigma_{dE/dx}$ are used to parametrize the Bethe–Bloch and relative resolution curves. Dashed lines show the Gaussian fits to the distribution for a given momentum bin, whereas shaded areas indicate the fit range considered during the fit.

Based on these considerations, the relevant $\langle dE/dx \rangle$ and $\sigma_{dE/dx}$ quantities are shown in Fig. 6.10 as a function of $\beta\gamma$ and $\langle dE/dx \rangle$, respectively. The obtained $\langle dE/dx \rangle$ values can be also visualized as full red circles overlaid on the external PID distributions in Fig. 6.7. The relative resolution $\sigma_{dE/dx}$ is parametrized by a parabolic function, which was found to describe the data well. The parametrized Bethe–Bloch and the (relative) resolution curves are shown, respectively, in Figs. 6.10a and 6.10b on the top of the external data points for two extreme pseudorapidity intervals, $|\eta| < 0.2$ and $0.6 \leq |\eta| < 0.8$. Curves for other η slices lie between these two extremes for the full range of $\beta\gamma$ and $\langle dE/dx \rangle$ reported here.

Examining the parametrized resolution curves shown in Fig. 6.10b, an obvious η dependence can be seen — due to its dependence on track-length discussed earlier — being the worst for protons and monotonically improves towards higher primary ionization values. Depending on $|\eta|$, the $\sigma_{dE/dx}$ is around 6.1 – 7.7% in the vicinity of the MIP region, whereas

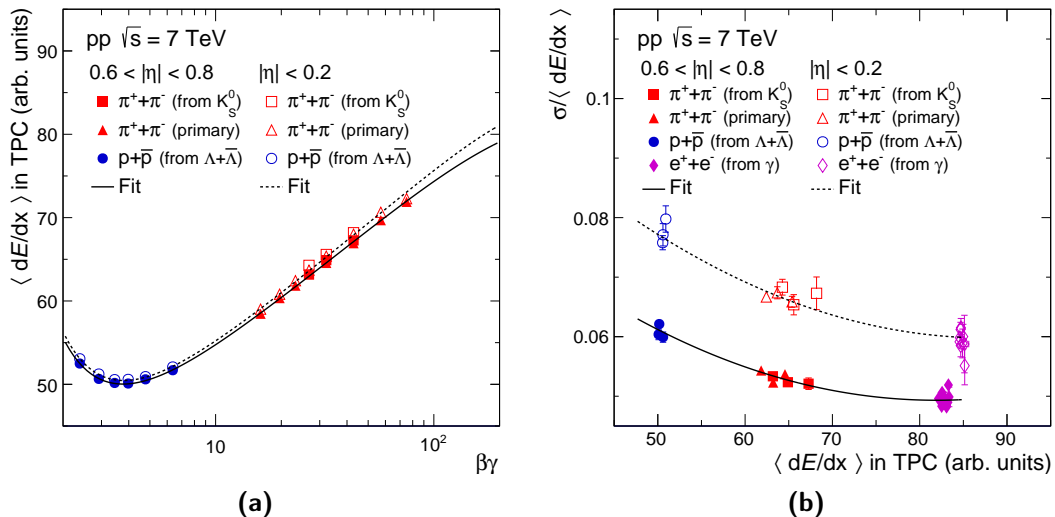


Figure 6.10: (a) Bethe–Bloch dE/dx and (b) relative resolution $\sigma_{dE/dx}$ curves in pp collision at $\sqrt{s} = 7$ TeV. Solid and dashed lines show the final parametrizations obtained for the Bethe–Bloch and relative resolution for long and short tracks, respectively. For pions, kaons, and protons, only the $\beta\gamma$ region relevant in this work is indicated. Figures are reproduced from Ref. [223].

it strengthens in the relativistic rise region to about 4.9 – 5.9%. One can see that with the use of primary pions (identified by TOF) the $\langle dE/dx \rangle$ parametrization can be covered for $\beta\gamma \lesssim 100$, corresponding to $p \lesssim 11$ GeV/ c . Above $\beta\gamma \sim 100$ the $\langle dE/dx \rangle$ of pions is restricted by the logarithmic rise until the $\langle dE/dx \rangle$ starts to approach the Fermi plateau region (for $p \gtrsim 14$ GeV/ c), where the $\langle dE/dx \rangle$ dependence on $\beta\gamma$ becomes more complex. Besides statistics, the lack of this additional constraint in this region obviously puts limitation on the applicability of the relativistic rise analysis..

Based on the discussions made so far, three (out of the four free) parameters a_0 , a_1 , and a_4 of Eq. (6.4) are fixed by fitting the Bethe–Bloch function to the dE/dx distributions at low $\beta\gamma(p)$ extracted using external PID informations as described above. In the next step, the extraction of the high- $\beta\gamma$ part of the $\langle dE/dx \rangle$ is performed where the last parameter, a_2 , is found by performing two dimensional fits to the dE/dx versus p distribution. The parametrizations resulting after this step are named in the following final parametrizations. In this procedure, all the parameters of the relative resolution curve are fixed, whereas for the Bethe–Bloch curve only the parameter a_2 — which regulates the approach to the plateau — is released. Note that in order for this to work one needs to include the factor a_1/a_2 in front the logarithmic term of Eq. (6.4) because this cancels the a_2 dependence for $\langle dE/dx \rangle$ in that region where PID information is available.

Figure 6.11 shows the extracted $\langle dE/dx \rangle$ and the final curves overlaid on the data for long tracks ($0.6 \leq |\eta| < 0.8$). From this figure one can see that the fits produce a nearly constant separation at high p for $\pi - K$, $p - K$, and $\pi - K$. This feature can be also seen from the S_σ separation power presented in Fig. 6.2 in Section 6.4, which was derived

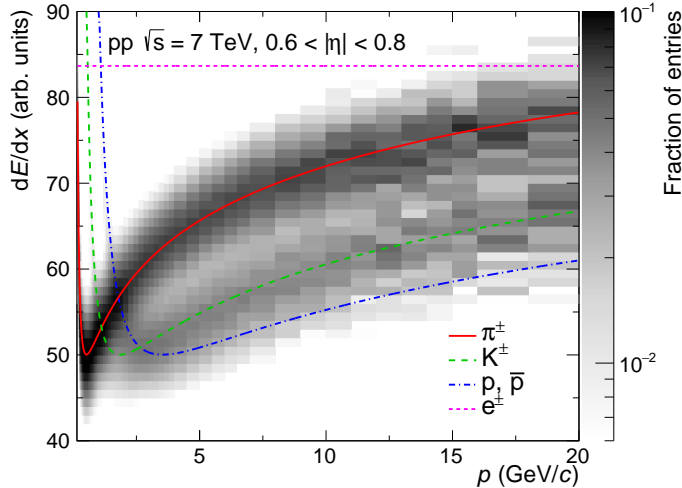


Figure 6.11: Specific energy loss, dE/dx , in the TPC as a function of momentum in the pseudorapidity range $0.6 \leq |\eta| < 0.8$ for minimum bias pp collisions at $\sqrt{s} = 7$ TeV. In each momentum bin the dE/dx distributions have been normalized to have unit integrals and only bins with more than 2% of the total entries are shown (making electrons not visible in the figure). The curves show the $\langle dE/dx \rangle$ response for pions, kaons, protons and electrons—obtained from the final parametrization. See the text for details. Figure is reproduced from Ref. [223].

using the final parametrizations. By examining other $|\eta|$ intervals, it turns out that the overall dE/dx increases as η decreases which is also consistent with the observation for the analogous distributions using secondary particles, see in Fig. 6.10a. Moreover, it is important to emphasize that the mean values of the fit are entirely determined by the $\langle dE/dx \rangle$ function where the fit is only used to fix one parameter. On the other hand, the widths are entirely determined by the $\sigma_{dE/dx}$ extracted from external PID data. Consequently, there are only the yields $\pi^+ + \pi^-$, $K^+ + K^-$, $p + \bar{p}$, and $e^+ + e^-$ left as free parameters. The present fit method works well if the corrections to the relativistic rise are small enough due to the transition to the plateau region. This implies that the analyzed data sample is restricted in momentum from above. With increased statistics and the use of additional constraints (for example cosmic muons) the momentum reach of the method may be extended further.

6.8 Fit method: extraction of raw particle yields

Having determined the Bethe–Bloch and resolution curves as described in the previous section, it is now straightforward to extract the raw (uncorrected) pion, kaon, (anti)proton, and electron yields. Using the final parametrizations, the dE/dx distribution of primary TPC tracks can be fitted in a given momentum bin to a sum of four Gaussian functions accounting for each particle species in question. For each momentum interval, the $\langle dE/dx \rangle$ and $\sigma_{dE/dx}$ of each Gaussian are fixed, whereas the yields are free parameters to be determined.

This procedure is applied in each $|\eta|$ -interval, from which two extreme cases ($|\eta| < 0.2$ and $0.6 \leq |\eta| < 0.8$) are shown in Fig. 6.12 for momentum intervals $3.4 < p < 3.6$ GeV/c, $6.0 < p < 6.5$ GeV/c, and $10 < p < 11$ GeV/c. Shaded regions represent the extracted particle yields obtained by integrating the area under the fitted curve for a given species. The amount of e^\pm is notably lower than that of other species and their yield is less than 1% of the total. For $p > 10$ GeV/c, it is no longer possible to have a clear $e - \pi$ separation and

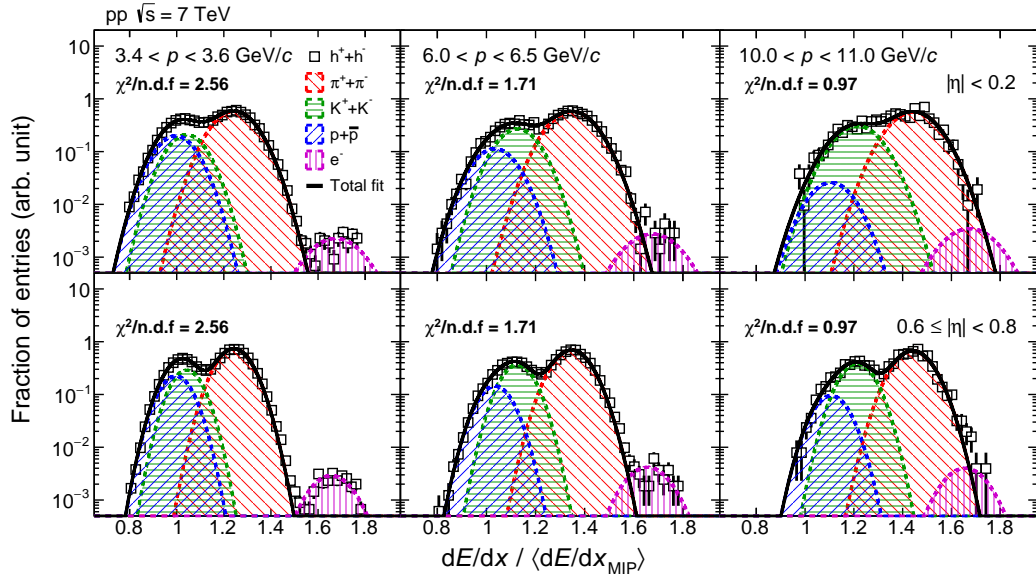


Figure 6.12: Four-Gaussian fits (solid lines) to the dE/dx distributions of π^\pm , K^\pm , $p(\bar{p})$, and e^\pm in various momentum p bins for $|\eta| < 0.2$ and $0.6 \leq |\eta| < 0.8$. Results were obtained from min. bias pp collisions at $\sqrt{s} = 7$ TeV. Figure is reproduced from Ref. [223].

the relative fraction of electrons is assumed to remain constant in this momentum regime. There is a small contamination of primary muons in the pion sample due to their similar mass, and so similar $\langle dE/dx \rangle$; the correction for this effect will be discussed in the next chapter. The contamination of (anti)deuterons in the (anti)proton sample is negligible.

For practical purposes, the yields obtained from the multi-Gaussian fits are normalized to the integral of the total distribution in a given p bin. The obtained quantity is the so-called particle fraction, denoted as $f'_s(p)$ for species $s \in \{\pi^\pm, K^\pm, p(\bar{p}), e^\pm\}$, which essentially determines the contribution of charged pions (π^\pm), kaons (K^\pm), (anti)protons ($p(\bar{p})$), and electrons (e^\pm) to the yield of inclusive charged particles.

Figure 6.13a shows the uncorrected particle fractions for pions, kaons, protons, and electrons for two extremes of η as a function of momentum p . For physical reasons, particle production is often studied as a function of the transverse momentum p_T instead of p . To go to particle fractions $f_s(p_T)$ as a function of p_T , a conversion is applied bin-by-bin using the following weighting procedure:

$$f_s((p_T)_i) = \sum_j f'_s((p)_j) R((p_T)_i, (p)_j), \quad (6.6)$$

where $f_s(f'_s)$ is given in $i(j)$ -th bins of $(p_T)_i((p)_j)$, and $R((p_T)_i, (p)_j)$ is a response matrix reflecting the relation between the measured $(p_T)_i$ and $(p)_j$ bins. The response matrices are obtained for all charged tracks. In a restricted $|\eta|$ window, there is a one-to-one correspondence between $f_s(p_T)$ and $f'_s(p)$. One can observe that going from p to p_T using long tracks the p_T of the particle fractions are slightly shifted to lower values with respect to the case

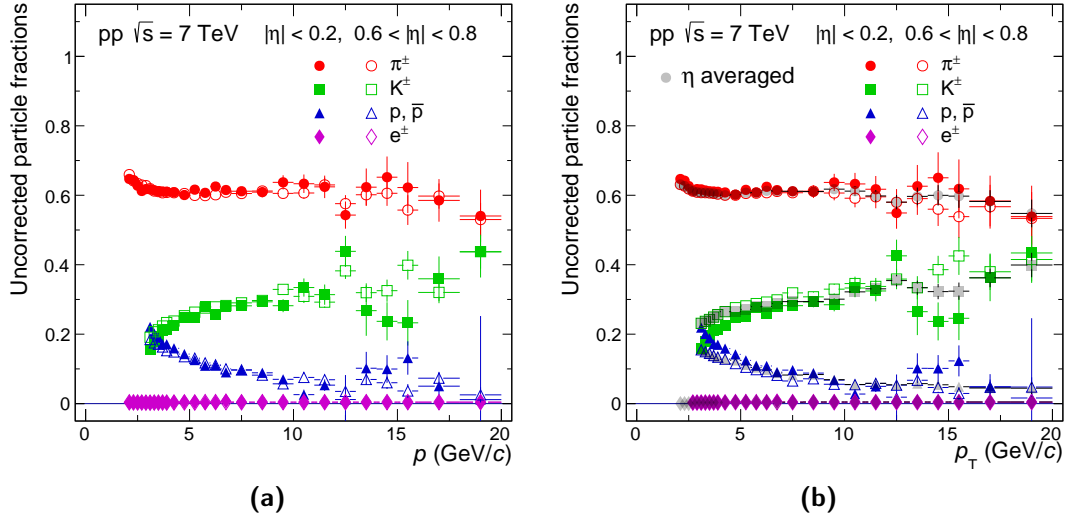


Figure 6.13: Uncorrected particle fractions as a function of (a) momentum and (b) transverse momentum for $|\eta| < 0.2$ (full markers) and $0.6 \leq |\eta| < 0.8$ (empty markers). In addition, the η -averaged fractions are also plotted in panel (b). The fraction of e^\pm is at the per mille level; making them hardly distinguishable from zero values in the linear scale of the y -axis in the plot. The error bars indicate the statistical errors. Figures are reproduced from Ref. [223].

using short tracks. The conversion introduces some smoothing on $f_s(p_T)$ as neighboring p_T fractions have contributions from the same p fractions. The transformation for tracks having $0.6 \leq |\eta| < 0.8$ pushes $f_s(p_T)$ to lower p_T bins, i.e. $p_T < p$ holds over the full p_T range. The $R((p_T)_i, (p)_j)$ matrices do not show any dependence on particle species which was verified by comparing them to each other and to all charged particles.

The relativistic rise approach cannot describe the MIP region with high accuracy where dE/dx curves of different particle species cross each other. Note that for $|\eta| < 0.2$, protons with momentum values $p = 3 \text{ GeV}/c$ ($\beta\gamma \approx 3.16$) are very close to MIPs, however, for $0.6 \leq |\eta| < 0.8$ with $p_T = 3 \text{ GeV}/c$ (corresponding to $p = 4 \text{ GeV}/c$) implies a larger $\beta\gamma$. Therefore, in this p_T regime one can get more accurate results at forward pseudorapidity.

The p_T -dependent fractions $f_s(p_T)$ were found to be consistent with each other for all the studied $|\eta|$ intervals. Hence, the final fractions are computed as the weighted average of those for the four pseudorapidity intervals, and they are shown as gray markers on top of the $|\eta|$ -sliced ones in Fig. 6.13b.

These particle fractions, after the proper corrections, are among the important components which will be required to build the identified invariant particle yields; these procedures are discussed in the next chapter.

CHAPTER 7

Measurement of identified charged hadron spectra at high p_T in pp and p–Pb collisions

In this chapter, the analysis technique to measure the production of π^\pm , K^\pm , and $p(\bar{p})$ in inelastic pp and non-single diffractive p–Pb collisions at mid-rapidities is presented. My analysis work is based on internal documentations of the ALICE collaboration [223, 230].

Three different data samples were analyzed ($\sqrt{s} = 7$ TeV pp, $\sqrt{s} = 13$ TeV pp, and $\sqrt{s_{NN}} = 5.02$ TeV p–Pb) to calculate the invariant yields $1/2\pi p_T \times d^2N/dy dp_T$ of the particle species under study. The invariant production yields measured at high p_T are studied in minimum-bias pp events, whereas for p–Pb, in bins of charged-particle multiplicity, where the multiplicity is estimated at forward rapidity.

7.1 The analysis strategy

The overall strategy to measure the p_T distributions of identified charged hadrons is presented. The conceptual framework is common for each collision system (pp and p–Pb) and at each collision energy. Its main ingredients are as follows:

- (1) First, “good” runs (explained later) are selected from the reconstructed datasets. Then, events are selected including appropriate trigger and vertex selection criteria. Additionally, pre-trigger selections are applied in order to remove events containing residual pile-up and those contaminated by beam-induced background outside the interaction region. Afterwards, several so-called “standard” track selection criteria are applied to select high-quality global tracks.
- (2) Thereafter, further quality selections are applied to the tracks in order to achieve the best possible performance for PID.
- (3) Event and track selection is followed by a step which is entirely based on the TPC dE/dx relativistic rise analysis. The goal here is to determine for each p_T interval, with a given kinematic set, the fraction of charged pions, kaons and protons to that of unidentified charged hadrons. The extraction of raw particle fractions is done via the multi-Gaussian fits described in Section 6.8.
- (4) The obtained raw particle fractions are corrected at track-level (depending on particle species) including relative (with respect to charged) tracking efficiencies and acceptance, and contamination from secondary particles (feed-down).

- (5) It is noteworthy that the event- and track selection cuts were identical to those applied in the unidentified charged-particle analysis. Therefore, the normalization (and systematic uncertainties where it is possible) due to event- and track selection are adopted.
- (6) Essentially, by multiplying the obtained corrected particle fractions $f_s(p_T)$ for the particle species under study with the unidentified charged hadron spectrum one can obtain the corrected identified particle p_T spectra.
- (7) The systematic uncertainties are evaluated and assigned point-to-point to each measured p_T bin. Here, certain sources of common uncertainties are calculated as well; their determination will be explained in detail.
- (8) In the last stage, the combination of corrected π^\pm , K^\pm , and $p(\bar{p})$ p_T spectra obtained in various independent analyses in ALICE is performed. This step is crucial in order to cover the whole (from low to high) measurable p_T range provided by the different detectors and identification techniques.

7.2 Kinematic range

The transverse momenta of the accepted tracks (see Section 7.5) in the combined ITS and TPC acceptance of $|\eta| < 0.8$ are restricted to $p_T \leq 20 \text{ GeV}/c$ for all the presented analyses in this work, which is a result, on the one hand, of the analyzed statistics and on the other of the (current) limitation of the TPC relativistic rise method.

7.2.1 Rapidity selection in p–Pb collisions

The twin design of the LHC dipole magnets [193] imposes the same rigidity (p/Z) for both particle beams. The charge over mass ratio is not the same for protons ($A_p = 1$, $Z_p = 1$) and for lead nuclei ($A_{Pb} = 208$, $Z_{Pb} = 82$). Therefore, the collisions between protons with beam energy of 4 TeV and lead nuclei with a beam energy of 1.58 TeV per nucleon resulted in a center-of-mass energy per nucleon pair of $\sqrt{s_{NN}} = 5.02 \text{ TeV}$ and the shift of the nucleon-nucleon center-of-mass system (cms) with respect to the laboratory (lab) frame with a rapidity of $\Delta y = 0.465$ in the direction of the proton beam (for details see Appendix A). For p–Pb collisions, the beam configuration was such that the direction of the proton beam was set to be clockwise, which resulted the proton (lead) beam fragmentation side to be found at negative (positive) rapidities. In turn, particles found at a given rapidity y in the nucleon-nucleon center-of-mass frame are detected at $y - 0.465$ in the laboratory frame. Hence, the nominal acceptance of the central barrel of the ALICE detector is not symmetric around mid-rapidity. In the following, quantities related to the analysis are quoted in the laboratory frame and y_{lab} (η_{lab}) is used to indicate the (pseudo)rapidity in the lab frame using the ALICE coordinate system convention. Final results in the center-of-mass system are reported using the standard convention where y_{cms} (η_{cms}) denotes the (pseudo)rapidity in the nucleon-nucleon center-of-mass reference frame.

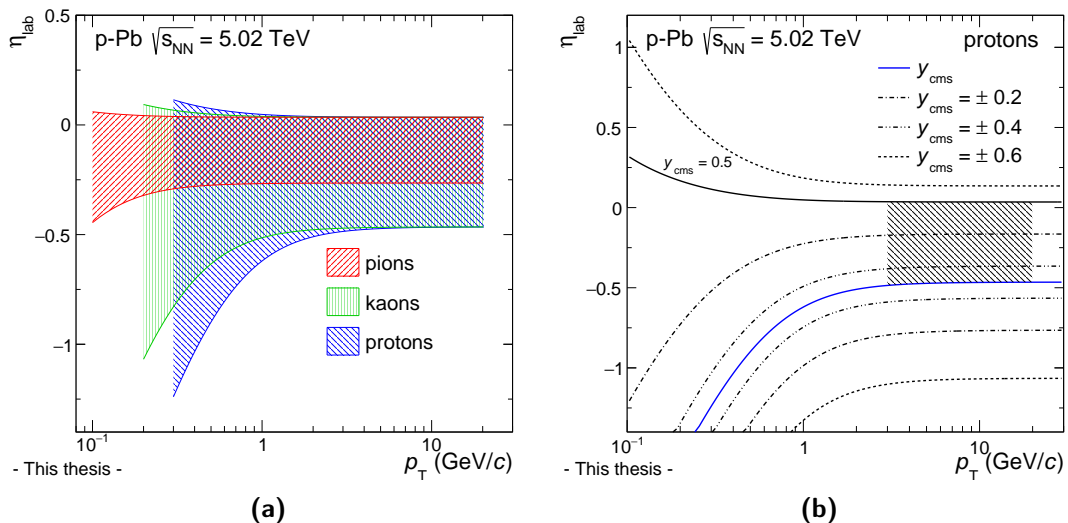


Figure 7.1: Acceptance in pseudorapidity in the laboratory frame (η_{lab}) as a function of transverse momentum for (a) pions, kaons, and (anti)protons and (b) protons indicating different rapidities y_{cms} in the center-of-mass reference frame. Shaded area represents the kinematic range considered in the TPC relativistic rise analysis.

For the analysis of p-Pb collision data, the selection of $|\eta| < 0.8$ applies to η ($= \eta_{\text{lab}}$) measured in the laboratory frame. In the nucleon-nucleon center-of-mass frame, this corresponds to roughly $0.3 < \eta_{\text{cms}} < 1.3$. Figure 7.1a shows the effect of the rapidity shift; it is more pronounced at low p_T and for heavier particles. Figure 7.1b shows the acceptance measured in η_{lab} for protons as a function of p_T for different y_{cms} values. The interval $|\eta_{\text{cms}}| < 0.3$ corresponds to the maximal overlap with the acceptance in pp collisions which is symmetric in $|\eta_{\text{cms}}|$; this motivates the choice for the acceptance in the p-Pb analysis. However, the asymmetric range of $-0.5 < y_{\text{cms}} < 0$ has been chosen, because, as it can be seen in Fig. 7.1b, a symmetric range around y_{cms} would require to restrict the analysis at large $|\eta_{\text{lab}}|$, with a corresponding degradation of the TPC dE/dx performance [125]. This choice ensures good detector acceptance and at the same time optimal particle identification performance. Moreover, the chosen kinematic range is identical to that used in the low- p_T PID analysis [53]. The latter will be of particular importance to the combination of different analyses; see later in Section 7.9.

It is worth noting that the choice of the rapidity interval in p-Pb collisions has a non-negligible effect on the interpretation of the data. It is shown in Ref. [119] that there is an indication of a softening of the p_T spectrum when going from central to forward pseudorapidity. In the low- p_T analysis [53], studies based on event generators and repetition of the analysis for a stricter interval of $|\eta| < 0.2$ indicate differences between the two rapidity selections (the nominal asymmetric and the stricter symmetric ones) smaller than 2% in the normalization and 3% in the shape of the transverse momentum distributions.

System	$\sqrt{s_{NN}}$	Year	Data sample	No. events*	MC sample	Generator
pp	7 TeV	2010	LHC10c, pass 3	4.7×10^7	LHC10d4a	PHOJET
p-Pb	5.02 TeV	2013	LHC13c, pass 2	8×10^7	LHC13b2_efix_p1	DPMJET
pp	13 TeV	2015	LHC15f, pass 2	5×10^7	LHC15g3a3,LHC15g3c3	PYTHIA 6 and 8

* Numbers are valid for real data only; for MC samples they might have slightly different.

Table 7.1: List of datasets and the corresponding (anchored) MC samples used for the analyses of pp and p-Pb data.

7.3 Data and Monte Carlo samples

In this section, the characterization of the datasets is presented. Several datasets have been analyzed: Monte Carlo simulations for cross checks and correction techniques, real data for the main analyses in pp and p-Pb collisions. The chosen data taking periods¹¹ are MB trigger periods and they are listed in Tab. 7.1. The notation, written with mono-spaced fonts, for the data and MC samples meets the one used in the ALICE Offline Software Framework [231–233].

Generally, due to the low pile-up and to the low beam-induced background, the analyzed collision data are ideally suited for the analysis of global event properties like transverse momentum spectra. The used datasets include physics data only, i.e. the unwanted background was kept as low as possible. For the analysis, only runs with stable detector conditions and verified Quality Assurance (QA) information have been selected which means that the quality of the calibration and reconstruction were both classified as good. This needs several (usually 2 or more) iterations in the calibration and reconstruction phases¹² until there are no or negligible signs of miscalibration left, provided there was no overall malfunctioning during the reconstruction. Additionally, the data samples have been also analyzed on a run-by-run basis to identify run-specific problems and verify the stability of the results.

The pp data taking at $\sqrt{s} = 7$ TeV took place in several periods in April–August 2010. The calibration and reconstruction steps have been iterated three times (pass 3). During those periods, the instantaneous luminosity at the ALICE interaction point was kept within the range $\mathcal{L} = (0.6 - 1.2) \times 10^{29} \text{ cm}^{-2} \text{ s}^{-1}$ to limit the collision pile-up probability. The mean number of pp interactions per bunch crossings during the runs for this data period is in the rangedifference between inclusive and identified cases shown in of $0.01 < \mu < 0.16$.

The first p-Pb collisions at the LHC were recorded during a short pilot run in September 2012. This was followed by the main p-Pb data taking period of the LHC in January–February 2013, which delivered larger luminosity with an increased number of bunches. In this work, the relativistic rise analysis is based on the p-Pb data collected during 2013. It consists of a large sample of minimum-bias triggered events, which was taken at a hadronic

¹¹The data taking period’s naming convention is “LHC”+“year”+“letter”.

¹²It is called “pass”+ an integer number indicating the number of iterations.

interaction rate of about 10 kHz — reaching near the maximum detector readout rate, and at the same time leaving the mean number of interactions per bunch crossing low to minimize the number of pile-up events in the same bunch crossing. The mean number of proton-nucleon interactions per bunch crossings is $\mu \approx 0.05$, which results in a fraction of pile-up events around 0.3% in the analyzed data sample. The maximum luminosity at the ALICE interaction point was $\mathcal{L} = 5 \times 10^{27} \text{ cm}^{-2} \text{ s}^{-1}$.

The pp data at $\sqrt{s} = 13 \text{ TeV}$ were collected after the startup of LHC Run 2 data taking period in June 2015. The luminosity was about $\mathcal{L} = 5 \times 10^{27} \text{ cm}^{-2} \text{ s}^{-1}$, corresponding to a rate of about 350 Hz for inelastic pp collision. The pile-up probability was estimated to be around 10^{-3} . The interaction probability per single bunch crossing is in the range 2 – 14%.

All data taking periods have corresponding Monte Carlo simulations which were used practically in two ways: 1) Determination of the corrections. This includes the trigger and vertex reconstruction efficiencies, the tracking efficiency as well as the contamination of the track sample with secondary tracks. 2) The analysis results of real collision data are compared to simulated events obtained from various MC event generators which use different models in describing particle production. It is noteworthy to mention that MC generators are used along with particle transport performed via a GEANT 3 [234] simulation of the ALICE detector. Detector configurations used in the detector simulation correspond to real, actual detector configurations present during data taking. The so-called “anchored” MC runs adopt the same detector configurations as they were during real physics runs. Table 7.1 reports the MC event generators which were used for different collision systems: PYTHIA 6.4 (tune Perugia 2011) [163], PYTHIA 8.2 (tune Monash 2013) [164] and PHOJET 1.12 [235] for pp data, whereas DPMJET 3.0-5 [236] for p–Pb data. The PHOJET and DPMJET event generators are based on the two-component Dual Parton Model [237], which integrates the ideas of Regge theory, non-perturbative and perturbative expansions of QCD within a common framework. While PHOJET describes hadron-hadron interactions, DPMJET is used for hadron-nucleus collisions — using PHOJET as a basis to generate individual hadron-hadron collisions — which was tuned to reproduce hadron production up to intermediate p_T at RHIC.

Considering the data taking conditions outlined above, the presented results in the following are obtained from 4.7×10^7 and 5×10^7 minimum bias pp collision events at $\sqrt{s} = 7 \text{ TeV}$ and $\sqrt{s} = 13 \text{ TeV}$ corresponding to integrated luminosities of about $\mathcal{L}_{\text{int}} = (0.76 \pm 0.03) \text{ nb}^{-1}$ and $\mathcal{L}_{\text{int}} = (0.87 \pm 0.02) \text{ nb}^{-1}$, respectively. For p–Pb data, approximately 100 million MB triggered events were selected for the analysis, corresponding to an integrated luminosity $\mathcal{L}_{\text{int}} = (47.8 \pm 1.6) \mu\text{b}^{-1}$; from which about 8×10^7 events were analyzed.

The integrated luminosity of each triggered sample was calculated with the number of analyzed events, N_{ev} , and the minimum bias cross section σ_{MB} (see Section 7.4.2), given by: $\mathcal{L}_{\text{int}} = N_{\text{ev}}/\sigma_{\text{MB}}$. The uncertainties enter from the cross section determination of minimum bias trigger, for details see Section 7.4.1.

7.4 Event selection

Not all events are used for data analysis, i.e. for simulated events as well as real data an event selection needs to be applied. Selection of events occurs in two stages. During data taking only a fraction of all events is recorded, this selection is controlled by the trigger and determines the online selection of events. In case of real data, the trigger selection for the analysis can be the same as that used in the hardware trigger during data acquisition and then this step is not necessary. Furthermore, in the offline data analysis further selection criteria are applied to the recorded events. This includes a re-evaluation of the trigger condition, selection of collision candidates (i.e. discrimination of beam-gas and pile-up events), acceptance and multiplicity selection criteria. This offline procedure is called the ALICE physics selection. For the analysis of the pp and p–Pb data, the event selection follows those used in the analyses of inclusive (unidentified) charged particle production [119, 238].

7.4.1 Trigger selection

The performed analyses use events selected by the ALICE minimum-bias trigger. Minimum bias triggers are designed to trigger on all inelastic interactions occurring in the detector, in turn, by imposing the least possible bias on the triggered sample. In ALICE this is implemented in a bunch-crossing (BC) trigger on the coincidence of two bunches crossing the detector at the same time. For the data taking of ALICE interaction triggers from the SPD and V0 detectors are used in coincidence with the bunch crossing. The applied online MB trigger condition varies for pp and p–Pb datasets.

For the analyzed pp data at $\sqrt{s} = 7$ TeV the MB trigger required a hit in the SPD, or in at least one of the V0 scintillator arrays in coincidence with the arrival of proton bunches from both directions. From now on the notation for the appropriate trigger conditions will be written as mono-spaced fonts, in this case denoted as MBOR, to meet the one used in the ALICE Offline Software Framework. This trigger selection essentially corresponds to the requirement of having at least one charged particle in 8 units of pseudorapidity in coincidence with a proton bunch crossing.

The minimum-bias trigger (denoted as VOAND) for $\sqrt{s} = 13$ TeV pp data in LHC Run 2 required at least one hit in both of the V0 scintillator arrays in coincidence with the arrival of proton bunches from both directions along the beam. A coincidence of signals in both V0A and V0C detectors removes contamination from single diffractives and electromagnetic events. The offline analysis to eliminate beam-induced background event, produced outside the interaction region, was done using the time information provided by the V0 detectors having time resolution better than 1 ns. Background events are further rejected by exploiting the correlation between the number of clusters and the multiplicity of tracklets in the SPD for the respective collision.

In pp analyses the focus is on inelastic (INEL) events originating from single-diffractive, double-diffractive, and non-diffractive processes. For pp at $\sqrt{s} = 7$ TeV, the INEL events selected by the MBOR trigger have been measured with an efficiency $\epsilon_{\text{MBOR}} = 85.2_{-3.0}^{+6.2}\%$, which was determined based on detector simulations with PYTHIA 6 and PHOJET MC event generators [98]. In ALICE, the luminosity determination is based on the visible cross sections measured in van der Meer (vdM) scans [239]. The visible cross section σ_{visible} seen by a given detector (or set of detectors) with a given trigger condition is a fraction of the total inelastic interaction cross section σ_{inel} : $\sigma_{\text{visible}} = \epsilon\sigma_{\text{inel}}$, where ϵ is the fraction of inelastic events that satisfy the trigger condition. The visible cross section σ_{MBOR} was measured to be (62.2 ± 2.2) mb with negligible statistical uncertainties with respect to the systematic ones. The total inelastic cross section resulted in $73.2_{-4.6}^{+2.0}$ (model) ± 2.6 (lumi) mb — with the latter uncertainty being the systematic uncertainty of the luminosity determination.

For $\sqrt{s} = 13$ TeV pp data, at the time of releasing preliminary results, there was no experimental information available regarding diffractive processes, therefore trigger (and event-selection) efficiencies are solely based on previous experimental data at lower collision energies and simulations with MC event generators. For this reason, the inelastic cross section value was adopted from Ref. [240], where the authors perform a fit using measured values from several experiments, including mainly ALICE, ATLAS, CMS, and TOTEM. Their obtained cross section value is $\sigma_{\text{inel}} = (77.6 \pm 1.0)$ mb. However, the visible cross section σ_{V0AND} has been measured by ALICE in vdM scans [241] and it amounts to $57.8 \text{ mb} \pm 2.2\%$.

All minimum bias p–Pb data have been taken with a minimum bias (hardware or online) trigger (denoted as V0AND), which is essentially the same as for $\sqrt{s} = 13$ TeV pp data. It was configured and optimized to have high, 99.2% efficiency for selecting non-single diffractive (NSD) hadronic interactions. It is shown in Ref. [242] that according to Monte Carlo studies, the inefficiency is observed mostly for events without reconstructed vertex, i.e. with no particles produced at mid-rapidities. The correction for this inefficiency will be discussed in Section 7.6.3. It was also pointed out that the contribution of single diffractive and electromagnetic interactions is negligible [242]. In the offline analysis, background events (due to beam-gas and other machine-induced background collisions) were further suppressed by requiring the arrival time of signals on the neutron Zero Degree Calorimeter which is positioned in the Pb-going direction, to be compatible with a nominal p–Pb collision occurring close to the nominal interaction point. The V0 and ZDC offline selection rejects about 0.5 – 1.0% of events triggered online. The resulting event sample (seen by the V0AND trigger) corresponds to the visible cross section of $\sigma_{\text{V0}} = (2.09 \pm 0.07)$ b [243].

7.4.2 Vertex selection

Events selected with minimum bias trigger are required to have exactly one reconstructed collision vertex (primary vertex) of good quality, which is ensured by the requirement that at

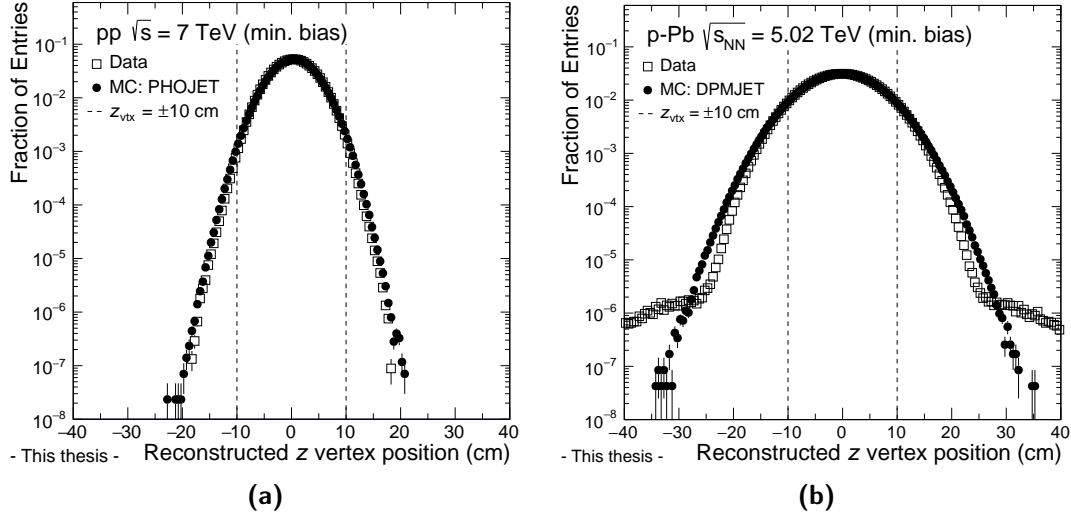


Figure 7.2: Distributions of reconstructed longitudinal (z) vertex positions in comparison to those obtained from MC simulations in (a) $\sqrt{s} = 7$ TeV pp data and (b) $\sqrt{s_{\text{NN}}} = 5.02$ TeV p–Pb data. The applied cuts on the vertex position are indicated as vertical dashed lines at $z = \pm 10$ cm.

least one track is used to reconstruct the vertex. For events with at least one reconstructed primary charged particle [244] in the common ITS and TPC acceptance ($|\eta| < 0.9$) the vertex reconstruction is fully efficient. The vertex position is determined from the tracks reconstructed in the ITS and TPC. For events that do not have a primary vertex (PV) reconstructed from tracks, which are essentially collisions with low multiplicity of charged particles, the PV is reconstructed from the SPD tracklets. The acceptance (η) of a detector depends on the z -position of the PV which is simply the effect of the detector geometry, and most pronounced for the detectors with small radii (e.g. SPD), while being negligible for the TPC. The reconstructed longitudinal vertex position needs to be within $|z_{\text{vtx}}| < 10$ cm with respect to the nominal interaction point at $z = 0$ cm along the z -axis, which ensures on the one hand that the vast majority of reconstructed tracks fall into the ITS-TPC acceptance, on the other reduces background events by removing unwanted collisions from satellite bunches. The efficiency of the z -vertex reconstruction depends on the position of PV. Within the selected range of $|z| < 10$ cm the efficiency is approximately independent of the vertex position. The accuracy of the z -vertex reconstruction improves if a larger number of tracks contribute. Additional selection criteria on the resolution and dispersion of the PV were applied to improve its quality.

The fraction of events that pass the z -vertex selection criterion for both pp and p–Pb datasets ranges between 90% and 95%. The distributions of the reconstructed vertex positions for $\sqrt{s} = 7$ TeV pp data and $\sqrt{s_{\text{NN}}} = 5.02$ TeV p–Pb data are shown in Figs. 7.2a and 7.2b. One can immediately see the excellent agreement of the distributions of real data and simulated data. The resolution of the primary vertex reconstruction can be studied using Monte Carlo simulations by comparing differences observed between the generated and re-

constructed primary vertices. The resolution of the PV improves with increasing number of contributing tracks which is better for p–Pb collisions (with respect to pp collisions) because of the higher average multiplicities. Note that the performance for pp at $\sqrt{s} = 13$ TeV is quite similar to that at $\sqrt{s} = 7$ TeV [223, 230].

Contaminations from pile-up events, having more than one pp or p–Pb collision per bunch crossing, were rejected offline by excluding multiple primary vertices reconstructed in the SPD in a single event [193]. In the offline analysis, reconstructed vertices are tagged as pile-up if they are sufficiently distant from the primary vertex (the default value is 8 mm) and they are formed by a sufficient number of contributing tracklets (by default three contributors) and are inside the collision diamond. The impact of the remaining pile-up events after the pile-up rejection is negligible. In addition, a tighter cut is applied for all tracks with a DCA in z -direction to the primary vertex of $\text{DCA}_z > 2$ cm are rejected from the analysis, see the following section for more details.

It is worth noting that the requirement for a vertex itself biases the data sample by rejecting events producing particles at mid-rapidity with no reconstructed vertex. This effect will be discussed later on in more detail in Section 7.6.3.

7.5 Track selection

Tracks from charged particles are reconstructed in the ITS and TPC detectors, and then propagated to the outer detectors and matched with the reconstructed space point in, e.g., the TOF and HMPID detectors. The required p_T resolution at high p_T can be achieved using ITS-TPC combined tracks (reconstructed using both the ITS and TPC) which will be referred to as global tracks in the following. The relativistic rise method in track selection, both for pp and p–Pb analyses, follows closely that of the unidentified charged particle analyses [238, 245], as it was already anticipated earlier; their components are discussed in the following.

7.5.1 Primary track selection

In this work, only primary charged particles are considered; these are charged particles with a mean proper decay length $c\tau$ larger than 1 cm, which are either produced directly in the interaction, or from decays of particles with $c\tau$ smaller than 1 cm, excluding particles produced in interactions with the material. Technically, the smallest distance between the reconstructed track curve and the primary vertex is evaluated with a DCA technique, separately in the z -direction (along the beam) and in the xy -plane due to the different impact parameter resolutions in z and xy .

If primary particle selection is demanded, high purity selection of primary charged particles is achieved with a p_T -dependent cut on the DCA between the track and the primary vertex in the plane perpendicular to the beam axis (DCA_{xy}), which is required to be less

than seven times the resolution of this quantity. For example, for $\sqrt{s} = 13$ TeV pp data it is set as follows: $DCA_{xy} < 7 \times (0.0015 + 0.05 \times (p_T / (\text{GeV}/c))^{-1.01})$ cm; the numerical factors might change for different datasets. A loose cut of 2 cm on the DCA_z in the beam-direction is also applied to remove tracks from (remaining) pile-up events.

7.5.2 Standard track selection

Several so-called “standard” track selection criteria are applied. These are required to limit the contamination due to secondary particles, to maximize tracking efficiency for primary charged particles and the dE/dx - and momentum resolution, and to guarantee an optimal PID quality. The most relevant selection criteria are listed below.

- (1) The minimum number of crossed rows n_{rows} in the TPC is required to be at least 70 (out of a maximum possible of 159), as already pointed out in Chapter 6. This guarantees that the tracks have a minimum quality. A crossed row means that clusters in two pads directly next to a row are reconstructed. The calculation of n_{rows} is performed from the number of all clusters that are assigned to the track n_{cl} , but taking into account clusters that are missing, for example, because they are sub-threshold (see Section 6.5.2). Pad rows, on which no cluster was found, but which have found clusters within two neighboring pad rows, are counted as missing.
- (2) Connected to the previous cut is the requirement that at least 80% of the theoretically findable clusters (known from trajectory) are found as crossed rows; avoiding this way poorly reconstructed tracks in the TPC. The number of findable clusters is the maximal number of possible clusters calculated from the track properties taking into account the geometrical effects of dead zones at the TPC sector boundaries and the dependence of the maximal number of clusters on the polar track angle (η -dependence). Dead channels or missing front-end readout cards in the TPC are considered as findable.
- (3) Shared clusters, n_{shared} , are clusters that belong to more than one track. Large fractions of shared clusters can originate from fake tracks or multiple reconstructed tracks and are removed by the corresponding cut on the fraction of shared clusters over all clusters $n_{\text{shared}}/n_{\text{cl}}$. While n_{cl} includes only clusters that contribute to the track fit, n_{shared} takes into account all clusters that are assigned to a track. Therefore, the ratio $n_{\text{shared}}/n_{\text{cl}}$ can be larger than unity. To reject mainly multiple reconstructed tracks, a track is only allowed to share 40% of its TPC clusters with another track.
- (4) The requirements of the TPC track refit (see Section 5.2) and the maximal χ^2 per TPC cluster (< 4) are the minimal quality criteria needed to remove tracks which are not or not properly reconstructed in the TPC. Tracks with succeeded TPC (and ITS) refit have significantly better momentum resolution.

Additionally, tracks must be associated with at least one cluster in the SPD, and the χ^2 per cluster in the ITS is limited to 36. Together with the small radial distance from

the primary vertex, this provides the good DCA resolution needed for the selection of primary particles. The momentum of each track must be greater than $150 \text{ MeV}/c$ and the pseudorapidity is restricted to $|\eta| < 0.8$ to avoid the edges of the acceptance of the TPC.

7.5.3 Vertex-constrained tracks

Tracks that have wrong ITS hits assigned or experienced scattering in the material between the ITS and the TPC can have a reconstructed momentum that is significantly different from the true one. This can lead to an excess yield in steeply falling p_T distribution at large p_T , which is not canceled by the p_T resolution correction.

To prevent this problem, a selection criterion is applied on a quantity called $\chi_{\text{TPC-ITS}}^2$, which takes the difference of the track parameters between TPC-ITS and the TPC-constrained track, and is normalized to the covariance matrices. The TPC-constrained track parameters are obtained from a track fit to the reconstructed TPC clusters, disregarding the ITS hits but using the reconstructed primary event vertex (track vertex if reconstructed, SPD vertex otherwise) as a constraint. The usage of the primary vertex to constrain the TPC-only track is only valid for primary particles which are produced at the vertex. Tracks of secondary particles are mostly not pointing to the primary vertex yielding larger $\chi_{\text{TPC-ITS}}^2$. So, the cut on this variable also helps to enhance the purity of primary tracks. Tracks for which the TPC constrained fit fails or no $\chi_{\text{TPC-ITS}}^2$ can be assigned are also excluded from the analysis.

7.6 Corrections

In this section, I review all the corrections which were applied to the identified particle fractions in the relativistic rise analysis, and briefly summarize those applied in the inclusive charged hadron analysis [238, 245]. The latter corrections were evaluated at the level of unidentified charged hadron yields which were directly taken over from the appropriate analysis in case of pp data. Regarding the p-Pb data, the unidentified charged spectrum was re-measured for this analysis in a different pseudorapidity window ($-0.5 < y < 0$). The related corrections to the new charged spectrum were calculated, except that related to the p_T resolution. This component results up to 1.9% correction in the minimum bias case together with a $\pm 1.3\%$ systematic uncertainty at most, according to the charged analysis [245]. It was verified that the two corrected spectra were found to be consistent with each other within $\pm 5\text{--}6\%$ in the entire p_T range in all V0A multiplicity classes.

The charged pion, kaon, and (anti)proton particle fractions extracted with the relativistic rise method need to be corrected for detector effects and secondary particle contamination. The estimation of these effects was carried out using MC simulations provided by various event generators PYTHIA, HIJING, PHOJET, DPMJET —depending on the collision system— using the same reconstruction algorithms, physics selection, and event selection criteria that are used in real data.

The corrections for detector effects can be essentially split into two groups: 1) track-level corrections: that may depend on p_T , event activity, i.e. event multiplicity in this case, and also on pseudorapidity. They might cause changes in the spectral shape and in the normalization. 2) event-level corrections: they are relevant mainly for the overall normalization of the results.. The track-level corrections have only moderate multiplicity and η dependence and therefore they are applied independently of multiplicity and pseudorapidity. For the calculation of the various correction factors, in some cases, the p_T binning are different which is motivated by the available statistics in the simulations. Moreover, no correction for finite p_T bin width was applied, and all results are averaged over the corresponding p_T intervals. Besides, correction due to bin shift was not taken into account which, in turn, results in data points to be drawn at bin centers.

7.6.1 Corrections inherited from the inclusive charged analysis

The corrections which are applied in the inclusive charged analysis [119, 238, 246], and are relevant for this work, are shortly summarized below. Tracking efficiencies and secondary contaminations are also calculated for the case of particle fractions, hence their definition is given here in the context of inclusive charged particles.

Tracking efficiency

The term tracking efficiency accounts also for acceptance limitations defined by the kinematic range, therefore, the overall efficiency is meant to be the efficiency times the acceptance ($\epsilon \times \text{Acc.}$). The corresponding multiplicative correction factor $1/(\epsilon \times \text{Acc.}) \equiv 1/\epsilon_{\text{tracking}}$ is calculated as the ratio of reconstructed primary tracks $dN^{\text{rec.}}/dp_T$ to generated primary particles $dN^{\text{gen.}}/dp_T$. In the analysis of p–Pb data, no dependence of the efficiency on multiplicity was observed, hence the efficiency was averaged over all multiplicity classes; it depends only on p_T and η .

The tracking efficiency also depends on the particle type under study which is more pronounced at low momenta while is universal at large momenta. The overall efficiency for primary charged particles is the average of the individual particle-type efficiencies weighted with their abundances. Except at very low p_T , the tracking efficiency is generally in the range of 55–80% both for pp and p–Pb collisions. Since the statistics available in the minimum bias simulations is limited at high p_T , and no p_T dependence of the efficiency is seen above $p_T = 4 \text{ GeV}/c$, a constant efficiency is assumed for $p_T > 4 \text{ GeV}/c$. For the 2013 p–Pb data, the tracking efficiency was estimated based on the measured fractions of pions, kaons and protons [53]. The effect of the difference in the acceptance ($-0.5 < y < 0$ versus $|y| < 0.3$) is negligible and the particle ratios were assumed to be equal in these two kinematic regimes.

Contamination of secondary particles

Even though primary particles are selected via a cut on the DCA with respect to the primary vertex, there are also reconstructed secondary particles that can pass the selection. They can be produced in decays of primary particles which originates from either weak decays of charged pions (e.g. $\pi^+ \rightarrow \mu^+ \bar{\nu}_\mu$) or neutral strange particles (e.g. $K_S^0 \rightarrow \pi^+ \pi^-$). Particles stemming from decays of secondaries are also secondaries, such as electrons produced from decays of neutral pions (e.g. $K_S^0 \rightarrow \pi^0 \pi^0$; $\pi^0 \rightarrow e^+ e^- \gamma$). Secondaries can also be produced in interactions with the detector material via electromagnetic or hadronic processes. The dominant source (apart from a small fraction of knock-out protons at low p_T) is electrons from pair production from photons via $\pi^0 \rightarrow \gamma \gamma$ decays. All secondary particles originating from these sources are considered as contamination in the measurement.

The secondary contamination of the primary particle yields is estimated from the fraction of physical primaries f_{prim} in the track sample passing all cuts on the detector level, i.e.

$$f_{\text{prim}} = \frac{N_{\text{prim,rec}}^{\text{MC}}}{N_{\text{prim,rec}}^{\text{MC}} + N_{\text{sec,rec}}^{\text{MC}}}, \quad (7.1)$$

where $N_{\text{prim,rec}}^{\text{MC}}$ and $N_{\text{sec,rec}}^{\text{MC}}$ are the number of reconstructed primary and secondary tracks in the sample in a given p_T bin, respectively. The related correction factor is $1 - f_{\text{prim}}$, and applied bin-by-bin.

A sizeable fraction of the weak decays originates from the decay of neutral strange particles such as K_S^0 and Λ . The yield of these strange particles is known to be underestimated in the event generators used to extract the corrections. To account for this effect, the number of secondaries from MC has been scaled up by scaling factor derived from fits to the DCA distributions. The resulting contamination is of the order of 10% for the lowest p_T bin and rapidly decreases below 1% for p_T above 2 GeV/ c which is a consequence of the decay kinematics and that the improved impact parameter resolution at high p_T leads to an improved selection of primary particles.

Transverse momentum resolution

As mentioned before, having a good transverse momentum resolution is crucial to measure p_T distributions up to very large momenta. It requires applying the necessary correction due to the finite resolution. The inverse of the transverse momentum is among the track parameters obtained during the track reconstruction and is directly related to the track curvature. The p_T resolution, obtained from the covariance matrix of the track fitting, has been verified and found to be in agreement with the observed width of the neutral kaon decay $K_S^0 \rightarrow \pi^0 \pi^0$.

The measured p_T distribution is a convolution of the true p_T distribution with the p_T resolution of the detector. The momentum resolution response function describes how the

detector and the tracking algorithm affects the momentum resolution. The unfolding procedure which was used to obtain the true distribution is based on the observation that the transverse momentum smearing has only a small effect on the spectrum. In the application of the procedure the measured p_T spectra have been parametrized by a power law fit for $p_T > 5 \text{ GeV}/c$ and folded with the p_T resolution obtained from the covariance matrix of the track fitting algorithm. The resulting correction factors depend on the spectral shape—the steeper the spectra the larger is the correction—and also on the p_T resolution which are different for pp and p–Pb data (see Section 5.2).

Acceptance correction in p–Pb analysis

Due to the asymmetry of the collision, the nucleon-nucleon c.m. frame moves with about $0.43c$, corresponding to a rapidity shift of $y = -0.465$ in the direction of the proton beam. For massless particles or particles with $p_T \gg m$, the pseudorapidity equals to the rapidity, i.e. $\eta = \eta_{\text{lab}} + y$. However, it is only an approximation and the proper transformation of η under a boost along the z -direction with rapidity y reads as $\sinh \eta = \sinh(\eta - y) - (\sqrt{m^2/p_T^2 + \cosh^2 \eta_{\text{lab}}} - \cosh \eta_{\text{lab}}) \times \sinh y$, with the second term being the additional correction. The boost makes particles to experience a shift within the acceptance but also into or out of the acceptance which effect has to be corrected for.

The correction is calculated p_T -bin by p_T -bin, using the measured pseudorapidity distributions and the primary particle composition [242]. The pseudorapidity distribution $dN/d\eta_{\text{lab}}$ was measured for inclusive charged particles and is assumed to be independent of the particle species. The overall acceptance correction for all charged particles is obtained as a weighted average of the single particle corrections. For the analysis of 2013 p–Pb data, the input of the relative fractions of charged pion, kaons and protons were taken from the measured particle composition [53]. The p_T - and η -dependent correction has a clear mass-ordering which is the largest for protons whereas negligible for electrons. For protons, the correction is less than 1% above $p_T = 3 \text{ GeV}/c$ for $|\eta| < 0.3$, and it is smaller than 2% for the more forward intervals of η .

7.6.2 Corrections of π^\pm , K^\pm , and p(\bar{p}) particle fractions

All the corrections related to the relativistic rise method, and outlined in this section, are applied to the uncorrected (raw) π^\pm , K^\pm and p(\bar{p}) particle fractions introduced in the previous chapter. The main contributions are shown in Fig. 7.3 applied both in pp and p–Pb analysis and they are as follows: 1) Relative (tracking-)efficiency correction: corrections of tracking efficiencies of identified charged particles with respect to those of inclusive charged particles 2) Feed-down correction: correction for the contamination from secondary particles, which are applied only to the pion and proton yields 3) Rapidity correction: correction accounting for the $(\eta, p_T) \rightarrow (y, p_T)$ phase space conversion has to be taken into account.

The quoted corrections are applied to all species, except that only pions and protons

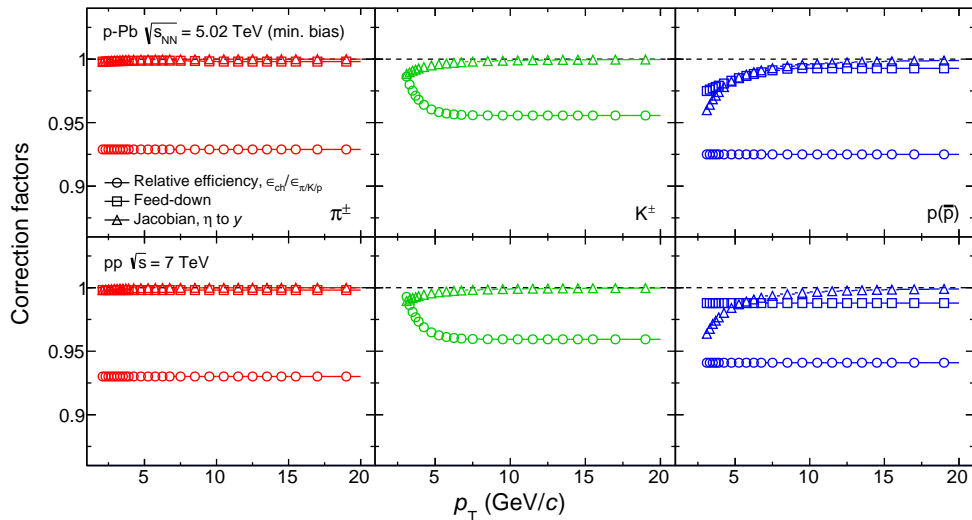


Figure 7.3: Main correction factors applied to π^\pm , K^\pm , and $p(\bar{p})$ raw particle fractions as a function of transverse momentum in pp and p–Pb analyses. Only pions and protons are corrected for feed down. The correction due to muon contamination in the pion particle fraction is less than 1% and is not shown in the figure. Figure is reproduced from Ref. [223].

are corrected for feed-down, and for the fractions of pions, the contamination due to muons are also present; however, their impact is less relevant (both for pp and p–Pb data). Note that the corrections for $\sqrt{s} = 13$ TeV pp data (not shown here) are very similar to those in $\sqrt{s} = 7$ TeV pp [223, 230].

For all species, the main part of the overall correction is related to the relative efficiency correction. For pions, the other corrections are relatively small, whereas for kaons, the Jacobian conversion factor matters only at low p_T (1% at $p_T = 4$ GeV/c), while for protons, both the Jacobian and the feed down corrections contribute (1% at $p_T = 6$ GeV/c).

Relative efficiency correction

The procedure of the relativistic rise analysis uses the p_T spectra from the inclusive unidentified charged hadron analysis. Since for p–Pb analysis no unidentified spectrum exists in the present pseudorapidity range, they were re-measured and corrected for tracking efficiency. The measured inclusive and identified charged hadron efficiencies show no dependence on event multiplicity and pseudorapidity. Hence, for further use, the MB sample is considered.

The difference between inclusive and identified cases shown in Figure 7.4a are used to obtain relative efficiencies—by dividing them—which are shown in Fig. 7.4b. To account for statistical fluctuations being present above a certain p_T , the curves were smoothed by using constant and exponential fits to the appropriate p_T ranges. In turn, at high p_T the corrections are nearly constant and their values range from 0.93 to 0.96, depending on particle species. It is worth noting that similar corrections values were obtained in the pp analyses. For the entire p_T range $\epsilon_{\pi/K/p} < 1$ holds, since there are weakly decaying strange baryons (e.g. Σ^+) which are not reconstructed during the selection of primary charged particles.

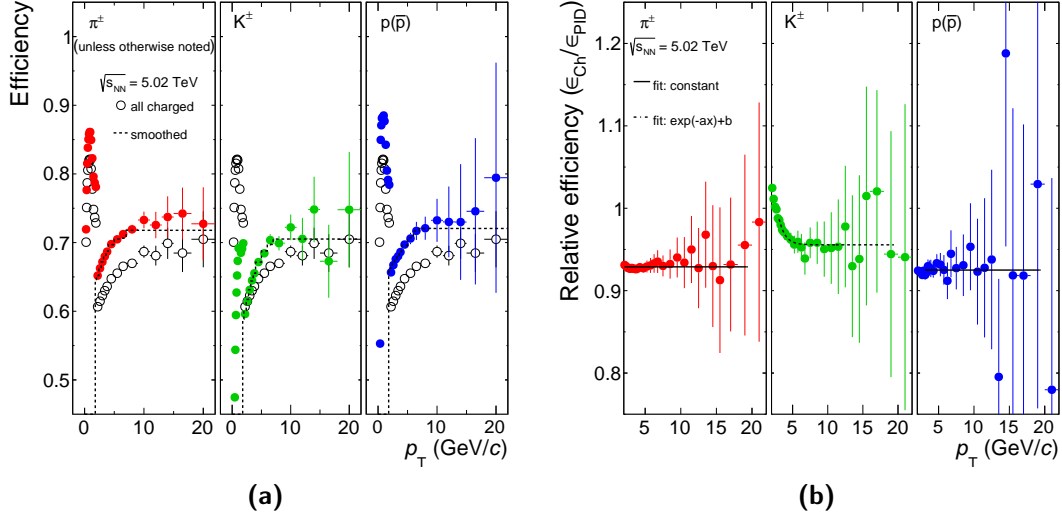


Figure 7.4: (a) Tracking efficiencies ϵ_{ch} and $\epsilon_{\pi/K/p}$ and (b) relative efficiency correction factors $\epsilon_{ch}/\epsilon_{\pi/K/p}$ as a function of p_T for all charged and identified primary charged particles simulated with DPMJET in p-Pb collisions at $\sqrt{s_{NN}} = 5.02$ TeV. Figures are reproduced from Ref. [223].

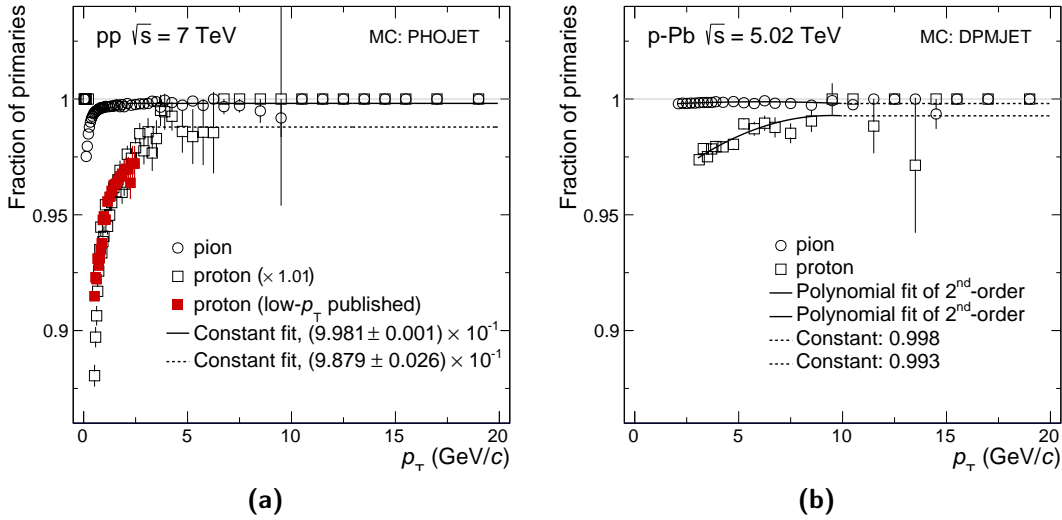


Figure 7.5: Feed-down correction factors as a function of p_T for (a) $\sqrt{s} = 7$ TeV pp data and (b) $\sqrt{s_{NN}} = 5.02$ TeV p-Pb data, obtained respectively by using PHOJET and DPMJET MC generators. Figures are reproduced from Ref. [223].

Feed-down correction

The correction for secondary particle contamination (feed-down) is relevant only for charged pions, protons and antiprotons in the studied p_T range. For kaons, the contamination from secondary particles is negligible above $p_T = 3$ GeV/c. The pion and proton fractions were corrected for feed-down from weak decays using simulated MC data. The relative fraction of secondaries in case of pp data were scaled to those extracted from the Monte Carlo DCA template fits to data [247]. Figure 7.5 shows the obtained feed down correction factors for pion and protons as a function of p_T both for pp and p-Pb data.

First, the secondary particle contamination to the fraction of pions and protons which passed the track selection criteria were obtained. Then, the derived correction factors are scaled to the correction computed using data driven methods. For pp data, protons were scaled up by 1% to match the DCA template fit results. The scaling was done in the overlapping p_T region, i.e. in the range of $p_T = 2 - 3 \text{ GeV}/c$. The size of the feed-down correction is obtained by a constant fit for $p_T > 3 \text{ GeV}/c$ leading to $1.01 \pm 0.3\%$ for protons; for p-Pb data, it amounts to 2.5% at $p_T = 3 \text{ GeV}/c$. For pions, the correction is around $1 - 2\%$ for $p_T \geq 2 \text{ GeV}/c$.

The corrections decrease with increasing p_T due to decay kinematics and due to the improved impact parameter resolution towards higher p_T . In the analysis, the correction is applied as a correction factor equal to the fraction of primary particles in the overall sample (primary and secondary). It is worth noting that the scaling between data and MC has a limited precision and could be slightly different at higher p_T .

Rapidity correction

The conversion $d\eta/dy$ accounting for the phase space conversion $(\eta, p_T) \rightarrow (y, p_T)$ is the $J_{\eta/y}$ Jacobian. The rapidity range is given as follows for species s : $\Delta y_s(\eta, p_T) = y_s(\eta_2, p_T) - y_s(\eta_1, p_T)$ with the rapidity cut of the measurement $\eta \equiv \eta_2 = -\eta_1 = 0.8$ and

$$y_s(p_T, \eta) = \frac{1}{2} \ln \left(\frac{\sqrt{m_s^2 + p_T^2 \cosh^2 \eta + p_T \sinh \eta}}{\sqrt{m_s^2 + p_T^2 \cosh^2 \eta - p_T \sinh \eta}} \right). \quad (7.2)$$

The $\Delta\eta/\Delta y$ rapidity correction is relevant only for heavier particles, such as (anti)protons, and for lower p_T region. At $p_T = 3 \text{ GeV}/c$, the correction is $\sim 4\%$ for protons, $\sim 1\%$ for kaons, and $\sim 0.1\%$ for pions, and it becomes practically negligible for $p_T \gtrsim 6 \text{ GeV}/c$ for all particle species.

Muon contamination

There is a small contamination of (primary) muons in the pion yields due to their similar mass (and therefore similar $\langle dE/dx \rangle$ values). The dE/dx resolution of the TPC does not allow for the separation of pions and muons. High- p_T muons are produced via semi-leptonic decay of heavy quarks and for those decays one expects muon and electron branching ratios to be similar. Therefore, the measured electron yield (fraction) — dominated by secondary electrons from photon conversions — is subtracted from the pion yield (fraction) bin-by-bin to correct for the muon contamination. The correction, i.e. the ratio of fractions: $\pi^\pm/(\pi^\pm + e^\pm)$, due to muon contamination ranges between 0.5% and 1% at all p_T bins, both for pp and p-Pb collisions. For $p_T > 8 \text{ GeV}/c$, the correction is independent of p_T . The correction changes the pion yield by about 0.6% in the full p_T range, in good agreement with the simulations obtained with PYTHIA MC event generator.

7.6.3 Event-level corrections

Apart from track-level corrections discussed so far, there are also corrections made at the event level. These are present due to inefficiencies of the applied trigger criteria and the primary vertex reconstruction. For the proper normalization of the p_T spectra, one has to take into account that events are missing mainly because they have not been triggered on or lack of a reconstructed primary vertex which results in signal losses.

Normalization to inelastic events in minimum bias pp analyses

The corrected p_T spectra have to be normalized to the number of inelastic pp collisions. To do so, one needs to convert the particle yield normalized to the number of triggered events N_{trig} to the yield normalized to the number of inelastic events N_{INEL} . The conversion is done via a multiplicative scaling factor f_{inel} defined as follows: $N_{\text{INEL}} = N_{\text{trig}} \times (\sigma_{\text{INEL}}/\sigma_{\text{visible}}) = N_{\text{trig}} f_{\text{inel}}^{-1}$, where f_{inel} is the ratio between the visible cross section σ_{visible} and the inelastic cross section σ_{INEL} for the corresponding collision energy.

As mentioned earlier, for $\sqrt{s} = 13 \text{ TeV}$ pp data, the inelastic cross section σ_{INEL} value was adopted from Ref. [240], and the visible cross section (σ_{VOAND} for the VOAND trigger) is measured by ALICE. In turn, one obtains the factor $f_{\text{inel}} = 0.7448 \pm 0.0190$ (2.55%). It is worth noting that the extracted f_{inel} factor is valid only for the analyzed data taking period at this collision energy. For $\sqrt{s} = 7 \text{ TeV}$ pp, the normalization factor f_{inel} was evaluated in Ref. [98] which is based on the measured MBOR trigger efficiency and it amounts to $f_{\text{inel}} = 0.852^{+0.062}_{-0.030}$.

Correction due to signal loss in pp and p–Pb analyses

Any measurement performed with ALICE event selections is done within an event class. The relevant event classes—ordered in such a way that a certain class contains only a subset of events from the previous one—in the current work are:

- (I) INEL or NSD class: These are all events selected from INEL or NSD collisions.
- (II) PS (Physics Selection) class: These are triggered events from class (I) which pass the physics selection criteria (see Section 7.4).
- (III) PS + Vertex selection (Vtx) class: These are events from class (II) that have a reconstructed primary vertex determined by either SPD or global tracking.
- (IV) PS + Vertex selection (Vtx) + Vertex $-z$ cut (Vtx $_z$) class: These are events from class (III) whose primary vertex position along the beam axis (z) are within $|z| < 10 \text{ cm}$ of the nominal IP (center of the ALICE barrel).

By convention, ALICE presents the (identified) charged hadron spectra results in the inelastic (or non-single diffractive) event class, denoted as (I). For real data, we only ever manage to store a subset of these events whereas in MC, INEL or NSD represents all generated events, and in that case one has access to all events. In any analysis in which one

only analyses a subset of events within a desired event class, an f_{SL} correction has to be applied due to event losses and signal losses. This implies to determine the components of this correction denoted by ϵ in the following equation:

$$\frac{1}{N_{ev}} \frac{dN_{\text{particles}}}{dp_{\text{T}}}(p_{\text{T}}) = \frac{1}{N_{ev}^{\text{accepted}}} \frac{dN_{\text{particles}}^{\text{accepted}}}{dp_{\text{T}}} \times \underbrace{\frac{\epsilon_{\text{events}}}{\epsilon_{\text{particles}}}}_{f_{\text{SL}}}. \quad (7.3)$$

Essentially, there are two possible approaches which are usually applied for such a correction: data-driven which makes assumptions for $\epsilon_{\text{particles}}$, and use counters for ϵ_{events} , and MC-driven which computes both. Both methods have been shown to provide consistent results within roughly 1%, depending on operational conditions.

For this work, a data-driven approach was implemented which relies less on MC and in which one assumes that the vertex-finding probability is independent of longitudinal position of the collision vertex. The reason for triggered events not having reconstructed vertex is that these events do not contain particles at mid-rapidity. The advantage of the method is that event counter losses are directly taken from data (without relying on MC) while its disadvantage being that it disregards all signal losses from vertex finding.

The inclusive p_{T} spectrum of primary charged particles dN/dp_{T} , considered as signal in the measurement and at the particle level normalized to $1/N_{ev}$, is evaluated in event classes (I)–(IV). Within each of the event classes one has the corresponding number of events determined, i.e. (I): $N_{ev} = N_{\text{INEL}}$, (II): $N_{ev} = N_{\text{ev}|_{\text{PS}}}$, (III): $N_{ev} = N_{\text{ev}|_{\text{PS} \& \text{Vtx}}}$, and (IV): $N_{ev} = N_{\text{ev}|_{\text{PS} \& \text{Vtx} \& \text{Vtx}_z}}$. By definition, one has to consider that $N_{\text{INEL}} \geq N_{\text{ev}|_{\text{PS}}} \geq N_{\text{ev}|_{\text{PS} \& \text{Vtx}}} \geq N_{\text{ev}|_{\text{PS} \& \text{Vtx} \& \text{Vtx}_z}}$, which also holds for the signals, $dN|_{\text{INEL}}/dp_{\text{T}} \geq dN|_{\text{PS}}/dp_{\text{T}}$, etc. To compute the correction, one has to make the following two assumptions:

- a) $1/N_{\text{ev}|_{\text{PS} \& \text{Vtx}}} \times dN|_{\text{PS} \& \text{Vtx}}/dp_{\text{T}} = 1/N_{\text{ev}|_{\text{PS} \& \text{Vtx} \& \text{Vtx}_z}} \times dN|_{\text{PS} \& \text{Vtx} \& \text{Vtx}_z}/dp_{\text{T}}$: The relative signal loss due to the cut on the longitudinal primary vertex position z is the same as the event counter loss. Essentially, this means that physics is not expected to depend on the primary vertex position. Besides, the approximation is quite reasonable given the small value of the normalization correction (see Tab. 7.2).
- b) $dN|_{\text{PS}}/dp_{\text{T}} = dN|_{\text{PS} \& \text{Vtx}}/dp_{\text{T}}$: Triggering and vertexing does not miss any mid-rapidity signal. This hypothesis was tested to be accurate within roughly 1%.

For $\sqrt{s} = 13$ TeV pp analysis, f_{SL} equals to $N_{\text{ev}|_{\text{PS} \& \text{Vtx}}}/(N_{\text{ev}|_{\text{PS}}} \times N_{\text{ev}|_{\text{PS} \& \text{Vtx} \& \text{Vtx}_z}})$. It was verified that option b) from the two assumptions above is not satisfied for the entire p_{T} range, therefore further correction, f'_{SL} , has to be applied to account for signal losses due to applied trigger condition. Such losses are more important at low p_{T} , since events that fail the trigger conditions or fail to have a reconstructed primary vertex tend to have softer particle p_{T} spectra than the average inelastic collision.

The f'_{SL} correction is the p_{T} -dependent ratio of the particle yield in inelastic collisions

$r^{\text{Data}} = \frac{N_{\text{ev} _{\text{PS}} - N_{\text{ev} _{\text{PS} \& \text{Vtx}}}}{N_{\text{ev} _{\text{PS} \& \text{Vtx}}}}$	$\epsilon^{\text{MC}} = \frac{N_{\text{ev} _{\text{PS}}} - N_{\text{ev} _{\text{PS} \& \text{Vtx}}}}{N_{\text{ev} _{\text{PS,NSD}}} - N_{\text{ev} _{\text{PS} \& \text{Vtx}}}}$	$f_{\text{SL}} = 1 - \frac{r^{\text{Data}}}{\epsilon^{\text{MC}}}$
0.008	0.232	0.964

Table 7.2: Components of normalization factors to correct for signal losses providing results, in this way, for visible cross section event class in minimum bias p–Pb collisions. First column indicates the relative event loss between events fulfilled “trigger+physics selection” (PS) and events passed “trigger+physics selection+vertex selection” (PS & Vtx).

with a simulated vertex with $|z| < 10$ cm to the particle yield in events that fulfill all trigger and vertex-selection conditions. The value of f'_{SL} calculated using the PYTHIA 8 MC dataset is taken as the central value and it varies from a few percent at low p_T to less than one percent at higher p_T (> 2 GeV/ c). The systematic uncertainty of f'_{SL} is estimated as one half of the difference between the central value of f'_{SL} and unity. This envelope includes the variations in f'_{SL} due to the different event generators.

In p–Pb collisions, for the MB results, the normalization is adopted such that to provide results in the so-called NSD visible cross section event class, i.e. normalizing to PS events which requires a correction for the vertex reconstruction efficiency. This means that there are triggered events which have no reconstructed vertex because there were no particles produced at mid-rapidity. From MC simulation one can estimate the probability that an event without a reconstructed vertex is selected, i.e. the vertex reconstruction efficiency:

$$\epsilon_{\text{Vtx}}^{\text{MC}} = (N_{\text{ev}|_{\text{PS}}} - N_{\text{ev}|_{\text{PS} \& \text{Vtx}}}) / (N_{\text{ev}|_{\text{PS,NSD}}} - N_{\text{ev}|_{\text{PS} \& \text{Vtx}}}). \quad (7.4)$$

Using these assumptions, Eq. (7.3) and so the corrections can be expressed as follows

$$\frac{1}{N_{\text{ev}}} \frac{dN_{\text{particles}}}{dp_T}(p_T) = \frac{1}{\epsilon_{\text{tracking}}} \times \frac{1}{N_{\text{ev}|_{\text{PS} \& \text{Vtx} \& \text{Vtx}_z}}} \frac{dN|_{\text{PS} \& \text{Vtx} \& \text{Vtx}_z}}{dp_T} \times \frac{r^{\text{Data}}}{\epsilon_{\text{Vtx}}^{\text{MC}}}, \quad (7.5)$$

where $r^{\text{Data}} = (N_{\text{ev}|_{\text{PS}}} - N_{\text{ev}|_{\text{PS} \& \text{Vtx}}}) / N_{\text{ev}|_{\text{PS} \& \text{Vtx}}}$. Table 7.2 summarizes the values obtained for the correction factors along with the total correction $f_{\text{SL}} = 1 - \frac{r^{\text{Data}}}{\epsilon_{\text{Vtx}}^{\text{MC}}}$. The systematic uncertainty on the correction is obtained by replacing the MC sample with data taken with ZDC-only trigger. As a result, one obtains 3.1% difference with respect to the nominal value. To be conservative, a symmetric uncertainty of $\pm 3.1\%$ is quoted. In turn, the MB results have been normalized to the total number of NSD events using a correction which amounts to $(3.6 \pm 3.1)\%$.

Regarding the results that are obtained in multiplicity classes, the normalization were performed to the visible (triggered) cross section correcting for the vertex reconstruction efficiency. The quoted corrections have to be extracted in each V0A multiplicity class. The dN/dp_T results are scaled by a factor of $N_{\text{ev}|_{\text{PS} \& \text{Vtx}}} / N_{\text{ev}|_{\text{PS}}}$. Table 7.3 summarizes the applied

Analyses	Normalization correction factors in V0A classes						
	0 – 5%	5 – 10%	10 – 20%	20 – 40%	40 – 60%	60 – 80%	80 – 100%
ITS+TPC+TOF	1	1	1	1	1.000	0.998	0.967
TPC rel. rise, HMPID	1	1	1	1	0.999	0.997	0.962

Table 7.3: Multiplicity-dependent normalization correction factors calculated in V0A multiplicity classes for the low- p_T (ITS, TPC, and TOF) and high- p_T (TPC rel. rise and HMPID) analyses in p–Pb collisions.

correction factors in V0A multiplicity classes for the low- p_T [53] (ITS, TPC, and TOF) and high- p_T [71] (TPC rel. rise and HMPID) analyses. As can be seen, in the current work, these values differ from unity only for the last three V0A multiplicity classes (40 – 60%, 60 – 80%, 80 – 100%), being of the order of around 4% for the lowest V0A multiplicity class (80 – 100%) and negligible for the other multiplicity classes.

7.7 Yield extraction at high p_T

After the determination of all the corrections in the relativistic rise analysis, the corrected invariant yields can be calculated from the corrected particle fractions using the following relations:

$$\frac{d^2 N_{\text{ch}}}{dp_T d\eta} \propto \frac{1}{\epsilon_{\text{ch}}} \times Y_{\text{ch}} , \quad (7.6)$$

$$\frac{d^2 N_{\pi/K/p}}{dp_T d\eta} \propto \frac{1}{\epsilon_{\pi/K/p}} \times Y_{\pi/K/p} , \quad (7.7)$$

where $\epsilon_{\pi/K/p}$ (ϵ_{ch}) and $Y_{\pi/K/p}$ (Y_{ch}) are the acceptance corrected tracking efficiency and the number of observed particles for the identified (unidentified) analysis, respectively. The yields $d^2 N_{\pi/K/p}/dp_T d\eta$ can be derived by simply dividing Eq. (7.7) by Eq. (7.6) where the p_T -dependent particle fraction $f_{\pi/K/p}(p_T) \equiv f_s(p_T) := Y_{\pi/K/p}/Y_{\text{ch}}$ is directly used:

$$\frac{d^2 N_{\pi/K/p}}{dp_T d\eta} = \frac{d^2 N_{\text{ch}}}{dp_T d\eta} \times \frac{\epsilon_{\text{ch}}}{\epsilon_{\pi/K/p}} \times f_{\pi/K/p}(p_T) . \quad (7.8)$$

It is straightforward to obtain, for example, the corrected pion spectrum from the particle fraction for pions using the corrected transverse momentum spectrum of inclusive charged particles and correcting for the relative efficiencies. Taking into account all the applied corrections, and indicating them explicitly, the normalized invariant yield of a particle species s , which can be π^\pm , K^\pm or $p(\bar{p})$, reads as follows:

$$\begin{aligned} \frac{1}{N_{\text{ev}}} \frac{1}{2\pi p_T} \frac{d^2 N_s}{dy dp_T} &= \frac{1}{N_{\text{ev}|_{\text{PS \& vtx \& Vtx}_z}}} \times \frac{f_{\text{SL}} \times f_{\text{prim},s}(p_T) \times f_{\pi-\mu}(p_T) \times f_{\text{INEL/NSD}}}{\epsilon_s(p_T)} \\ &\times \epsilon_{\text{trig}} \times \frac{1}{2\pi p_T} \frac{\Delta N(\Delta p_T)}{\Delta y_s(p_T, \eta) \Delta p_T} \times f_s(p_T) \times J_{\eta/y} . \end{aligned} \quad (7.9)$$

Here, $N_s = N_s(p_T, y, N_{\text{mult}}^{\text{V0A}})_{\text{ev}|_{\text{PS} \& \text{vtx} \& \text{Vtxz}}}$ is the corrected yield for a particle species s with a given transverse momentum p_T and rapidity y in a given event class after trigger and vertex selection and, alternatively, in a given multiplicity class, $N_{\text{mult}}^{\text{V0A}}$, chosen by the V0A forward multiplicity estimator. Note that $N_{\text{ev}|_{\text{PS}}}$ implicitly may contain additional pre-trigger selections such as removal of events tagged as pile-up.

During the analysis, all variables are binned into discrete intervals which define the granularity/resolution of the measurement. The particle yield N_s is extracted from a given number of (INEL or NSD) events N_{ev} . The total number of inclusive charged tracks $\Delta N(\Delta p_T)$ in the considered data sample are extracted at a given p_T with bin width Δp_T and in a given rapidity (defined by Eq. 7.2) with bin with $\Delta y_s(p_T, \eta)$, whereas $f_s(p_T)$ denotes the p_T -dependent particle fraction for a given species s . The quantities $f_{\text{prim},s}(p_T)$ and $f_{\pi-\mu}(p_T)$ are, respectively, the fraction of primary particles and the fraction of pions (π^\pm) in the “ $\pi^\pm + \mu^\pm$ ” sample. The correction factor $\epsilon_s(p_T)$ refers to the inverse of the relative efficiency correction, $\epsilon_{\text{ch}}/\epsilon_{\pi/K/p}$, where the part related to the inclusive unidentified analysis ϵ_{ch} is composed from the following components: overall tracking efficiency correction, secondary correction, p_T resolution correction. In case of p–Pb collisions an additional correction factor is applied to account for the modified acceptance due to the asymmetry of the collision. The ϵ_{trig} denotes the trigger efficiency whenever it is available. $J_{\eta/y}$ is the Jacobian to convert from pseudorapidity η to rapidity y . f_{SL} is the signal loss correction, whereas $f_{\text{INEL/NSD}}$ is the normalization factor to INEL or NSD events.

7.8 Estimation of systematic uncertainties

In this section, the systematic uncertainties related to the applied corrections to particle fractions are discussed. The systematic uncertainties mainly consist of two components: the first is due to the event and track selection, whereas the second one is due to the PID. The first component was obtained in the analysis of unidentified charged particles. For INEL pp collisions at $\sqrt{s} = 7$ and $\sqrt{s} = 13$ TeV, the uncertainties were taken respectively from Refs. [238] and [246]. For $\sqrt{s_{\text{NN}}} = 5.02$ TeV p–Pb collisions, there are no unidentified measurements in the rapidity window reported in this work ($-0.5 < \eta < 0$). However, it has been shown that the uncertainty exhibits negligible dependence on η and charged particle multiplicity for the p_T range attained by the relativistic rise analysis [16]. In turn, the systematic uncertainties reported in Ref. [119] have been assigned to the re-measured charged hadron p_T spectrum for all the V0A multiplicity classes. The second component was measured following the procedure described in Ref. [111] where the largest contribution is related to the uncertainties in the parameterization of the Bethe–Bloch and (relative) resolution curves used to constrain the multi-Gaussian fits for yield extraction. The estimation of this component is extensively discussed in the following.

In this work, all contribution of systematic uncertainties are treated as symmetric and

assumed to be Gaussian in nature, with their magnitudes corresponding to the standard deviation. In some cases, maximal deviations are considered instead of standard deviations. In the unidentified charged analysis the uncertainties are mostly asymmetric, however the size of asymmetry is small compared to the magnitude of the uncertainty; therefore it has been symmetrized by using the larger deviation leading to the effect that the overall uncertainty estimate is rather conservative. Generally, for the combination of all contributions they have been added quadratically assuming the uncertainties are uncorrelated. Correlated systematic uncertainties across V0A multiplicity classes have been evaluated for the multiplicity-dependent identified measurement in the high- p_T analysis in case of p–Pb collisions.

7.8.1 Uncertainty due to incomplete knowledge of the Bethe–Bloch and resolution curves

The uncertainty in the determination of particle fractions is mainly due to the incomplete knowledge of the Bethe–Bloch $\langle dE/dx \rangle$ and the associated resolution $\sigma_{dE/dx}$ curves used to constrain the multi-Gaussian fits (see Section 6.8). There are different components of this systematic uncertainty. One of the sources can be related to calibration effects such that the $\langle dE/dx \rangle$ does not depend on $\beta\gamma$ alone. Other sources arise, on the one hand, from the incomplete description of the data by the used parametrization and, on the other hand, from the statistical precision of the external PID datasets.

Indeed, a large fraction of the systematic uncertainty on the particle fractions is primarily due to misidentification, i.e. one identifies a pion as a kaon. As a consequence, these uncertainties are absolute in their nature, i.e., one misidentifies a certain amount of kaons which is typically composed from different fractions of kaons and pions. The main possibility for misidentification is that one can easily misassign a kaon as a pion or as a (anti)proton and vice versa. At the same time, it is rather difficult to wrongly assign a pion as a proton. This observation is based on the nature of the dE/dx distribution and implies that one expects the absolute systematic uncertainty on kaons to be the largest, corresponding roughly to $\sigma_{K^\pm}^2 \sim \sigma_{\pi^\pm}^2 + \sigma_{p(\bar{p})}^2$.

That being said, the systematic uncertainties should capture two main components: the signal extraction itself for a given set of parameters, and the variation of the signal as $\langle dE/dx \rangle$ and $\sigma_{dE/dx}$ are varied within a reasonable range.

To evaluate the uncertainty due to these effects, the relative variations of the measured average values $\langle dE/dx \rangle$ and the corresponding widths $\sigma_{dE/dx}$ (obtained from the analysis of the external pion, proton, and electron samples) with respect to the final fits as a function of $\beta\gamma$ and $\langle dE/dx \rangle$ are calculated, respectively. Figure 7.6 shows these variations, respectively, for the $\sigma_{dE/dx}$ (Fig. 7.6a) and the Bethe–Bloch curves (Fig. 7.6b) integrated for the full data sample in the four $|\eta|$ slices and in case of p–Pb collisions, additionally for all V0A multiplic-

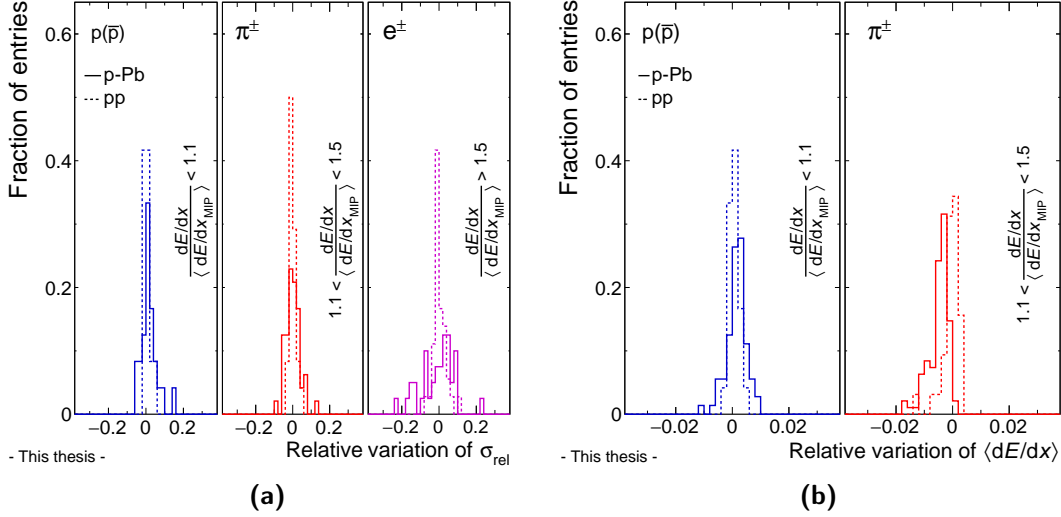


Figure 7.6: Relative variation of (a) the $\sigma_{dE/dx}$ and (b) the Bethe–Bloch $\langle dE/dx \rangle$ parametrizations with respect to the measured values in different $dE/dx / \langle dE/dx_{MIP} \rangle$ intervals. Solid and dashed lines indicate the variations for $\sqrt{s} = 7$ TeV pp and $\sqrt{s_{NN}} = 5.02$ TeV p–Pb data. Distributions were obtained using the full data sample integrated for the four $|\eta|$ slices and for all multiplicity classes. See the text for details.

ity classes. The relative variations are presented in different $dE/dx / \langle dE/dx_{MIP} \rangle$ intervals: $dE/dx / \langle dE/dx_{MIP} \rangle < 1.1$, $1.1 < dE/dx / \langle dE/dx_{MIP} \rangle < 1.5$, $dE/dx / \langle dE/dx_{MIP} \rangle > 1.5$, including in these ranges the samples of protons, pions, and electrons, respectively. In a given interval of $dE/dx / \langle dE/dx_{MIP} \rangle$, the standard deviation of the distribution was taken as an estimate of the systematic uncertainty associated with the extraction of the widths.

In order to account for the statistical limitation in the fits made to the external PID data, an additional source was taken into account estimated from the covariance matrix of the performed fit. The error propagation was done separately for each narrow η_{lab} intervals. For the Bethe–Bloch curves, the size of this contribution stays at around the per mille level while for resolution curves it is found to be negligible. This second contribution was added quadratically to the previously discussed contribution and was assigned as the total systematic uncertainty on the parametrization of the corresponding curve. These uncertainties are shown as shaded bands in Fig. 7.7 where cases for both short (small η_{lab}) and long (large η_{lab}) tracks are indicated for p–Pb data, as an example. It is worth noticing that the data points are covered by the relative systematic uncertainty bands; apart from some outliers which have large statistical uncertainties.

The propagation of the uncertainties on the Bethe–Bloch and resolution curves to the particle fractions is done by refitting the dE/dx distributions by randomly varying the constrained fit parameters, $\langle dE/dx \rangle$ and $\sigma_{dE/dx}$, within the uncertainty for the parametrizations, assuming uniform variation within $\pm 1\sigma$ around the nominal value. For each p_T bin, η bin, and — in case of p–Pb data — V0A multiplicity class, all the $\langle dE/dx \rangle$ and $\sigma_{dE/dx}$ values were randomly varied and refitted 1000 times. The resulting distributions for a given p_T bin

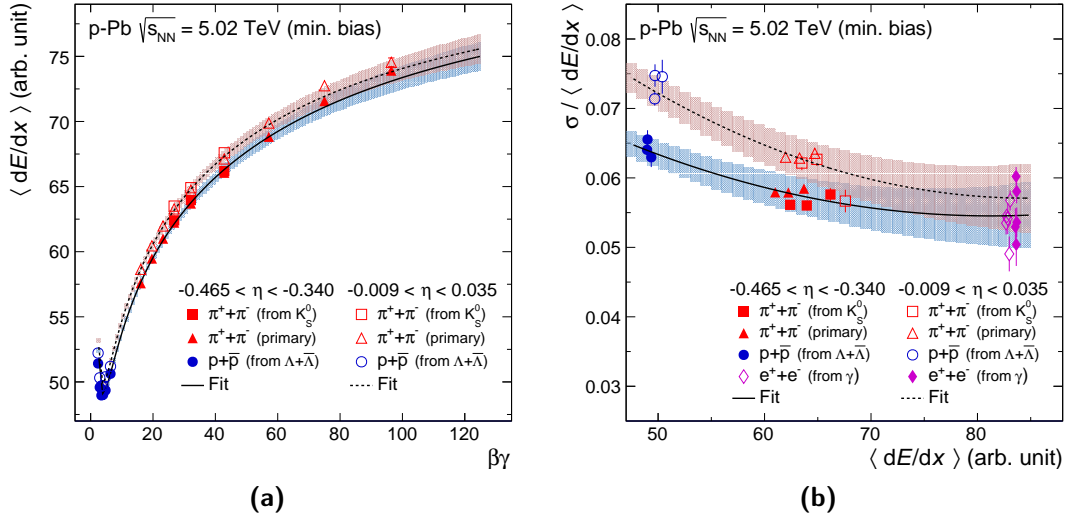


Figure 7.7: (a) Bethe–Bloch and (b) relative resolution curves obtained in MB p–Pb collision at $\sqrt{s_{NN}} = 5.02$ TeV. Bethe–Bloch curves are shown in regions relevant for the selection of charged pions, kaons, and (anti)protons in the analysis. Shaded bands represent the systematic uncertainty of the parametrizations. Figures are reproduced from Ref. [223].

($4.5 - 5$ GeV/ c) are exemplified for $\sqrt{s} = 7$ TeV pp and for the 0 – 5% V0A p–Pb data, and they are shown in Fig. 7.8a. The systematic uncertainties assigned to the particle fractions are the standard deviation of the related distributions. The procedure is repeated for the four considered η intervals, and in a given p_T bin, the maximum of the standard deviations is taken as uncertainty. Although this choice is somewhat conservative, it is based on the assumption that the precision of the curves is similar among the different η intervals, knowing that the effect worsens for some cases due to lower resolution/separation. As already mentioned earlier, the assigned uncertainties to the particle fractions are absolute in magnitude which matters for the case of kaons at most. At high p_T , the variation becomes dominated by statistical fluctuations due to the limited amount of data. However, the particle fractions are nearly constant in that region, and so is the separation, a constant absolute systematic uncertainty is assigned for $p_T > 7 - 8$ GeV/ c , depending on the studied datasets.

The estimated uncertainty values calculated in different p_T bins shows that kaons and (anti)protons have largest uncertainties around $p_T \sim 2$ GeV/ c , where the dE/dx curves cross each other, and they decrease towards higher p_T following the observed trend of the particle fractions. At higher p_T , the kaon and (anti)proton uncertainties were smoothed, due to statistical fluctuations, using a constant fit motivated by the p_T -independent nature of particle fractions in that p_T region; it resulted the uncertainties to remain under $\lesssim 10\%$ and $\lesssim 20\%$, respectively for π^\pm and $p(\bar{p})$. It is worth noting that the observations for MB $\sqrt{s} = 7$ TeV pp data (and also for $\sqrt{s} = 13$ TeV pp data not shown here) follow the same behavior as those obtained for the multiplicity-dependent p–Pb analysis at $\sqrt{s_{NN}} = 5.02$ TeV.

The systematic uncertainties on the K/π and p/π particle ratios are evaluated essentially

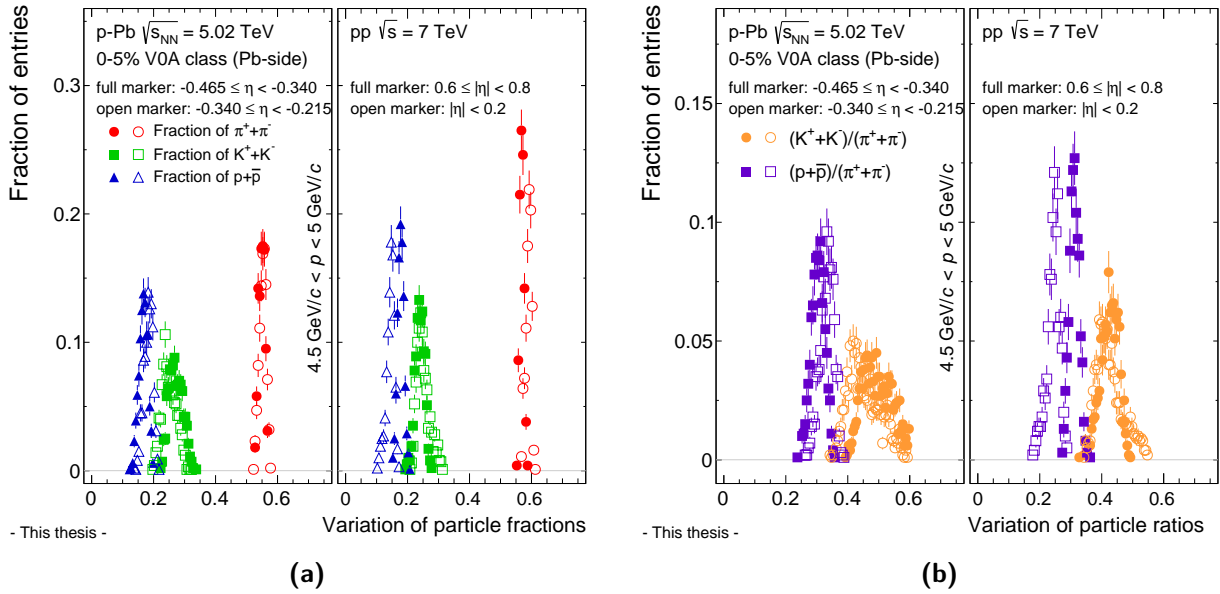


Figure 7.8: Variation of (a) extracted particle fractions of pions, kaons, and (anti)protons, and (b) K/π , p/π particle ratios in case of random variation of $\langle dE/dx \rangle$ and $\sigma_{dE/dx}$. Results are reported for MB pp and 0 – 5% (V0A multiplicity class) p–Pb collisions, respectively.

in the same manner as was done in the case of particle fractions. However, in this case, particle ratios are directly extracted from the fit procedure to guarantee the correct treatment of those component of uncertainties which are largely correlated between the different species. Therefore, in the multi-Gaussian fits—which are used to extract the raw particle yield for a given species—the ratio of yields are considered as free fit parameters. The results of the procedure are shown in Fig. 7.8b. Then, the systematic uncertainty on the parametrizations is propagated to the ratios by varying the constrained parameters, $\langle dE/dx \rangle$ and $\sigma_{dE/dx}$, within the ranges discussed above. The resulting uncertainties on the ratios are significantly larger for the K/π than for the p/π .

The systematic uncertainty of the secondary correction for each species is propagated to the ratios with the assumption that the applied correction factors of the two considered species are completely uncorrelated. As a matter of fact, since the sources of the secondary particles can be different (pions from K_S^0 and protons from Λ decays), the related uncertainties are at least partially correlated. Therefore, treating them as fully uncorrelated is a more conservative estimate.

Figure 7.9a shows the corrected π^\pm , K^\pm , and $p(\bar{p})$ particle fractions as a function of p_T for different V0A multiplicity classes; the open boxes represent the PID systematic uncertainties. Since the applied corrections have only moderate p_T dependence at low p_T and show constant behavior at higher p_T , the corrected particle fractions experience an approximately constant shift in their magnitude with respect to the uncorrected results in all p_T bins. For the lowest multiplicity bin (80 – 100% V0A class) statistical fluctuations start to dominate on the fractions for $p_T \gtrsim 10$ GeV/ c , nevertheless the argument on their p_T evolution remains

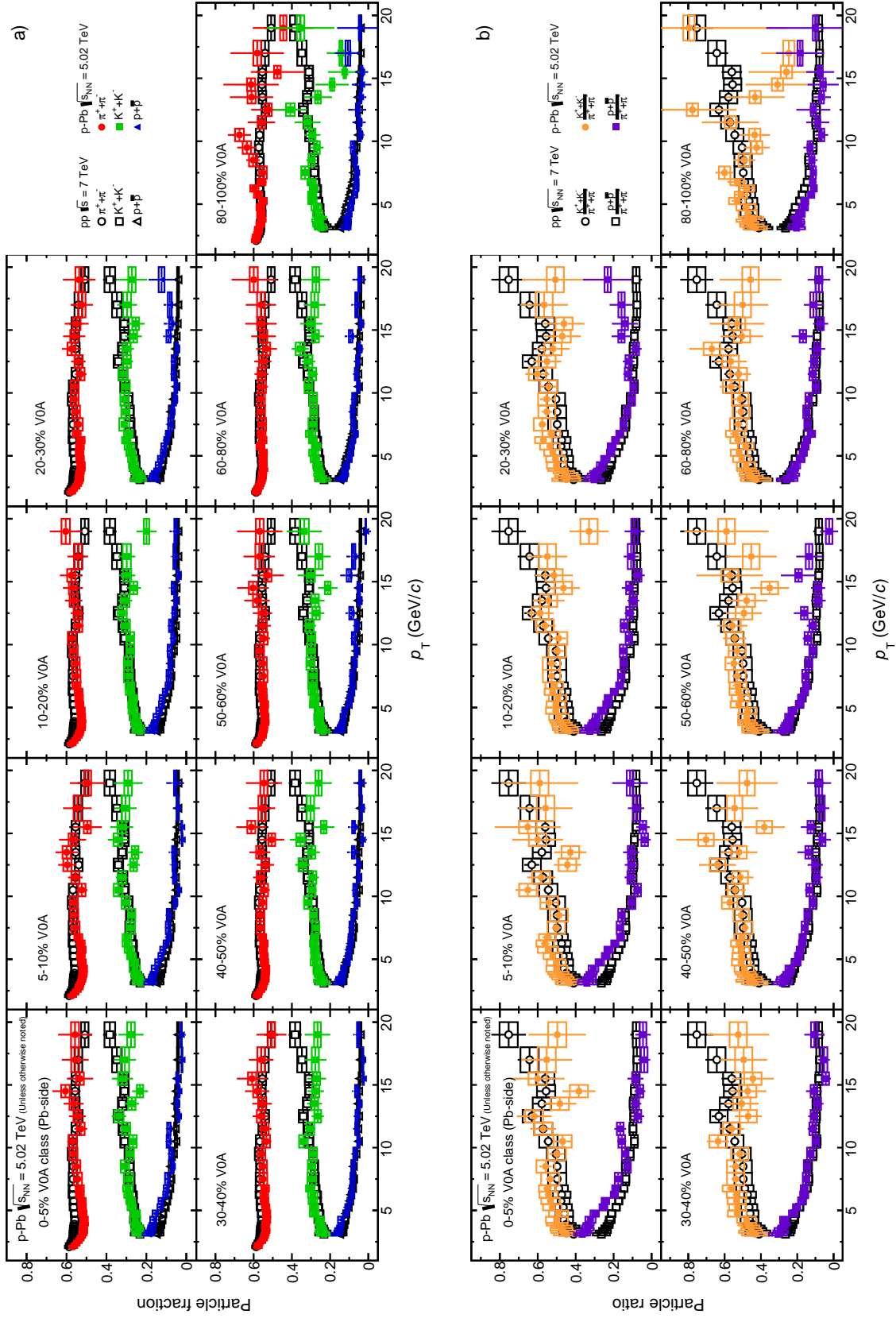


Figure 7.9: (a) Corrected pion, kaon, and (anti)proton particle fractions and (b) corrected kaon-to-pion and proton-to-pion ratios in minimum bias pp collisions at $\sqrt{s} = 7$ TeV and in p-Pb collisions at $\sqrt{s_{NN}} = 5.02$ TeV in V0A multiplicity classes. Systematic uncertainties obtained from the PID procedure are shown as open boxes around the central points, whereas vertical error bars show statistical uncertainties. Figures are reproduced from Ref. [223].

valid. In addition, MB pp results are superimposed over the multiplicity-dependent data points, which allows us to make direct comparisons on the level of particle composition in different collision systems. It indicates that the absolute yields of particle abundances have an evolution with multiplicity, being present for all particle species for $p_T \lesssim 6-7 \text{ GeV}/c$, whereas above that range they tend to show the same behavior and agree within uncertainties. Figure 7.9b shows the corrected kaon and (anti)proton production yields normalized to that of pions, i.e. the K/π and p/π particle ratios, together with the pp results and with the inclusion of the propagated PID systematic uncertainties. Such a plot shows a relative comparison to the pion particle fractions and essentially tells us that kaons have no evolution with multiplicity in this respect in the full reported p_T interval while protons experience a change below $p_T \sim 6-7 \text{ GeV}/c$. These effects will be further investigated with the help of the p_T spectra and the p_T -dependent particle ratios for a given collision system. The difference between pp and p-Pb collisions will be reviewed via the discussion of the nuclear modification factors in Chapter 9.

7.8.2 Multiplicity-dependent uncertainties in the p-Pb analysis

The systematic uncertainties of the p-Pb results, discussed in the preceding sections, are strongly correlated across different multiplicity classes. These type of uncertainties are independent of multiplicity meaning that they may produce identical fractional shifts in all multiplicity classes. In contrast, there exists a multiplicity-dependent part of the uncertainties which refers to deviations that result in different fractional shifts in all multiplicity classes and, this way, they are treated as uncorrelated among different multiplicity classes. In order to estimate them, the minimum bias result was taken as a reference for the calculations. Moreover, only the PID component of the uncertainties is taken into account, because those related to event and track selections are fully correlated and independent of multiplicity, as shown in Ref. [16].

To estimate whether a given uncertainty changes with multiplicity, one has to compare the fractional deviation observed in each event multiplicity class to that observed in the minimum bias sample. In doing so, for each systematic variation of a measurement of dE/dx signal S , the following quantity has to be computed:

$$R_\delta = \frac{S_\delta^i/S^i}{S_\delta^{\text{MB}}/S^{\text{MB}}}, \quad (7.10)$$

where S^i is the measured signal in a given event multiplicity class i , S^{MB} is the measured signal in the minimum bias sample, and the subscript δ stands for the systematic variation being studied. The minimum bias case were constructed by integrating the sample measured in multiplicity bins in order to have an equivalent sample of 0 – 100% V0A multiplicity class. The departure of S_δ from unity quantify how the fractional deviations in a certain

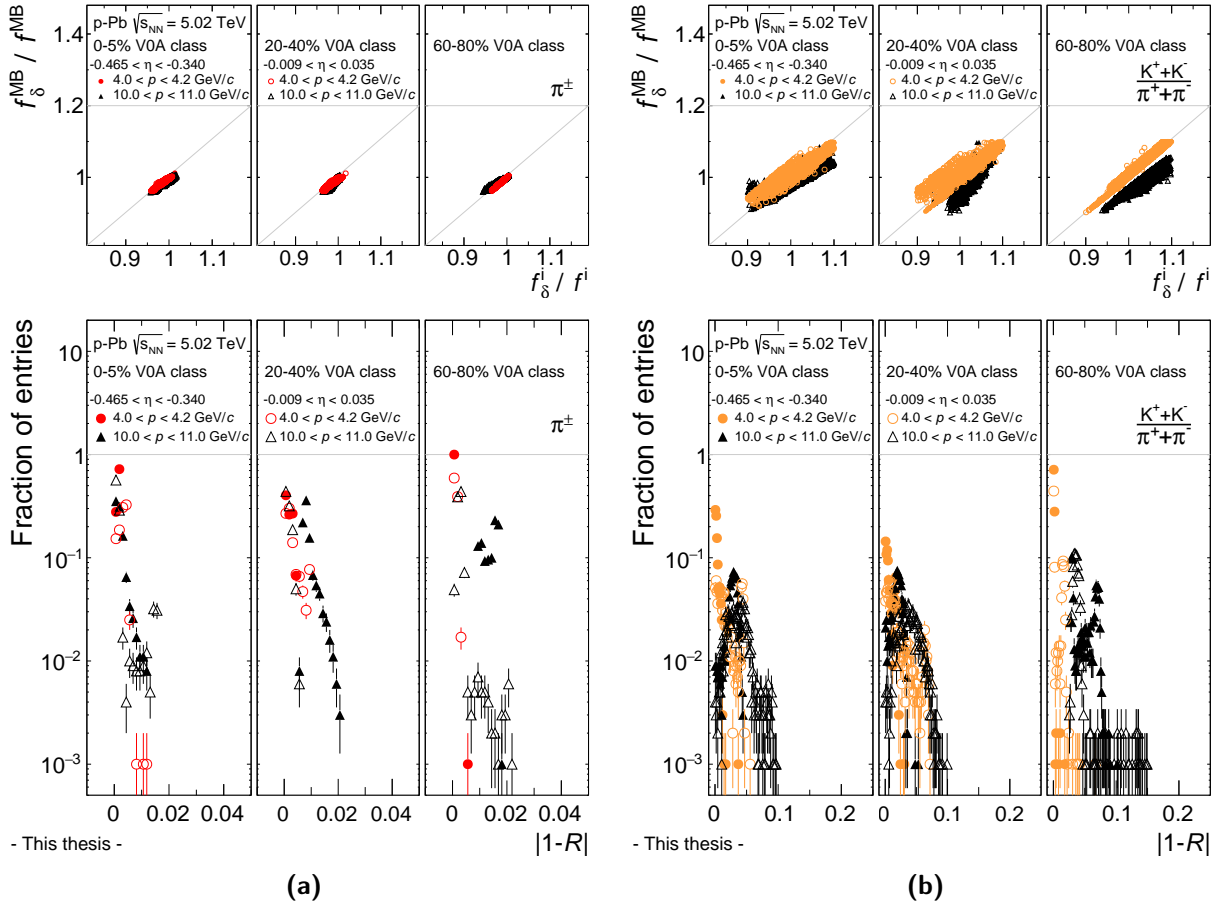


Figure 7.10: Auxiliary distributions used for the estimation of multiplicity-dependent systematic uncertainties due to multiplicity variation of the dE/dx signal measured in p–Pb collisions at $\sqrt{s_{\text{NN}}} = 5.02$ TeV. Examples of distributions, differentially in p_T and η bins, are shown for (a) π^\pm particle fraction and (b) K/π particle ratio. See the text for details.

multiplicity event class i differ from those in the minimum bias sample: if $S_\delta = 1$ then, by construction, the deviations are identical. Therefore, by taking this ratio, effects which are correlated between multiplicity intervals cancel. In this case, the uncorrelated uncertainty due to systematic source (being under variation) δ is:

$$\left(\frac{\Delta S^i}{S^i}\right)_\delta = |R_\delta - 1|. \quad (7.11)$$

The signal S in the relativistic rise analysis corresponds to the extracted (p_T -dependent) particle fraction f of a given particle species. Consequently, f_δ^i and f_δ^{MB} will refer to the variation of the given particle fraction measured in a given multiplicity class i and in the minimum bias sample, respectively. Following the procedure for the estimation of the PID systematic uncertainties, f_δ^i and f_δ^{MB} are determined from multi-Gaussian fits to dE/dx distributions, where in the fit procedure, both $\langle dE/dx \rangle$ and $\sigma/\langle dE/dx \rangle$ are varied within a given range. The nominators of f_δ^i/f^i of Eq. (7.10) are shown in the upper panel of Fig. 7.10a correlated with its denominators $f_\delta^{\text{MB}}/f^{\text{MB}}$ in case of pions for V0A multiplicity classes 0–5%

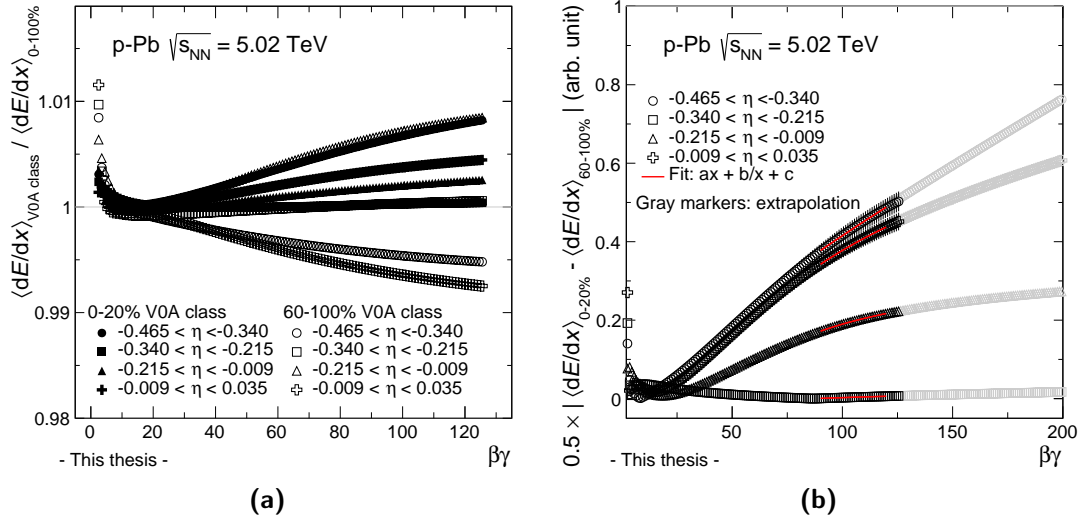


Figure 7.11: Auxiliary distributions used for the estimation of multiplicity-dependent systematic uncertainties due to multiplicity variation of the $\langle dE/dx \rangle$ parametrization as a function of $\beta\gamma$: panel (a) shows the variation at low and high multiplicities in different pseudorapidity slices, while panel (b) shows the estimated uncertainties and their extrapolations into the high $\beta\gamma$ regions.

(left), 20 – 30% (middle), and 60 – 80% (right). It should be noted that similar distributions were obtained for kaons and (anti)protons. The correlations determined differentially in p_T and in η , and they are shown for two particular p_T and η bins as examples. The diagonal part of the correlation matrix is the common part, whereas the off-diagonal components are uncommon, meaning that if a correlation coefficient is zero (non-zero) then there is no common (uncommon) part. The lower panel of Fig. 7.10a shows the distribution of the calculated $|1 - R|$ quantity based on Eq. (7.11). Following the same procedure, the same quantities have been calculated for the case of K/π and p/π particles ratios. Figure 7.10b reports the distributions for K/π ; similar distributions were obtained for the p/π ratio.

There is an additional component to $|R_\delta - 1|$ one has to deal with, which is related to the multiplicity dependence of the parametrization of the Bethe–Bloch curve. This contribution can be estimated by comparing the parametrizations of $\langle dE/dx \rangle$ for low (0 – 20%) and high (60 – 100%) V0A multiplicity classes in each pseudorapidity interval. In this study, the choice of the larger width of the V0A class is entirely due to statistics limitation. In Fig. 7.11a such a comparison is shown for the four η slices relative to that of the default minimum bias case (V0A 0 – 100%)—which was used for the parametrizations (see Section 6.7). It is worth noticing the slow monotonic increase of the $\langle dE/dx \rangle_{V0A\ class}$ to $\langle dE/dx \rangle_{0-100\%}$ ratio towards larger $\beta\gamma$. The estimation of this component follows the same procedure described above, where for the fit variation only the Gaussian parameter related to $\langle dE/dx \rangle$ is taken into account. To be conservative, half of the absolute difference $|\langle dE/dx \rangle_{0-20\%} - \langle dE/dx \rangle_{60-100\%}|/2$ is used as variation range. As shown in Fig. 7.11b, for higher $\beta\gamma$ an extrapolated value is considered.

After performing the variations for particle fractions and for particle ratios, the standard deviation of the $|1 - R|$ distribution is taken as an estimate of the uncorrelated uncertainty. The results over all η bins were averaged, and smoothed for $p_T > 6 \text{ GeV}/c$ due to statistical fluctuations. The total uncorrelated uncertainty is the quadratic sum of the two discussed components. For pions, the contribution related to the Bethe–Bloch parametrization defines an upper boundary of that of the particle fraction and the overall uncertainty (which is their quadratic sum) stays below 0.5% in the full p_T range. For kaons, taking the lowest p_T bin, the overall uncertainty reaches around 6% and decreases to around 2% for $p_T \geq 6 \text{ GeV}/c$. The uncertainty for protons show similar behavior as that for kaons, and it is around 3–4% at higher p_T , except for the 0–5% V0A event class where they tend to increase up to 7–8% at $p_T = 20 \text{ GeV}/c$ due to the larger uncertainty on the Bethe–Bloch parametrization in that region. Regarding the K/π and p/π particle ratios, their uncertainties follow the same behavior than that of K^\pm and $p(\bar{p})$, and reach, respectively, $\sim 3 - 4\%$ and $\sim 4 - 5\%$ towards higher p_T . To account for any residual multiplicity-dependent effect, an additional 2% added quadratically to the total uncertainties.

7.8.3 Remaining components of the uncertainties

Apart from the main components of uncertainties related to the signal determination in the PID procedure, there are other sources which come into play and have to be taken into account as remaining but also sizeable contributions. These are as follows:

- Uncertainty due to muon (μ^\pm) contamination: as discussed previously, the correction due to muon contamination (in the pion yield) was applied in a way that the electron yield is subtracted from pion yield—this was based on the assumption that a similar amount of muons are present below the pion peak. The uncertainty is assigned in a conservative way meaning that it is set to the number of electrons; it is less than 0.4–0.5% for pp and p–Pb data, being no p_T and multiplicity dependent to a large extent.
- Uncertainty due to feed-down correction: as a conservative estimate, the half of the applied correction was assigned. It is below 0.2% for pions independent of p_T , collision system and multiplicity. For protons, in the p–Pb data sample it is around 3% in the first p_T bin and decreases to 0.8% up to $p_T = 6 \text{ GeV}/c$ and it remains constant from that p_T onward. For pp data, the uncertainty is around 1% for the full p_T range.

There are additional sources to the total uncertainties due to normalization of different observables both in pp and p–Pb measurements. The normalization to INEL events in pp at $\sqrt{s} = 7$ and $\sqrt{s} = 13 \text{ TeV}$ carries $\pm 3.6\%$ and $\pm 2.6\%$ systematic uncertainties, respectively. The uncertainty due to normalization to NSD events in p–Pb measurement at $\sqrt{s_{NN}} = 5.02 \text{ TeV}$ amounts to $\pm 3.1\%$. The global normalization uncertainties are assumed to be uncorrelated and added quadratically to the total uncertainties.

Based on earlier studies, the relativistic rise method has been benchmarked using MC

Collision system, $\sqrt{s_{NN}}$, event class (optional)	$\pi^+ + \pi^-$		$K^+ + K^-$		$p + \bar{p}$		K/π		p/π	
	p_T (GeV/c)									
pp, $\sqrt{s} = 7$ TeV	8%		21%	11%	25%	17%	18%	10%	17%	20%
pp, $\sqrt{s} = 13$ TeV (Prel.)	8%		17%	11%	19%	15%	16%	10%	17%	16%
p-Pb, $\sqrt{s_{NN}} = 5.02$ TeV										
0–5% V0A class	5%		17%	9%	16%	14%	16%	11%	13%	12%
20–40% V0A class	5%		16%	8%	17%	14%	19%	9%	17%	19%
60–80% V0A class	5%		16%	8%	20%	14%	21%	9%	23%	19%

Table 7.4: Total systematic uncertainties estimated in pp and p-Pb collisions respectively at $\sqrt{s} = 7$ [71] and $\sqrt{s} = 13$ TeV (Preliminary), and at $\sqrt{s_{NN}} = 5.02$ TeV [71]. The values are reported for low and high p_T .

simulations. In these closure tests the reconstructed output was compared with the generated input, and it resulted in a less than 1% systematic deviation for all particle yields. Furthermore, for all analyses, the applied corrections were extracted by a certain type of MC event generator. In order to account for the different choice of event generators an additional $\pm 1\%$ uncertainty summed quadratically to the total systematic uncertainty.

7.8.4 Total systematic uncertainties

The total systematic uncertainties are summarized in Tab. 7.4. Values are reported for two specific (low and high) p_T bins for all the studied particle species and particle ratios.

For pions, the largest contribution is related to the event and track selection (and the associated common corrections), and it amounts to around 7% in pp collisions, independent of p_T and collision energy. For p-Pb collisions, the same component is independent of multiplicity class, and it is around 3.3–3.6%, depending on p_T . At the same time, since, the energy loss band for pions is well separated from all other particle species, their uncertainty due to signal determination is rather small, being $\sim 1.5 - 2\%$, independent of p_T , collision system and multiplicity. The resulted total uncertainties are 8% and 5% for pp and p-Pb collisions.

For kaons and (anti)protons, in contrast to pions, the dominant source of systematic uncertainties arise from the PID procedure. Generally, the largest uncertainties are estimated in in the range of $p_T = 2 - 4$ GeV/c (for kaons) and $p_T = 3 - 5$ GeV/c (for (anti)protons), and it is related to effects caused around the dE/dx crossing region where the separation power becomes small. Going towards higher p_T these uncertainties decrease. In p-Pb, the uncertainties for kaons increase with multiplicity, while for protons the multiplicity dependence is the opposite. This variation mainly reflects the changes in the particle ratios with p_T and multiplicity. Particle ratios (K/π , p/π) at $p_T \sim 2 - 3$ GeV/c carry somewhat larger uncertainties than those reported for K^\pm and $p(\bar{p})$, and the uncertainties go slightly beyond 20% at low multiplicities.

Besides the TPC relativistic rise technique, there are also exists other analysis techniques that rely on different detectors. These analyses can provide precise measurement results, restricted only to low and intermediate p_T . The combination of the different analysis techniques will help us to measure particle production in a broad p_T range, and to keep the systematic uncertainties associated to PID as low as possible in the overlapping p_T range by the different measurements.

7.9 Combination of p_T -spectra from different analyses

The final p_T spectra are reported in the full p_T range measured from 0.1/0.2/0.3 GeV/ c to 20 GeV/ c for $\pi^\pm/K^\pm/p(\bar{p})$, respectively. In order to measure the production of primary charged pions, kaons, (anti)protons over a wide range of p_T , several independent analyses with distinct PID techniques are combined. Each of these analyses focus on a sub-range of the total p_T range in the same (pseudo)rapidity window to optimize the signal extraction. An extensive description for all analysis techniques applied earlier measurements during LHC Run 1 are explained in Refs. [51, 125, 247, 248]. For the analysis of the measurement performed in pp collisions at $\sqrt{s} = 13$ TeV during LHC Run 2, on the top of these techniques the so-called ‘‘TPC Multi-Template Fit’’ method is incorporated [249].

Both for pp and p–Pb collisions, the low- p_T measurements (ITS-sa, TPC, TOF, and HMPID) were incorporated together with the TPC relativistic rise measurement. The p_T -differential yields $d^2N/dp_T dy$ obtained from different analyses are combined together using a weighted mean procedure. This has the advantage of reduced systematic uncertainties of the combined results. In this procedure, the total uncommon systematic uncertainties among the various analyses are used as weights. Since the uncertainties due to normalization and global tracking are common to all the analyses, they were added quadratically to each other and to the uncertainty attributed to the distinct PID methods. It is noteworthy that in the p–Pb analysis both the multiplicity correlated and uncorrelated systematic uncertainties were determined with the present procedure. The multiplicity uncorrelated uncertainties above $p_T = 2 - 3$ GeV/ c , for pions, kaons, and (anti)protons are only taken from the relativistic rise analysis since the components relevant to the low- p_T analysis are overall smaller, and those for the HMPID analysis were found to be negligible. In those p_T regions, where the different analyses overlap statistical errors are generally much smaller than the systematic uncertainties, therefore they are considered to be negligible and not included in the weights.

Taking two independent analyses, A and B, their combined p_T -differential production yields $d^2N^{A+B}/dp_T dy$ for a given particle species can be obtained as follows:

$$\frac{d^2N^{A+B}}{dp_T dy} = (w_A + w_B)^{-1} \times \left(\frac{1}{\sigma_A^2} \frac{d^2N^A}{dp_T dy} + \frac{1}{\sigma_B^2} \frac{d^2N^B}{dp_T dy} \right), \quad (7.12)$$

$$\sigma^{A+B} = (w_A + w_B)^{-1} \times \sqrt{(\sigma_A^2 w_A^2 + \sigma_B^2 w_B^2)}, \quad (7.13)$$

where $w_{A/B} = 1/\sigma_{A/B}^2$, σ_A and σ_B are the uncorrelated uncertainties from the analyses A and B, respectively; σ_{A+B} is the propagated uncertainty for the sum of the two analyses, and N^{A+B} is the corresponding combined yield. Uncorrelated systematic uncertainties and statistical errors of the individual measurements are propagated accordingly through the weighted-mean procedure to estimate systematic uncertainties and statistical errors of the combined spectra. As a necessary cross check before performing any combination is the verification of the agreement for the ratio of yields between two given analyses, e.g. the low- p_T and the high- p_T analysis. In some cases, due to the different binning between different analysis methods, simple rebinning on some of the individual spectra are applied in the region where they overlap to allow a valid combination.

In general, there is good agreement between the different analyses in all studied collision systems, and they are consistent within their quoted uncorrelated systematic uncertainties. Therefore, they can be safely combined p_T -bin-by- p_T -bin using their appropriate uncertainties as weights as described above. Note that, for $\sqrt{s} = 7$ TeV pp collisions, some outliers are seen for kaons towards higher p_T which is caused by the dedicated analysis using topological kaon identification inside the TPC, the so-called kink analysis. Since this analysis technique was included in the low- p_T results, it was not possible to conclude the present measurement otherwise. Although, the deviation is still covered by the systematic uncertainties, it is worth noting that it corresponds to the largest tension between the presented results.

An important part of the applied method, being as an other crucial cross check, can be seen in Fig. 7.12 where the ratios of individual spectra to the combined spectrum are shown in the p_T range where analyses overlap. Since the p_T binning is different between the low- and high- p_T measurements, linear interpolation is used to obtain the value for the denominator in these ratios. The individual analyses with their respective p_T reach can be read off from the ratios. The gray bands indicate the combined systematic uncertainties obtained from the procedure. The p_T -independent uncertainty due to global tracking—which amounts to 3%—is common to all the analyses and it was added quadratically to the final combined results. This extra component of the uncertainty is marked as solid black lines, hardly visible in Fig. 7.12. For the p-Pb measurement performed in multiplicity classes, the appropriate systematic uncertainty for the combined spectra is also propagated using the same procedure as described above. Since in the measurement there is a multiplicity-uncorrelated component (see Section 7.8.2) of the uncertainty, it is important to mention that in the combination of results always the total (i.e. fully correlated across multiplicity) systematic uncertainty is used. The ratio of individual to combined spectra are shown in panels (b), (d), and (f) of Fig. 7.12 where only the highest multiplicity (0 – 5% V0A, Pb-going side) event class is reported, which has high statistics. Individual analyses show excellent agreement with the combined spectrum for all particle species. Note that similar level of agreement were obtained within the quoted uncertainties for all seven V0A multiplicity classes.

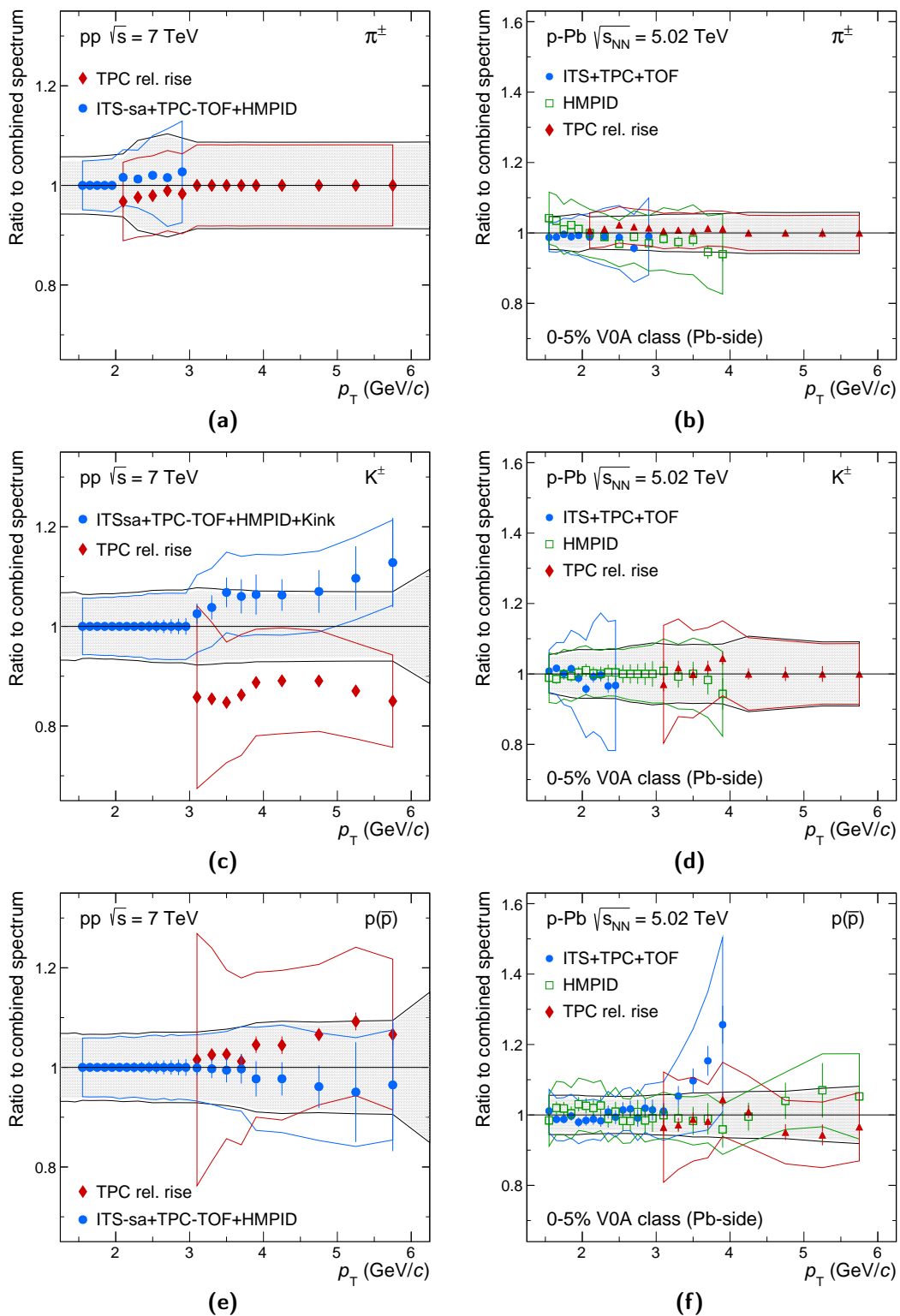


Figure 7.12: Ratio of individual spectra to the combined spectrum as a function of p_T for pions, kaons, (anti)protons respectively shown in the first, second, and third row, measured in pp collision at $\sqrt{s} = 7$ TeV (first column) and in p-Pb collision at $\sqrt{s_{NN}} = 5.02$ TeV in the 0 – 5% V0A class (second column). Statistical errors and systematic uncertainties are shown as vertical error bars and error bands, respectively. Shaded gray band shows the combined uncorrelated uncertainty, while black solid line indicates the final combined uncertainty. Note that only the p_T ranges where individual analyses overlap are shown. See the text for details. Figs. are reproduced from Ref. [223].

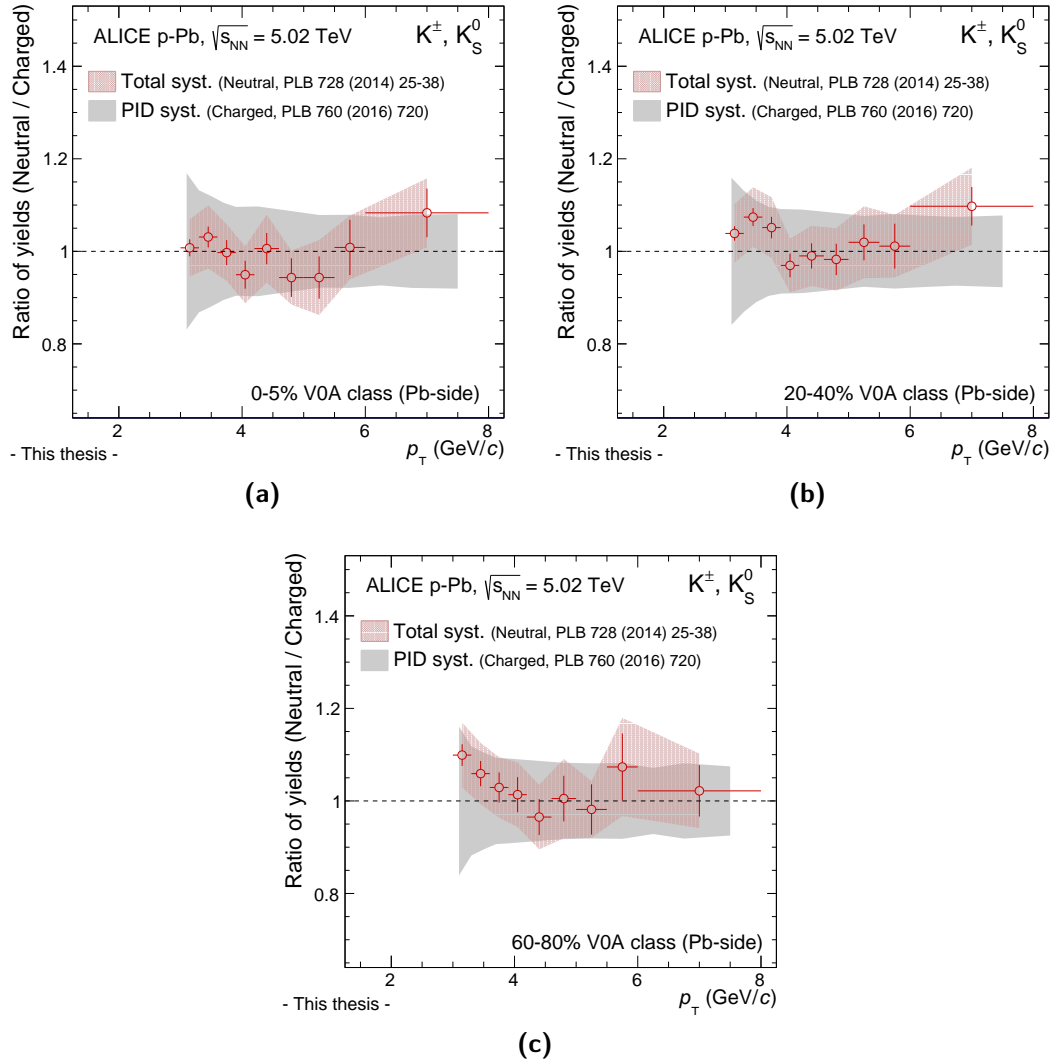


Figure 7.13: Comparison of yields of charged and neutral kaons as a function of p_T . Panels (a), (b), and (c) show the V0A multiplicity class 0–5%, 20–40%, and 60–80%, respectively. Charged kaons are from the relativistic rise measurement [71], whereas neutral kaons are from Ref. [53]. The gray band indicates the systematic uncertainty due to PID for the TPC relativistic rise analysis, while transparent band represents the total systematic uncertainty assigned for the K_S^0 analysis.

The validity of the multiplicity-dependent p–Pb analysis can be verified from the comparison of charged kaons to neutral kaons measured in the neutral hadron analysis [53]. The invariant yields of charged kaons (K^\pm) are compared to results of neutral kaons (K_S^0) in Fig. 7.13 for different V0A multiplicity classes. The results for all multiplicity classes typically vary by about 10% at most, depending on p_T . The charged kaon spectra are consistent with the neutral kaon spectra scaled by a factor of two within the reported uncertainties in the overlapping p_T range. The excellent agreement of the two analyses, in turn, further justifies the accuracy of the TPC dE/dx relativistic rise method.

CHAPTER 8

Energy dependence of π^\pm , K^\pm , and $p(\bar{p})$ production in pp collisions

In this chapter, I discuss results on the measurements of primary charged pion (π^\pm), charged kaon (K^\pm), and (anti)proton ($p(\bar{p})$) production at mid-rapidity ($|y| < 0.5$) in inelastic (INEL) pp collisions at center-of-mass energies going from $\sqrt{s} = 7$ to $\sqrt{s} = 13$ TeV. The transverse momentum (p_T) spectra have been measured at $\sqrt{s} = 7$ TeV to extend the earlier measurement [247] up to $p_T = 20$ GeV/ c . They were needed to allow the interpolation of a pp reference p_T -differential cross section at $\sqrt{s} = 5.02$ TeV, which serves as a crucial input for the measurement of the nuclear modification factor (R_{pPb}) in NSD p-Pb collisions at $\sqrt{s_{NN}} = 5.02$ TeV. The presented pp results at $\sqrt{s} = 5.02$ and $\sqrt{s} = 7$ TeV are published in Ref. [71]. The measurement of p_T spectra at $\sqrt{s} = 13$ TeV has been performed during LHC Run 2 and the produced preliminary results are also discussed in this chapter [230]. At the time of writing this thesis, the finalization of the results and the related publication from the ALICE collaboration — additionally including weakly decaying strange hadrons as well as strongly decaying resonances — is under preparation [250].

I evaluated the invariant p_T -differential production yields and yield ratios at high p_T (up to $p_T = 20$ GeV/ c) for the considered identified charged hadrons, using the TPC dE/dx relativistic rise method discussed in the preceding chapters. The p_T -integrated production yields dN/dy , yield ratios, and average transverse momenta $\langle p_T \rangle$ were obtained from the measurements. The evolution of the measured observables as a function of the collision energy \sqrt{s} are discussed and compared to previous experimental results. I evaluate an empirical scaling of measurements at different collision energies using the scaling variable $x_T = 2p_T/\sqrt{s}$ over the reported p_T range. I also discuss the validity of the empirical transverse mass (m_T) scaling law of the identified hadron spectra in terms of the K/π particle ratio. The results are compared to theoretical predictions based on NLO pQCD calculations using the DSS — and additionally DSS14 for π^\pm — fragmentation functions and to pQCD-inspired model predictions from various general-purpose Monte Carlo event generators.

8.1 Transverse momentum spectra at $\sqrt{s} = 7$ and 13 TeV

In Fig. 8.1a the p_T -differential particle yields are shown for π^\pm , K^\pm , and $p(\bar{p})$ at $\sqrt{s} = 7$ and $\sqrt{s} = 13$ TeV. The spectra reported for mid-rapidity ($|y| < 0.5$) are normalized to the number of inelastic events (N_{INEL}) of the collision. The uncertainties due to normalization to INEL collisions (not shown) amount to $\pm 3.6\%$ and $\pm 2.6\%$ respectively for $\sqrt{s} = 7$ TeV

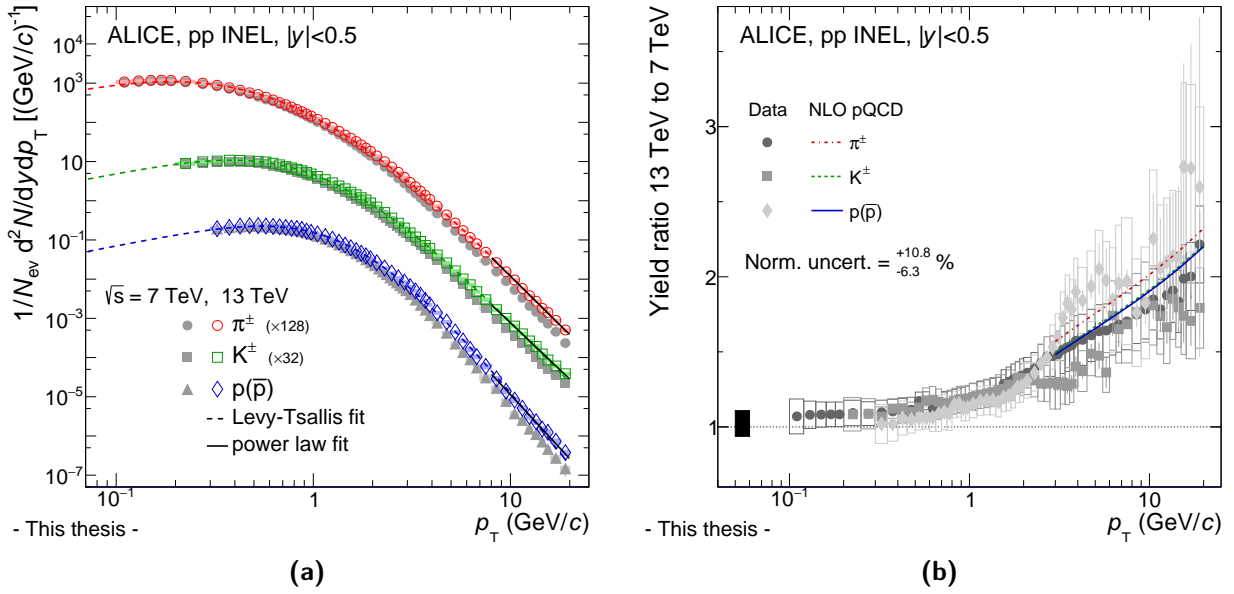


Figure 8.1: (a) p_T -differential particle yields of π^\pm , K^\pm , and $p(\bar{p})$ measured at mid-rapidity ($|y| < 0.5$) in inelastic (INEL) pp collisions at $\sqrt{s} = 7$ (full markers) and $\sqrt{s} = 13$ TeV (open markers). Solid (dashed) lines represent Lévy–Tsallis (power law) fits to the data points. (b) Ratios of p_T spectra of π^\pm , K^\pm , and $p(\bar{p})$ in minimum bias INEL pp collisions measured at $\sqrt{s} = 13$ TeV to those at $\sqrt{s} = 7$ TeV. Solid lines show predictions from next-to-leading order (NLO) pQCD calculation using DSS fragmentation functions [251]. Statistical and systematic uncertainties are shown as vertical error bars and boxes, respectively. Full box at low p_T around unity indicates the uncertainty ($+10.8\%$, -6.3%) due to normalization.

and $\sqrt{s} = 13$ TeV. The log-log scale of the plot already allows to see the power law nature of the spectra in the high- p_T region. Above $p_T = 10$ GeV/ c the pp spectrum is well described by a pure power law $d^2N/dp_T dy \propto 1/p_T^n$. The data points were fitted with this function for $p_T > 10$ GeV/ c , which yields an exponent $n = 4.94 \pm 0.04$, $n = 4.78 \pm 0.05$, and $n = 5.44 \pm 0.11$ respectively for pions, kaons, and protons with goodness-of-fit values in the range $\chi^2/\text{ndf} = 0.9 - 1.3$. It is remarkable that the obtained value for charged pions is significantly smaller than that, for example, for neutral pions ($n = 8.10 \pm 0.05$ for $p_T > 4$ GeV/ c) reported by the PHENIX collaboration at $\sqrt{s} = 200$ GeV [252]. Besides, the p_T spectra indicate a progressive and significant evolution of the spectral shape at high p_T with increasing collision energy, which is similar for all particle species under study. This behavior is better visualized in Fig. 8.1b which shows the ratios of p_T -spectra at $\sqrt{s} = 13$ TeV to those at $\sqrt{s} = 7$ TeV for π^\pm , K^\pm , and $p(\bar{p})$. The systematic uncertainties between these two collision energies are largely uncorrelated; therefore the quadratic sum of those is taken as systematic uncertainties on the ratios. The uncertainty due to normalization (shown as filled box at low p_T) amounts to $+10.8\%$, -6.3% . The ratios for all species are above unity which indicates that there is a $\sim 15\%$ increase of the average pseudorapidity density of charged particles produced in the pseudorapidity region $|\eta| < 0.5$ going from $\sqrt{s} = 7$ TeV to $\sqrt{s} = 13$ TeV [246]. Furthermore, all the ratios exhibit a clear increase as a function of p_T , pointing out that hard

scattering is expected to be the dominant particle production process at high p_T . The p_T dependence demonstrates that the spectral shapes are significantly harder at $\sqrt{s} = 13$ TeV than at $\sqrt{s} = 7$ TeV, and a universal shape—being p_T independent within uncertainties—can be observed for all species in the soft regime, $p_T \lesssim 1$ GeV/ c . The latter observation is consistent with the scaling properties of the underlying event at the LHC energies which have been recently reported [253]. It is worth noting that the hardening of the p_T spectra with increasing collision energy has also been reported for inclusive charged particles in Ref. [246], where the trend was found to be well captured by PYTHIA and EPOS MC generators.

8.1.1 Scaling properties of hadron production

Two kinds of universal scaling of identified particle production has been observed in high energy pp collisions: x_T scaling, found at higher p_T , and transverse mass scaling, originally seen in the lower p_T region. In the following, I will present results from the investigation on identified particle production in terms of these variables.

The x_T scaling

The invariant differential cross section of inclusive charged particles exhibits an approximate power-law scaling behavior for hard processes in hadronic collisions, with the variable x_T :

$$E d^3\sigma/dp^3 = F(x_T)/p_T^{n_{\text{eff}}(x_T, \sqrt{s})} = G(x_T)/(\sqrt{s})^{n_{\text{eff}}(x_T, \sqrt{s})}. \quad (8.1)$$

It is a robust pQCD prediction and is known as x_T scaling [254–258]. From dimensional analysis $E d^3\sigma/dp^3$ for high- p_T particle production in pp collisions factorizes into dimensional and dimensionless parts indicated above, where $F(x_T)$ and $G(x_T)$ are universal, dimensionless scaling functions depending on the variable x_T and are independent of \sqrt{s} . The effective exponent n_{eff} is characteristic for the type of interaction between constituent partons. In the original parton model, the power law fall-off of the p_T spectrum is described by the exponent $n = 4$ since the underlying $2 \rightarrow 2$ leading-twist subprocess amplitude for point-like partons is scale invariant. However, in QCD small scaling violations appear due to the running of the strong coupling $\alpha_S(Q^2)$, the evolution of the PDFs and FFs, and the higher-twist (HT) phenomena [257]. Consequently, n_{eff} is not constant, but it depends on x_T and \sqrt{s} , i.e. $n_{\text{eff}} = n_{\text{eff}}(x_T, \sqrt{s})$. At mid-rapidity, the NLO pQCD predictions including leading-twist (LT) processes, i.e. in which particles produced by fragmentation, the power law exponent n_{eff} increases slowly ($n_{\text{eff}} \sim 5 - 6$), with a weak dependence on hadron species [257]. In HT processes, i.e. in which the detected hadron can be produced directly in the hard subprocess reaction as in an exclusive reaction, n_{eff} is significantly larger than that in LT processes. According to Ref. [257], the evidence for HT effects is the larger value of the exponent for baryons (protons) than for mesons (pions).

The empirical scaling suggested by Eq. (8.1) is well satisfied in $p\bar{p}$ measurements at

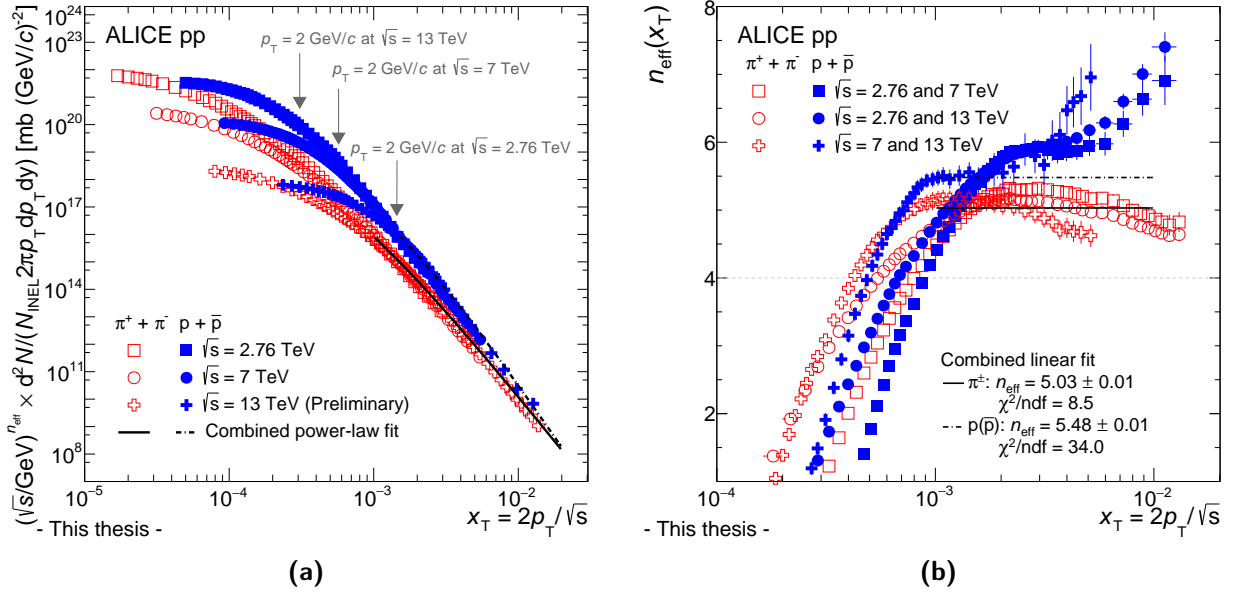


Figure 8.2: (a) Scaled invariant yields of π^\pm and $p(\bar{p})$ as a function of $x_T = 2p_T/\sqrt{s}$ at different collision energies. (b) The scaling factor $n_{\text{eff}}(x_T)$ as determined from the ratio of yields as a function of x_T for π^\pm and $p(\bar{p})$ in pp collisions at various collision energies indicated in the legend.

lower collision energies [259–261] as well as in recent measurements at the CERN LHC, see e.g. Ref. [262]. All the p_T spectra feature power law behavior at high p_T and, as discussed earlier, the higher the collision energy the smaller the exponent of the fall-off (see Fig.8.1). Practically, the exponent n_{eff} corresponds to the logarithmic variation of the production yield ratios at the same x_T for different values of \sqrt{s} [257]. In determining n_{eff} , the variation of the logarithm of the invariant cross section (σ) ratios were calculated at two different collision energies, $\sqrt{s_1}$ and $\sqrt{s_2}$:

$$n_{\text{eff}}(x_T, \sqrt{s_1}, \sqrt{s_2}) = \frac{\log\left(\sigma(x_T, \sqrt{s_1})/\sigma(x_T, \sqrt{s_2})\right)}{\log(\sqrt{s_2}/\sqrt{s_1})}. \quad (8.2)$$

A power law function is used for the measurement at higher collision energy to evaluate that at lower \sqrt{s} , making this way the ratios of the cross sections at two different energies directly calculable. Figure 8.2a shows the x_T -scaled spectra for pions and (anti)protons at three different collision energies, $\sqrt{s} = 2.76$ TeV, $\sqrt{s} = 7$ TeV, and $\sqrt{s} = 13$ TeV, with the latter two were measured in this work. The spectra were scaled by $(\sqrt{s}/\text{GeV})^{n_{\text{eff}}}$, where n_{eff} is obtained according to Eq. (8.2). In order to extract a common exponent from the various data sets for a given particle species, the n_{eff} was calculated as a function of x_T for different pairs of \sqrt{s} , and the results are shown in Fig. 8.2b. One can observe that the shape and magnitude of the presented curves are quite similar. The overall rise visible in the low- x_T region is due to soft processes whereas at higher x_T the constant behavior of n_{eff} is a consequence of pQCD processes [263]. A typical value is found by performing a combined constant fit to the data points in a range where the saturation is seen. Within this range,

the best scaling is achieved with an exponent of $n_{\text{eff}} = 5.03 \pm 0.01$ and $n_{\text{eff}} = 5.48 \pm 0.01$ for pions and (anti)protons, respectively. Drawn as a visual aid are solid and dashed black lines with the quoted values for pions and protons. In Fig. 8.2a a common trend is observed in the high- x_T region (above $\sim 10^{-3}$), i.e. the scaled spectra collapse on top of each other over a wide x_T region which corresponds to the saturation of n_{eff} in x_T . At lower x_T , a deviation from the common trend is seen which can be attributed to transition between soft and hard processes, depending on \sqrt{s} .

The quality of the scaling can be verified from the ratio of the differential cross sections, scaled by $(\sqrt{s})^{5.03}$ and $(\sqrt{s})^{5.48}$ respectively for pion and (anti)protons, to a global power law fit to the data. The fitting function is of the form $G(x_T) = a \cdot [1 + (x_T/b)]^c$, where a , b , and c are free parameters and the region below $x_T = 10^{-3}$ for pions and $x_T = 1.5 \times 10^{-3}$ for protons is excluded to avoid the dominant contribution from soft particle production, which does not follow x_T -scaling. Results show that, in spite of the naive power-law function and the expected non-scaling behavior, as discussed in Ref. [264], the measurements are in agreement with the global power law fits within roughly $\pm 30\%$ for the region where data overlap ($10^{-3} \lesssim x_T \lesssim 5 \times 10^{-3}$). The measurements performed in this work at $\sqrt{s} = 7$ and $\sqrt{s} = 13$ TeV are consistent over the accessible x_T range with the empirical x_T scaling defined by Eq. (8.1) and established at lower energy of $\sqrt{s} = 2.76$ TeV from ALICE.

Transverse mass scaling

The universal transverse mass m_T scaling proposed by Hagedorn was first seen to hold approximately at ISR energies [265, 266]. It was then observed by the STAR collaboration to hold only separately for mesons and baryons at RHIC energies, by applying the approximate m_T scaling relation respectively for pions and protons [267]. At $\sqrt{s} = 900$ GeV a disagreement was observed for charged kaons and $\phi(1020)$ meson, which pointed out the breaking of the generalized scaling behavior [268]. Moreover, recent studies based on identified particle spectra measured in pp collisions at $\sqrt{s} = 7$ TeV by ALICE indicate that m_T scaling breaks also in the low- p_T region [269]. These observations motivate studies of the applicability of m_T scaling of particle production through the precise measurement of identified particles over wide p_T ranges at different collision energies.

Following Refs. [269, 270], instead of using the m_T variable for the spectra, the scaling law can be better studied as a function of p_T , knowing that the invariant yields are equal in terms of these variables, see Appendix A. This requires changing the functional form of the parameterization of the invariant yield by applying the $p_T \rightarrow \sqrt{m_T^2 - m_0^2}$ substitution. In doing so, the p_T -differential invariant particle yield $Y_{s'}$ of a particle species s' can be obtained by scaling the parameterization of the yield Y_s^{ref} for particle species s , which is taken as a reference. Evaluating both spectra at the same transverse mass, $(p_{T,s}^2 + m_{0,s}^2) = (p_{T,s'}^2 + m_{0,s'}^2)$, the yield for species s reads as follows: $Y_{s'}(p_{T,s'}) = c \times Y_s^{\text{ref}}(\sqrt{m_{0,s'}^2 + p_{T,s'}^2 - m_{0,s}^2})$, where

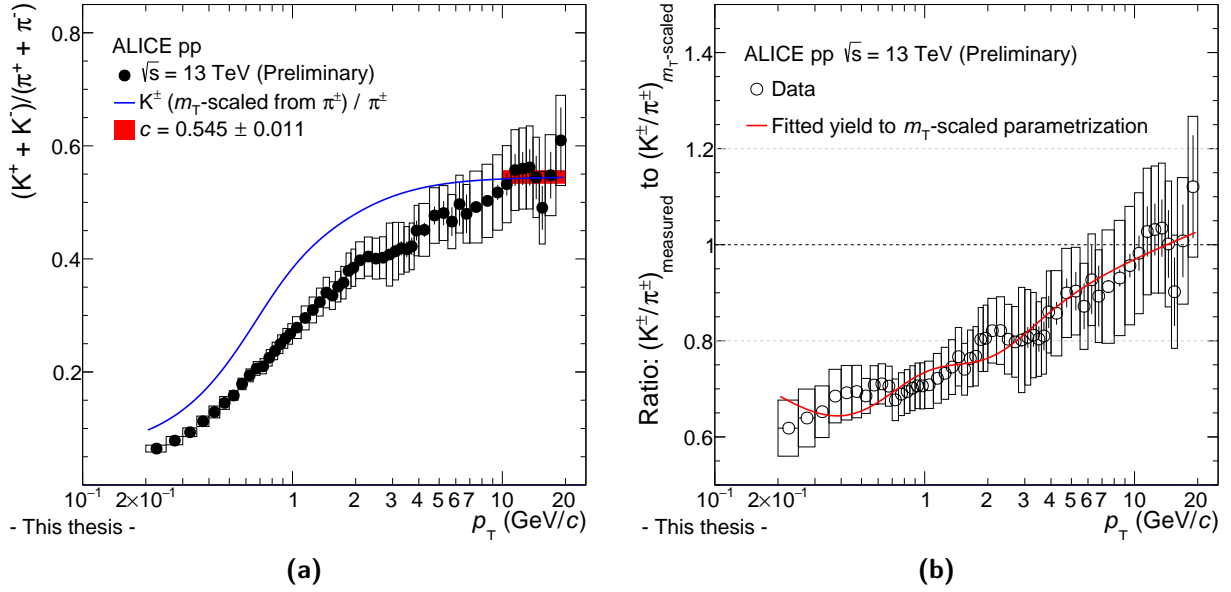


Figure 8.3: (a) Preliminary K/π ratio as a function of p_T measured in pp collisions at $\sqrt{s} = 13$ TeV. The measured ratio is reported together with that obtained from transverse mass (m_T) scaling of charged pions shown as solid line. (b) Ratio of measured K/π to that obtained from m_T -scaled parameterization of π^\pm . Solid line shows the ratio of fitted kaon yield to the m_T -scaled parameterization.

c denotes a constant offset between the particle yields for species s and s' and is to be determined.

Due to the available pion and kaon p_T spectra determined in this work, I used charged pions as reference particles and tested the m_T scaling on the K/π particle ratio for pp collisions at $\sqrt{s} = 13$ TeV. The reference p_T spectrum of π^\pm was parameterized with the modified Hagedorn function [268] which was found to describe the data within 5–10% in its entire p_T range. Afterwards, the scaling relation was applied to the parameterization of the pion yield. The appropriate offset parameter c was determined by fitting the measured K/π particle ratio in the high- p_T region where it shows a saturation trend to a constant value. Using data points only with their statistical errors for the fit, it was found to be valid for $p_T > 10$ GeV/ c and a value of $c = 0.545 \pm 0.011$ (stat) was obtained, indicated as shaded band (reporting its statistical error) in Fig. 8.3a. Along the measured K/π particle ratio, the same figure shows (with solid blue lines) the ratio of the m_T -scaled parameterization for kaons to the reference parameterization for pions. A significant deviation from the measured K/π ratio is observed below $p_T \sim 5 - 6$ GeV/ c which points to the trivial breaking of the scaling. In order to quantify the effect, the ratio between the measured K/π particle ratio and that based on the m_T -scaled parameterization is evaluated and the result is shown in Fig. 8.3b. Solid line shows the ratio of kaon yield, fitted using modified Hagedorn function with similar goodness-of-fit value as the reference, to the m_T -scaled parameterization. The ratio points below the p_T threshold $p_T = 10$ GeV/ c , that is used for the determination of

the offset parameter c , show systematically decreasing trend towards the lower p_T region and they go beyond -20% for $p_T \lesssim 2$ GeV/ c . For the m_T scaling hypothesis, the global significance of the deviation far from the threshold, i.e. $p_T < 6$ GeV/ c , amounts to 4.3σ , considering that adjacent p_T bins are fully uncorrelated. This clearly indicates the breaking of the empirical scaling law for the quoted p_T region.

The presence of collective effects, such as radial flow, can modify the scaling behavior to some degree which has more relevance at low p_T and does not play a role in the high- p_T region. More importantly, as it is shown in a recent study in Ref. [269], there is a significant feed-down contribution from resonance decays to the π^\pm yield, mostly from ρ and ω decays. Note that the primary π^\pm spectrum is only corrected for feed-down from weak decays. Notably, the presence of resonance decays affects the low- p_T ($\lesssim 1$ GeV/ c) part of the spectrum with increasing importance towards higher collision energies. Therefore, if a heavier particle (instead of π^\pm) is used as a reference then the influence of resonances decreases.

8.2 Construction of pp reference at $\sqrt{s} = 5.02$ TeV

To enable the comparison of particle production in pp to p-Pb collisions in terms of the nuclear modification factor (see Section 9.2), a pp reference spectrum is required. Since, during LHC Run 1 no pp collisions took place at the same collision energy as for p-Pb collision at $\sqrt{s} = 5.02$ TeV, the reference spectrum had to be constructed out of the existing measurements at $\sqrt{s} = 2.76$ TeV and 7 TeV. The spectra at $\sqrt{s} = 2.76$ TeV are taken from Ref. [125] whereas those at $\sqrt{s} = 7$ TeV have been measured up to $p_T = 20$ GeV/ c in this work [71], in order to extend the p_T reach of the previous measurement.

Different approaches are available for the determination of the p_T spectrum at a given \sqrt{s} by scaling existing data at different energies. Such approaches assume general scaling properties of perturbative QCD or rely on next-to-leading order pQCD calculations. The present analysis follows a data-driven approach by applying the interpolation method described in detail in Ref. [108]. In what follows, I discuss the procedure of constructing the pp reference spectra at $\sqrt{s} = 5.02$ TeV up to $p_T = 20$ GeV/ c for charged pions, kaons, and (anti)protons. The measured differential cross sections at $\sqrt{s} = 2.76$ TeV and at $\sqrt{s} = 7$ TeV are interpolated p_T -bin-by- p_T -bin, assuming a power-law behavior of the differential cross section as a function of \sqrt{s} at fixed p_T . The differential cross section is calculated as $d^2\sigma/dy dp_T = \sigma_{\text{inel}} \times d^2N/dy dp_T$ with $d^2N/dp_T dy$ being the per event differential yield of charged particles in minimum bias collisions and σ_{inel} is the inelastic cross section. As a first step, the measured spectral yields $d^2N/dp_T dy$ for both energies have been scaled up by the appropriate cross sections $\sigma_{\text{inel}} = 62.8$ mb for $\sqrt{s} = 2.76$ TeV and $\sigma_{\text{inel}} = 73.2$ mb for $\sqrt{s} = 7$ TeV, both determined in Ref. [98]. The data points were fitted with a power law function of the form $a \times (\sqrt{s})^b$ in each p_T bin. As an example, Fig. 8.4 shows such fits for

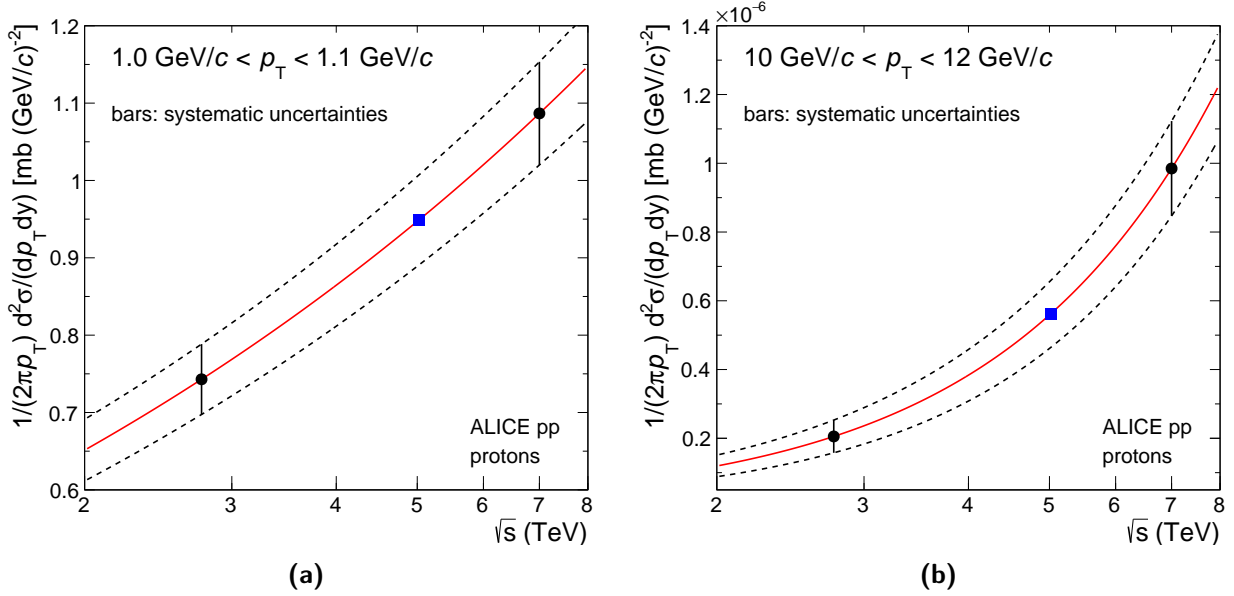


Figure 8.4: Power law fit $a \times (\sqrt{s})^b$ to interpolate the pp reference cross section at $\sqrt{s} = 5.02$ TeV, showing examples of (a) low- and (b) high- p_T bins for (anti)protons. The interpolated reference point at $\sqrt{s} = 5.02$ TeV is marked by (blue) full square superimposed over the (red) solid interpolated curve. Dashed lines represent the power law fits to the upper and lower bounds of the systematic uncertainties of the measured invariant cross sections to evaluate the systematic uncertainty of the interpolated point. Figures are reproduced from Ref. [223].

(anti)protons in two particular (low and high) p_T bins, where the blue filled square marks the interpolated reference yield at $\sqrt{s} = 5.02$ TeV. To estimate the differential cross section, the interpolated value of the fit function at $\sqrt{s} = 5.02$ TeV is evaluated. The systematic uncertainties of the reference value are estimated by fitting the upper and lower bounds of the systematic uncertainties of the measured data points at $\sqrt{s} = 2.76$ TeV and 7 TeV, and can be seen as dashed lines in Fig. 8.4. Statistical errors of the measurements, both at $\sqrt{s} = 2.76$ TeV and 7 TeV, are uncorrelated and they were propagated to the reference spectrum based on the fit function using the covariance matrix method. Systematic uncertainties on the pp reference spectrum are dominated by the measured spectra, however additional uncertainties arise from the interpolation procedure. The interpolation method was verified using events simulated by PYTHIA 8 (tune 4C) [271], where the difference between the interpolated and the simulated reference was found to be negligible. The validity of the method was also checked using results based on different approaches for the construction of the reference. The inclusive charged analysis below $p_T = 5$ GeV/ c uses the same interpolation procedure as presented here, whereas from $p_T = 5$ GeV/ c onward it is based on NLO pQCD calculations, see the details in Ref. [245]. The presented procedure is applied to the case of unidentified inclusive charged-hadron measurements and the result was compared to the published charged-hadron measurement [245]. An overall good agreement was found within the systematic uncertainties of the published reference. The systematic uncertainty of the pp reference was estimated as the maximum relative systematic uncertainty of the

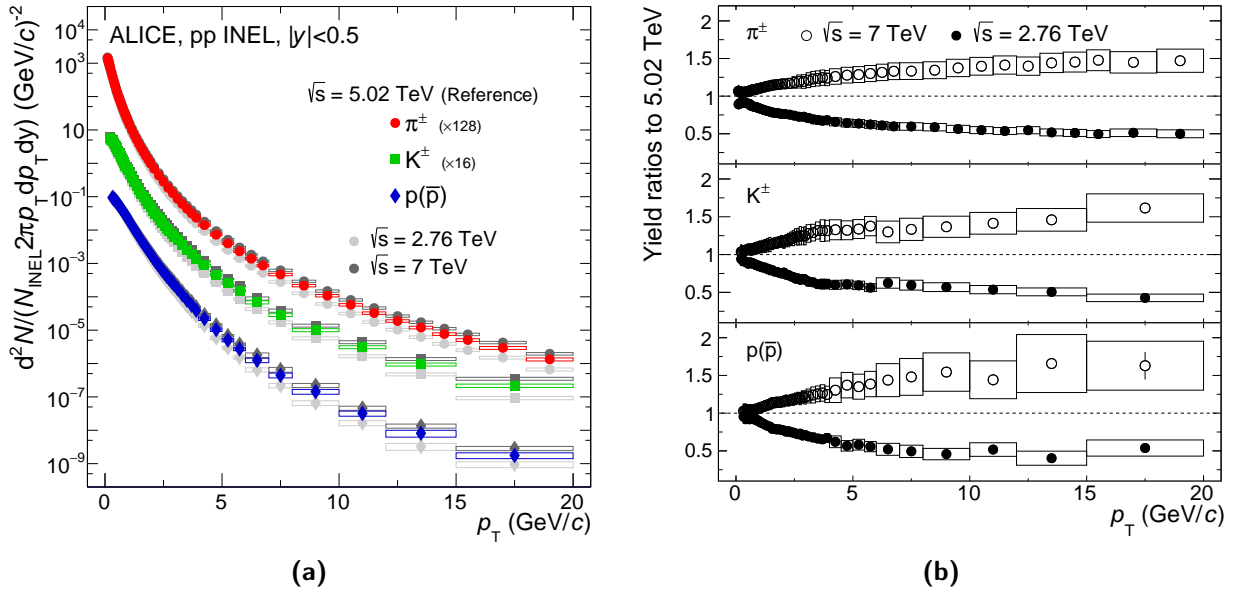


Figure 8.5: (a) Pion, kaon, and (anti)proton pp reference spectra at $\sqrt{s} = 5.02$ TeV shown in comparison with measured yields at $\sqrt{s} = 2.76$ TeV and at $\sqrt{s} = 7$ TeV. (b) Ratio of measured yield at $\sqrt{s} = 7$ TeV to the reference yield at $\sqrt{s} = 5.02$ TeV. Statistical errors and systematic uncertainties are plotted as vertical error bars and boxes, respectively. Additional uncertainties due to normalization are not shown. Figures are reproduced from Ref. [71].

underlying measurements. As a total systematic uncertainty, the quadratic sum of the systematic and statistical errors was assigned. The overall systematic uncertainties (excluding normalization) for pions and kaons for $3 < p_T < 10$ GeV/c are about 9 – 10%. As expected, for (anti)protons the uncertainties are somewhat larger, and they are about 8 – 18% for the same p_T range as for pions and kaons. In Fig. 8.5a the invariant yields are shown, where the interpolated p_T spectra are compared to those measured in INEL pp collisions at $\sqrt{s} = 2.76$ and $\sqrt{s} = 7$ TeV. Figure 8.5b shows the p_T evolution of the ratios of the measured yields at $\sqrt{s} = 2.76$ TeV and $\sqrt{s} = 7$ TeV to the reference yield at $\sqrt{s} = 5.02$ TeV. Since the uncertainties between the measured and reference spectra are largely correlated, only uncertainties of the interpolated spectra are shown on the ratios. The ratio of yields $\sqrt{s} = 7$ TeV to 5.02 TeV indicates a gradual hardening, which is a similar behavior as reported for the ratio $\sqrt{s} = 13$ TeV to 7 TeV in Fig. 8.1b.

It is important to note that the pp reference spectrum is constructed in the full acceptance $|\eta| < 0.8$, which might have consequences in the construction of the nuclear modification factor in p–Pb collisions, since the asymmetric collision results in an acceptance $-0.3 < \eta_{\text{cms}} < 1.3$ in the nucleon-nucleon center-of-mass frame. The symmetric η_{cms} range $|\eta_{\text{cms}}| < 0.3$ would correspond to the maximal overlap with the acceptance in pp collision. However, instead of reanalyzing all the pp data in a restricted $|\eta| < 0.3$ range, the full acceptance was used, since — as discussed in Ref. [245] — only a weak pseudorapidity dependence of the p_T spectra is observed for $|\eta| < 0.8$.

8.3 Particle production as a function of collision energy

The wealth of pp collision data collected by ALICE at different center-of-mass energies, made it possible to study particle production as a function of \sqrt{s} , ranging from $\sqrt{s} = 0.9$ TeV to top energy of $\sqrt{s} = 13$ TeV. These measurements serve valuable information on hadronization processes and final state interactions.

It should be noted that the presented quantities (integrated yields and average transverse momenta) have already been calculated for the official $\sqrt{s} = 13$ TeV pp preliminary results in ALICE. Therefore, the results of the current study were compared to those and they were found fully compatible within systematic uncertainties.

8.3.1 Integrated yields and average transverse momenta

The p_T distributions $d^2N/dp_T dy$ at $\sqrt{s} = 13$ TeV, presented in Fig. 8.1a in Section 8.1, are fitted with a Lévy–Tsallis function [272, 273] multiplied with p_T to account for the spectra being non-invariant. This function phenomenologically describes both the low- p_T exponential and the high- p_T power law behaviors, using only few parameters. The performed fit describes well the spectra over the full measured p_T range. The χ^2/ndf values of the fit are 42.1/55 for pions, 16.7/50 for kaons, and 30.9/48 for protons. All three values are below unity, which is most likely due to residual correlations in the point-to-point systematic uncertainties. The fit function is used in order to extrapolate the spectra to unmeasured p_T regions, i.e. down to zero p_T , similar to what was done in previous ALICE measurements [247, 248]. The procedure allows the p_T -integrated yields dN/dy and the average transverse momentum $\langle p_T \rangle$ to be extracted. The fractions of yields related to the low- p_T extrapolation region accounts for $\sim 8\%$, $\sim 9\%$, $\sim 11\%$ of the total dN/dy , respectively for pions, kaons, and protons.

The systematic uncertainties are very similar to those from earlier measurements at lower collision energies and they are obtained from the sum of two independent contributions. The first contribution is related to the systematic uncertainties on the measured p_T -differential yields and it was estimated by repeating the Lévy–Tsallis fits moving the measured points within their systematic uncertainties. The second contribution is due to the extrapolation to $p_T = 0$ GeV/ c , i.e. the choice of spectrum fit function. It is estimated using different fitting functions, namely the Boltzmann–Gibbs blast wave function [188], the modified Hagedorn [268, 274], the two-component model function proposed by Bylinkin and Rostovtsev in Ref. [275], and the UA1 parameterization [276]. The dN/dy is recalculated for each of these fits. The resulted values are compared to the default value and the maximum difference is taken as the systematic uncertainty. The systematic uncertainty of the fitted yields at low p_T is in the range 2–4% for dN/dy , and 2–3% for $\langle p_T \rangle$. The statistical uncertainties in the extracted yields are given by the fit uncertainties and are negligible, while the systematic uncertainties are the quadratic sum of the independent contributions. The total systematic

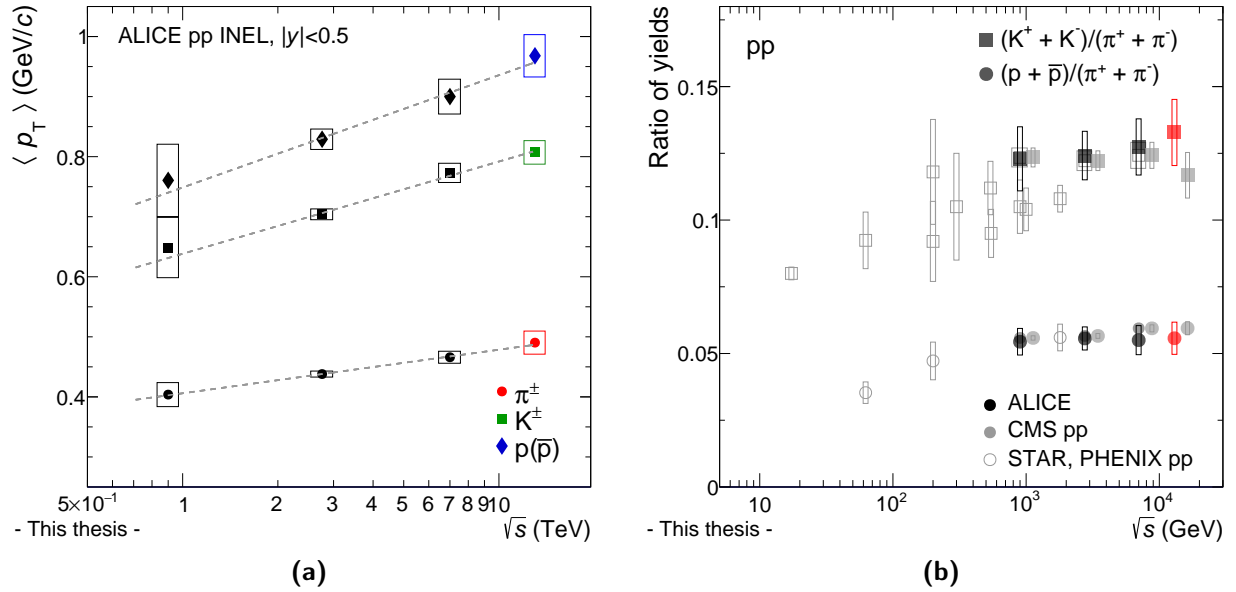


Figure 8.6: (a) The average transverse momenta $\langle p_T \rangle$ of pions, kaons, and (anti)protons and (b) p_T -integrated ratios of particle yields for kaons and protons to that of pions measured in inelastic (INEL) pp collisions as a function of collision energy. Dashed curves show linear fits in $\log s$ for $\langle p_T \rangle$. Results from ALICE are compared to those from CMS [277] and with STAR and PHENIX results from RHIC measured at $\sqrt{s} = 200$ GeV. CMS data points are slightly shifted horizontally for clarity. Open boxes represent statistical (negligible) and systematic uncertainties added quadratically.

uncertainties (excluding normalization) for dN/dy is in the range 6 – 8% whereas for $\langle p_T \rangle$ it ranges between 2% and 4%.

Both the average yields dN/dy and the average transverse momenta $\langle p_T \rangle$ show an increase with the collision energy \sqrt{s} . Going from $\sqrt{s} = 7$ TeV to $\sqrt{s} = 13$ TeV the dN/dy and $\langle p_T \rangle$ increase respectively by about 8%/13%/10% and 5%/4%/8% for $\pi^\pm/K^\pm/p(\bar{p})$. Figure 8.6a reports the average transverse momenta $\langle p_T \rangle$ as a function of \sqrt{s} . The moderate increase of $\langle p_T \rangle$ with increasing \sqrt{s} is attributed to the increasing importance of hard processes towards higher collision energies. The evolution with \sqrt{s} is steeply rising for heavier particles seen in earlier measurements at lower collision energies [247]. The measurement of the collision energy dependence of the $\langle p_T \rangle$ is particularly useful for the saturation scale of the gluons inside the proton, see the discussion in Ref. [278]. Figure 8.6b shows the ratio of particle yields to pions, p/π and K/π , as a function of the collision energy. The results for pp collisions at $\sqrt{s} = 13$ TeV are compared to earlier measurements from ALICE reported at lower collision energies [125, 247, 248], to those from CMS at $\sqrt{s} = 13$ TeV [277], and to those measured by PHENIX/STAR at the BNL RHIC at $\sqrt{s} = 200$ GeV [184, 279]. Both the p/π and K/π ratios indicate saturation in the LHC-energy regime.

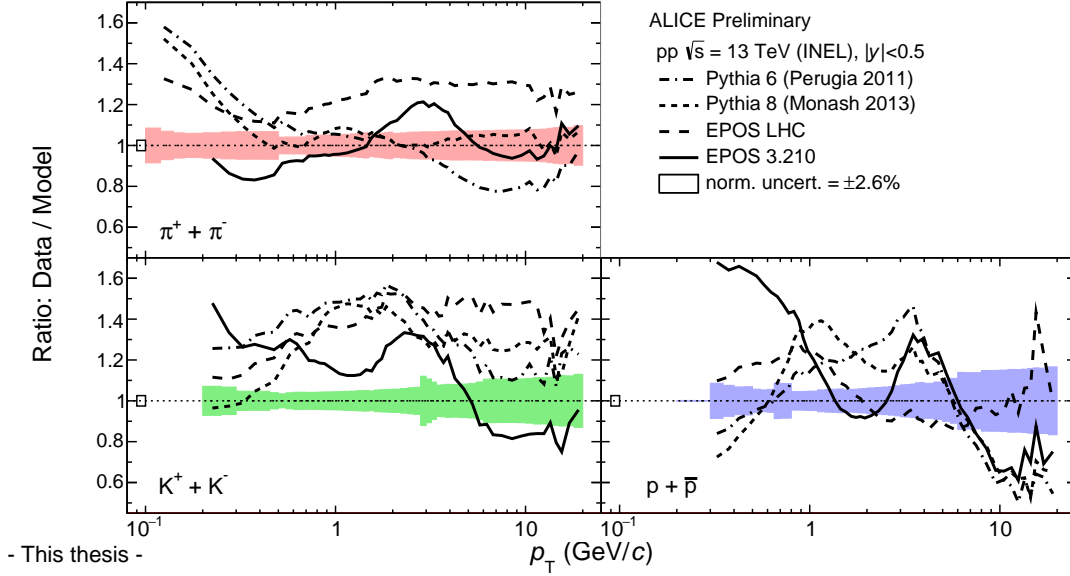


Figure 8.7: Ratios of p_T spectra of π^\pm , K^\pm , and $p(\bar{p})$ from Monte Carlo model predictions to those measured in pp collisions at $\sqrt{s} = 13$ TeV. The total fractional uncertainties of the data are shown as shaded boxes. The additional normalization uncertainty of the data amounts to $\pm 2.6\%$ and is shown as open box at low p_T around unity.

8.4 Comparisons to theoretical models

The comparison between the measured p_T spectra of π^\pm , K^\pm , and $p(\bar{p})$ and the predictions from several Monte Carlo event generators as well as NLO pQCD calculations gives useful information on hadron production mechanisms. In the following, I discuss each model individually, compared with the preliminary experimental data measured at $\sqrt{s} = 13$ TeV.

8.4.1 Comparison to Monte Carlo models

Figure 8.7 shows the comparison of measured π^\pm , K^\pm , and $p(\bar{p})$ p_T spectra at $\sqrt{s} = 13$ TeV with several Monte Carlo event generators: PYTHIA 6.425 (Perugia 2011 tune [163]), PYTHIA 8.210 (Monash 2013 tune [164]), EPOS-LHC (with the CRMC package 1.5.4) [280], and EPOS 3.210 [128–130]. As discussed in Section 3.3.1, both PYTHIA and EPOS are tuned to reproduce certain aspects of the existing data available from the LHC Run 1. The PYTHIA model uses a color reconnection (CR) mechanism, which is able to mimic collective effects such as radial flow observed in Pb–Pb collisions [82], moreover it gives a proper description of the charged-particle multiplicity dependence of the $\langle p_T \rangle$ confirmed by many experiments at CERN SPS and LHC [83, 281–283]. The effect of CR leads to the production of less inclusive charged particles with larger p_T , see e.g. Ref. [284]. The EPOS models incorporate collective (flow-like) effects as well, though these are only treated via parametrizations in the EPOS-LHC version. The EPOS 3 model with pomeron-dependent saturation scale and full 3D hydrodynamical treatment of the event is able to reproduce many features of the data, notably collective effects in small collision systems, see the discussion in Chapter 4.

For the comparison to the MC generators, the total fractional uncertainties of the data are shown, i.e. the statistical and systematic uncertainties of the measurement have been added quadratically. The description of the shape and normalization of the spectra by the models are affected due to different processes embedded in the generators. On the one hand, the total yield with respect to that produced in inelastic events are solely modified due to diffractive processes. Note that $\sim 32\%$ of all inelastic events are single or double diffractive [98]. On the other hand, the overall shape of the p_T spectrum is dominated by non-diffractive collisions¹³. This is because diffractive processes produce only few particles at mid-rapidity (see Section 3.3). It is noteworthy that MC generators, in general, have difficulties in describing diffractive processes [98]. The PYTHIA 8 model with the widely-used Monash 2013 tune, presented here and also used for corrections in case of $\sqrt{s} = 13$ TeV pp data, already has an improved description of diffractive processes with respect to its earlier version PYTHIA 6. For the comparisons, it is also important to emphasize that the low- p_T (soft) and high- p_T (hard) regimes of the spectrum are handled differently in the models. For the former phenomenological approaches are used, while for the latter perturbative QCD calculations are incorporated in the generators.

In Fig. 8.7, it is shown that, with the exception of the p_T region below $p_T \simeq 1$ GeV/ c , EPOS-LHC describes the best all the particle yields in the intermediate to high p_T regions both in normalization and shape, simultaneously. The PYTHIA 8 and EPOS 3 models capture the pion spectrum for $p_T \gtrsim 5$ GeV/ c , both qualitatively and quantitatively. For kaons at low p_T , PYTHIA 8 provides a better agreement with the data than PYTHIA 6, as expected. None of the MC generators agree with the kaon spectrum in normalization, although PYTHIA 6 and EPOS 3 show marginal agreement with the data from $p_T = 6 - 7$ GeV/ c onward. However, all the generators predict the spectral shape rather well in the region 6 GeV/ $c \lesssim p_T \lesssim 15$ GeV/ c ; above $p_T \simeq 15$ GeV/ c the statistical fluctuations do not allow to make definite conclusion. Both PYTHIA 6 and 8 underestimate the strange particle production almost in the entire p_T range, which is a well-known feature of these models and it is more significant when one compares the yield of kaons to that of pions, see below. For the proton spectrum, PYTHIA 8 describes the shape and normalization above $p_T \simeq 2$ GeV/ c . Remarkably, EPOS 3 follows closely the PYTHIA 6 prediction. However, one has to keep in mind that the current version is still under development and to date it is not released for public use [285].

The relative contribution of the hardening observed in the p_T spectra (see Fig. 8.1) between different particle species is better seen in terms of particle ratios. On the other hand, the comparison of the p_T -dependent particle ratios with MC models allows the different hadronization mechanisms implemented in the generators to be tested. The K/π and p/π particle ratios are shown in Fig. 8.8 as a function of p_T measured in pp collisions at $\sqrt{s} = 13$ TeV and are compared with the same MC models presented above for the case of p_T

¹³Diffractive processes can contribute less to the shape of the p_T spectrum and only for $p_T \lesssim 1$ GeV/ c .

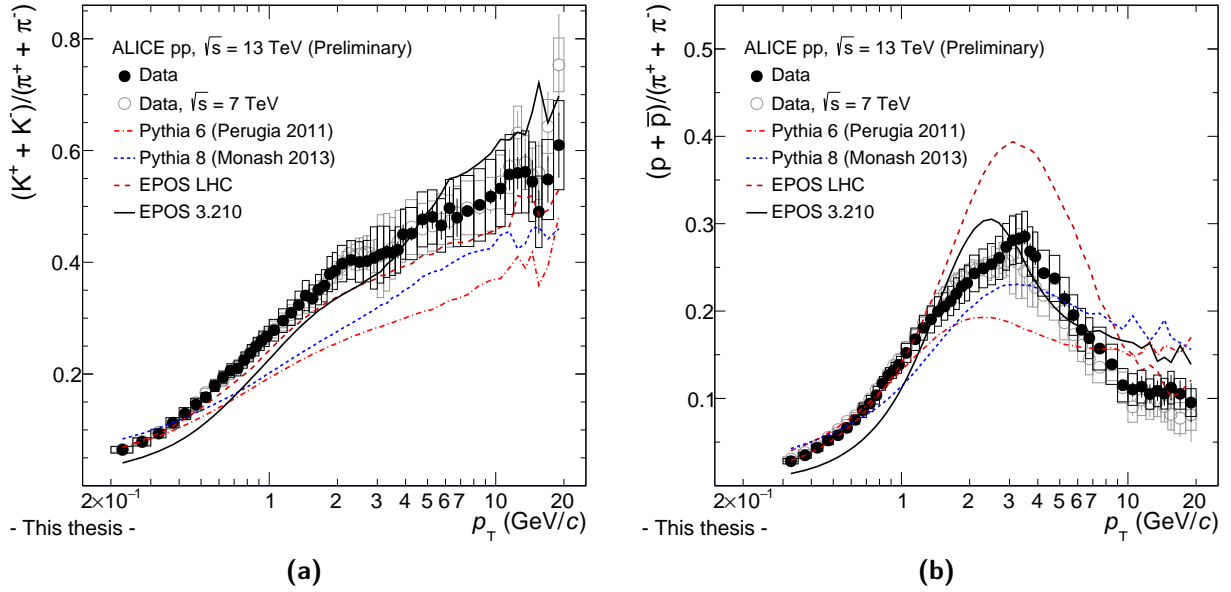


Figure 8.8: Comparison of p_T -dependent particle ratios (a) $(K^+ + K^-)/(\pi^+ + \pi^-)$ and (b) $(p + \bar{p})/(\pi^+ + \pi^-)$ with Monte Carlo event generators measured in pp collisions at $\sqrt{s} = 13$ TeV. In addition to $\sqrt{s} = 13$ TeV data (full circles), the $\sqrt{s} = 7$ TeV data (open circles) are also shown [71].

spectra. Even though EPOS-LHC overshoots both the pion and kaon p_T spectra, it gives a reasonable description of the K/π ratio for $p_T \gtrsim 3$ GeV/ c . The same observation is valid for EPOS 3, which models better the low- p_T part of the ratio, but it gives a larger enhancement for strangeness production at higher p_T . As discussed earlier, the PYTHIA models also fail to describe strange particle production relative to that of pions, however, PYTHIA 8 (due to improvements) gives somewhat better description of the K/π ratio. A similar deviation is observed in various earlier measurements at lower collision energies, for example, by the ALICE collaboration and not only for single-strange but also for multi-strange particles, depending on the strange valence quark content of the produced hadron [63, 286].

The p/π ratio shown in Fig. 8.8b is qualitatively well described by EPOS-LHC, but it predicts more baryons in the region (and above) where the so-called baryon anomaly — an increased baryon-to-meson production ratio at intermediate transverse momenta (p_T of a few GeV/ c) — takes place. The EPOS 3 model approaches the data with a slight worsening in describing the low- p_T behavior and the position of the measured peak observed around $p_T = 3$ GeV/ c . In the intermediate p_T region (2 GeV/ $c \lesssim p_T \lesssim 6$ GeV/ c), although EPOS 3 captures the baryon enhancement, PYTHIA exhibits smaller deviation from the data with only a gradually decreasing trend towards higher p_T .

The comparison between data and MC models indicate that none of the predictions give adequate description of the data for the full p_T range, they allow only to characterize the ratio of yields partially — suggesting that further improvements in the generators are needed. The high-precision measurements reported here are crucial for giving useful inputs for the generators for further tuning and to better understand the particle production mechanisms at the investigated collision energies.

8.4.2 Comparison to perturbative QCD calculation

The invariant charged pion, kaon, and (anti)proton yield is related to the invariant cross section as $E d^3\sigma/dp^3 = \sigma_{\text{inel}} \times E d^3N/dp^3$, where σ_{inel} is the inelastic cross section and for $\sqrt{s} = 13 \text{ TeV}$ pp data it is determined in Ref. [240]. The measured invariant cross sections are compared to calculations in next-to-leading order (NLO) perturbative QCD using CT10NLO proton PDF [287] with DSS (de Florian, Sassot, and Stratmann [157, 288]) FF set. For charged pions a new version of DSS FFs, the DSS14 FF [158] set is available. The NLO calculations are based on Ref. [251] which apply the same factorization scale value, $\mu = p_T$ for the factorization, renormalization and fragmentation scales. The variation of the scales to $\mu = p_T/2$ and $\mu = 2p_T$ gives an estimate of the theoretical uncertainty; the PDF errors are negligibly small in comparison to the scale uncertainty. The rather large scale uncertainty observed at lower p_T ($2 < p_T < 10 \text{ GeV}/c$) stabilizes $\pm 20 - 30\%$ beyond $p_T \simeq 10 \text{ GeV}/c$, which is the region where the NLO calculations are trustworthy and are free from non-perturbative effects. The production of π^\pm , K^\pm , and $p(\bar{p})$ from hard scattering becomes more dominated by the fragmentation of gluon jets (over the quark fragmentation) with increased collision energy in the p_T range of the measurement [157]. The presented identified charged-hadron spectrum can therefore help to constrain the gluon-to-charged-hadron fragmentation function [289] which is of crucial importance in having better description of the LHC charged-hadron data with NLO pQCD, see e.g. Ref. [238].

Figure 8.9 shows the ratios between the measured inclusive π^\pm , K^\pm , and $p(\bar{p})$ invariant cross sections (circles) and the NLO pQCD calculations using the DSS FF set. The various curves indicate the NLO calculations obtained with other FF sets, like the KKP: Kniehl, Kramer, and Potter [290], KRE: Kretzer [291], and the DSS14, relative to DSS FFs. The behavior of measured data relative to the NLO calculations in all panels of Fig.8.9 is very similar. In the low to intermediate p_T region large deviation in shape and normalization is observed, however in the high- p_T ($> 10 \text{ GeV}/c$) region they closely follow the spectral shapes of the measured p_T distributions. Calculations using the Kretzer FFs follow the measured pion and kaon data points above $p_T = 6 - 7 \text{ GeV}/c$.

For the direct comparison to NLO calculations, the measured data points are fitted with a Lévy–Tsallis function to avoid that bin-by-bin fluctuations in the data make the comparison less clear to interpret. Figure 8.10a shows the comparisons for the species under study. Since, to date, no calculation exists for scale uncertainties of the DSS14, only the DSS FFs with the corresponding scale uncertainties are reported in the figure [292]. In Fig. 8.10b the ratios of data and NLO pQCD calculations to the Lévy–Tsallis fits of π^\pm , K^\pm , and $p(\bar{p})$ spectra are shown. Above $p_T = 10 \text{ GeV}/c$ the NLO pQCD calculation, employing the DSS14 FFs (using the DSS scale uncertainties), overpredicts the measured pion cross section by up to about a factor of two, but describe the shape of the p_T spectrum rather well. Similar

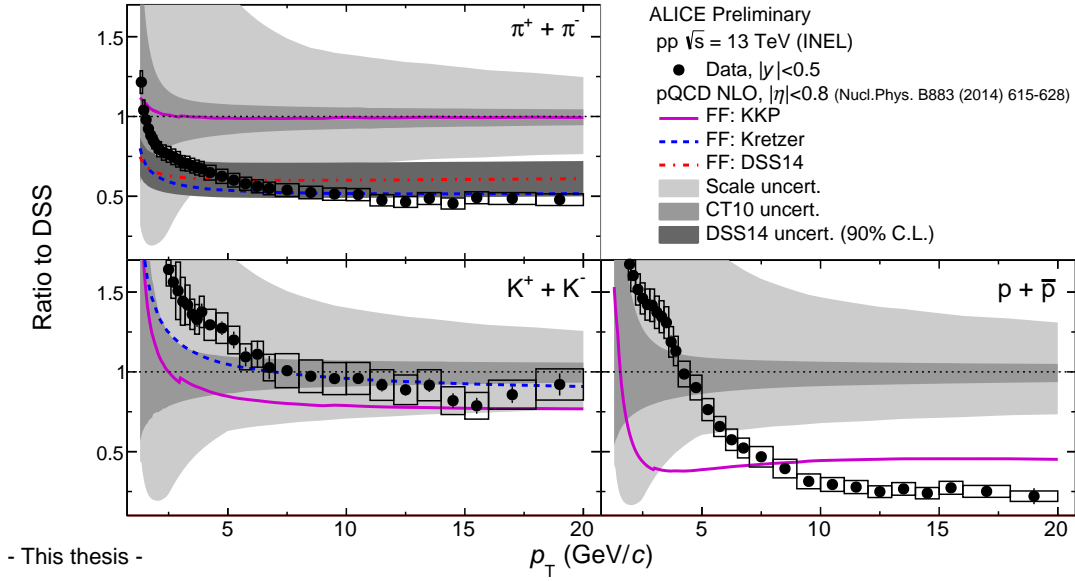


Figure 8.9: Ratios between the inclusive charged pion, kaon, and (anti)proton invariant cross sections measured by the ALICE collaboration (circles) and the NLO pQCD calculations using DSS (de Florian, Sassot, and Stratmann [157, 288]) FF set. The curves indicate the NLO calculations obtained with other FF sets as indicated in the legends: KKP: Kniehl, Kramer, and Potter [290], KRE: Kretzer [291], and DSS14 [158] relative to DSS FFs. The light gray bands quantify the QCD scale uncertainty, the medium gray bands indicate the CT10 error range, and the dark gray bands represent the uncertainty derived from the DSS14 FF (90% confidence level) error sets.

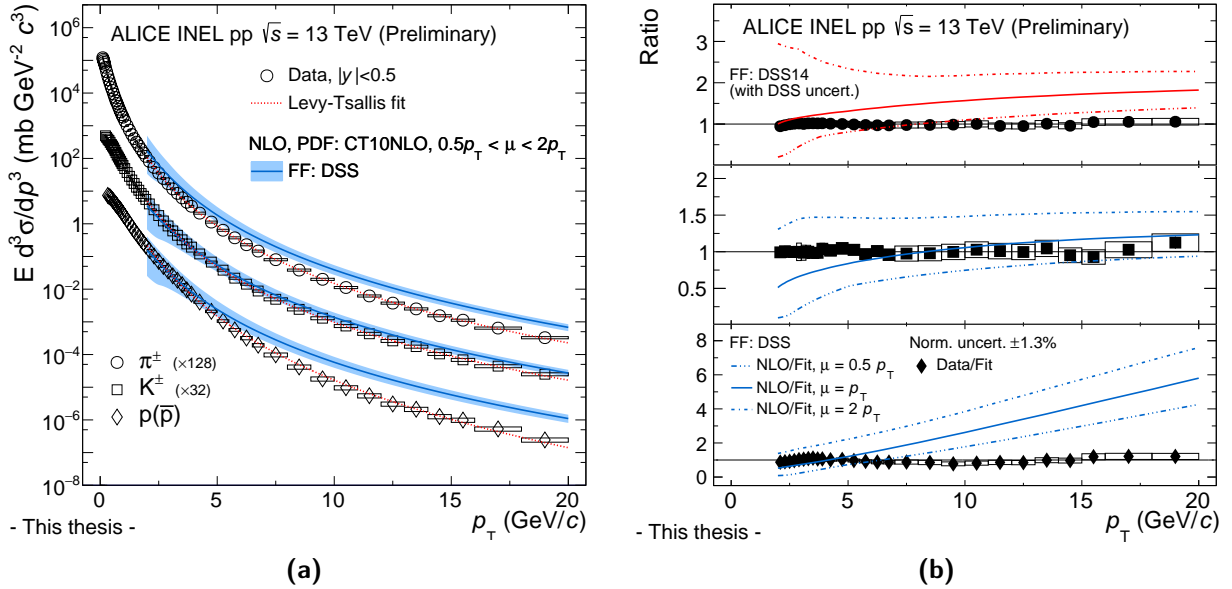


Figure 8.10: (a) Invariant differential cross sections for charged pion, kaon, and (anti)proton production in comparison to NLO pQCD calculations using CT10NLO PDFs with DSS14 FF for π^\pm and DSS FF for K^\pm and $p(\bar{p})$. The shaded band around the NLO calculations corresponds to the scale uncertainty. (b) Ratio of data (points) or NLO (lines) calculations to a Lévy–Tsallis function that is fitted to the data. The ratio NLO/FIT is shown for the scale $\mu = p_T$ and the variations $\mu = p_T/2$ and $\mu = 2p_T$. The fully correlated normalization uncertainty is indicated in the legend.

discrepancies between NLO pQCD calculations and the measured cross sections have also been reported for the measurements of neutral pions (π^0) at $\sqrt{s} = 7$ and 8 TeV [293, 294] from ALICE, leaving room for future improvements in the calculations. It is worth noting that the published π^0 measurement at $\sqrt{s} = 7$ TeV [293] adds important constraints for gluon FFs which helps reduce FF uncertainties; however, to date, there are no results that would confirm this statement [292]. The NLO calculations describe charged kaons better than pions, which is reflected from the good agreement on the data-to-fit ratio points within the quoted uncertainties. The predictions for protons deviate the most from the measurement for all μ scale choices; these calculations significantly overestimate the measured data. Below $p_T = 10$ GeV/ c the discrepancy of NLO and data is reduced for pions and kaons, however, the calculation does not describe the shape of the spectrum well for any of the considered particle species. In this p_T regime, soft parton interactions and resonance decays dominate the particle production, which cannot be well described within the framework of pQCD.

Though the p_T dependence of the cross sections at a given collision energy is not described well by the NLO calculations, a better prediction is achieved for the relative dependence on p_T of the ratio of cross sections at two distinct \sqrt{s} . Such a comparison is shown in Fig. 8.1b of Section 8.1, where the ratio of invariant yields in INEL pp collisions at $\sqrt{s} = 7$ and $\sqrt{s} = 13$ TeV is compared to the same ratio calculated from NLO pQCD. The agreement between the data and NLO calculations is notably improved compared to the spectra themselves. Taking a double ratio where the ratios of spectra at $\sqrt{s} = 13$ and $\sqrt{s} = 7$ TeV for data are divided by that of NLO calculations, the observed difference is below 10% (20%) for pions (kaons and protons). The presented results show that the independent fragmentation works rather well for mesons, in particular for $p_T > 6$ GeV/ c , however for (anti)protons the spectral shape is completely off for $p_T < 10$ GeV/ c . It is worth noting that the same observation is seen for the nuclear modification factor in p-Pb collisions (see Section 9.4) where the enhancement of (anti)protons requires some additional production mechanism.

CHAPTER 9

Multiplicity dependence of π^\pm , K^\pm , and $p(\bar{p})$ production in p–Pb collisions

In this chapter, results on the measurements of primary charged pion (π^\pm), charged kaon (K^\pm), and (anti)proton ($p(\bar{p})$) production in non-single diffractive (NSD) p–Pb collisions at $\sqrt{s_{\text{NN}}} = 5.02$ TeV at mid-rapidity ($-0.5 < y < 0$) are discussed. The previously published [53] transverse momentum (p_{T}) distributions were extended to include measurements up to $p_{\text{T}} = 20$ GeV/ c for seven event multiplicity classes based on a forward-rapidity estimator. The interpolated pp reference p_{T} spectrum at $\sqrt{s} = 5.02$ TeV is used for the creation of the nuclear modification factor R_{pPb} . Apart from the NSD p_{T} spectra, p_{T} -dependent particle ratios have been extracted as a function of charged-particle multiplicity and are compared to inelastic pp as well as to peripheral Pb–Pb collisions measured at different collision energies. Such a comparison allows us to study the system size dependence of observables sensitive to (radial) flow or fragmentation modified by the presence of the nuclear environment. By studying the size and density (dN/dy) dependence of particle ratios, one gains better understanding on the dynamics of hadronization which links the confined hadronic and deconfined partonic phases. The results presented here were published in Ref. [71].

9.1 Transverse momentum spectra as a function of charged-particle multiplicity

The charged pion, kaon and (anti)proton p_{T} -spectra for different V0A multiplicity event classes (measured by the forward-rapidity estimator) are shown in Fig. 9.1. The multiplicity-dependent results have been normalized to the visible (triggered) cross section corrected for the vertex reconstruction efficiency – which was not done for the published low- p_{T} results [53]. The NSD spectra, obtained from a weighted average of the multiplicity-dependent results, are normalized to the total number of NSD events using a trigger and vertex reconstruction efficiency correction (see Section 7.6.3) which amounts to $(3.6 \pm 3.1)\%$ [242]. The spectra were scaled for clarity. As expected at this collision energy, the ratio of invariant yields of particles to that of antiparticles are identical within uncertainties, and are independent of both p_{T} and charged-particle multiplicity, which is consistent with the ratios in pp collisions. The behavior of the spectral shape at low p_{T} ($\lesssim 2$ GeV/ c) compared to those in Pb–Pb collisions are very much alike as it is also reported in Ref. [53]. The p_{T} distributions show a clear evolution, becoming harder as the multiplicity increases (V0A 60–80% \rightarrow V0A 0–5%) and this change is more pronounced for heavier particles, such as (anti)protons. This is a

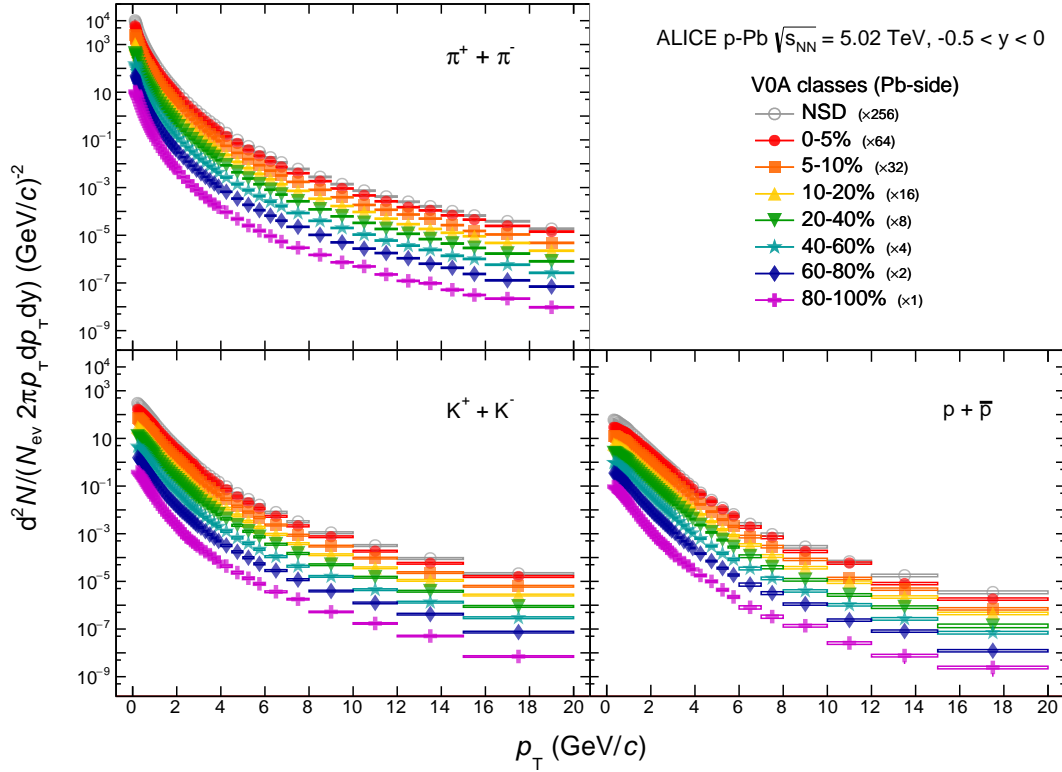


Figure 9.1: Transverse momentum spectra of charged pions, kaons, and (anti)protons measured for different V0A multiplicity event classes in p–Pb collisions at $\sqrt{s_{\text{NN}}} = 5.02$ TeV. Statistical errors and systematic uncertainties are plotted as vertical error bars and boxes, respectively. The spectra (measured for NSD events and for different V0A multiplicity classes) have been scaled by the indicated factors in the legend for better visibility. Figure is reproduced from Ref. [71].

well-known effect in heavy-ion collisions and it is commonly attributed to radial flow [50, 51], which can be described quantitatively well with hydrodynamic models, see e.g. Ref. [295]. In fact, the flattening of the p_T spectra and its mass ordering is explained by the collective radial expansion of the system, which was tested in the blast-wave framework in Ref. [53]. It was found that the parameters of the model, i.e. the kinetic freeze-out temperature and the radial flow velocity, show a similar trend as the ones obtained in Pb–Pb. In turn, although within the limitations of the applied model, the observation is consistent with the presence of radial flow in p–Pb collisions. For larger p_T , the spectra follow an approximate power-law behavior which is expected from the pQCD scaling behavior seen also for the case of pp collisions in Chapter 8.

Figure 9.2 shows a comparison of π^\pm , K^\pm , and $p(\bar{p})$ p_T spectra between small (pp and p–Pb) and large (Pb–Pb) collision systems at identical collision energy $\sqrt{s_{\text{NN}}} = 5.02$ TeV, restricting the p_T reach to $p_T = 5$ GeV/c in order to help one see better the change in spectral shape. Published p–Pb results [71] in 0–5% V0A multiplicity event class are plotted against the preliminary results in minimum-bias pp [296], and central (0–5%) as well as peripheral (60–80%) Pb–Pb [296]. Both the former and the latter are measured in LHC Run 2 at $\sqrt{s_{\text{NN}}} = 5.02$ TeV. For the comparison with central (0–5%) Pb–Pb p_T -spectra, shown in

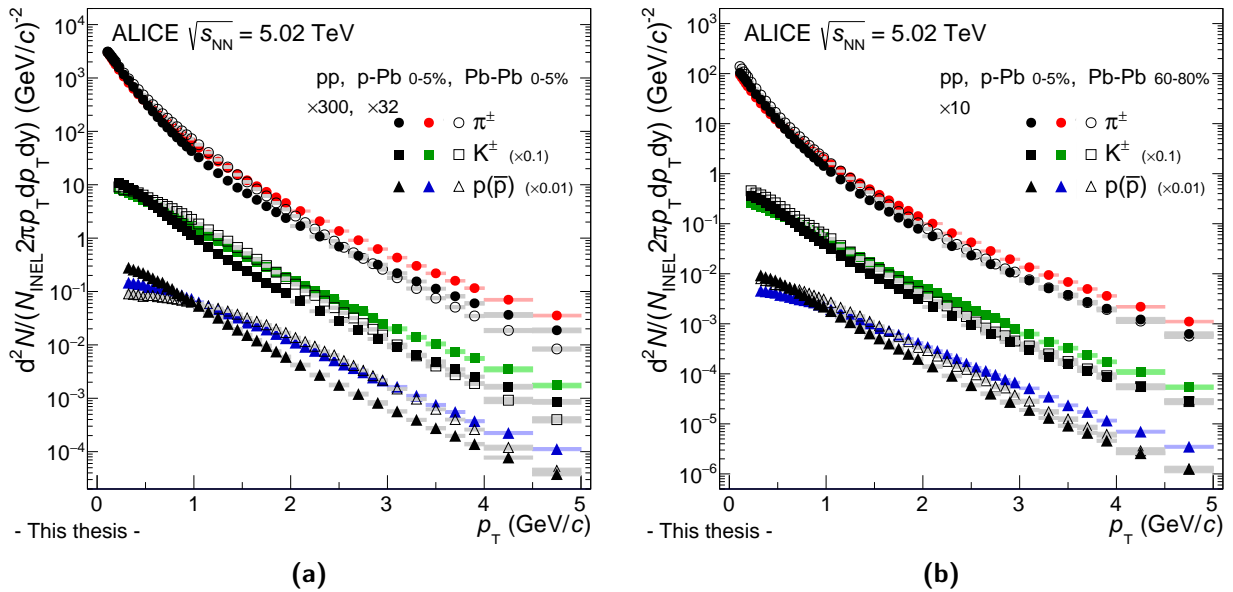


Figure 9.2: Transverse momentum spectra of π^\pm , K^\pm , and $p(\bar{p})$ measured in p–Pb collisions at $\sqrt{s_{NN}} = 5.02$ TeV in the 0 – 5% V0A multiplicity class (Pb-going side). Results are compared with preliminary measurements in pp collisions at $\sqrt{s} = 5.02$ TeV, and (a) central (0 – 5% centrality) and (b) peripheral (60 – 80% centrality) Pb–Pb collisions measured at $\sqrt{s_{NN}} = 5.02$ TeV.

Fig. 9.2a, one can observe the change in magnitudes compared to pp and p–Pb spectra which is progressive for the former and moderate for the latter case. Note that pp and Pb–Pb yields were scaled by a factor of 300 and 32, respectively. This significant change in the yields is partially expected from the change of the average charged-particle mid-pseudorapidity densities among different event classes for the presented systems: $\langle dN_{ch}/d\eta \rangle_{|\eta_{lab}| < 0.5} = 45 \pm 1$ for 0 – 5% V0A event class in Pb–Pb collisions, being ~ 2.7 times larger than the charged-particle pseudorapidity density measured in NSD p–Pb collisions at $\sqrt{s_{NN}} = 5.02$ TeV [242]. For central (0 – 5%) and peripheral (60 – 80%) Pb–Pb collisions [25], and for MB pp at $\sqrt{s} = 7$ TeV [297] the corresponding pseudorapidity densities are 1601 ± 60 , 55.5 ± 5.0 , and $4.60^{+0.34}_{-0.17}$, respectively. On the other hand, by comparing the p_T -spectra at the highest multiplicity (0 – 5% V0A class) in p–Pb collisions to those of peripheral (60 – 80% centrality) Pb–Pb, their magnitudes seem to be similar, although the underlying physical mechanisms might be different. For pp, the relative yields are still significantly lower by about a factor of 10.

9.2 Nuclear modification factor for charged pions, kaons, and (anti)protons

The most commonly used tool to measure nuclear matter effects is the nuclear modification factor. It is constructed from minimum bias NSD p–Pb spectra and compared to a reference p_T spectra in pp collisions at the same collision energy. From this comparison, one can

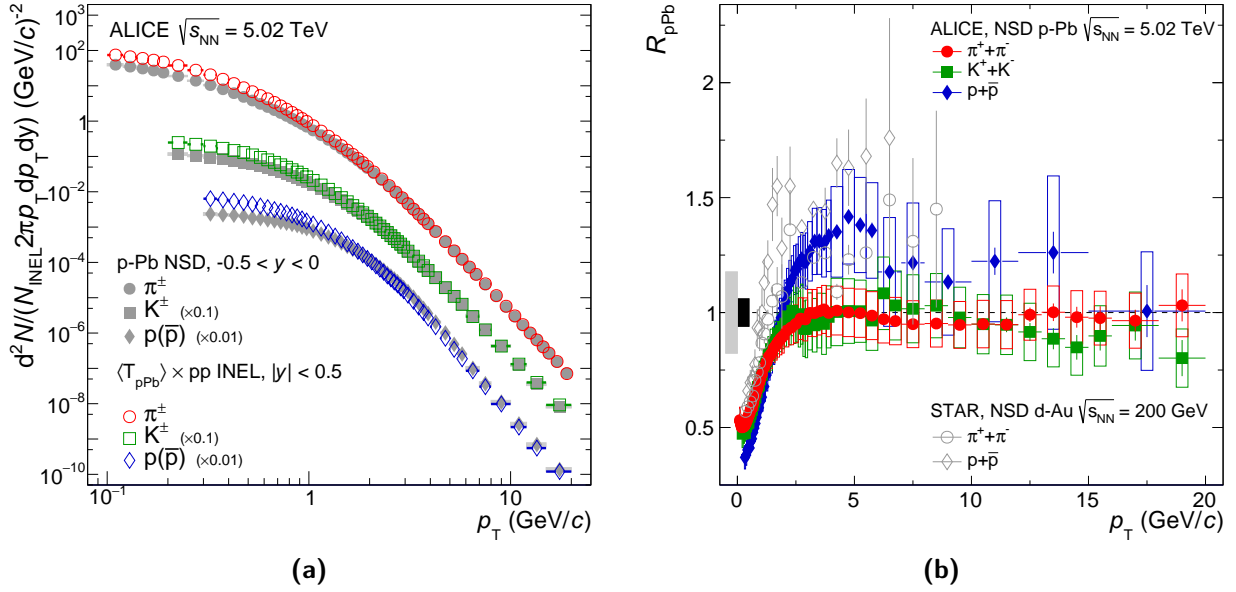


Figure 9.3: (a) Measured invariant yields of π^\pm , K^\pm , and $p(\bar{p})$ in non-single diffractive (NSD) p–Pb collisions at $\sqrt{s_{\text{NN}}} = 5.02$ TeV in comparison with the $\langle T_{\text{pPb}} \rangle$ -scaled INEL pp reference spectra at equivalent collision energy. (b) The nuclear modification factor R_{pPb} as a function of transverse momentum in NSD p–Pb collisions at $\sqrt{s_{\text{NN}}} = 5.02$ TeV for π^\pm , K^\pm , and $p(\bar{p})$ [245]. Results are compared with measurements from BNL STAR in NSD d–Au collisions at $|y| < 0.5$ [298]. Additional normalization uncertainties of 6% (ALICE) and 17.7% (STAR) are shown as filled boxes around unity near $p_T = 0$ GeV/c. Figures are reproduced from Ref. [71].

quantify how the presence of nuclear environment affects the particle production in p–Pb collision with respect to pp. As the spectra have only been measured in V0A multiplicity event classes, the NSD spectrum for all particle species has been obtained by summing the spectra from all multiplicity classes and applying an additional normalization correction ($3.6 \pm 3.1\%$) [242] in order to correct for trigger and vertex inefficiencies (see Section 7.6.3). The resulting NSD p–Pb spectra (open circle) for π^\pm , K^\pm , and $p(\bar{p})$ is shown on the top of the multiplicity-dependent results in Fig. 9.1 where it was scaled for clarity. In a better visualization, the NSD spectra are shown in Fig. 9.3a where the INEL pp reference spectra, scaled by the average nuclear overlap function $\langle T_{\text{pPb}} \rangle$, are plotted in addition. To remind the reader, the overlap function is calculated from a Glauber MC model with the average taken over all events with at least one binary nucleon-nucleon collision. It is defined as $\langle T_{\text{pPb}} \rangle = \langle N_{\text{coll}} \rangle / \sigma_{\text{NN}}^{\text{INEL}}$, where $\sigma_{\text{NN}}^{\text{INEL}}$ (70 ± 5) mb is the inelastic nucleon-nucleon cross section and $\langle N_{\text{coll}} \rangle = 6.9 \pm 0.7$ is the number of binary collisions with $N_{\text{part}} = N_{\text{coll}} + 1$. The scaled pp reference and the NSD p–Pb spectrum are in quite good agreement for all particle species at high p_T (> 10 GeV/c) where particle production is expected to be dominated by fragmentation of hard-scattered partons. In contrast, deviations are seen in the low to intermediate p_T regime, being significantly present for (anti)protons up to about $p_T \sim 6$ GeV/c. The NSD event class in p–Pb collisions corresponds to events in which at least one of the individual proton-nucleus collisions is non-single diffractive based on the Glauber model.

For example, if one imagines an event with three participants and two collisions out of which one is single diffractive and one is non-single diffractive, then it fulfills the NSD definition of p–Pb. The NSD event class is, therefore, best compared to the INEL class in pp collisions. Actually, it would be more natural to use INEL p–Pb collisions since the invariant yields between NSD and INEL event selection might differ in shape and normalization. However, from MC studies, as discussed in Ref. [119], it was estimated that diffractive events cause less than 0.5% change in the spectral shapes only at low p_T (< 2 GeV/ c) while the INEL yields are $\sim 3 - 4\%$ lower with respect to the NSD yields affecting the normalization. The nuclear modification factor can be calculated which, for the case of NSD p–Pb collisions, is defined as:

$$R_{\text{pPb}} = \frac{d^2 N_{\text{pPb}}/dydp_T}{\langle N_{\text{coll}} \rangle d^2 N_{\text{pp}}^{\text{INEL}}/dydp_T} = \frac{d^2 N_{\text{pPb}}/dydp_T}{\langle T_{\text{pPb}} \rangle d^2 \sigma_{\text{pp}}^{\text{INEL}}/dydp_T}, \quad (9.1)$$

where for minimum bias (NSD) p–Pb collisions the average nuclear overlap function, $\langle T_{\text{pPb}} \rangle$, corresponds to $(0.0983 \pm 3.4\%) \text{ mb}^{-1}$ [119]. The inelastic cross section $d^2 \sigma_{\text{pp}}^{\text{INEL}}/dydp_T$ for identified hadron production in INEL pp collisions was obtained by interpolating between data measured at $\sqrt{s} = 2.76$ TeV and at $\sqrt{s} = 7$ TeV, as described in Section 8.2.

Figure 9.3b shows the calculated identified charged-hadron R_{pPb} . The systematic uncertainties on R_{pPb} are largely correlated between adjacent p_T bins which have (together with the statistical errors) sources from both the p–Pb and the pp measurements. Uncertainties among measurements in different collisions are uncorrelated therefore they are propagated directly to R_{pPb} . The total systematic uncertainty on the normalization is the quadratic sum of the uncertainty on $\langle T_{\text{pPb}} \rangle$, the normalization of the pp reference and p–Pb spectra and it amounts to 6.0% as indicated by a vertical scale of the full box at around $p_T = 0$ GeV/ c .

At high p_T ($\gtrsim 10$ GeV/ c), all nuclear modification factors are consistent with unity within systematic and statistical uncertainties, indicating that no strong nuclear effects are present in p–Pb collisions in that p_T regime. It also means that particle production can be described by superimposing $N_{\text{coll}} \approx \sigma_{\text{pp}}/\sigma_{\text{pPb}} \sim 7$ independent pp collisions, consistently with the expectation of binary collision scaling. The initial rise observed in the low- p_T region is attributed to soft particle production mechanism through N_{part} scaling below $p_T = 2$ GeV/ c . At around $p_T \sim 3 - 4$ GeV/ c the charged pion R_{pPb} reaches its maximum and shows saturation from that p_T onward. Remarkably, a comparison of charged pions to preliminary results obtained for neutral pions showed excellent agreement in the entire p_T range within uncertainties, indicating that the particle production mechanism is similar [299]. It is noteworthy that the inclusive charged hadron R_{pPb} shows a moderate enhancement above unity, being however barely significant within the quoted uncertainties [245]. A (more pronounced) enhancement in this particular p_T region was already noticed at lower energies in fixed-target experiments [300, 301] and is commonly referred to as Cronin peak or Cronin enhancement. Also, the charged kaon R_{pPb} is below that of

charged particles. As a matter of fact, without the inclusion of kaons identified from topological weak decays (kinks), kaons seem to follow the trend (in magnitude and shape) of charged hadrons showing a slight enhancement due to initial state multiple scatterings or anti-shadowing. At the same time, the (anti)proton enhancement is about three times larger than that for charged particles. A similar pattern has been observed by STAR and PHENIX collaborations in d–Au collisions at $\sqrt{s_{NN}} = 200$ GeV. In Fig. 9.3b the analogous R_{dAu} is also shown for charged pions and (anti)protons measured in NSD d–Au collisions, which indicates an enhancement in the range $2 < p_T < 5$ GeV/ c yielding to $R_{dAu} = 1.24 \pm 0.13$ and $R_{dAu} = 1.49 \pm 0.17$ respectively for π^\pm and $p(\bar{p})$ [298]. In the same p_T interval, the average (anti)proton R_{pPb} amounts to $\langle R_{pPb} \rangle = 1.286 \pm 0.006$ (stat.) ± 0.151 (syst.), whereas it takes value of $\langle R_{pPb} \rangle = 1.206 \pm 0.015$ (stat.) ± 0.029 (syst.) for $5 < p_T < 10$ GeV/ c , and $\langle R_{pPb} \rangle = 1.126 \pm 0.064$ (stat.) ± 0.282 (syst.) for high p_T (> 10 GeV/ c). This decrease of the nuclear modification factor suggests that the effect can be dominantly attributed to the higher initial energy densities created at larger collision energy at the LHC rather than from the harder initial parton p_T spectra. An enhancement of (anti)protons in the same p_T range is also witnessed in heavy-ion collisions [111, 125], where it is commonly interpreted as radial-flow.

Regarding R_{pPb} , in addition to measurements in minimum bias (event-activity averaged) NSD p–Pb collisions, the event-activity or multiplicity dependence of hard processes would also be interesting to study. It would probe the impact parameter dependence of nPDF modification or, in general, give insight into the soft and hard particle production processes. However, the multiplicity-dependent invariant yields in the entire p_T range are only available in the presented event-activity classes using the forward-rapidity (V0A) estimator. The use of such an estimator suffers from a potential multiplicity bias when one determines the multiplicity-dependent nuclear modification factor, called Q_{pPb} . This effect arises because the increased event multiplicity, associated with the presence of a hard parton-parton scattering, results in categorizing hard-scatter p–Pb events to be in a higher event-activity multiplicity class than that obtained with the multiplicity calibration—which uses minimum bias events typically without a hard scattering. In fact, by cutting on multiplicity (in V0A classes) one biases the hard physics when only a few participants are present. The bias causes large variation of the nuclear modification factor, for example, a kinematics-independent increase (decrease) of the yield in high- and low-multiplicity collisions, which in turn complicates a direct measurement of this quantity. The experiments at the LHC have found several methods to correct for or eliminate this bias. In the so-called “hybrid method” developed by ALICE, p–Pb events are categorized based on the energy of slow neutrons measured in the zero-degree calorimeter far downstream of the Pb nucleus and an estimate of N_{coll} is made from a data-driven approach inspired by the wounded nucleon model [16].

Here, the construction of Q_{pPb} would not allow for drawing any conclusion about event

multiplicity dependence of physics phenomena in p–Pb collisions like suppression or saturation. As discussed in Ref. [16] all the difficulties caused by multiplicity bias can be overcome by using the mentioned hybrid method. Since no identified hadron measurements were performed at low p_T using the suggested method at the time of writing, in the next section, I study the multiplicity dependence of the invariant yield ratios. It allows to further investigate the effects seen for protons and examine whether they are more enhanced with respect to pions as a function of charged-particle multiplicity.

9.3 Transverse momentum and multiplicity dependence of particle ratios

Using particle ratios, one has the advantage that in the ratios the systematic uncertainty associated with the inclusive charged particle p_T spectra normalization cancels. Also, the stronger multiplicity dependence of the spectral shapes of heavier particles seen in Fig. 9.1 is evident when looking at the particle ratios themselves. The p_T -dependent kaon-to-pion (K/π) and the proton-to-pion (p/π) ratios are shown in Fig. 9.4 for low-, mid-, and high-multiplicity p–Pb events, corresponding to V0A event multiplicity classes 60–80%, 20–40% and 0–5%, respectively. The $\sqrt{s_{NN}} = 5.02$ TeV p–Pb results are compared to measurement for INEL pp collisions at $\sqrt{s} = 7$ TeV [247], serving as an approximate baseline, and to those measured in peripheral (60–80% centrality) Pb–Pb collisions at $\sqrt{s_{NN}} = 2.76$ TeV [111]. As it was pointed out earlier, the average multiplicities at mid-rapidity for peripheral Pb–Pb collisions (60–80%) and high multiplicity p–Pb collisions (0–5% V0A class) are comparable. Therefore, it seems to be interesting to compare these collision systems having similar underlying activity, even if the physical mechanisms for particle production might be different. First, the K/π ratios show no multiplicity dependence within the uncorrelated systematic uncertainties. In fact, the results are similar to those for INEL pp and peripheral Pb–Pb collisions. In contrast, the p/π ratios indicate a clear multiplicity evolution at low and intermediate p_T (< 10 GeV/ c) regions which is qualitatively similar to the centrality evolution seen in Pb–Pb collisions [111, 125] and in high-multiplicity d–Au collisions at BNL-RHIC [124]. Moreover, the baryon-to-meson ratio shows a significant enhancement at intermediate p_T around 3 GeV/ c , qualitatively reminiscent of that measured in Pb–Pb collisions [111], where it is generally discussed in terms of collective flow or quark recombination. Namely, the p/π ratios are below the pp baseline for $p_T < 1$ GeV/ c and above it for $p_T > 1.5$ GeV/ c . However, quantitative disagreements are present between p–Pb and Pb–Pb results which can be attributed to the differences in the initial state overlap geometry and the beam energy. The magnitude of the observed effects, i.e. the maximum of the p/π ratio, differs significantly in high-multiplicity p–Pb and central Pb–Pb collisions, by about a factor of 2, the latter being the larger. In the 0–5% V0A multiplicity class of p–Pb, the maximum

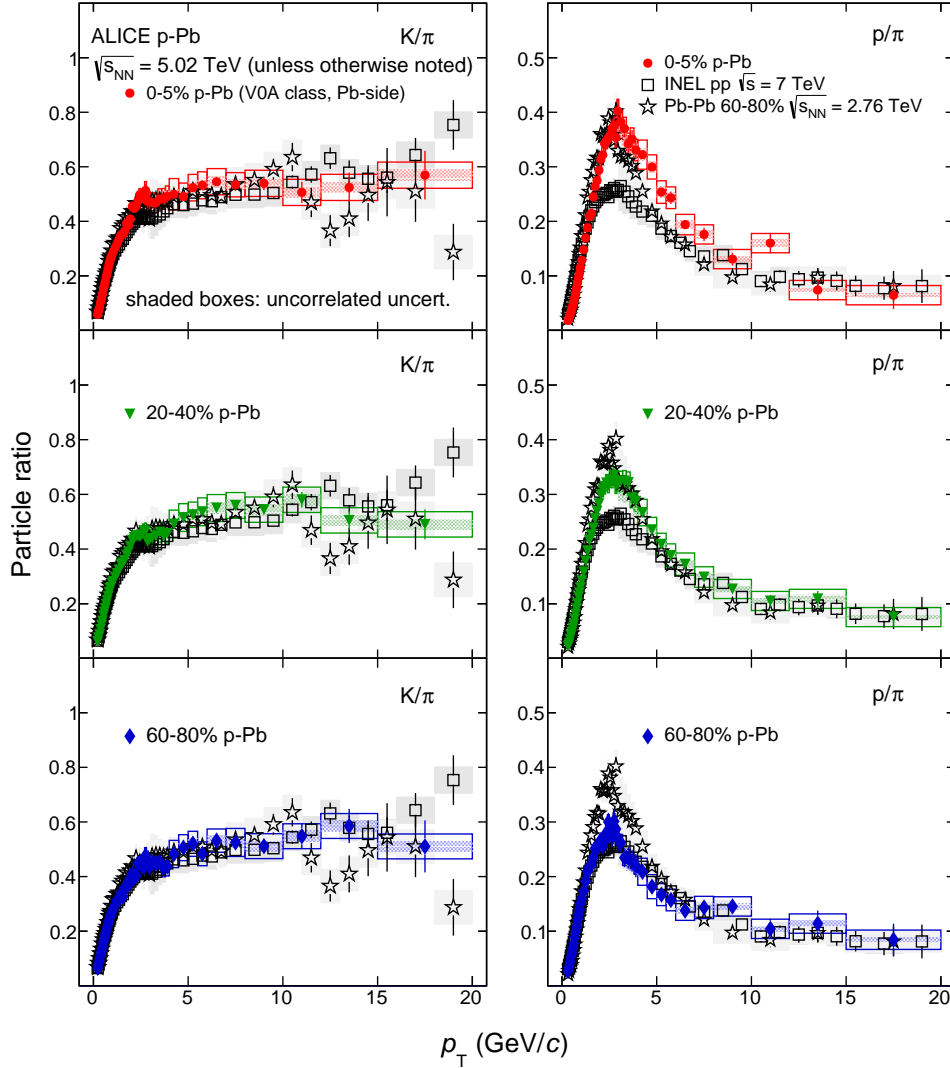


Figure 9.4: Kaon-to-pion (K/π ; left) and proton-to-pion (p/π ; right) particle ratios as a function of p_T for different V0A multiplicity event classes (indicated in the legends) measured in p–Pb collisions at $\sqrt{s_{NN}} = 5.02$ TeV. Results are compared to measurements in INEL pp and peripheral (60 – 80% centrality) Pb–Pb collisions at $\sqrt{s} = 7$ TeV and $\sqrt{s_{NN}} = 2.76$ TeV, indicated by open symbols. The statistical and multiplicity uncorrelated (correlated) systematic uncertainties are plotted as vertical error bars and open (shaded) boxes, respectively. Figure is reproduced from Ref. [71].

of the p/π is close to the 60 – 80% centrality class in Pb–Pb collisions but differs somewhat in shape at lower p_T . These observations suggest that the modification of the (anti)proton spectral shape going from pp to p–Pb collisions could play the dominant role in the Cronin enhancement observed for inclusive charged particle R_{pPb} at $\sqrt{s_{NN}} = 5.02$ TeV reported in Ref. [245]. However, further studies are required based on the multiplicity-dependent measurement of the R_{pPb} , to confirm the results.

The binary nucleon scaling (N_{coll}) behavior shown by the R_{pPb} for all of the investigated hadrons above $p_T \simeq 10$ GeV/ c (see Fig. 9.3b) implies that the particle ratios are similar in pp and p–Pb collisions. Since in the high- p_T regime, where particle production is mainly driven by parton fragmentation, the particle ratios are independent of p_T , the integrated

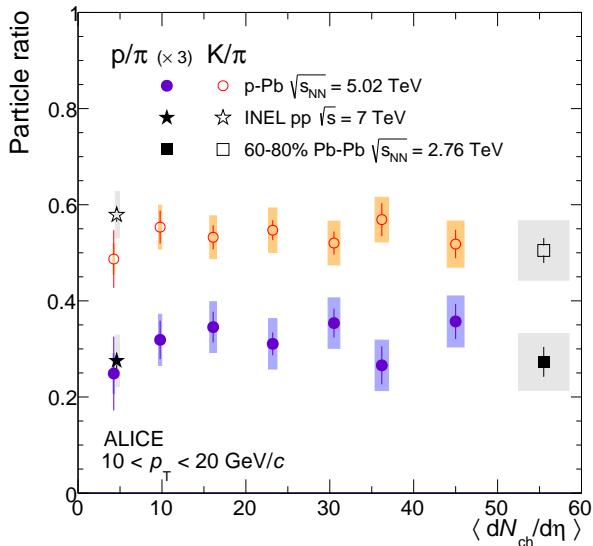


Figure 9.5: Particle ratios as a function of $\langle dN_{ch}/d\eta \rangle$ corresponding to each measured V0A multiplicity class in p–Pb collisions. The p_T -dependent ratios are integrated in the range of $10 < p_T < 20$ GeV/ c . p–Pb results are compared to peripheral (60–80% centrality) Pb–Pb results measured at $\sqrt{s_{NN}} = 2.76$ TeV and minimum-bias INEL pp result obtained at $\sqrt{s} = 7$ TeV. The p/π ratios were scaled by a factor of 3 for clarity. $\langle dN_{ch}/d\eta \rangle$ values are taken (and calculated) based on Refs. [25, 111, 297]. Note that this kaon-to-pion (proton-to-pion) “high- p_T ” ratio is ~ 4 (~ 2) times larger than that integrated in the entire p_T range [53]. Figure is reproduced from Ref. [71].

p_T -dependent particle ratios (in the range $10 < p_T < 20$ GeV/ c) are studied to demonstrate the precision with which the binary-collision-scaled expectation for pions, kaons, and (anti)protons is satisfied. In Fig. 9.5 the resulted p_T -integrated p/π and K/π particle ratios are shown as a function of charged-particle multiplicity densities $\langle dN_{ch}/d\eta \rangle$ measured at mid-pseudorapidity corresponding to different V0A multiplicity classes determined in p–Pb collisions [53]. It is worth noting that the K/π and p/π ratios are respectively ~ 4 and ~ 2 times larger than that integrated in the entire p_T interval [53]. These ratios are compared to minimum-bias INEL pp results at $\sqrt{s} = 7$ TeV and peripheral (60–80% centrality) Pb–Pb results [111] at $\sqrt{s_{NN}} = 2.76$ TeV, obtained by integrating them in the same p_T interval at high p_T . Such a representation of the particle ratios as a function of multiplicity for different collision systems can be thought of as viewing them as a function of the size of the collision systems. One can see in Fig. 9.5 that the ratios show no apparent evolution with charged-particle multiplicity within the quoted uncertainties ($\sim 10 - 20\%$). Furthermore, it was shown in Ref. [111] that in Pb–Pb they are independent of the centrality of the collision which, in turn, allows one to conclude that particle ratios are system-size independent at high p_T . Further measurements using LHC Run 2 (and Run 3) data with improved precision might reveal possible particle-species dependent effects.

9.4 Comparison to theoretical calculation

Figure 9.6 compares the R_{pPb} measurements to recent predictions for π^\pm , K^\pm , and $p(\bar{p})$ nuclear modification factors from next-to-leading order (NLO) pQCD calculations. The NLO pQCD calculation, based on Ref. [251], is performed at $y = 0$ and it employs the CT10 free proton PDFs and the CT10 PDFs modified by the EPS09 NLO [137] nuclear modifications. In addition to the nuclear modifications, these calculations also depend on the parton-to-hadron fragmentation functions. The current calculation uses DSS FFs, however one has to

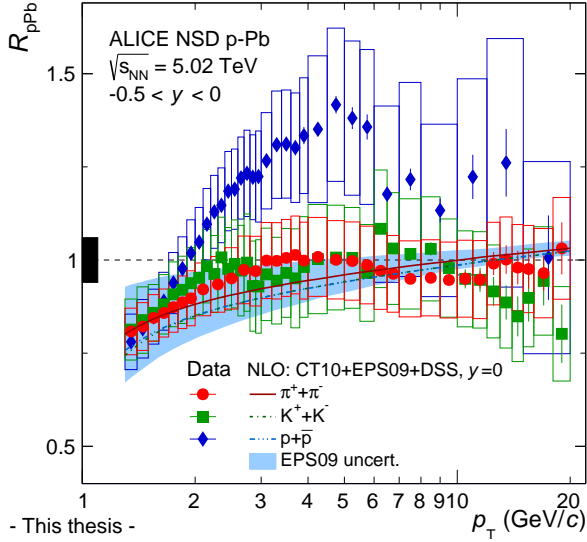


Figure 9.6: The nuclear modification factor R_{pPb} as a function of transverse momentum in NSD p-Pb collisions at $\sqrt{s_{NN}} = 5.02 \text{ TeV}$ for π^\pm , K^\pm , and $p(\bar{p})$ in comparison with NLO pQCD calculation (lines) using CT10 proton PDFs with EPS09 [137] nuclear PDFs and DSS FFs. Shaded band indicates the uncertainty calculated from the error sets of EPS09 using the DSS FFs.

remember, as discussed for the case of pp data in Section 8.4.2 and conjectured in Ref. [289], that none of the currently available sets of FFs can optimally reproduce the LHC data. The uncertainties are calculated from the error sets of EPS09 using the DSS FFs; those related to the proton PDF, scale variations and FF are negligible.

As shown in the figure, the NLO calculation captures the trend for mesons accurately. A similar level of agreement is reported for charged hadrons in Ref. [302], which is also valid separately both for p-Pb and pp data; and the data-to-theory ratios are approximately flat for $p_T > 10 \text{ GeV}/c$. The calculation assumes independent hadronization and results in no considerable differences between different particle species. On the other hand, the same calculation fails to reproduce the Cronin enhancement of (anti)protons at intermediate p_T ($2 \lesssim p_T \lesssim 6 \text{ GeV}/c$). This likely to be caused by the missing final state effects which are not taken into account in the calculation.

CHAPTER 10

Summary

This Ph.D. thesis mainly focuses on the measurements of single-inclusive charged particle transverse momentum (p_T) spectra of pions, kaons, and (anti)protons at high p_T (up to 20 GeV/ c). Results are presented in inelastic (INEL) proton-proton (pp) collisions at $\sqrt{s} = 7$ and $\sqrt{s} = 13$ TeV, and in non-single diffractive (NSD) proton-lead (p-Pb) collisions at $\sqrt{s_{NN}} = 5.02$ TeV at the mid-rapidity region, using the ALICE detector at the CERN LHC. The interpretation of the jet-quenching and bulk-collective effects observed as signatures of the strongly interacting Quark-Gluon Plasma, created in ultra-relativistic heavy-ion collisions, requires comparisons with control (or reference) measurements carried out in pp and p-Pb. Proton-lead collision systems are thought to be sensitive to cold nuclear matter effects that is the modification of the matter due to the binding of nucleons in the nuclei. The measurements performed in p-Pb collisions constrain how much of the observed suppression in Pb-Pb may be expected from initial state rather than final state effects. Therefore, they serve as a necessary and important reference for the heavy-ion results.

Intriguing results have emerged from the analysis of these (reference) collision data in high-multiplicity events at the CERN LHC. Results on particle production revealed phenomena which are similar to those seen in Pb-Pb collisions, where they are attributed to bulk collective effects, which is one of the key experimental signatures of the QGP. Besides, the absence of obvious jet quenching signatures in p-Pb collisions is notable, and it suggests that other physical mechanisms could also play a role in producing collective-like behavior in small collision systems. The origin of these phenomena is investigated, and the analysis of pp and p-Pb collision data presented in this work provides further inputs to this discussion.

In addition to the detailed analysis on collision data in small systems from ALICE, my work was complemented with phenomenological studies to search for collective behavior in low-multiplicity pp events as well as with the determination of basic characteristics of an asymmetric multi-wire proportional chamber.

My main scientific results are summarized in the following points:

1. I performed a double-differential study in pp collisions at LHC energies using two general-purpose Monte Carlo event generators, such as PYTHIA 8 and EPOS 3, which are extensively applied in high-energy collider and cosmic-ray physics. I explored an observable which is aimed at ruling out or validating the underlying physics mechanism (hydrodynamics or color reconnection) generating radial flow patterns in pp collisions. To this end, I studied the p_T spectra of charged pions, kaons and (anti)protons as a function of charged-particle multiplicity and the p_T^{jet} of the leading (highest transverse

- momentum) jet. I found that in extremely-low multiplicity events, it is possible to find an event class where radial flow patterns arise — regardless of the weakness of hydrodynamics and color reconnection effects in those events. I showed that the agreement between the blast wave model and the simulation improves with the increase of the leading jet p_T^{jet} , suggesting that the presence of the collective-like behavior is caused by jets. The results indicate that the average transverse expansion velocity $\langle\beta_T\rangle$ is more affected by jets in PYTHIA 8 than in EPOS 3. I found that in high-multiplicity events, generated by EPOS, the magnitude of the p/π ratio at intermediate p_T increases with decreasing p_T^{jet} . No such evolution is present in PYTHIA, suggesting that hadrochemical composition is very different between PYTHIA 8 and EPOS 3 in this event class. The results are published in Ref. [174], and motivate the high-energy physics community to perform a similar analysis using experimental data from BNL RHIC and CERN LHC.
2. I measured the invariant yields of charged pion, kaon, and (anti)proton in non-single diffractive p–Pb collisions at $\sqrt{s_{\text{NN}}} = 5.02$ TeV as a function of charged-particle multiplicity up to $p_T = 20$ GeV/ c at mid-rapidity. I found that at intermediate p_T ($2 - 10$ GeV/ c) the p/π ratio shows a monotonic, precipitous increase with multiplicity towards higher values. However, a similar effect is not present for the K/π ratio. I showed that the p_T -dependent structure of such an increase is qualitatively similar to those observed in pp and Pb–Pb collisions, albeit the underlying particle production mechanism might be different. I found that at high p_T (> 10 GeV/ c) the p_T -integrated particle ratios are system-size independent for pp, p–Pb and Pb–Pb collisions [71, 223].
 3. I measured the invariant yields of charged pion, kaon, and (anti)proton in minimum bias inelastic pp collisions at $\sqrt{s} = 7$ TeV up to $p_T = 20$ GeV/ c at mid-rapidity. I determined the $\sqrt{s} = 5.02$ TeV pp reference cross section based on previously published data at $\sqrt{s} = 2.76$ TeV and those measured in this work at $\sqrt{s} = 7$ TeV, and constructed the nuclear modification factor R_{pPb} for the studied particle species. I showed that at intermediate p_T the (anti)proton R_{pPb} indicates a characteristic enhancement, while pions and kaons show little or no nuclear modification, which is compatible with next-to-leading order (NLO) pQCD predictions obtained with the EPS09 nuclear parton distribution functions. This observation confirms that the modest enhancement reported earlier for unidentified charged particles can be attributed to the modification of the proton spectral shape going from pp to p–Pb collisions. I found that the R_{pPb} for charged pions, kaons, and (anti)protons at high p_T is consistent with unity within statistical and systematic uncertainties, indicating binary nucleon scaling [71, 223, 303].
 4. I measured the invariant yields of charged pion, kaon, and (anti)proton in minimum bias inelastic pp collisions at $\sqrt{s} = 13$ TeV up to $p_T = 20$ GeV/ c at mid-rapidity. I found that the identified particle spectra are consistent with the empirical x_T scaling over the accessible x_T range in the hard scattering regime. I showed that a relation

between the charged pion and kaon invariant yields is given by the transverse mass scaling for $p_T \gtrsim 6 \text{ GeV}/c$, however a significant deviation from the empirical scaling law is observed below $p_T \simeq 6 \text{ GeV}/c$ in the K/π ratio. I found that the p_T -dependent p/π ratio in the intermediate p_T region shows a modest departure towards higher p_T going from $\sqrt{s} = 7$ to $\sqrt{s} = 13 \text{ TeV}$, while the K/π ratio does not feature any dependence on collision energy. The results for the p_T -integrated particle ratios indicate saturation in the LHC-energy regime. Results for the average transverse momentum $\langle p_T \rangle$ show a monotonic increase with center-of-mass energy in minimum bias pp collisions, with the $\langle p_T \rangle$ being larger for heavier hadrons [230, 286]. The comparison of data to NLO pQCD calculations shows that the theoretical calculations overpredict the measured identified particle yields, suggesting that the fragmentation functions are not well tuned at the accessible kinematic regime at the LHC.

5. I constructed and successfully tested a prototype asymmetric multi-wire proportional chamber with a reduced size, based on techniques developed by the Hungarian RE-GARD Group [212]. For this purpose, I was involved in numerous test beam campaigns at the CERN PS accelerator, and I measured the position resolution of several prototype chambers [210]. Using their analog data, I found significant improvement, by more than a factor of 6 with respect to the digital readout, of the position resolution of the prototype chamber measured on their segmented cathode planes [212]. I contributed with a physics performance study to the Letter of Intent (LoI) document of the ALICE VHMPID where the results obtained from the detector and physics performance studies are summarized. I wrote a dedicated section (Section 4.4.2) in the LoI, including my Monte Carlo simulation studies performed using identified two-particle angular correlations to help to verify the applicability of the ALICE VHMPID for physical analysis [209, 214].

To conclude, the presented measurements in pp and p–Pb collisions combined with previously published data at lower p_T provide a comprehensive dataset of the charged pion, kaon, and (anti)proton p_T spectra with unprecedented systematic precision and p_T reach. The obtained results have raised questions whether some form of collectivity, similar to those observed in heavy-ion collisions where they are attributed to the QGP, is present also in these small collision systems. These observations might be naturally related to comparable or even common physics origin, for example, to the existence of a QGP. The formation of a deconfined system in such small collision systems, even in minimum bias case, can not a priori be excluded, since the energy density might reach and go beyond the critical value.

In spite of the observed effects, more detailed investigations are still needed—on both the theoretical and experimental sides—to further understand the physics in the small collision systems. Hence, experimentally, p–Pb collisions performed during Run 2 of the LHC at $\sqrt{s_{NN}} = 5.02$ and 8.16 TeV extend the available statistics and the existing collision

energy to provide measurements at higher multiplicity and energy density. As the most significant contribution to the systematic uncertainties of the presented measurement came from the yield extraction procedure, the increased statistics would allow both the statistical and systematic uncertainties of the multiplicity-dependent measurement to be reduced.

One has to remember, however, that the measurement of jet-quenching related observables, such as the nuclear modification factor, in p–Pb becomes more challenging, on the one hand, due to the increasing contribution from multiple-parton interactions and on the other due to the complex interplay of hard, multiple semi-hard and soft processes, which need to be disentangled from nuclear modification. Apart from p–Pb collisions, it will also be of crucial importance to study pp collisions as a function of multiplicity at the highest available collision energy which will then be comparable (in multiplicity) to p–Pb measured at lower collision energy.

APPENDIX A

Kinematic variables

This appendix introduces the basic kinematic variables used throughout the thesis. A right-handed Cartesian coordinate system, identical to that of the ALICE Experiment [189], and the commonly adopted convention of $\hbar = c = 1$ are applied.

A particle, with the energy E , the rest mass m , and the momentum p , is described by its four-momentum $p_\mu = (E, \mathbf{p}) = (E, p_x, p_y, p_z)$ with p_z being the momentum along the beam axis. The three-momentum of a particle can be decomposed into its longitudinal- and transverse momentum, defined to be $p_L = p_z$ and $p_T = \sqrt{p_x^2 + p_y^2}$, respectively, with its magnitude being $p = \sqrt{p_L^2 + p_T^2}$. The energy of a given particle is defined to be $E = \sqrt{m_T^2 + p_L^2}$ with $m_T = \sqrt{m^2 + p_T^2}$ being the transverse mass. From the measured momentum and energy of the particle the rapidity can be derived $y = \frac{1}{2} \left(\frac{E+p_L}{E-p_L} \right)$. The rapidity transforms additively under a Lorentz boost along z . Hence, rapidity differences are invariant under longitudinal boosts and remain the same in all collinear frames. To characterize the rapidity of a particle, we need to measure its E and p_L . However, the determination of the rapidity is complicated because E cannot be easily measured without determining the particle type. In many experiments, it is only possible to measure the emission angle θ . Thus, the pseudorapidity η is employed for the case of $E \gg m$ and it is defined as $\eta = -\ln \tan \frac{\theta}{2}$. For ultra-relativistic particles ($E \simeq p$) $y \approx \eta$, that is the rapidity of the particle only depends on θ . In asymmetric collisions, in which the laboratory frame and the center-of-mass (c.m.) frame do not coincide, the particles are shifted in rapidity with

$$\Delta y \simeq \frac{1}{2} \ln \frac{Q_1 A_2}{Q_2 A_1}, \quad (\text{A.0.1})$$

where Q_1, Q_2 are the charges, and A_1, A_2 are the atomic mass numbers of the two different colliding systems.

For two colliding nuclei with four-momenta p_1^μ, p_2^μ and rest masses m_1, m_2 , the center-of-mass energy is calculated from the Lorentz-invariant s Mandelstam variable being $s = (p_1 + p_2)^\mu (p_1 + p_2)_\mu$. The c.m. energy is the square-root of s and is given by $\sqrt{s} = \sqrt{2(E_1 E_2 + \mathbf{p}_1 \mathbf{p}_2) + m_1^2 + m_2^2}$. In symmetric collision systems, where $\mathbf{p}_1 + \mathbf{p}_2 = 0$ per definition, and $E_1 = E_2$, thus it is $\sqrt{s} = 2E$. In the general case of two particle beams by using the approximation that the collision energy is much larger than the projectile masses, $\sqrt{s} \approx 2\sqrt{E_1 E_2}$. In a heavy-ion collision the collision energy is commonly given by the c.m. energy of the nucleon-nucleon pair of the two ions $\sqrt{s_{\text{NN}}}$. In the per-nucleon representation, the energies E_i have to be normalized by the corresponding mass number A_i . Additionally, in the case of collisions taking place at the LHC, the particle momenta are directly related

by $p_i = Q_i p_{\text{proton}}$. This is due to the two-in-one magnet design of the LHC [41]. Therefore, with $E_i \approx p_i$, it follows

$$\sqrt{s_{\text{NN}}} \approx 2p_{\text{proton}} \sqrt{\frac{Q_1 Q_2}{A_1 A_2}} \approx 2E_{\text{proton}} \sqrt{\frac{Q_1 Q_2}{A_1 A_2}}. \quad (\text{A.0.2})$$

The invariant differential particle yield is defined as the number of particles in a $dy dp_{\text{T}}$ phase space segment, which is commonly described in cylindrical coordinates:

$$E \frac{d^3 N}{dp^3} = E \frac{d^2 N}{p_{\text{T}} dp_{\text{T}} p_{\text{L}} d\phi} = \frac{d^2 N}{p_{\text{T}} dp_{\text{T}} d\phi dy}, \quad (\text{A.0.3})$$

where $dy = \frac{dp_{\text{L}}}{E}$ and $\frac{d^3 p}{E}$ is Lorentz invariant which can be expressed in terms of experimentally measurable quantities as follows: $\frac{d^3 p}{E} = d\mathbf{p}_{\text{T}} dy = p_{\text{T}} dp_{\text{T}} d\phi dy = m_{\text{T}} dm_{\text{T}} d\phi dy$.

For unpolarized beam, the particle production is axially symmetric. Hence there is no ϕ dependence and a factor of $1/2\pi$ results in the final form

$$\frac{d^3 N}{dp^3} = \frac{d^2 N}{2\pi m_{\text{T}} dm_{\text{T}} dy} = \frac{d^2 N}{2\pi p_{\text{T}} dp_{\text{T}} dy}. \quad (\text{A.0.4})$$

Usually, the measurement is performed in terms of pseudorapidity η instead of rapidity y , which requires particle identification and that is not always possible to perform. In this case, the particle yield is calculated by changing variables from (y, p_{T}) to (η, p_{T}) : $\frac{d^2 N}{d\eta dp_{\text{T}}}$. The transformation is given by the Jacobian

$$\eta(y) = \sinh^{-1} \left(\frac{\sqrt{m^2 + p_{\text{T}}^2}}{p_{\text{T}}} \cdot \sinh y \right). \quad (\text{A.0.5})$$

The measurements of particle spectra are generally constrained both in y and in p_{T} . To describe the whole range of the p_{T} spectrum, one has to extrapolate to the unmeasured kinematical regions, i.e. to zero and ‘‘infinite’’ transverse momenta. The extrapolation in p_{T} is not unique and various fit functions can be used. In this thesis, the Lévy–Tsallis function [272] is used to extract spectra properties (e.g. p_{T} -integrated yields dN/dy), which is capable of describing the p_{T} distribution in the entire measured p_{T} range rather well:

$$\frac{d^2 N}{dy dp_{\text{T}}} = p_{\text{T}} \frac{dN}{dy} \cdot \frac{(n-1)(n-2)}{nC(nC + m(n-2))} \cdot \left(1 + \frac{m_{\text{T}} - m}{nC} \right)^{-n}, \quad (\text{A.0.6})$$

where c , N , and the yield dN/dy are free parameters. The function has an inverse slope parameter C to describe low- p_{T} part of the spectrum and the exponent n of the high- p_{T} power-law tail.

APPENDIX B

Aspects of improved position resolution of a novel MWPC

This appendix is dedicated to shortly discuss the important aspects for improved position resolution measured with a novel asymmetric multi-wire proportional chamber constructed with small size [212]. Such a prototype chamber is based on the so-called Close Cathode Chamber technology developed by the MTA Lendület Innovative Detector Development Research (REGARD) group at the Wigner RCP in Budapest. The technical details of the construction of the CCCs, as well as their performance, have been presented in several earlier works of the REGARD group [208, 211–213]. In construction of a small-sized detector — having finer pad segmentation (i.e. larger granularity) with respect to the general layout — the requirements of having good position resolution and low material budget were kept under focus without worsening the mechanical stability and the performance of the detector. A specific data analysis technique was used in order to extract the best possible position resolution in the current layout.

B.1 Test beam setup

The measurement setup, shown in Fig. B.1, contained the photon detector along with the pressurized radiator vessel as well as the small-sized CCC MIP detectors to arrange the VHMPID prototype [209, 210]. Both in the front and the rear, the setup contains two CCCs, aligned along the beam line defined in z -direction, to provide reliable beam definition during the tests.

The setup was installed downstream at the T10 beamline located in the East Hall experimental area [304] of the CERN PS accelerator during the test beam campaign in June–July 2012. The T10 is a secondary beam line produced from a $p = 24 \text{ GeV}/c$ primary proton beam slowly extracted from the Proton Synchrotron. The beam is delivered uniformly with about 400 ms spill¹⁴ which, depending on scheduling, is provided typically once or twice per minute. It provides secondary (either positively or negatively charged) particles such as electrons and pions with small contamination of muons, kaons, and protons in the momentum range of $p = 1 - 7 \text{ GeV}/c$. As a standard equipment of the beam line, a threshold Cherenkov counter was used to provide e^- signal only which can be included in the trigger condition or in the offline tagging of events. The beam stopper at the end of the beam line with a combination of scintillators in front and behind of it was suitable for muon veto by effective selection of

¹⁴The spill is defined as the duration time the beam particle extraction lasts.

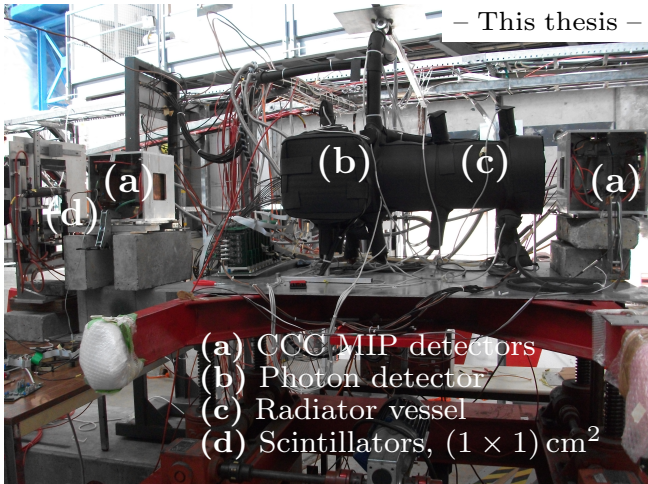


Figure B.1: Side view of the test beam setup at the T10 beamline located in the East Hall experimental area of the CERN PS accelerator. The main components of the setup are indicated in the legends.

charged pions. The small contamination of protons was unnecessary to be identified since in the applied momentum range they do not induce Cherenkov ring in the VHMPID at all.

The standard trigger definition (which was occasionally changed for different kind of studies) included the beam trigger provided by the time coincidence of two, suitably arranged pairs of scintillators along the beam, in logical AND with the spill start signal. The front and back scintillators define $(1 \times 1) \text{ cm}^2$ and $(20 \times 20) \text{ cm}^2$ effective area, respectively, covering the full beam cross section. The nominal beam optics was made available to change by setting the currents of the bending magnets and the position of the horizontal and vertical collimators. The former helped to alter the deflexion which implied the change of the momentum of the beam while the latter helped in setting the particle rate. With the above-mentioned settings, the typical beam intensity was kept around $10^3 - 10^4$ particles/spill.

Given the small effective detector area of the MIP chambers, an accurate position alignment along the beam was needed in order to maximize the number of tracks passing through their active surface. For this reason, they were installed in an Al box which could be then mounted easily on an $X - Y$ -table capable of moving in the x - and y -directions. The box was opened on both sides along the beam in order to avoid unwanted secondary interactions with the material. During assembling each side of the box was able to be removed.

For the data acquisition (DAQ) system the standard HMPID electronics were used, integrating this way the CCCs into the standard data-transfer system. The required operating low voltages for the readout electronics were provided by low-voltage suppliers placed inside the beam area. The high-voltage supply for the detector itself as well as for the scintillators were provided from the counting room.

The triggered data collected in a Front-End Electronics (FEE) card are transferred to the DAQ via standard ALICE Detector Data Link [305]. The main digital component of the FEE card is the DILOGIC chip which performs zero suppression after the digitization [306]. The pedestals are taken before each run which are then loaded into the DILOGIC via the DDLs. Afterwards, the physics data transferred through the DDLs are buffered in the ALICE

Readout Receiver Board (RORC) located in the counting room. The data fragments collected from the RORCs are then built into one sub-event which is — in case of global runs — directed to the event-builder computer. This latter step during test beams is skipped since the data were taken in stand-alone mode and, in turn, recorded locally. The resulted raw data for a given run then was converted by AliRoot [233] — using HMPID-specific reconstruction routines — to ASCII output format which was better suited for my analysis framework.

B.2 Data analysis

The reconstruction of tracks passing through the active volume of the CCC is based on a sequence of algorithms I developed using object-oriented program language. The basic methods well known in HEP experiments were adopted and their simplified versions were implemented for the current work. The reconstruction algorithm starts with the raw, ASCII-converted data on a digit level. For each run, the pad and field-shaping wire (field wire (FW) in the following) coordinates and their appropriate charges (in ADC units) are stored on an event-by-event basis. These informations are gathered together with the event time stamp for every readout channel which were participating in the readout. Furthermore, at this stage for the sake of data reduction zero suppression is applied. It is based on a typically $1 - 2\sigma$ cut imposed on the pedestal values taken before every physics run.

The presented layout of the CCC has two-dimensional projective geometry which means that track coordinates measured in the wire and pad directions are treated independently. The logic of this separation is also kept during the analysis. First, a simple calibration test was run in order to ensure the good quality of the data. This included the removal of noisy FEE channels from further analysis in order to eliminate fake tracks for the cluster finder algorithm. After the calibration, the cluster finder was initiated. A certain readout channel (pad or wire) is defined as “fired” when a produced signal on it is larger than a pre-defined threshold value. Every fired channel (referred to as hit in the following) in the chamber can be collected into clusters based on the fired neighboring channels. Figure B.2 illustrates the situation for a randomly-chosen event from one run taken during beam test environment provided by $p = 6 \text{ GeV}/c$ pions at the CERN PS T10 East Hall area. The particle beam is coming along the z direction approximately perpendicular to the layers. Channels showing no physical hit (i.e. being below threshold) marked as “.” whereas those containing any hit (either in the wire or pad directions) are marked as “X”. The number of consecutive hits defines the size of the cluster which position is calculated. In case of digital readout to each FW/Pad hit an (in)efficiency tag is assigned which is set based on the simple geometrical average called as the centroid of the total charge. With this method a detection efficiency larger than 99% can be reached. In case of analog readout — from which the digital output is also derived — the collected ADC charges were considered. Due to the possibility of overlapping clusters, a standard pre-selection is applied. A simple unfolding routine is

B.3 Measurement results on position resolution

The position resolution of the chamber is calculated from the difference between the reconstructed centroids of clusters and the track intersection calculated from track residuals. During the beam test a dedicated measurement was done to determine the best possible position resolution σ of the chambers, both for pads (σ_{PAD}) and field wires (σ_{FW}). Also, the σ resolutions were evaluated by using both analog and digital readout and the obtained results were compared to each other. From performance studies it is shown that the resolution deteriorates with increasing angle of incidence which, in turn, results less precise position resolution. Therefore, the measurement has been realized by exposing the four aligned chambers to the particle beam providing approximately perpendicular tracks to the pads and the field wires. The accuracy with which the position can be determined depends on a number of other parameters such as: the diffusion of electrons and positive ions, the spread of the discharge along the wire, and the effect of δ -electrons.

In this study, a sub-sample of the selected events was defined by requiring exactly one hit in each of the four chambers. A track fit is performed in both horizontal and vertical directions, and the extrapolated impact position of the track to one of the inner/outer chamber is calculated. The operational parameters of the chambers were set to nominal values where detection and tracking efficiencies were optimal. For this study, one high statistics run was analyzed. With standard scintillator triggers about 70 triggers have been collected during one spill, resulting in $\sim 95 \times 10^3$ recorded events in total.

For digital readout, ideally when it is known accurately which pad or field wire was closest to the particle's track, one expects position resolution in RMS of $1/\sqrt{12}$ times the position segmentation. In case of pad and anode segmentation this results about 1.15 mm and 0.58 mm resolutions in RMS, respectively. As demonstrated in the left panels of Fig. B.3a and B.3b the measured values are quite close to these expectations.

In the case of analog readout for the pads, the center-of-gravity of clusters has been considered. The induced signals on the pads are largest on the pad(s) neighboring to the anode wire on which the avalanche took place. The intersection point can simply be estimated as $\sum_i Q_i y_i / \sum_i Q_i$, where Q_i is the charge measured on pad i with its coordinate being y_i [307]. For the current situation, a tighter track selection criteria was applied with respect to the standard one presented so far. This implies the selection of tracks which approximately hit a certain field wire in the very first chamber counting from the incoming particle beam. This is done by a cut imposed on the position correlation between tracks having three FW clusters in the first chamber, and those that were extrapolated from the 2nd and 4th chambers based on their pad cluster information. For the above-selected sub-sample of tracks the correlation of pad positions between the 2nd and the 4th chambers can be calculated and the result is shown in Fig. B.4. This figure serves as a quality check from which one can immediately see

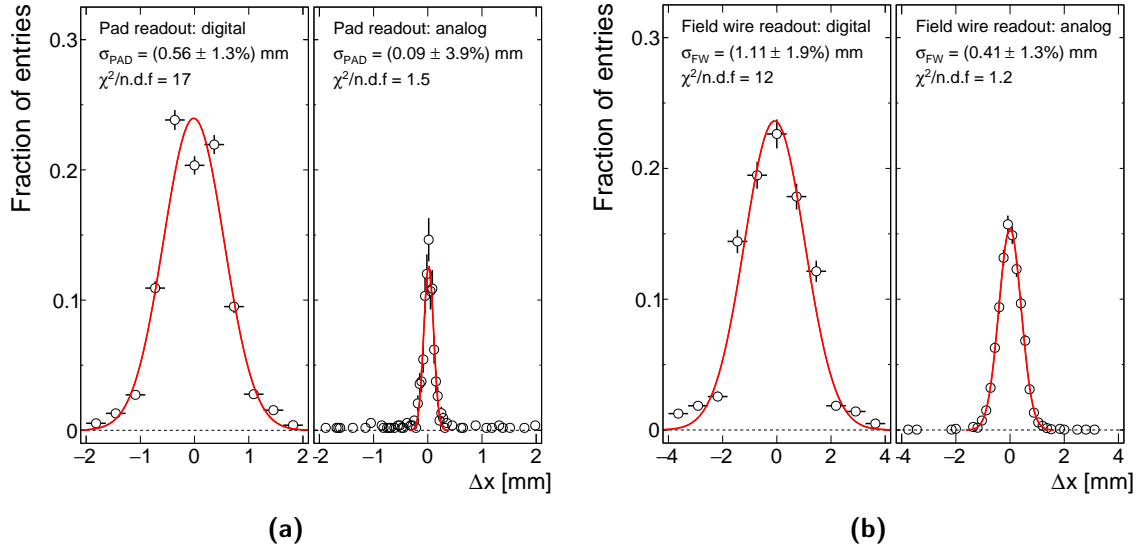


Figure B.3: Position resolution measured on (a) pads and on (b) field wires of the small-sized CCC MIP chamber. Left and right panels of each figure refer to digital and analog readout, respectively. The quantity Δx indicates the difference between the reconstructed centroids of clusters and the track intersection calculated from track residuals. The curves are single Gaussian fits to the data. Figures are reproduced from Ref. [212].

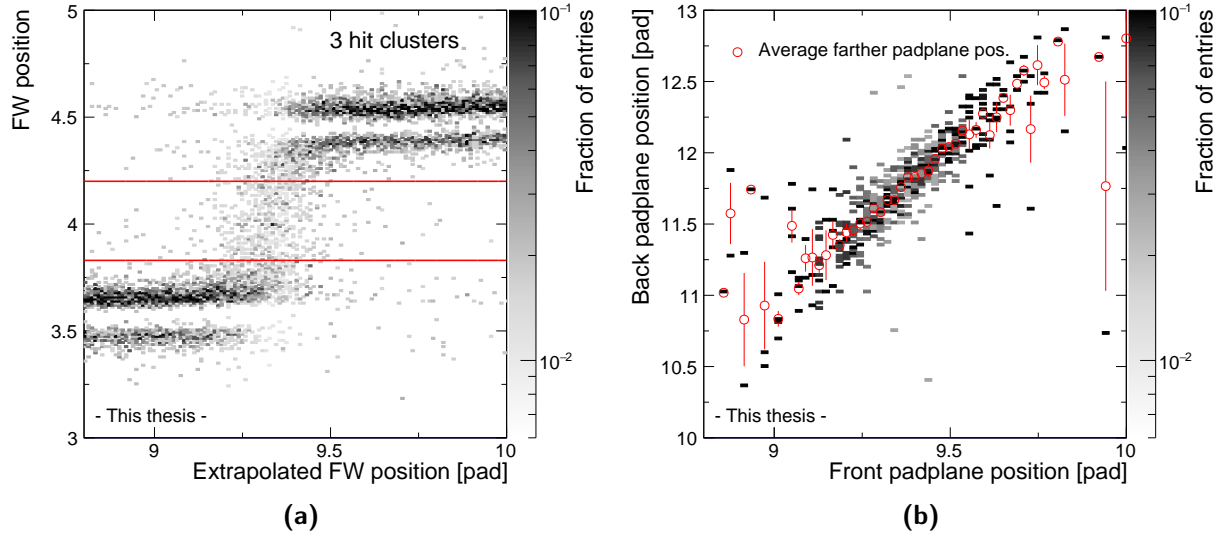


Figure B.4: (a) Correlation between measured (including 3-hit clusters) and back-calculated (based on PAD informations) FW positions. A specific FW position is selected inside the solid lines given as $y = 4 \pm 0.2$. (b) Correlation between cluster positions measured on pads of the 2nd and 4th chambers. See the text for details.

the goodness of the position resolution (i.e. the spread of the points), and the angular divergence of the tracks (mainly caused by beam divergence and multiple scattering). Using these informations, the position resolution on the pads of the 2nd chamber can be calculated by measuring the difference between the interpolated pad position and the centroid of the pad cluster of the original track. The interpolation is done using the 1st (FW direction) and 3rd (PAD direction) chambers. The resulted distribution — after the conversion to mm units — is

fitted by a Gaussian distribution and, in turn, the position resolution σ_{PAD} can be obtained. The right panel of Fig. B.3a shows the obtained position resolution of $\sigma_{\text{PAD}} = 90 \mu\text{m}$ with relative error of around $\pm 4\%$. Obviously, it is an improvement by more than a factor of 6 with respect to the case obtained by digital readout. The improvement between digital and analog readout is typically around this magnitude which has been shown earlier in Ref. [307].

For the case of field wires one cannot use the center-of-gravity method since the induced signals—caused by the avalanche process on the sense wires—among adjacent wires share to first approximation equal charges. In addition, since the two signals are not exactly the same the charge sharing method presented in Ref. [308] has been incorporated for the current study. The position resolution of FWs was calculated using the same chamber which was used previously for the determination of the resolution on the pads. A quantity, denoted as Q_{shared} , proportional to the charge sharing between the FWs is defined. It is calculated from the information relying on three FWs in the vicinity of the particle trajectory. Moreover, it takes into account the two largest ADC charges and the absolute position of the middle FW. Q_{shared} is calculated event-by-event and correlated with the beam position on the same chamber. The beam is localized and determined from the interpolated position of the two outer reference chambers based on their pad informations.

Figure B.5a shows the obtained correlation. The inset plot is zoomed into the range around a cluster where the average Q_{shared} value is indicated by red open circles. The clustering effect along the FWs is visible showing discrete steps occurring at odd values in pad units which refer to places where the particle hits the FW—showing strong localization. The slope of the clusters around their centers shows the left-right charge sharing effect which can be better seen in the projection of Q_{shared} along its y -axis in Fig. B.5b. The two distinct peak indicates those tracks which pass the corresponding wire on its left/right side. Based on the correlation presented in Fig. B.5a, for every Q_{shared} the average cluster position in pad units is calculated which, in turn, helps to identify the position (in pad units) of the particle's track for every FW. In the next step, it is straightforward to calculate the difference between the position calculated from the reconstructed centroids of clusters based on pad information and the position based on the charge sharing between the FWs. Figure B.5c reports such a difference as a function of beam position provided by the outer reference chambers. The wave-like evolution along the x -axis is the feature of the applied method. It is worth noting that one would expect a uniform distribution around $\Delta x = \pm 1$ pad in the case when only digital information—regarding the FW's position—would be available. The distribution of the difference, shown in the right panel of Fig. B.3b in mm units is then fitted by a Gaussian to get an estimate for the position resolution. As a result, a resolution of $\sigma_{\text{FW}} = 0.41 \text{ mm}$ is obtained with a relative error of around $\pm 1\%$.

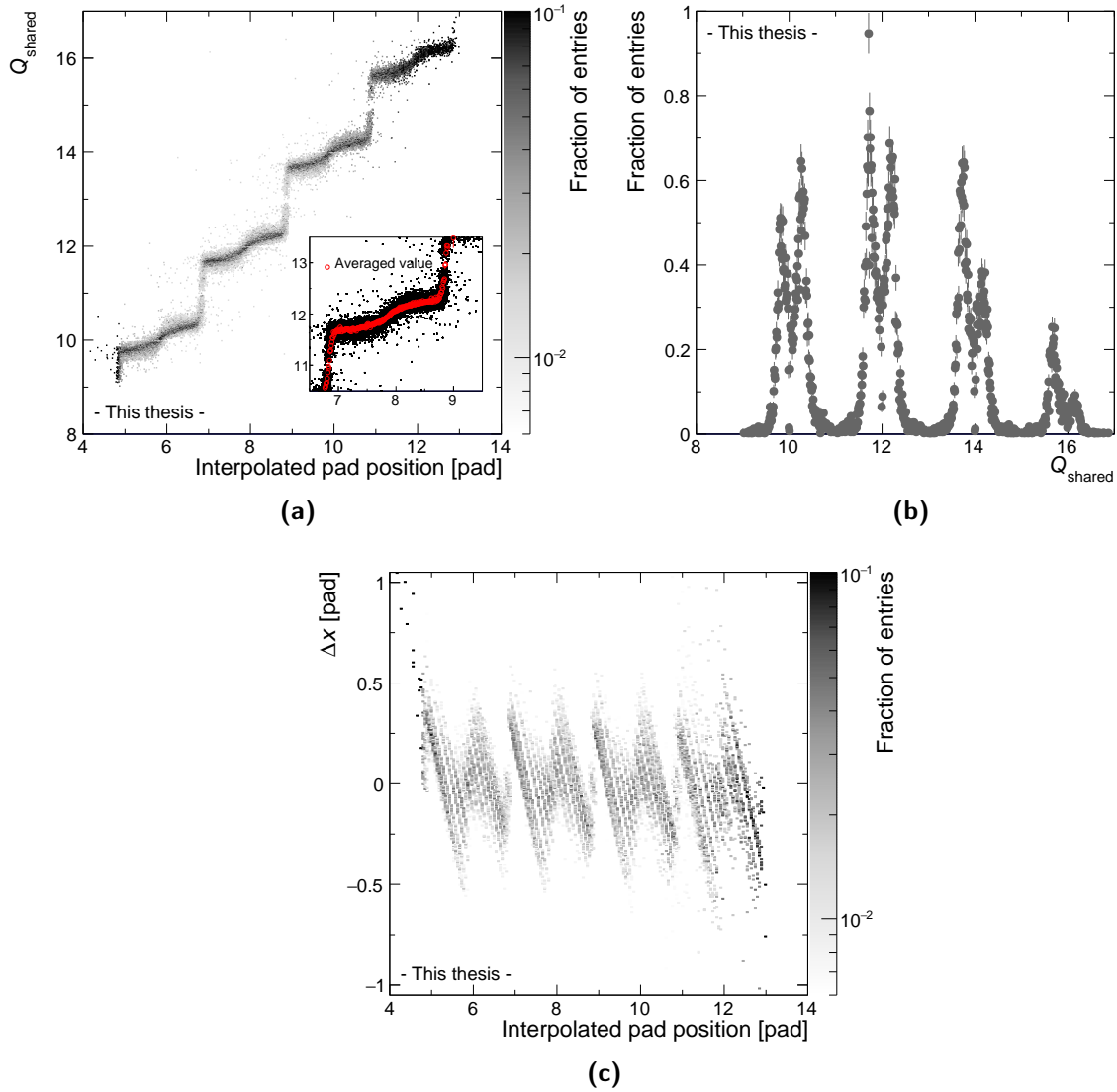


Figure B.5: (a) Correlation of shared cluster charges and interpolated pad position in pad units. (b) Q_{shared} distribution obtained by integrating the distribution shown in panel (a) for all interpolated pad positions. (c) Distribution of the position differences between calculated centroids from pads and charge sharing between the FWs. See the text for details.

Acronyms

ADC Analog-to-Digital Converter	MIP Minimum-Ionizing Particle
ALEPH Apparatur for LEP pPhysics	MPI Multiple Parton Interaction
ALICE A Large Ion Collider Experiment	MWPC Multi-Wire Proportional Chamber
ASCII American Standard Code for Information Interchange	NBD Negative Binomial Distribution
ATLAS A Toroidal LHC ApparatuS	ND non-diffractive
BNL Brookhaven National Laboratory	ndf Number of Degrees of Freedom
CCC Close Cathode Chamber	NLO Next-to-Leading Order
CERN Conseil Européen pour la Recherche Nucléaire	NNLO Next-to-Next-to-Leading Order
CMS Compact Muon Solenoid	NSD non-single diffractive
CNM Cold Nuclear Matter	PID particle identification
CR Color Reconnection	pQCD perturbative QCD
DCA Distance of Closest Approach	PV Primary vertex
DD double-diffractive	QCD Quantum Chromodynamics
DGLAP Dokshitzer–Gribov–Lipatov–Altarelli–Parisi	QGP Quark-Gluon Plasma
DIS Deep Inelastic Scattering	RHIC Relativistic Heavy-Ion Collider
FW Field wire	RICH Ring Imaging Cherenkov
GEM Gas Electron Multiplier	RMS Root Mean Square
HEP High Energy Physics	SD single-diffractive
HERA Hadron-Electron Ring Accelerator	SDD Silicon Drift Detector
HMPID High Momentum Particle Identification Detector	SM Standard Model
INEL Inelastic	SPD Silicon Pixel Detector
ISR Intersecting Storage Rings	SPS Super Proton Synchrotron
ITS Inner Tracking System	SSD Silicon Strip Detector
LEP Large Electron-Positron collider	STAR Solenoidal Tracker At RHIC
LHC Large Hadron Collider	TOF Time-of-Flight Detector
LO Leading Order	TPC Time Projection Chamber
LQCD Lattice QCD	V0 forward scintillator detector
MC Monte Carlo	V0A V0 detector located upstream ($z > 0$) of the interaction point
	VHMPID Very High Momentum Particle Identification Detector
	ZDC Zero Degree Calorimeter

Bibliography

- [1] S. Hands, “The phase diagram of QCD”, *Contemporary Physics* **42** no. 4, (2001) 209–225.
- [2] J. Letessier and J. Rafelski, *Hadrons and Quark–Gluon Plasma*. Cambridge Monographs on Particle Physics, Nuclear Physics and Cosmology. Cambridge University Press, 2002.
- [3] H.-T. Ding, F. Karsch, and S. Mukherjee, “Thermodynamics of strong-interaction matter from Lattice QCD”, *Int. J. Mod. Phys.* **E24** no. 10, (2015) 1530007.
- [4] CMS Collaboration, *CMS Physics: Technical Design Report v.2: Addendum on High Density QCD with Heavy Ions*, vol. 34 of *Technical Design Report CMS*. 2007. <http://cds.cern.ch/record/1019832>.
- [5] Y. Aoki, G. Endrodi, Z. Fodor, S. D. Katz, and K. K. Szabo, “The Order of the quantum chromodynamics transition predicted by the standard model of particle physics”, *Nature* **443** (2006) 675–678.
- [6] M. Cheng *et al.*, “The Transition temperature in QCD”, *Phys. Rev.* **D74** (2006) 054507.
- [7] F. Karsch, K. Redlich, and A. Tawfik, “Thermodynamics at nonzero baryon number density: A Comparison of lattice and hadron resonance gas model calculations”, *Phys. Lett.* **B571** (2003) 67–74.
- [8] D. Boyanovsky, H. J. de Vega, and D. J. Schwarz, “Phase transitions in the early and the present universe”, *Ann. Rev. Nucl. Part. Sci.* **56** (2006) 441–500.
- [9] A. Kurkela and G. D. Moore, “Thermalization in Weakly Coupled Nonabelian Plasmas”, *JHEP* **12** (2011) 044.
- [10] P. Romatschke, “Do nuclear collisions create a locally equilibrated quark–gluon plasma?”, *Eur. Phys. J.* **C77** no. 1, (2017) 21.
- [11] H. Petersen, C. Coleman-Smith, S. A. Bass, and R. Wolpert, “Constraining the initial state granularity with bulk observables in Au+Au collisions at $\sqrt{s_{NN}} = 200$ GeV”, *J. Phys.* **G38** (2011) 045102.
- [12] U. Heinz and J. S. Moreland, “Energy dependent growth of the nucleon and hydrodynamic initial conditions”, *Phys. Rev.* **C84** (2011) 054905.
- [13] J. Noronha-Hostler, B. Betz, J. Noronha, and M. Gyulassy, “Event-by-event hydrodynamics + jet energy loss: A solution to the $R_{AA} \otimes v_2$ puzzle”, *Phys. Rev. Lett.* **116** no. 25, (2016) 252301.
- [14] M. L. Miller, K. Reygers, S. J. Sanders, and P. Steinberg, “Glauber modeling in high energy nuclear collisions”, *Ann. Rev. Nucl. Part. Sci.* **57** (2007) 205–243.
- [15] R. J. Glauber, “Cross-sections in deuterium at high-energies”, *Phys. Rev.* **100** (1955) 242–248.

- [16] ALICE Collaboration, “Centrality dependence of particle production in p-pb collisions at $\sqrt{s_{\text{nn}}} = 5.02$ TeV”, *Phys. Rev.* **C91** no. 6, (2015) 064905.
- [17] R. Barrett and D. Jackson, *Nuclear Sizes and Structure*. The International Series of Monographs on Physics. Oxford University Press, Incorporated, 1977.
<https://books.google.hu/books?id=-hxRAAAAMAAJ>. ISBN 9780198512721.
- [18] C.-Y. Wong, “Lectures on the Near-Side Ridge, Landau Hydrodynamics, and Heavy Quarkonia in High Energy Heavy-Ion Collisions”, *EPJ Web Conf.* **7** (2010) 01006.
- [19] J. D. Bjorken, “Highly Relativistic Nucleus-Nucleus Collisions: The Central Rapidity Region”, *Phys. Rev.* **D27** (1983) 140–151.
- [20] J. Schukraft, “Heavy ions at the LHC: Physics perspectives and experimental program”, *Pramana* **57** (2001) 345–354.
- [21] F. Prino, *Study of the phase transition to QGP at the CERN SPS with the NA50 multiplicity detector*. PhD thesis, Turin U., 2001.
<http://inspirehep.net/record/887300/files/cer-002584612.pdf>.
- [22] B. B. Back *et al.*, “The PHOBOS perspective on discoveries at RHIC”, *Nucl. Phys.* **A757** (2005) 28–101.
- [23] E. Iancu and R. Venugopalan, “The Color glass condensate and high-energy scattering in QCD”, in *In *Hwa, R.C. (ed.) et al.: Quark gluon plasma* 249-3363*.
- [24] J. Stachel *et al.*, “Quark-gluon plasma physics: from fixed target to lhc, lecture, university of heidelberg”, 2001. http://www.physi.uni-heidelberg.de/~reygers/lectures/2011/qgp/qgp_lecture_ss2011.html. Last accessed 01/03/2019.
- [25] ALICE Collaboration, “Centrality dependence of the charged-particle multiplicity density at mid-rapidity in Pb-Pb collisions at $\sqrt{s_{NN}} = 2.76$ TeV”, *Phys. Rev. Lett.* **106** (2011) 032301.
- [26] S. A. Bass *et al.*, “Microscopic models for ultrarelativistic heavy ion collisions”, *Prog. Part. Nucl. Phys.* **41** (1998) 255–369.
- [27] P. Braun-Munzinger, K. Redlich, and J. Stachel, “Particle production in heavy ion collisions”, in *In *Hwa, R.C. (ed.) et al.: Quark gluon plasma* 491-599*
- [28] W. Florkowski, *Phenomenology of Ultra-Relativistic Heavy-Ion Collisions*. 2010. ISBN 9789814280662.
- [29] ALICE Collaboration, “Two-pion Bose-Einstein correlations in central Pb-Pb collisions at $\sqrt{s_{NN}} = 2.76$ TeV”, *Phys. Lett.* **B696** (2011) 328–337,
- [30] G. Roland, K. Safarik, and P. Steinberg, “Heavy-ion collisions at the LHC”, *Prog. Part. Nucl. Phys.* **77** (2014) 70–127.
- [31] P. Braun-Munzinger, J. Stachel, and C. Wetterich, “Chemical freezeout and the QCD phase transition temperature”, *Phys. Lett.* **B596** (2004) 61–69.
- [32] J.-Y. Ollitrault, “Anisotropy as a signature of transverse collective flow”, *Phys. Rev.* **D46** (1992) 229–245.

- [33] P. Huovinen and P. V. Ruuskanen, “Hydrodynamic Models for Heavy Ion Collisions”, *Ann. Rev. Nucl. Part. Sci.* **56** (2006) 163–206.
- [34] A. Taranenko, “PHENIX studies of the scaling properties of elliptic flow at RHIC”, *J. Phys.* **G34** (2007) S1069–1072.
- [35] E. L. Simili, “Elliptic flow measurement at ALICE. Meting van elliptische stroming met ALICE”, 2009. <https://cds.cern.ch/record/2041414>. presented 27 Mar 2009.
- [36] R. Snellings, “Elliptic flow: a brief review”, *New Journal of Physics* **13** no. 5, (2011) 055008. <http://stacks.iop.org/1367-2630/13/i=5/a=055008>.
- [37] ALICE Collaboration, “Elliptic flow of identified hadrons in Pb-Pb collisions at $\sqrt{s_{NN}} = 2.76$ TeV”, *JHEP* **06** (2015) 190.
- [38] S. A. Voloshin, A. M. Poskanzer and R. Snellings, “Collective phenomena in non-central nuclear collisions,” *Landolt-Bornstein* **23**, 293 (2010)
- [39] U. A. Wiedemann, “Jet Quenching in Heavy Ion Collisions,” *Landolt-Bornstein* **23**, 521 (2010)
- [40] M. Gyulassy, “The QGP discovered at RHIC”, in *Proceedings of Structure and dynamics of elementary matter. NATO Advanced Study Institute, Camyuva-Kemer, Turkey, September 22-October 2, 2003*, pp. 159–182.
- [41] C. A. Salgado *et al.*, “Proton-Nucleus Collisions at the LHC: Scientific Opportunities and Requirements”, *J. Phys.* **G39** (2012) 015010.
- [42] CMS Collaboration, “Observation of Long-Range Near-Side Angular Correlations in Proton-Proton Collisions at the LHC”, *JHEP* **09** (2010) 091.
- [43] CMS Collaboration, “Observation of long-range near-side angular correlations in proton-lead collisions at the LHC”, *Phys. Lett.* **B718** (2013) 795–814.
- [44] ALICE Collaboration, “Long-range angular correlations on the near and away side in p -Pb collisions at $\sqrt{s_{NN}} = 5.02$ TeV”, *Phys. Lett.* **B719** (2013) 29–41.
- [45] ATLAS Collaboration, “Observation of Associated Near-Side and Away-Side Long-Range Correlations in $\sqrt{s_{NN}}=5.02$ TeV Proton-Lead Collisions with the ATLAS Detector”, *Phys. Rev. Lett.* **110** no. 18, (2013) 182302.
- [46] ATLAS Collaboration, “Measurement with the ATLAS detector of multi-particle azimuthal correlations in p +Pb collisions at $\sqrt{s_{NN}} = 5.02$ TeV”, *Phys. Lett.* **B725** (2013) 60–78.
- [47] CMS Collaboration, “Multiplicity and transverse momentum dependence of two- and four-particle correlations in p Pb and PbPb collisions”, *Phys. Lett.* **B724** (2013) 213–240.
- [48] C. Loizides, “First results from p -Pb collisions at the LHC”, *EPJ Web Conf.* **60** (2013) 06004.
- [49] P. Bożek, “Small systems – hydrodynamics”, *Nuclear Physics A* **956** (2016) 208 – 215. The XXV International Conference on Ultrarelativistic Nucleus-Nucleus Collisions: Quark Matter 2015.

- [50] ALICE Collaboration, “Pion, Kaon, and Proton Production in Central Pb–Pb Collisions at $\sqrt{s_{NN}} = 2.76$ TeV”, *Phys. Rev. Lett.* **109** (2012) 252301.
- [51] ALICE Collaboration, “Centrality dependence of π , K, p production in Pb-Pb collisions at $\sqrt{s_{NN}} = 2.76$ TeV”, *Phys. Rev.* **C88** (2013) 044910.
- [52] ALICE Collaboration, “Light flavor hadron spectra at low p_T and search for collective phenomena in high multiplicity pp, p–Pb and Pb–Pb collisions measured with the ALICE experiment”, *Nucl. Phys.* **A931** (2014) 888–892.
- [53] ALICE Collaboration, “Multiplicity Dependence of Pion, Kaon, Proton and Lambda Production in p-Pb Collisions at $\sqrt{s_{NN}} = 5.02$ TeV”, *Phys. Lett.* **B728** (2014) 25–38.
- [54] ALICE Collaboration, “Harmonic decomposition of two-particle angular correlations in Pb-Pb collisions at $\sqrt{s_{NN}} = 2.76$ TeV”, *Phys. Lett.* **B708** (2012) 249–264.
- [55] ALICE Collaboration, “Elliptic flow of charged particles in Pb-Pb collisions at 2.76 TeV”, *Phys. Rev. Lett.* **105** (2010) 252302.
- [56] ALICE Collaboration, “Higher harmonic anisotropic flow measurements of charged particles in Pb-Pb collisions at $\sqrt{s_{NN}}=2.76$ TeV”, *Phys. Rev. Lett.* **107** (2011) 032301.
- [57] ALICE Collaboration, “Pseudorapidity dependence of the anisotropic flow of charged particles in Pb-Pb collisions at $\sqrt{s_{NN}} = 2.76$ TeV”, *Phys. Lett.* **B762** (2016) 376–388.
- [58] CMS Collaboration, “Evidence for collectivity in pp collisions at the LHC”, *Phys. Lett.* **B765** (2017) 193–220.
- [59] ALICE Collaboration, “Anisotropic flow of charged hadrons, pions and (anti-)protons measured at high transverse momentum in Pb-Pb collisions at $\sqrt{s_{NN}}=2.76$ TeV”, *Phys. Lett.* **B719** (2013) 18–28.
- [60] ALICE Collaboration, “Higher harmonic flow coefficients of identified hadrons in Pb-Pb collisions at $\sqrt{s_{NN}} = 2.76$ TeV”, *JHEP* **09** (2016) 164.
- [61] ALICE Collaboration, “Long-range angular correlations of β , K and p in p-Pb collisions at $\sqrt{s_{NN}} = 5.02$ TeV”, *Phys. Lett.* **B726** (2013) 164–177.
- [62] CMS Collaboration, “Azimuthal anisotropy harmonics from long-range correlations in high multiplicity pp collisions at $\sqrt{s} = 7$ TeV”, CMS-PAS-HIN-15-009, 2015.
- [63] ALICE Collaboration, “Enhanced production of multi-strange hadrons in high-multiplicity proton-proton collisions”, *Nature Phys.* **13** (2017) 535–539.
- [64] ALICE Collaboration, “Multi-strange baryon production in p-Pb collisions at $\sqrt{s_{NN}} = 5.02$ TeV”, *Phys. Lett.* **B758** (2016) 389–401.
- [65] CMS Collaboration, “Multiplicity and rapidity dependence of strange hadron production in pp, pPb, and PbPb collisions at the LHC”, *Phys. Lett.* **B768** (2017) 103–129.
- [66] CMS Collaboration, “Study of the production of charged pions, kaons, and protons in pPb collisions at $\sqrt{s_{NN}} = 5.02$ TeV”, *Eur. Phys. J.* **C74** no. 6, (2014) 2847.

- [67] E. Shuryak and I. Zahed, “High-multiplicity pp and pA collisions: Hydrodynamics at its edge”, *Phys. Rev.* **C88** no. 4, (2013) 044915.
- [68] G. Başar and D. Teaney, “Scaling relation between pA and AA collisions”, *Phys. Rev.* **C90** no. 5, (2014) 054903.
- [69] ALICE Collaboration, “ K_S^0 and Λ production in Pb-Pb collisions at $\sqrt{s_{NN}} = 2.76$ TeV”, *Phys. Rev. Lett.* **111** (2013) 222301.
- [70] ALICE Collaboration, “ ϕ -meson production at forward rapidity in p-Pb collisions at $\sqrt{s_{NN}} = 5.02$ TeV and in pp collisions at $\sqrt{s} = 2.76$ TeV”, *Phys. Lett.* **B768** (2017) 203–217.
- [71] ALICE Collaboration, “Multiplicity dependence of charged pion, kaon, and (anti)proton production at large transverse momentum in p-Pb collisions at $\sqrt{s_{NN}} = 5.02$ TeV”, *Phys. Lett.* **B760** (2016) 720–735.
- [72] R. J. Fries, B. Muller, C. Nonaka, and S. A. Bass, “Hadron production in heavy ion collisions: Fragmentation and recombination from a dense parton phase”, *Phys. Rev.* **C68** (2003) 044902.
- [73] J. Zimanyi, T. S. Biro, T. Csorgo and P. Levai, “Quark liberation and coalescence at CERN SPS,” *Phys. Lett. B* **472**, 243 (2000)
- [74] C. Shen, C. Park, J.-F. Paquet, G. S. Denicol, S. Jeon, and C. Gale, “Direct photon production and jet energy-loss in small systems”, *Nucl. Phys.* **A956** (2016) 741–744.
- [75] ALICE Collaboration, “Measurement of charged jet production cross sections and nuclear modification in p-Pb collisions at $\sqrt{s_{NN}} = 5.02$ TeV”, *Phys. Lett.* **B749** (2015) 68–81.
- [76] ATLAS Collaboration, “Measurement of long-range pseudorapidity correlations and azimuthal harmonics in $\sqrt{s_{NN}} = 5.02$ TeV proton-lead collisions with the ATLAS detector”, *Phys. Rev.* **C90** no. 4, (2014) 044906.
- [77] Z.-B. Kang, I. Vitev, and H. Xing, “Effects of cold nuclear matter energy loss on inclusive jet production in p+A collisions at energies available at the BNL Relativistic Heavy Ion Collider and the CERN Large Hadron Collider”, *Phys. Rev.* **C92** no. 5, (2015) 054911.
- [78] G. G. Barnafoldi, J. Barrette, M. Gyulassy, P. Levai and V. Topor Pop, “Predictions for $p + Pb$ at 4.4A TeV to Test Initial State Nuclear Shadowing at energies available at the CERN Large Hadron Collider,” *Phys. Rev. C* **85**, 024903 (2012)
- [79] G. G. Barnafoldi, G. Fai, P. Levai, B. A. Cole and G. Papp, “Cold Nuclear Modifications at RHIC and LHC,” *Indian J. Phys.* **84**, 1721 (2010)
- [80] T. Sjostrand and M. van Zijl, “A Multiple Interaction Model for the Event Structure in Hadron Collisions”, *Phys. Rev.* **D36** (1987) 2019.
- [81] T. Sjöstrand, S. Ask, J. R. Christiansen, R. Corke, N. Desai, P. Ilten, S. Mrenna, S. Prestel, C. O. Rasmussen, and P. Z. Skands, “An Introduction to PYTHIA 8.2”, *Comput. Phys. Commun.* **191** (2015) 159–177.

- [82] A. Ortiz Velasquez, P. Christiansen, E. Cuautle Flores, I. Maldonado Cervantes, and G. Paić, “Color Reconnection and Flowlike Patterns in pp Collisions”, *Phys. Rev. Lett.* **111** no. 4, (2013) 042001.
- [83] ALICE Collaboration, “Multiplicity dependence of the average transverse momentum in pp , p -Pb, and Pb-Pb collisions at the LHC”, *Phys. Lett.* **B727** (2013) 371–380.
- [84] Z.-W. Lin, C. M. Ko, B.-A. Li, B. Zhang, and S. Pal, “A Multi-phase transport model for relativistic heavy ion collisions”, *Phys. Rev.* **C72** (2005) 064901.
- [85] T. S. Biro, H. B. Nielsen and J. Knoll, “Color Rope Model for Extreme Relativistic Heavy Ion Collisions,” *Nucl. Phys. B* **245**, 449 (1984).
- [86] C. Bierlich, G. Gustafson, L. Lönnblad, and A. Tarasov, “Effects of Overlapping Strings in pp Collisions”, *JHEP* **03** (2015) 148.
- [87] F. Gelis, E. Iancu, J. Jalilian-Marian, and R Venugopalan, “The Color Glass Condensate”, *Annual Review of Nuclear and Particle Science* **60** (2010) 463-489.
- [88] K. Dusling and R. Venugopalan, “Comparison of the color glass condensate to dihadron correlations in proton-proton and proton-nucleus collisions”, *Phys. Rev.* **D87** no. 9, (2013) 094034.
- [89] K. Dusling, P. Tribedy, and R. Venugopalan, “Energy dependence of the ridge in high multiplicity proton-proton collisions”, *Phys. Rev.* **D93** no. 1, (2016) 014034.
- [90] B. Schenke, S. Schlichting, P. Tribedy, and R. Venugopalan, “Mass ordering of spectra from fragmentation of saturated gluon states in high multiplicity proton-proton collisions”, *Phys. Rev. Lett.* **117** no. 16, (2016) 162301.
- [91] K. Dusling, W. Li, and B. Schenke, “Novel collective phenomena in high-energy proton–proton and proton–nucleus collisions”, *Int. J. Mod. Phys.* **E25** no. 01, (2016) 1630002.
- [92] Y. L. Dokshitzer, “Calculation of the Structure Functions for Deep Inelastic Scattering and $e^+ e^-$ Annihilation by Perturbation Theory in Quantum Chromodynamics.”, *Sov. Phys. JETP* **46** (1977) 641–653. [*Zh. Eksp. Teor. Fiz.*73,1216(1977)].
- [93] V. N. Gribov and L. N. Lipatov, “Deep inelastic $e p$ scattering in perturbation theory”, *Sov. J. Nucl. Phys.* **15** (1972) 438–450.
- [94] V. N. Gribov and L. N. Lipatov, “ $e^+ e^-$ pair annihilation and deep inelastic $e p$ scattering in perturbation theory”, *Sov. J. Nucl. Phys.* **15** (1972) 675–684.
- [95] G. Altarelli and G. Parisi, “Asymptotic Freedom in Parton Language”, *Nucl. Phys.* **B126** (1977) 298–318.
- [96] S. Donnachie, H. G. Dosch, O. Nachtmann, and P. Landshoff, “Pomeron physics and QCD”, *Camb. Monogr. Part. Phys. Nucl. Phys. Cosmol.* **19** (2002) 1–347.
- [97] CMS Collaboration, “Measurement of diffraction dissociation cross sections in pp collisions at $\sqrt{s} = 7$ TeV”, *Phys. Rev.* **D92** no. 1, (2015) 012003.

- [98] ALICE Collaboration, “Measurement of inelastic, single- and double-diffraction cross sections in proton–proton collisions at the LHC with ALICE”, *Eur. Phys. J.* **C73** no. 6, (2013) 2456.
- [99] V. N. Gribov, “A Reggeon diagram technique”, *Sov. Phys. JETP* **26** (1968) 414–422.
- [100] T. Sjostrand, S. Mrenna and P. Z. Skands, *JHEP* **0605**, 026 (2006)
- [101] H. J. Drescher, M. Hladik, S. Ostapchenko, T. Pierog, and K. Werner, “Parton based Gribov-Regge theory”, *Phys. Rept.* **350** (2001) 93–289.
- [102] K. Kajantie, “Physics of LHC (theory)”, *Nucl. Phys.* **A715** (2003) 432–440.
- [103] J. C. Collins, D. E. Soper, and G. F. Sterman, “Factorization of Hard Processes in QCD”, *Adv. Ser. Direct. High Energy Phys.* **5** (1989) 1–91.
- [104] D. d’Enterria, “Jet quenching”, *Landolt-Bornstein* **23** (2010) 471.
- [105] G.-Y. Qin and X.-N. Wang, “Jet quenching in high-energy heavy-ion collisions”, *Int. J. Mod. Phys.* **E24** no. 11, (2015) 1530014.
- [106] D. G. d’Enterria, “Hard scattering cross-sections at LHC in the Glauber approach: From pp to pA and AA collisions”, [arXiv:nucl-ex/0302016](https://arxiv.org/abs/nucl-ex/0302016) [nucl-ex].
- [107] ATLAS Collaboration, “Observation of a Centrality-Dependent Dijet Asymmetry in Lead-Lead Collisions at $\sqrt{s_{NN}} = 2.77$ TeV with the ATLAS Detector at the LHC”, *Phys. Rev. Lett.* **105** (2010) 252303.
- [108] ALICE Collaboration, “Suppression of Charged Particle Production at Large Transverse Momentum in Central Pb-Pb Collisions at $\sqrt{s_{NN}} = 2.76$ TeV”, *Phys. Lett.* **B696** (2011) 30–39.
- [109] CMS Collaboration, “Observation and studies of jet quenching in PbPb collisions at nucleon-nucleon center-of-mass energy = 2.76 TeV”, *Phys. Rev.* **C84** (2011) 024906.
- [110] ALICE Collaboration, “Centrality Dependence of Charged Particle Production at Large Transverse Momentum in Pb–Pb Collisions at $\sqrt{s_{NN}} = 2.76$ TeV”, *Phys. Lett.* **B720** (2013) 52–62.
- [111] ALICE Collaboration, “Centrality dependence of the nuclear modification factor of charged pions, kaons, and protons in Pb-Pb collisions at $\sqrt{s_{NN}} = 2.76$ TeV”, *Phys. Rev.* **C93** no. 3, (2016) 034913.
- [112] P. Christiansen, K. Tywoniuk, and V. Viskovic, “Universal scaling dependence of QCD energy loss from data driven studies”, *Phys. Rev.* **C89** no. 3, (2014) 034912.
- [113] PHENIX Collaboration, “Suppression of hadrons with large transverse momentum in central Au+Au collisions at $\sqrt{s_{NN}} = 130$ -GeV”, *Phys. Rev. Lett.* **88** (2002) 022301.
- [114] CMS Collaboration, “Measurement of isolated photon production in pp and PbPb collisions at $\sqrt{s_{NN}} = 2.76$ TeV”, *Phys. Lett.* **B710** (2012) 256–277.
- [115] CMS Collaboration, “Study of W boson production in PbPb and pp collisions at $\sqrt{s_{NN}} = 2.76$ TeV”, *Phys. Lett.* **B715** (2012) 66–87.

- [116] CMS Collaboration, “Study of Z boson production in PbPb collisions at $\sqrt{s_{NN}} = 2.76$ TeV”, *Phys. Rev. Lett.* **106** (2011) 212301.
- [117] JET Collaboration, “Extracting the jet transport coefficient from jet quenching in high-energy heavy-ion collisions”, *Phys. Rev.* **C90** no. 1, (2014) 014909.
- [118] S. Acharya *et al.* [ALICE Collaboration], “Transverse momentum spectra and nuclear modification factors of charged particles in pp, p-Pb and Pb-Pb collisions at the LHC,” *JHEP* **1811**, 013 (2018)
- [119] ALICE Collaboration, “Transverse momentum distribution and nuclear modification factor of charged particles in p -Pb collisions at $\sqrt{s_{NN}} = 5.02$ TeV”, *Phys. Rev. Lett.* **110** no. 8, (2013) 082302.
- [120] R. J. Fries, B. Muller, C. Nonaka, and S. A. Bass, “Hadronization in heavy ion collisions: Recombination and fragmentation of partons”, *Phys. Rev. Lett.* **90** (2003) 202303.
- [121] D. G. d’Enterria, “Quark-Gluon Matter”, *J. Phys.* **G34** (2007) S53–S82.
- [122] STAR Collaboration, “Identified baryon and meson distributions at large transverse momenta from Au+Au collisions at $\sqrt{s_{NN}} = 200$ -GeV”, *Phys. Rev. Lett.* **97** (2006) 152301.
- [123] STAR Collaboration, “Identified hadron compositions in p+p and Au+Au collisions at high transverse momenta at $\sqrt{s_{NN}} = 200$ GeV”, *Phys. Rev. Lett.* **108** (2012) 072302.
- [124] PHENIX Collaboration, “Spectra and ratios of identified particles in Au+Au and d +Au collisions at $\sqrt{s_{NN}} = 200$ GeV”, *Phys. Rev.* **C88** no. 2, (2013) 024906.
- [125] ALICE Collaboration, “Production of charged pions, kaons and protons at large transverse momenta in pp and Pb–Pb collisions at $\sqrt{s_{NN}} = 2.76$ TeV”, *Phys. Lett.* **B736** (2014) 196–207.
- [126] P. Bozek and I. Wyskiel-Piekarska, “Particle spectra in Pb-Pb collisions at $\sqrt{s_{NN}} = 2.76$ TeV”, *Phys. Rev.* **C85** (2012) 064915.
- [127] P. Bozek, “Hydrodynamic flow from RHIC to LHC”, *Acta Phys. Polon.* **B43** (2012) 689.
- [128] K. Werner, B. Guiot, I. Karpenko, and T. Pierog, “Analysing radial flow features in p-Pb and p-p collisions at several TeV by studying identified particle production in EPOS3”, *Phys. Rev.* **C89** no. 6, (2014) 064903.
- [129] K. Werner, I. Karpenko, T. Pierog, M. Bleicher, and K. Mikhailov, “Evidence for hydrodynamic evolution in proton-proton scattering at 900 GeV”, *Phys. Rev.* **C83** (2011) 044915.
- [130] K. Werner, I. Karpenko, T. Pierog, M. Bleicher, and K. Mikhailov, “Event-by-Event Simulation of the Three-Dimensional Hydrodynamic Evolution from Flux Tube Initial Conditions in Ultrarelativistic Heavy Ion Collisions”, *Phys. Rev.* **C82** (2010) 044904.

- [131] M. Veldhoen, T. Peitzmann, and M. van Leeuwen, “Identified particle yield associated with a high- p_T trigger particle at the LHC”, PhD thesis, Utrecht U., 2016. <https://cds.cern.ch/record/2151947>. presented 14 Mar 2016.
- [132] J. Sollfrank, F. Becattini, K. Redlich, and H. Satz, “Canonical strangeness enhancement”, *Nucl. Phys.* **A638** (1998) 399C–402C.
- [133] J. Letessier and J. Rafelski, “Strangeness chemical equilibration in QGP at RHIC and CERN LHC”, *Phys. Rev.* **C75** (2007) 014905.
- [134] C. A. Salgado, “The physics potential of proton-nucleus collisions at the TeV scale”, *J. Phys.* **G38** (2011) 124036.
- [135] J. L. Albacete *et al.*, *Nucl. Phys. A* **972**, 18 (2018)
- [136] S. Dulat, T.-J. Hou, J. Gao, M. Guzzi, J. Huston, P. Nadolsky, J. Pumplin, C. Schmidt, D. Stump, and C. P. Yuan, “New parton distribution functions from a global analysis of quantum chromodynamics”, *Phys. Rev.* **D93** no. 3, (2016) 033006.
- [137] K. J. Eskola, H. Paukkunen, and C. A. Salgado, “EPS09: A New Generation of NLO and LO Nuclear Parton Distribution Functions”, *JHEP* **04** (2009) 065.
- [138] M. Hirai, S. Kumano, and T. H. Nagai, “Nuclear parton distribution functions and their uncertainties”, *Phys. Rev.* **C70** (2004) 044905.
- [139] D. de Florian and R. Sassot, “Nuclear parton distributions at next-to-leading order”, *Phys. Rev.* **D69** (2004) 074028.
- [140] D. de Florian, R. Sassot, M. Stratmann, and P. Zurita, “Global Analysis of Nuclear PDFs”, in *Proceedings of 20th International Workshop on Deep-Inelastic Scattering and Related Subjects (DIS 2012): Bonn, Germany, March 26-30, 2012*, pp. 421–424.
- [141] K. J. Eskola, V. J. Kolhinen, and P. V. Ruuskanen, “Scale evolution of nuclear parton distributions”, *Nucl. Phys.* **B535** (1998) 351–371.
- [142] K. J. Eskola, V. J. Kolhinen, and C. A. Salgado, “The Scale dependent nuclear effects in parton distributions for practical applications”, *Eur. Phys. J.* **C9** (1999) 61–68.
- [143] K. J. Eskola, V. J. Kolhinen, H. Paukkunen, and C. A. Salgado, “A Global reanalysis of nuclear parton distribution functions”, *JHEP* **05** (2007) 002.
- [144] M. Hirai, S. Kumano, and T. H. Nagai, “Determination of nuclear parton distribution functions and their uncertainties in next-to-leading order”, *Phys. Rev.* **C76** (2007) 065207.
- [145] A. Kusina, J. P. Lansberg, I. Schienbein and H. S. Shao, *Phys. Rev. Lett.* **121**, no. 5, 052004 (2018)
- [146] J. Ashman *et al.* [European Muon Collaboration], *Phys. Lett. B* **202**, 603 (1988). doi:10.1016/0370-2693(88)91872-2
- [147] M. Arneodo *et al.* [European Muon Collaboration], *Phys. Lett. B* **211**, 493 (1988). doi:10.1016/0370-2693(88)91900-4

- [148] W. G. Seligman, “A Next-to-Leading-Order QCD Analysis of Neutrino-Iron Structure Functions at the Tevatron”, PhD thesis, (CCFR) Columbia University, 1997. <https://www.nevis.columbia.edu/~seligman/ccfr/thesis/>.
- [149] New Muon Collaboration, “A Reevaluation of the nuclear structure function ratios for D, He, Li-6, C and Ca”, *Nucl. Phys.* **B441** (1995) 3–11.
- [150] J. Gomez *et al.*, “Measurement of the a dependence of deep-inelastic electron scattering”, *Phys. Rev. D* **49** (May, 1994) 4348–4372.
- [151] J. C. Collins, D. E. Soper, and G. Sterman, “Factorization for short distance hadron-hadron scattering”, *Nuclear Physics B* **261** (1985) 104 – 142.
- [152] N. Armesto, “Nuclear shadowing”, *J. Phys.* **G32** (2006) R367–R394.
- [153] ZEUS Collaboration, “A ZEUS next-to-leading-order QCD analysis of data on deep inelastic scattering”, *Phys. Rev.* **D67** (2003) 012007.
- [154] M. Froissart, “Asymptotic behavior and subtractions in the mandelstam representation”, *Phys. Rev.* **123** (Aug, 1961) 1053–1057.
- [155] J. W. Cronin, H. J. Frisch, M. J. Shochet, J. P. Boymond, P. A. Piroué, and R. L. Sumner, “Production of hadrons at large transverse momentum at 200, 300, and 400 GeV”, *Phys. Rev. D* **11** (Jun, 1975) 3105–3123.
- [156] A. Accardi, “Cronin effect in proton nucleus collisions: A Survey of theoretical models”, arXiv:hep-ph/0212148 [hep-ph].
- [157] D. de Florian, R. Sassot, and M. Stratmann, “Global analysis of fragmentation functions for protons and charged hadrons”, *Phys. Rev.* **D76** (2007) 074033.
- [158] D. de Florian, R. Sassot, M. Epele, R. J. Hernández-Pinto, and M. Stratmann, “Parton-to-Pion Fragmentation Reloaded”, *Phys. Rev.* **D91** no. 1, (2015) 014035.
- [159] D. de Florian, M. Epele, R. J. Hernandez-Pinto, R. Sassot, and M. Stratmann, “Parton-to-Kaon Fragmentation Revisited”, *Phys. Rev.* **D95** no. 9, (2017) 094019.
- [160] G. A. Schuler and T. Sjostrand, “Hadronic diffractive cross-sections and the rise of the total cross-section”, *Phys. Rev.* **D49** (1994) 2257–2267.
- [161] H. L. Lai *et al.* [CTEQ Collaboration], *Eur. Phys. J. C* **12**, 375 (2000)
- [162] B. Andersson, “The Lund String Model”, in *Proceedings of 7th European Symposium on Antiproton Interactions: From LEAR to the Collider and Beyond*, Durham, England, July 9-13, 1984, pp. 447–462. 1986.
- [163] P. Z. Skands, “Tuning Monte Carlo generators: The Perugia tunes”, *Phys. Rev.* **D82** (2010) 074018.
- [164] P. Skands, S. Carrazza, and J. Rojo, “Tuning PYTHIA 8.1: the Monash 2013 Tune”, *Eur. Phys. J.* **C74** no. 8, (2014) 3024.
- [165] P. Z. Skands and D. Wicke, “Non-perturbative QCD effects and the top mass at the Tevatron”, *Eur. Phys. J.* **C52** (2007) 133–140.

- [166] K. Werner, M. Bleicher, B. Guiot, I. Karpenko, and T. Pierog, “Evidence for flow from hydrodynamic simulations of p –Pb collisions at 5.02 TeV from v_2 mass splitting”, *Phys. Rev. Lett.* **112** (Jun, 2014) 232301.
- [167] K. Werner, “Core-corona separation in ultra-relativistic heavy ion collisions”, *Phys. Rev. Lett.* **98** (2007) 152301.
- [168] J. S. Schwinger, “On gauge invariance and vacuum polarization”, *Phys. Rev.* **82** (1951) 664–679.
- [169] T. Martin, P. Skands, and S. Farrington, “Probing Collective Effects in Hadronisation with the Extremes of the Underlying Event”, *Eur. Phys. J.* **C76** no. 5, (2016) 299.
- [170] S. Porteboeuf, T. Pierog, and K. Werner, “Producing Hard Processes Regarding the Complete Event: The EPOS Event Generator”, in *Proceedings of 45th Rencontres de Moriond on QCD and High Energy Interactions: La Thuile, Italy, March 13-20, 2010*, pp. 135–140, Gioi Publishers. Gioi Publishers, 2010.
- [171] K. Werner, “Lambda-to-kaon ratio enhancement in heavy ion collisions at several TeV”, *Phys. Rev. Lett.* **109** (Sep, 2012) 102301.
- [172] K. Werner, I. Karpenko, and T. Pierog, “Ridge in proton-proton scattering at 7 TeV”, *Phys. Rev. Lett.* **106** (Mar, 2011) 122004.
- [173] D. Sarkar and S. Chattopadhyay, “Ridge from jet-medium interaction in p -pb collisions at $\sqrt{s_{NN}} = 5.02$ TeV”, *Phys. Rev. C* **95** (Apr, 2017) 044906.
- [174] A. Ortiz, G. Bencedi, and H. Bello, “Revealing the source of the radial flow patterns in proton-proton collisions using hard probes”, *J. Phys.* **G44** no. 6, (2017) 065001.
- [175] A. Ortiz, G. Paić, and E. Cuautle, “Mid-rapidity charged hadron transverse sphericity in pp collisions simulated with Pythia”, *Nucl. Phys.* **A941** (2015) 78–86.
- [176] S. Floerchinger and K. C. Zapp, “Hydrodynamics and Jets in Dialogue”, *Eur. Phys. J.* **C74** no. 12, (2014) 3189.
- [177] B. Andersson, G. Gustafson, G. Ingelman, and T. Sjostrand, “Parton Fragmentation and String Dynamics”, *Phys. Rept.* **97** (1983) 31–145.
- [178] X. Artru and G. Mennessier, “String model and multiproduction”, *Nuclear Physics B* **70** no. 1, (1974) 93 – 115.
- [179] ALICE Collaboration, B. A. Hess, “Measurement of hadron composition in charged jets from pp collisions with the ALICE experiment”, in *Proceedings of 2nd Conference on Large Hadron Collider Physics Conference (LHCP 2014): New York, USA, June 2-7, 2014*. 2014.
- [180] M. Cacciari, G. P. Salam, and G. Soyez, “FastJet User Manual”, *Eur. Phys. J.* **C72** (2012) 1896.
- [181] ALICE Collaboration, “Measurement of hadron composition in charged jets from pp collisions with the ALICE experiment”, *Nucl. Phys.* **A931** (2014) 428–432.
- [182] ALICE Collaboration, “ p/π Ratio in Di-Hadron Correlations”, *Nucl. Phys.* **A910-911** (2013) 306–309.

- [183] ALICE Collaboration, “ K_S^0 and Λ production in charged particle jets in p–Pb collisions at $\sqrt{s_{NN}} = 5.02$ TeV with ALICE”, *Nucl. Phys.* **A931** (2014) 444–448.
- [184] STAR Collaboration, “Systematic Measurements of Identified Particle Spectra in p+p, d+Au and Au+Au Collisions from STAR”, *Phys. Rev.* **C79** (2009) 034909.
- [185] V. Begun, W. Florkowski, and M. Rybczynski, “Transverse-momentum spectra of strange particles produced in Pb+Pb collisions at $\sqrt{s_{NN}} = 2.76$ TeV in the chemical non-equilibrium model”, *Phys. Rev.* **C90** no. 5, (2014) 054912.
- [186] V. Begun and W. Florkowski, “Bose-Einstein condensation of pions in heavy-ion collisions at the CERN Large Hadron Collider (LHC) energies”, *Phys. Rev.* **C91** (2015) 054909.
- [187] V. Begun, “Fluctuations as a test of chemical non-equilibrium at the LHC”, *Phys. Rev.* **C94** no. 5, (2016) 054904.
- [188] E. Schnedermann, J. Sollfrank, and U. W. Heinz, “Thermal phenomenology of hadrons from 200-A/GeV S+S collisions”, *Phys. Rev.* **C48** (1993) 2462–2475.
- [189] ALICE Collaboration, “The ALICE experiment at the CERN LHC”, *JINST* **3** (2008) S08002.
- [190] O. S. Bruning, P. Collier, P. Lebrun, S. Myers, R. Ostojic, J. Poole, and P. Proudlock, *LHC Design Report*. CERN, Geneva, 2004. <https://cds.cern.ch/record/782076>.
- [191] L. Evans and P. Bryant, “LHC machine”, *Journal of Instrumentation* **3** no. 08, (2008) S08001. <http://stacks.iop.org/1748-0221/3/i=08/a=S08001>.
- [192] ALICE Collaboration, *ALICE physics performance: Technical Design Report*. Technical Design Report ALICE. CERN, Geneva, 2005. <https://cds.cern.ch/record/879894>. revised version submitted on 2006-05-29 15:15:40.
- [193] ALICE Collaboration, “Performance of the ALICE Experiment at the CERN LHC”, *Int. J. Mod. Phys.* **A29** (2014) 1430044.
- [194] P. L. Betev, “Definition of the alice coordinate system and basic rules for sub-detector components numbering.” https://alice-servotech.web.cern.ch/ALICE-ServoTech/HELP_DCDB-SVT/Help_Files/ALICE-INT-2003-038.pdf, 03/10/2003. ALICE-INT-2003-038. Last accessed 01/03/2019.
- [195] ALICE Collaboration, “ALICE technical design report of the inner tracking system (ITS)”, CERN-LHCC-99-12 (1999). <http://cds.cern.ch/record/391175>.
- [196] ALICE Collaboration, “Alignment of the ALICE Inner Tracking System with cosmic-ray tracks”, *J. Inst.* **5** (2010) P03003.
- [197] J. Alme *et al.*, “The ALICE TPC, a large 3-dimensional tracking device with fast readout for ultra-high multiplicity events”, *Nucl. Instrum. Methods Phys. Res. A* **622** (2010) 316–67.
- [198] E. Segrè, *Nuclei and particles: an introduction to nuclear and subnuclear physics*. W. A. Benjamin, 2nd ed., 966 p, (1977). ISBN 9780805386011.

- [199] ALICE Collaboration, “ALICE: Physics performance report, volume II”, *J. Phys.* **G32** (2006) 1295–2040.
- [200] A. Maire and C. Kuhn, *Production des baryons multi-étranges au LHC dans les collisions proton-proton avec l’expérience ALICE*. PhD thesis, Strasbourg U., 2011. <https://cds.cern.ch/record/1490315>. Presented 13 Oct 2011.
- [201] ALICE Collaboration, “Performance of the ALICE VZERO system”, *JINST* **8** (2013) P10016.
- [202] ALICE Collaboration, “Centrality determination of Pb-Pb collisions at $\sqrt{s_{NN}} = 2.76$ TeV with ALICE”, *Phys. Rev.* **C88** no. 4, (2013) 044909.
- [203] A. Bialas, M. Bleszynski, and W. Czyz, “Multiplicity Distributions in Nucleus-Nucleus Collisions at High-Energies”, *Nucl. Phys.* **B111** (1976) 461–476.
- [204] ALICE Collaboration, J. Adam *et al.*, “W and Z boson production in p-Pb collisions at $\sqrt{s_{NN}} = 5.02$ TeV”, *JHEP* **02** (2017) 077.
- [205] ALICE Collaboration, J. Adam *et al.*, “Centrality dependence of charged jet production in p-Pb collisions at $\sqrt{s_{NN}} = 5.02$ TeV”, *Eur. Phys. J.* **C76** no. 5, (2016) 271.
- [206] ALICE Collaboration, “Charged-particle multiplicity measurement in proton-proton collisions at $\sqrt{s} = 7$ TeV with ALICE at LHC”, *Eur. Phys. J.* **C68** (2010) 345–354.
- [207] B. Abelev *et al.* [ALICE Collaboration], “Upgrade of the ALICE Experiment: Letter Of Intent,” *J. Phys. G* **41**, 087001 (2014).
- [208] G. Hamar, “Nagy impulzusú részecskék vizsgálata nehézionütközésekben”, PhD thesis, Eötvös Loránd University, 2014. http://teo.elte.hu/minosites/ertekezes2014/hamar_g.pdf.
- [209] ALICE Collaboration, “A Very High Momentum Particle Identification Detector”, *Eur. Phys. J. Plus* **129** (2014) 91.
- [210] T. V. Acconcia *et al.*, “VHMPID RICH prototype using pressurized C₄F₈O radiator gas and VUV photon detector”, *Nucl. Instrum. Meth.* **A767** (2014) 50–60.
- [211] D. Varga, G. Hamar, and G. Kiss, “Asymmetric multi-wire proportional chamber with reduced requirements to mechanical precision”, *Nucl. Instrum. Meth.* **A648** (2011) 163–167.
- [212] D. Varga, G. Kiss, G. Hamar, and G. Bencédi, “Close cathode chamber: Low material budget MWPC”, *Nucl. Instrum. Meth.* **A698** (2013) 11–18.
- [213] L. Oláh, “Research and development of particle detectors for muon tomography and the CERN ALICE experiment”, PhD thesis, Eötvös Loránd University, 2017. <http://hdl.handle.net/10831/33500>.
- [214] G. Bencédi, G. G. Barnaföldi, and L. Molnár, “Identified Two-particle Correlations and Quantum Number Conservations in p-p and Pb-Pb Collisions at LHC Energies”, *J. Phys. Conf. Ser.* **805** no. 1, (2017) 012014.

- [215] H. Bethe, “Zur theorie des durchgangs schneller korpuskularstrahlen durch materie”, *Annalen der Physik* **397** no. 3, 325–400.
- [216] ALICE Collaboration, “First results of the ALICE detector performance at 13 TeV”, <https://cds.cern.ch/record/2047855>.
- [217] ALICE Collaboration, “Particle identification in ALICE: a Bayesian approach”, *Eur. Phys. J. Plus* **131** no. 5, (2016) 168.
- [218] Particle Data Group Collaboration, C. Patrignani *et al.*, “Review of Particle Physics”, *Chin. Phys.* **C40** no. 10, (2016 and 2017 update) 100001.
- [219] U. Fano, “Penetration of protons, alpha particles, and mesons”, *Annual Review of Nuclear Science* **13** no. 1, (1963) 1–66.
- [220] D. Wilkinson, “Ionization energy loss by charged particles part I.: the Landau distribution”, *Nucl. Instrum. Meth.* **A383** no. 2, (1996) 513 – 515.
- [221] W. Blum, W. Riegler, and L. Rolandi, *Particle detection with drift chambers; 2nd ed.* Springer, Berlin, 2008. <https://cds.cern.ch/record/1105920>.
- [222] A. Kalweit, “Production of light flavor hadrons and anti-nuclei at the LHC”, PhD thesis, Darmstadt, Tech. U., 2012. <https://cds.cern.ch/record/2119440>.
- [223] G. Bencedi (ALICE Collaboration), “Identification of π^\pm , k^\pm and $p(\bar{p})$ at high p_T in pp collisions at $\sqrt{s} = 7$ Tev and in p-pb collisions at $\sqrt{s_{NN}} = 5.02$ TeV”, ALICE Analysis Note, ALICE-AN 428, 2016.
- [224] ALICE Collaboration, “ALICE: Technical design report of the time projection chamber”, <http://cds.cern.ch/record/451098>.
- [225] ALICE Collaboration, “The Laser calibration system of the ALICE time projection chamber”, *Czech. J. Phys.* **55** (2005) 1671–1674.
- [226] S. Rossegger, B. Schnizer, W. Riegler, and L. Betev, “Simulation and Calibration of the ALICE TPC including innovative Space Charge Calculations”, PhD thesis, Graz, Tech. U., Graz, 2009. <http://cds.cern.ch/record/1217595>. Presented on 30 Oct 2009.
- [227] ALEPH Collaboration, D. Buskulic *et al.*, “Performance of the ALEPH detector at LEP”, *Nucl. Instrum. Meth.* **A360** (1995) 481–506.
- [228] P. Christiansen (ALICE Collaboration), “High- p_T identified particle production in ALICE”, *Nucl. Phys.* **A910-911** (2013) 20–26.
- [229] ALICE Collaboration, “Strange particle production in proton-proton collisions at $\sqrt{s} = 0.9$ TeV with ALICE at the LHC”, *Eur. Phys. J.* **C71** (2011) 1594.
- [230] G. Bencedi (ALICE Collaboration), “Charged pion, kaon and (anti)proton production in pp collisions at 13 TeV”, ALICE Analysis Note ALICE-AN 3034, 2017.
- [231] I. Antcheva *et al.*, “ROOT: A C++ framework for petabyte data storage, statistical analysis and visualization,” *Comput. Phys. Commun.*, vol. 180, pp. 2499–2512, 2009.

- [232] R. Brun and F. Rademakers, “ROOT: An object oriented data analysis framework,” *Nucl. Instrum. Meth.*, vol. A389, pp. 81–86, 1997.
- [233] ALICE Collaboration, “The alice off-line project,” <http://alroot-docs.web.cern.ch/alroot-docs/>, 2011. Last accessed 01/03/2019.
- [234] R. Brun, F. Bruyant, F. Carminati, S. Giani, M. Maire, A. McPherson, G. Patrick, and L. Urban, “GEANT Detector Description and Simulation Tool”, Geneva, CERN Program Library Long Writeup W5013, 430 p. (1993).
- [235] R. Engel, J. Ranft, and S. Roesler, “Hard diffraction in hadron hadron interactions and in photoproduction”, *Phys. Rev.* **D52** (1995) 1459–1468.
- [236] S. Roesler, R. Engel, and J. Ranft, “The Monte Carlo event generator DPMJET-III”, in *Proceedings of Advanced Monte Carlo for radiation physics, particle transport simulation and applications. Conference, MC2000, Lisbon, Portugal, October 23-26, 2000*, pp. 1033–1038. 2000.
- [237] A. Capella, U. Sukhatme, C.-I. Tan, and J. Tran Thanh Van, “Dual parton model”, *Phys. Rept.* **236** (1994) 225–329.
- [238] ALICE Collaboration, “Energy dependence of the transverse momentum distributions of charged particles in pp collisions Measured by ALICE”, *Eur. Phys. J.* **C73** no. 12, (2013) 2662.
- [239] S. van der Meer, “Calibration of the effective beam height in the ISR”, Tech. Rep. CERN-ISR-PO-68-31. ISR-PO-68-31, CERN, Geneva, 1968. <http://cds.cern.ch/record/296752>.
- [240] C. Loizides, J. Kamin and D. d’Enterria, *Phys. Rev. C* **97**, no. 5, 054910 (2018) Erratum: [*Phys. Rev. C* **99**, no. 1, 019901 (2019)]
- [241] ALICE Collaboration, “ALICE luminosity determination for pp collisions at $\sqrt{s} = 13$ TeV”,. <https://cds.cern.ch/record/2160174>.
- [242] ALICE Collaboration, “Pseudorapidity density of charged particles in $p + \text{Pb}$ collisions at $\sqrt{s_{NN}} = 5.02$ TeV”, *Phys. Rev. Lett.* **110** no. 3, (2013) 032301.
- [243] ALICE Collaboration, “Measurement of visible cross sections in proton-lead collisions at $\sqrt{s_{NN}} = 5.02$ TeV in van der Meer scans with the ALICE detector”, *JINST* **9** no. 11, (2014) P11003.
- [244] ALICE Collaboration, “The ALICE definition of primary particles”, ALICE-PUBLIC-2017-005 (Jun 2017), <https://cds.cern.ch/record/2270008>.
- [245] ALICE Collaboration, “Transverse momentum dependence of inclusive primary charged-particle production in p-Pb collisions at $\sqrt{s_{NN}} = 5.02$ TeV”, *Eur. Phys. J.* **C74** no. 9, (2014) 3054.
- [246] ALICE Collaboration, “Pseudorapidity and transverse-momentum distributions of charged particles in proton–proton collisions at $\sqrt{s} = 13$ TeV”, *Phys. Lett.* **B753** (2016) 319–329.
- [247] ALICE Collaboration, “Measurement of pion, kaon and proton production in proton–proton collisions at $\sqrt{s} = 7$ TeV”, *Eur. Phys. J.* **C75** no. 5, (2015) 226.

- [248] ALICE Collaboration, “Production of pions, kaons and protons in pp collisions at $\sqrt{s} = 900$ GeV with ALICE at the LHC”, *Eur. Phys. J.* **C71** (2011) 1655.
- [249] B. A. Hess, H. R. Schmidt, and W. Vogelsang, “Particle Identification in Jets and High-Multiplicity pp Events with the ALICE TPC”, PhD thesis, Tübingen U., Jun, 2015. <https://cds.cern.ch/record/2058633>. Presented 09 Oct 2015.
- [250] G. Bencedi, Y. Morales, P. Kalinak, A. Knospe, V. Vislavicius and S. Kundu (ALICE Collaboration), “Production of light flavor hadrons in pp collisions at $\sqrt{s} = 7$ and $\sqrt{s} = 13$ TeV”, ALICE Paper Draft ALICE-ID 3429, 2017. <https://aliceinfo.cern.ch/ArtSubmission/node/3429>. Last accessed 01/03/2019.
- [251] I. Helenius, K. J. Eskola, H. Honkanen, and C. A. Salgado, “Impact-Parameter Dependent Nuclear Parton Distribution Functions: EPS09s and EKS98s and Their Applications in Nuclear Hard Processes”, *JHEP* **07** (2012) 073.
- [252] PHENIX Collaboration, “A Detailed Study of High- $p(T)$ Neutral Pion Suppression and Azimuthal Anisotropy in Au+Au Collisions at $\sqrt{s_{NN}} = 200$ GeV”, *Phys. Rev.* **C76** (2007) 034904.
- [253] A. Ortiz and L. Valencia Palomo, “Universality of the underlying event in pp collisions”, *Phys. Rev.* **D96** no. 11, (2017) 114019.
- [254] S. J. Brodsky and G. R. Farrar, “Scaling Laws at Large Transverse Momentum”, *Phys. Rev. Lett.* **31** (1973) 1153–1156.
- [255] D. Sivers, S. J. Brodsky, and R. Blankenbecler, “Large transverse momentum processes”, *Physics Reports* **23** no. 1, (1976) 1 – 121.
- [256] R. Blankenbecler, S. J. Brodsky, and J. F. Gunion, “Magnitude of large-transverse-momentum cross sections”, *Phys. Rev. D* **18** (Aug, 1978) 900–926.
- [257] F. Arleo, S. J. Brodsky, D. S. Hwang, and A. M. Sickles, “Higher-Twist Dynamics in Large Transverse Momentum Hadron Production”, *Phys. Rev. Lett.* **105** (2010) 062002.
- [258] F. Arleo, D. d’Enterria, and A. S. Yoon, “Single-inclusive production of large- p_T charged particles in hadronic collisions at TeV energies and perturbative QCD predictions”, *JHEP* **06** (2010) 035.
- [259] CDF Collaboration, “Measurement of Particle Production and Inclusive Differential Cross Sections in $p\bar{p}$ Collisions at $\sqrt{s} = 1.96$ -TeV”, *Phys. Rev.* **D79** (2009) 112005.
- [260] C. Albajar *et al.*, “A study of the general characteristics of proton-antiproton collisions at $\sqrt{s} = 0.2$ to 0.9 TeV”, *Nuclear Physics B* **335** no. 2, (1990) 261 – 287.
- [261] CDF Collaboration, “Transverse Momentum Distributions of Charged Particles Produced in $p\bar{p}$ Interactions at $\sqrt{s} = 630$ GeV and 1800 GeV”, *Phys. Rev. Lett.* **61** (1988) 1819.
- [262] CMS Collaboration, “Charged particle transverse momentum spectra in pp collisions at $\sqrt{s} = 0.9$ and 7 TeV”, *JHEP* **08** (2011) 086.

- [263] S. M. Berman, J. D. Bjorken, and J. B. Kogut, “Inclusive Processes at High Transverse Momentum”, *Phys. Rev.* **D4** (1971) 3388.
- [264] R. Sassot, P. Zurita, and M. Stratmann, “Inclusive Hadron Production in the CERN-LHC Era”, *Phys. Rev.* **D82** (2010) 074011.
- [265] British-Scandinavian Collaboration, “The Production of Charged Particles with High Transverse Momentum in Proton-Proton Collisions at the CERN ISR”, *Nucl. Phys.* **B87** (1975) 19.
- [266] Bonn-Brussels-Cambridge-CERN-Stockholm Collaboration, UA5 Collaboration Collaboration, “First results on complete events from $p\bar{p}$ collisions at the cm energy of 540 GeV”, *Phys. Lett. B* **107** no. CERN-EP-81-152, (Nov, 1981) 310–314. 12 p. <https://cds.cern.ch/record/134495>.
- [267] STAR Collaboration, “Strange particle production in $p + p$ collisions at $\sqrt{s} = 200$ GeV”, *Phys. Rev. C* **75** (Jun, 2007) 064901.
- [268] P. K. Khandai, P. Sett, P. Shukla, and V. Singh, “Transverse Mass Spectra and Scaling of Hadrons at RHIC and LHC Energies”, [arXiv:1205.0648 \[hep-ph\]](https://arxiv.org/abs/1205.0648), 2012.
- [269] L. Altenkämper, F. Bock, C. Loizides and N. Schmidt, “Applicability of transverse mass scaling in hadronic collisions at energies available at the CERN Large Hadron Collider,” *Phys. Rev. C* **96**, no. 6, 064907 (2017)
- [270] J. Schaffner-Bielich, D. Kharzeev, L. D. McLerran, and R. Venugopalan, “Generalized scaling of the transverse mass spectrum at the relativistic heavy ion collider”, *Nucl. Phys.* **A705** (2002) 494–507.
- [271] R. Corke and T. Sjostrand, *JHEP* **1103**, 032 (2011)
- [272] C. Tsallis, “Possible Generalization of Boltzmann-Gibbs Statistics”, *J. Statist. Phys.* **52** (1988) 479–487.
- [273] STAR Collaboration, “Strange particle production in $p+p$ collisions at $\sqrt{s} = 200$ GeV”, *Phys. Rev.* **C75** (2007) 064901.
- [274] PHENIX Collaboration, “Detailed measurement of the e^+e^- pair continuum in $p + p$ and Au+Au collisions at $\sqrt{s_{NN}} = 200$ GeV and implications for direct photon production”, *Phys. Rev.* **C81** (2010) 034911.
- [275] A. A. Bylinkin and A. A. Rostovtsev, “Parametrization of the shape of hadron-production spectra in high-energy particle interactions”, *Phys. Atom. Nucl.* **75** (2012) 999–1005.
- [276] “A study of the general characteristics of proton-antiproton collisions at $\sqrt{s} = 0.2$ to 0.9 TeV”, *Nucl. Phys. B* **335** no. CERN-EP-89-85, (Jul, 1989) 261–287. 30 p. <http://cds.cern.ch/record/199418>.
- [277] CMS Collaboration, “Measurement of charged pion, kaon, and proton production in proton-proton collisions at $\sqrt{s} = 13$ TeV”, *Phys. Rev.* **D96** no. 11, (2017) 112003.
- [278] D. d’Enterria and T. Pierog, “Global properties of proton-proton collisions at $\sqrt{s} = 100$ TeV”, *JHEP* **08** (2016) 170.

- [279] PHENIX Collaboration, “Measurement of neutral mesons in p+p collisions at $\sqrt{s}=200$ GeV and scaling properties of hadron production”, *Phys. Rev.* **D83** (2011) 052004.
- [280] T. Pierog, I. Karpenko, J. M. Katzy, E. Yatsenko, and K. Werner, “EPOS LHC: Test of collective hadronization with data measured at the CERN Large Hadron Collider”, *Phys. Rev.* **C92** no. 3, (2015) 034906.
- [281] UA1 Collaboration, “A Study of the General Characteristics of $p\bar{p}$ Collisions at $\sqrt{s} = 0.2$ TeV to 0.9 TeV”, *Nucl. Phys.* **B335** (1990) 261–287.
- [282] CMS Collaboration, “Charged particle multiplicities in pp interactions at $\sqrt{s} = 0.9, 2.36,$ and 7 TeV”, *JHEP* **01** (2011) 079.
- [283] ATLAS Collaboration, “Charged-particle multiplicities in pp interactions measured with the ATLAS detector at the LHC”, *New J. Phys.* **13** (2011) 053033,
- [284] M. L. Knichel, “Transverse momentum distributions of primary charged particles in $pp, p\text{-Pb}$ and $Pb\text{-Pb}$ collisions measured with ALICE at the LHC”, PhD thesis, Darmstadt, Tech. U., 2015. <https://cds.cern.ch/record/2119438>.
- [285] Klaus Werner, Private communication.
- [286] G. Bencédi (ALICE Collaboration), “New results on the multiplicity and centre-of-mass energy dependence of identified particle production in pp collisions with ALICE,” in *Proceedings of The European Physical Society Conference on High Energy Physics (EPS-HEP 2017)*, Venice, Italy, 5-12 July, 2017, PoS EPS **-HEP2017**, 359 (2018).
- [287] H.-L. Lai, M. Guzzi, J. Huston, Z. Li, P. M. Nadolsky, J. Pumplin, and C. P. Yuan, “New parton distributions for collider physics”, *Phys. Rev.* **D82** (2010) 074024.
- [288] D. de Florian, R. Sassot, and M. Stratmann, “Global analysis of fragmentation functions for pions and kaons and their uncertainties”, *Phys. Rev.* **D75** (2007) 114010.
- [289] D. d’Enterria, K. J. Eskola, I. Helenius, and H. Paukkunen, “Confronting current NLO parton fragmentation functions with inclusive charged-particle spectra at hadron colliders”, *Nucl. Phys.* **B883** (2014) 615–628.
- [290] B. A. Kniehl, G. Kramer, and B. Potter, “Fragmentation functions for pions, kaons, and protons at next-to-leading order”, *Nucl. Phys.* **B582** (2000) 514–536.
- [291] S. Kretzer, “Fragmentation functions from flavor inclusive and flavor tagged e^+e^- annihilations”, *Phys. Rev.* **D62** (2000) 054001.
- [292] Ilkka Helenius, Private communication.
- [293] ALICE Collaboration, “Neutral pion and η meson production in proton-proton collisions at $\sqrt{s} = 0.9$ TeV and $\sqrt{s} = 7$ TeV”, *Phys. Lett.* **B717** (2012) 162–172.
- [294] ALICE Collaboration, “ π^0 and η meson production in proton-proton collisions at $\sqrt{s} = 8$ TeV,” *Eur. Phys. J. C* **78**, no. 3, 263 (2018)
- [295] P. Bozek, “Collective flow in p-Pb and d-Pd collisions at TeV energies”, *Phys. Rev.* **C85** (2012) 014911.

- [296] I. Ravasenga (ALICE Collaboration), “Production of $\pi/k/p$ in pp and pb–pb collisions at $\sqrt{s} = 5.02$ TeV”, ALICE Analysis Note, ALICE-AN 3545, 2017.
- [297] ALICE Collaboration, “Charged-particle multiplicities in proton–proton collisions at $\sqrt{s} = 0.9$ to 8 TeV”, *Eur. Phys. J.* **C77** no. 1, (2017) 33.
- [298] STAR Collaboration, “Identified hadron spectra at large transverse momentum in p+p and d+Au collisions at $\sqrt{s_{NN}} = 200$ GeV”, *Phys. Lett.* **B637** (2006) 161–169.
- [299] T. Okubo and T. Sugitate, “Neutral pion measurement in p-Pb collisions at $\sqrt{s_{NN}} = 5.02$ TeV”, Jan, 2017. <https://cds.cern.ch/record/2255065>. Presented 16 Feb 2017.
- [300] D. Antreasyan, J. W. Cronin, H. J. Frisch, M. J. Shochet, L. Kluberg, P. A. Piroué, and R. L. Sumner, “Production of hadrons at large transverse momentum in 200-, 300-, and 400-GeV $p - p$ and p -nucleus collisions”, *Phys. Rev. D* **19** (Feb, 1979) 764–778.
- [301] J. W. Cronin, H. J. Frisch, M. J. Shochet, J. P. Boymond, P. A. Piroué, and R. L. Sumner, “Production of Hadrons with Large Transverse Momentum at 200 GeV and 300 GeV.”, *Phys. Rev. Lett.* **31** (Dec, 1973) 1426–1429.
- [302] J. L. Albacete *et al.*, “Predictions for p +Pb Collisions at $\sqrt{s_{NN}} = 5$ TeV: Comparison with Data”, *Int. J. Mod. Phys.* **E25** no. 9, (2016) 1630005.
- [303] G. Bencedi (ALICE Collaboration), “Nuclear modification factor of charged particles and light-flavour hadrons in p–Pb collisions measured by ALICE”, in *Proceedings of 51st Rencontres de Moriond on QCD and High Energy Interactions*, La Thuile, Italy, March 19-26, 2016. 2016. [arXiv:1609.05665](https://arxiv.org/abs/1609.05665) [nucl-ex].
- [304] L. Gatignon, “Secondary beams and areas”, 11 November 2013. <http://sba.web.cern.ch/sba/BeamsAndAreas/East/East.htm>. Last accessed 01/03/2019.
- [305] ALICE Collaboration, “ALICE trigger data-acquisition high-level trigger and control system: Technical Design Report”, Technical Design Report ALICE. CERN, Geneva, 2004. <https://cds.cern.ch/record/684651>.
- [306] ALICE Collaboration, “ALICE high-momentum particle identification: Technical Design Report”, Technical Design Report ALICE. CERN, Geneva, 1998. <https://cds.cern.ch/record/381431>.
- [307] G. Charpak, G. Melchart, G. Petersen, and F. Sauli, “High Accuracy Localization of Minimum Ionizing Particles Using the Cathode Induced Charge Center of Gravity Readout”, *Nucl. Instrum. Meth.* **167** (1979) 455.
- [308] A. H. Walenta, M. Kramer, E. Roderburg, G. Zech, H. Kapitza, and L. Jonsson, “Study of the IDC as a high rate vertex detector for the Zeus experiment”, *Nucl. Instrum. Meth.* **A265** (1988) 69–77.

Acknowledgments

First of all, I would like to thank my supervisors Péter Lévai and Gergely Gábor Barnaföldi for the constant source of support during my Ph.D.

I wish to express my gratitude to my colleague and friend Antonio Ortiz Velasquez for his guidance, patience, encouragement and for the useful conversations throughout the analysis works and paper writing periods. I appreciate that he provided support and supervision while I was at ICN/UNAM in Mexico City.

I am particularly thankful for the hospitality, shared ideas and support of Guy Paić and Eleazar Cautle during my stay at the ICN/UNAM.

I thank Luciano Diaz and Eduardo Murrieta for the technical support in running Monte Carlo simulations on the computer clusters at ICN/UNAM.

I am grateful to all members of the Light-Flavor Working Group in ALICE for the fruitful discussions and the friendly atmosphere.

I would also like to express my thanks to Ilkka Helenius for providing me theoretical calculations to the $\sqrt{s_{NN}} = 5.02$ TeV p-Pb and $\sqrt{s} = 7$ and $\sqrt{s} = 13$ TeV pp collision data presented in this thesis.

I also owe a debt to Klaus Werner for allowing me the use of the latest (unpublished) version of the EPOS 3 code in order to simulate $\sqrt{s} = 7$ and $\sqrt{s} = 13$ TeV pp collisions for this work.

At last but not least, I wish to express my special gratitude to Dezső Varga, Gergő Hamar, György Bencze, and Levente Molnár for their valuable help during my first period in my Ph.D. work.

Support for this work has been received from the following sources: Hungarian OTKA Grants NK106119 and K120660, Wigner GPU Laboratory, The European Particle physics Latin America NETWORK (EPLANET), CONA-CyT under the grant number 293375 and PAPIIT-UNAM under Project No. IN102118.

Summary

The wealth of data collected by the CERN LHC during Run 1 (2009–2013) data taking period, and the unprecedented center-of-mass (\sqrt{s}) energies reached during Run 2 (2015–2018) made it possible to study identified hadron production in new kinematic regimes. Measuring identified particle production over wide kinematic ranges is considered an informative probe of strong interactions at high energies.

This Ph.D. thesis mainly focuses on the measurements of single-inclusive particle transverse momentum (p_T) spectra of charged pions (π^\pm), kaons (K^\pm), and (anti)protons ($p(\bar{p})$) up to $p_T = 20 \text{ GeV}/c$. Particle production is studied at mid-rapidity in minimum bias inelastic proton-proton (pp) collisions as a function of \sqrt{s} and in non-single diffractive (NSD) proton-lead (p–Pb) collisions as a function of event charged-particle multiplicity measured at forward rapidity using the ALICE detector at the CERN LHC. The increase of \sqrt{s} reached at the LHC opens up domains in Bjorken- x where the contribution of gluons to inclusive hadron production becomes dominant. Therefore, identified particle spectra at the top LHC energy in pp collisions provide new constraints on gluon fragmentation in theoretical calculations and gives input to tune the modeling of several contributions in state-of-the-art Monte Carlo (MC) event generators. Also, in this kinematic regime, the nuclear modification to hadronic structure is expected to be sizable. By using a proton instead of a heavy nucleus as a projectile, measurements of p–Pb collisions have unique sensitivity to the initial-state nuclear wave function. High- p_T identified particle spectra measured in p–Pb collisions provide new constraints on the nuclear-modified parton distribution functions (nPDFs) and the flavor dependence of sea-quark nPDFs, which are key inputs in interpreting a large amount of experimental data like deuterium-gold and deep inelastic scattering.

My main scientific results are summarized in the following points:

1. I performed a double-differential analysis to study the production of π^\pm , K^\pm , and $p(\bar{p})$ as a function of charged-particle multiplicity and the p_T of the leading (highest transverse momentum) jet in pp collisions generated by general-purpose MCs. I found that the presence of jets plays an important role in describing collective-like phenomena in small collision systems.
2. I measured the invariant yields of π^\pm , K^\pm , and $p(\bar{p})$ in NSD p–Pb collisions at $\sqrt{s_{NN}} = 5.02 \text{ TeV}$ as a function of charged-particle multiplicity up to $p_T = 20 \text{ GeV}/c$ around mid-rapidity. I found that at intermediate p_T ($2\text{--}10 \text{ GeV}/c$) the p/π ratio shows a monotonic increase with multiplicity, which is qualitatively reminiscent of that measured in Pb–Pb collisions. I found that at high p_T ($> 10 \text{ GeV}/c$) the p_T -integrated particle ratios are system-size independent for pp, p–Pb, and Pb–Pb collisions.
3. I measured the invariant yields of π^\pm , K^\pm , and $p(\bar{p})$ in minimum bias inelastic pp collisions at $\sqrt{s} = 7$ and $\sqrt{s} = 13 \text{ TeV}$ up to $p_T = 20 \text{ GeV}/c$ at mid-rapidity. I determined the $\sqrt{s} = 5.02 \text{ TeV}$ pp reference cross section, and I constructed the nuclear modification factor (R_{pPb}) for the studied hadrons. I showed that at intermediate p_T the R_{pPb} for $p(\bar{p})$ indicates a characteristic (Cronin) enhancement. I found that the R_{pPb} for $p_T > 10 \text{ GeV}/c$ follows binary nucleon scaling.
4. For $\sqrt{s} = 13 \text{ TeV}$ pp data, I found that the identified particle spectra are consistent with the empirical x_T ($= 2p_T/\sqrt{s}$) scaling in the hard scattering regime and that the K/π ratio shows a significant deviation from the empirical transverse mass scaling law for $p_T \lesssim 6 \text{ GeV}/c$. I found that the p_T -dependent p/π ratio in the intermediate p_T region shows a modest departure towards higher p_T going from $\sqrt{s} = 7$ to $\sqrt{s} = 13 \text{ TeV}$.
5. I constructed and successfully tested a prototype asymmetric multi-wire proportional chamber with reduced size and showed that a significant improvement can be reached in its position resolution by measuring analog signals on their segmented cathode planes. I contributed with a physics performance study to the Letter of Intent document of the ALICE VHMPID upgrade project where I wrote a dedicated section summarizing my Monte Carlo simulation studies performed using identified two-particle angular correlations.

Összefoglalás

A CERN LHC gyorsító lehetővé tette proton-proton (pp) és nehézion ütközések kísérleti vizsgálatát, az erősen kölcsönható kvarkanyag tanulmányozását korábban nem látott magas ütközési energiákon ($\sqrt{s_{NN}} = 0.9 - 13$ TeV). A CERN LHC által a Run 1 (2009–2013) és a Run 2 (2015–2018) futási periódusokban felvett jelentős mennyiségű adat hozzájárult az azonosított hadronok hozamának új kinematikai tartományokban történő tanulmányozásához.

Doktori értekezésemben nagy transzverzális impulzusú (p_T) töltött pionok (π^\pm), kaonok (K^\pm) és (anti)protonok ($p(\bar{p})$) hozamát vizsgáltam a $p_T < 20$ GeV/c tartományban középrapiditásnál a CERN LHC ALICE kísérleti együttműködésben. Az említett részecskék hozamait a kísérlet detektora által felvett rugalmatlan proton-proton (pp) és nem-egyszeresen diffraktív proton-ólom (p-Pb) ütközésekben tanulmányoztam, rendre az ütközési energia (\sqrt{s}) és a részecske-multiplicitás függvényében. Az ütközési energia növelésével új, korábbinál alacsonyabb Bjorken- x tartomány vizsgálata vált lehetővé az LHC gyorsítónál, ahol a gluonok inkluzív hadron-produkcióbeli szerepe jelentőssé válik. Ez pp ütközéseket tekintve fontos kísérleti információt jelent: egyrészt a gluon-hadron fragmentációs függvényeknek az elméleti számolásokbeli pontosabb meghatározását illetően, másrészt a széleskörűen alkalmazott Monte Carlo (MC) eseménygenerátorok továbbfejlesztéséhez. Proton-ólom ütközéseket tekintve, az új, alacsony x régióban a nukleáris effektusok hadronszerkezet-módosító hatásai felerősödnek. Továbbá, ezen típusú ütközések érzékenyek lesznek a kezdetiállapot-effektusokra. A nagy transzverzális impulzusú azonosított részecskék p-Pb ütközésekben történő mérése új kísérleti információt nyújt a nukleáris környezet által módosított partoneloszlás-függvények (és azok ízfüggésének) pontosabb ismeretéhez.

Főbb tudományos eredményeimet az alábbi pontokban összegzem:

1. A legújabb, széleskörűen alkalmazott Monte Carlo eseménygenerátorokkal szimulált pp eseményekben tanulmányoztam az azonosított töltött részecskék hozamának az esemény multiplicitásától és az eseményben talált jetek p_T -jétől való függését. Azt találtam, hogy a jet jelenléte az eseményben jelentősen befolyásolja a kis ütközési rendszereknél megfigyelt kollektív effektusokat.
2. Megmértem a nagy transzverzális impulzusú π^\pm , K^\pm és $p(\bar{p})$ invariáns hozamokat p-Pb ütközésekben az esemény-multiplicitás függvényében $\sqrt{s_{NN}} = 5.02$ TeV ütközési energián és azt találtam, hogy a közepes p_T tartományban ($p_T = 2 - 10$ GeV/c) a p/π arány az esemény-multiplicitással monoton nő, hasonlóan az ólom-ólom (Pb-Pb) eseményekben megfigyeltekkel. Továbbá azt találtam, hogy nagy p_T (> 10 GeV/c) esetén az integrált részecskearányok függetlenek az ütközési rendszerek (pp, p-Pb és Pb-Pb) méretétől.
3. Megmértem a nagy transzverzális impulzusú π^\pm , K^\pm és $p(\bar{p})$ invariáns hozamokat pp ütközésekben $\sqrt{s} = 7$ TeV és $\sqrt{s} = 13$ TeV ütközési energiákon középrapiditásnál. Új, $\sqrt{s} = 5.02$ TeV-es pp referencia-adatsorokat határoztam meg, melyeket felhasználva megkonstruáltam a nukleáris módosulási faktort (R_{pPb}) az említett hadronokra. Azt találtam, hogy a közepes p_T tartományban az R_{pPb} (anti)protonokra közel háromszoros Cronin növekedést mutat a töltött hadronokhoz képest, míg nagy p_T értékekre az R_{pPb} a vizsgált részecskékre a páronkénti nukleon-nukleon ütközések számával skálázik.
4. A $\sqrt{s} = 13$ TeV-es pp adatokat kiértékelve azt találtam, hogy a π^\pm , K^\pm és $p(\bar{p})$ p_T spektrumok a kemény szórási régióban követik az empirikus $x_T = 2p_T/\sqrt{s}$ skálázást, míg a K/π részecskearányánál $p_T = 6$ GeV/c alatt jelentősen sérül a transzverzális tömeg szerinti empirikus skálázás. Továbbá azt találtam, hogy a közepes p_T tartományban a p/π arány az ütközési energia ($\sqrt{s} = 7$ TeV-ről $\sqrt{s} = 13$ TeV-re történő) növekedésével enyhe eltolódást mutat nagyobb p_T értékek felé.
5. Megépítettem és teszteltem egy új típusú, kisméretű, gáztöltésű, sokszálas proporcionális kamrát az ALICE VHMPID detektorához. Ezen prototípus kamra analóg jeleit vizsgálva meghatároztam annak helyfelbontását és megmutattam, hogy vele kiváló ($90 \mu\text{m} \pm 4\%$) helyfelbontás érhető el. Az ALICE VHMPID Letter Of Intent dokumentumához kétrészecske-korrelációs MC szimulációkat készítettem, amelyeknek eredményeit annak egy külön fejezetében foglaltam össze.

ADATLAP

a doktori értekezés nyilvánosságra hozatalához*

I. A doktori értekezés adatai

A szerző neve: Bencédi Gyula

MTMT-azonosító: 10039346

A doktori értekezés címe és alcíme:

Study of charged pion, kaon, and (anti)proton production at high transverse momenta in pp and p--Pb collisions with the ALICE experiment at the CERN LHC

DOI-azonosító⁴⁶: 10.15476/ELTE.2019.033

A doktori iskola neve: Eötvös Loránd Tudományegyetem Fizika Doktori Iskola

A doktori iskolán belüli doktori program neve: Részecskefizika és csillagászat

A témavezető neve és tudományos fokozata: Dr. Lévai Péter, Dr. Barnaföldi Gergely Gábor

A témavezető munkahelye: MTA Wigner Fizikai Kutatóközpont

II. Nyilatkozatok

1. A doktori értekezés szerzőjeként

a) hozzájárulok, hogy a doktori fokozat megszerzését követően a doktori értekezésem és a tézisek nyilvánosságra kerüljenek az ELTE Digitális Intézményi Tudástárban. Felhatalmazom a Természettudományi kar Dékáni Hivatali Doktori, Habilitációs és Nemzetközi Ügyek Csoportjának ügyintézőjét, hogy az értekezést és a téziseket feltöltse az ELTE Digitális Intézményi Tudástárba, és ennek során kitöltse a feltöltéshez szükséges nyilatkozatokat.

b) kérem, hogy a mellékelt kérelemben részletezett szabadalmi, illetőleg oltalmi bejelentés közzétételéig a doktori értekezést ne bocsássák nyilvánosságra az Egyetemi Könyvtárban és az ELTE Digitális Intézményi Tudástárban;

c) kérem, hogy a nemzetbiztonsági okból minősített adatot tartalmazó doktori értekezést a minősítés (dátum)-ig tartó időtartama alatt ne bocsássák nyilvánosságra az Egyetemi Könyvtárban és az ELTE Digitális Intézményi Tudástárban;

d) kérem, hogy a mű kiadására vonatkozó mellékelt kiadó szerződésre tekintettel a doktori értekezést a könyv megjelenéséig ne bocsássák nyilvánosságra az Egyetemi Könyvtárban, és az ELTE Digitális Intézményi Tudástárban csak a könyv bibliográfiai adatait tegyék közzé. Ha a könyv a fokozatszerzést követően egy évig nem jelenik meg, hozzájárulok, hogy a doktori értekezésem és a tézisek nyilvánosságra kerüljenek az Egyetemi Könyvtárban és az ELTE Digitális Intézményi Tudástárban.

2. A doktori értekezés szerzőjeként kijelentem, hogy

a) az ELTE Digitális Intézményi Tudástárba feltöltendő doktori értekezés és a tézisek saját eredeti, önálló szellemi munkám és legjobb tudomásom szerint nem sértem vele senki szerzői jogait;

b) a doktori értekezés és a tézisek nyomtatott változatai és az elektronikus adathordozón benyújtott tartalmak (szöveg és ábrák) mindenben megegyeznek.

3. A doktori értekezés szerzőjeként hozzájárulok a doktori értekezés és a tézisek szövegének plágiumkereső adatbázisba helyezéséhez és plágiumellenőrző vizsgálatok lefuttatásához.

Kelt: Budapest, 2019. március 8.


.....
a doktori értekezés szerzőjének aláírása

*ELTE SZMSZ SZMR 12. sz. melléklet